

# Investigation of the magnetic and electronic structure of Fe in molecules and chalcogenide systems

---

by Christian Taubitz

Dissertation for the degree of Doktor der  
Naturwissenschaften (Dr. rer. nat.)

presented to the

**Department of Physics**  
**University of Osnabrück**

Osnabrück

April 2010



**Supervisor and first reviewer:**

apl. Prof. Prof. h.c. Dr. Dr. h.c. Manfred Neumann

**Second reviewer:**

Prof. Dr. Joachim Wollschläger



[www.metallobjekte-fetzer.de](http://www.metallobjekte-fetzer.de)

*”Nachdem ich Feynmans Beschreibung einer Rose gelesen hatte -, in der er erläuterte, dass er den Duft und die Schönheit der Blume zu würdigen wisse wie jeder andere, dass aber seine physikalischen Kenntnisse dieses Erlebnis ausserordentlich intensivierten, weil er auch das Wunder und die Herrlichkeit der zugrunde liegenden molekularen, atomaren und subatomaren Prozesse einbeziehen könne -, war ich den Naturwissenschaften auf immer verfallen.”*

–Brian Green (\*9.Februar 1963 in New York City), US-amerikanischer Physiker, bedeutender Vertreter der Stringtheorie.

**In diesem Zusammenhang zum Eisen (Anmerkung des Autors):**

Im Urknall entstanden nur die leichten Elemente wie Wasserstoff und Helium. Schwerere Elemente wie Kohlenstoff, Sauerstoff oder gar Silizium wurden nachfolgend in Sonnen ”gebacken”.

Doch zur Entstehung von Elementen wie Eisen mussten Sonnen sterben und in einer Supernova vergehen.



# Contents

<b>Introduction</b>	<b>1</b>
<b>1 History and Basics</b>	<b>3</b>
1.1 The history of X-ray spectroscopy . . . . .	3
1.2 Experimental X-ray spectroscopic techniques . . . . .	6
1.2.1 X-ray Photoelectron Spectroscopy (XPS) . . . . .	6
1.2.1.1 Spectral characteristics . . . . .	9
1.2.2 X-ray Absorption Spectroscopy (XAS) . . . . .	14
1.2.2.1 X-ray Magnetic Circular Dichroism (XMCD) . . . . .	17
1.3 Instrumentation . . . . .	20
1.3.1 The photoelectron spectrometer PHI 5600ci . . . . .	20
1.3.2 Measurements at synchrotron endstations . . . . .	21
1.4 X-ray absorption in multiplet theory . . . . .	26
1.4.1 Single-particle approximation . . . . .	26
1.4.2 The multiplet effect . . . . .	27
1.5 Magnetism . . . . .	34
1.5.1 Magnetism in solids . . . . .	34
1.5.2 Magnetism in theory . . . . .	38
<b>2 Fe in different molecules and chalcogenide systems</b>	<b>41</b>
2.1 Introduction . . . . .	41
2.1.1 Calculation overview . . . . .	43
2.2 Results . . . . .	54
2.2.1 Fe in $\text{Sr}_2\text{FeMoO}_6$ . . . . .	56
2.2.2 Fe in $\text{Fe}_{0.5}\text{Cu}_{0.5}\text{Cr}_2\text{S}_4$ . . . . .	58
2.2.3 Fe in $\text{LuFe}_2\text{O}_4$ . . . . .	59
2.2.4 Fe in the Ferric star . . . . .	65
2.2.5 Fe in $\text{Mo}_{72}\text{Fe}_{30}$ and $\text{W}_{72}\text{Fe}_{30}$ . . . . .	74
2.3 Conclusion . . . . .	77
<b>3 Investigation of the Fe valence state in <math>\text{Sr}_2\text{FeMoO}_6</math></b>	<b>81</b>
3.1 Introduction . . . . .	81
3.2 Results . . . . .	83
3.3 Conclusion . . . . .	87

<b>4</b>	<b>Valence states in <math>\text{Fe}_{1-x}\text{Cu}_x\text{Cr}_2\text{S}_4</math></b>	<b>89</b>
4.1	Introduction . . . . .	89
4.2	Experimental Details . . . . .	94
4.3	Results . . . . .	94
4.3.1	Investigation of the Cr valence . . . . .	95
4.3.2	Investigation of the Cu valence . . . . .	96
4.3.3	Investigation of the Fe valence . . . . .	98
4.3.4	Investigation of the XMCD measurements . . . . .	106
4.4	Discussion . . . . .	113
4.4.1	Magnetism in $\text{Fe}_{1-x}\text{Cu}_x\text{Cr}_2\text{S}_4$ . . . . .	114
4.4.2	Conduction and magnetoresistance in $\text{Fe}_{1-x}\text{Cu}_x\text{Cr}_2\text{S}_4$ . . . . .	117
4.5	Conclusion . . . . .	124
<b>5</b>	<b>Summary and Outlook</b>	<b>127</b>
5.1	Summary . . . . .	127
5.1.1	Fe in different chalcogenide compounds . . . . .	127
5.1.2	Ageing effect in $\text{Sr}_2\text{FeMoO}_6$ . . . . .	128
5.1.3	Valence states in $\text{Fe}_{1-x}\text{Cu}_x\text{Cr}_2\text{S}_4$ . . . . .	129
5.2	Outlook . . . . .	129
	<b>Acknowledgement</b>	<b>131</b>
	<b>Bibliography</b>	<b>133</b>
	<b>List of Publications</b>	<b>145</b>

# List of Figures

1.1	Heinrich Hertz (1857 - 1894) (left), Wilhelm Hallwachs (1859 - 1922) (middle) and Joseph Thomson (1856 - 1940) (right) . . . . .	3
1.2	Albert Einstein (1879 - 1955) . . . . .	4
1.3	Robert Millikan (1868 - 1953) (left) and Arthur Compton (1892 - 1962) (right)	5
1.4	Albert Einstein (1879 - 1955) . . . . .	5
1.5	Kai Siegbahn (1918 - 2007) . . . . .	6
1.6	The principle of X-ray photoelectron spectroscopy (XPS). More details are given in the text. . . . .	8
1.7	The <i>chemical shift</i> of the Fe 2p XPS spectrum of FeO and Fe <sub>2</sub> O <sub>3</sub> compared to metallic Fe. The origin of the line splitting and the satellites will be explained in the sections below. . . . .	10
1.8	Illustration of a charge transfer excitation in a transition metal oxide (Kuepper, 2005). . . . .	13
1.9	The principle of X-ray absorption spectroscopy (XAS). More details are given in the text. . . . .	16
1.10	Illustration of a $2p \rightarrow 3d$ excitation with right circularly polarised light to empty d-continuum states in a solid (according to Kapusta <i>et al.</i> (1999)). The excitation is separated in transitions from the core $p_{\frac{1}{2}}$ ( $L_2$ ) levels (upper panel) and the ones from the $p_{\frac{3}{2}}$ ( $L_3$ ) levels (lower panel). Note that here the magnetisation of the sample is assumed to be antiparallel to the photon wave vector ( $\Delta m_l = +1$ ). . . . .	18
1.11	Layout of the PHI 5600ci multitechnique spectrometer. More details are given in the text. . . . .	20
1.12	Pictures of the BESSY II in Berlin (a), the NSRRC in Taiwan (b), the ALS in Berkeley (USA) (c), the ELETTRA in Trieste (Italy) (d) and the SLS in Villigen (Switzerland) (e). . . . .	22
1.13	Schematic plot of a synchrotron. More details are given in the text. . . . .	23
1.14	Illustration of the an undulator (top) and an APPLE-type undulator (bottom). More details are given in the text. . . . .	24
1.15	Schematic plot of a typical beamline setup. . . . .	25
1.16	Atomic multiplet calculation of a Ti <sup>4+</sup> XAS spectrum. . . . .	29
1.17	Splitting patterns of d orbitals in ligand fields for (a) linear ML <sub>2</sub> , (b) tetrahedral ML <sub>4</sub> , (c) square planar ML <sub>4</sub> , (d) trigonal-bipyramidal ML <sub>5</sub> and (e) octahedral ML <sub>6</sub> . . . . .	30

1.18	Ligand-field multiplet calculations of $\text{Ti}^{4+}$ XAS spectra with different cubic crystal-field values. a) selected calculations together with their unbroadened lines. b) calculation overview attached from de Groot (2001) in steps of 0.3 eV. Bottom spectrum has a crystal-field of 0.0 eV, top spectrum of 4.5 eV.	31
1.19	Series of charge-transfer multiplet calculations for the ground state $3d^8 + 3d^9\bar{L}$ , attached from de Groot (2001).	33
1.20	An overview of different types of magnetism. The strength and direction of the spontaneous magnetisation and the induced magnetisation by an external magnetic field are illustrated (below the Curie temperature and Néel temperature, respectively). Inspired by Günther (2003).	37
2.1	Overview of Fe properties: a) the classic electron shell, b) information about Fe in a periodic table, c) the atomic electron configuration, d) and e) the two possible crystal structures.	42
2.2	Fe 2p XAS atomic multiplet calculation for $\text{Fe}^{2+}$ and $\text{Fe}^{3+}$ .	43
2.3	Fe 2p XAS and XMCD multiplet calculations for $\text{Fe}^{3+}$ in $O_h$ (left panel) and $T_d$ (right panel) symmetry with different crystal-field (CF) values. The crystal-field is changed from 0 eV to 3.6 eV with an increment of 0.3 eV. For all calculations the influence of the temperature and charge transfer is neglected. More details are given in the text.	44
2.4	Comparison of the $\text{Fe}^{3+}$ XAS and XMCD multiplet calculations in $O_h$ symmetry with the ones in $T_d$ symmetry. The crystal-field was set to 0.3 eV and 1.5 eV.	45
2.5	Illustration of the high-spin and low-spin ground states for $\text{Fe}^{3+}$ in $O_h$ (left panel) and $T_d$ (right panel) ligand field symmetry.	46
2.6	Fe 2p XAS and XMCD multiplet calculations for $\text{Fe}^{2+}$ in $O_h$ (left panel) and $T_d$ (right panel) symmetry with different crystal-field (CF) values. The crystal-field is changed from 0 eV to 3.0 eV with an increment of 0.3 eV. For all calculations the influence of the temperature and charge transfer is neglected. More details are given in the text.	47
2.7	Comparison of the $\text{Fe}^{2+}$ XAS and XMCD multiplet calculations in $O_h$ symmetry with the ones in $T_d$ symmetry. The crystal-field was set to 0.3 eV and 1.5 eV.	48
2.8	Illustration of the high spin and low spin states for $\text{Fe}^{2+}$ in $O_h$ (left panel) and $T_d$ (right panel) ligand field symmetry.	49
2.9	Fe 2p XAS and XMCD charge transfer multiplet calculations for $\text{Fe}^{3+}$ with the $\Delta$ value changed from 12 eV to -12 eV with an increment of 3 eV. For all calculations the influence of the temperature and crystal field is neglected. More details are given in the text.	50
2.10	Fe 2p XAS and XMCD charge transfer multiplet calculations for $\text{Fe}^{2+}$ with the $\Delta$ value changed from 12 eV to -12 eV with an increment of 3 eV. For all calculations the influence of the temperature and crystal field is neglected. More details are given in the text.	51
2.11	Fe 2p XAS and XMCD multiplet calculations for $\text{Fe}^{3+}$ (panel a), b)) and $\text{Fe}^{2+}$ (panel c), d)) with the temperature set to $T = 0$ K and $T = 400$ K. For all calculations the influence of charge transfer and crystal field is neglected. More details are given in the text.	52



2.12	The calculated $\mu^+$ , $\mu^-$ and $\mu^0$ Fe 2p spectra for $\text{Fe}^{3+}$ (panel a), b)) and $\text{Fe}^{2+}$ (panel c), d)) together with the corresponding XAS and XMCD spectra. The temperature was set to $T = 0$ K and $T = 400$ K, respectively. The influence of charge transfer and crystal field is neglected. More details are given in the text. . . . .	53
2.13	Overview of Fe 2p XAS measurements of various chalcogenide systems. . .	54
2.14	Overview of Fe 2p XMCD measurements of various chalcogenide systems. .	56
2.15	Fe 2p XAS (upper panel) and XMCD (lower panel) CT multiplet calculation of a mixed 50% $\text{Fe}^{2+}$ / 50% $\text{Fe}^{3+}$ valence state. In addition to the mixed spectra (black line) also the separated $\text{Fe}^{2+}$ (red line) and $\text{Fe}^{3+}$ (green line) calculations are shown. . . . .	57
2.16	Fe 2p XAS measurement of $\text{Fe}_{0.5}\text{Cu}_{0.5}\text{Cr}_2\text{S}_4$ and corresponding crystal-field (CF) and charge transfer (CT) multiplet calculations. . . . .	59
2.17	Left: Crystal structure of $\text{LuFe}_2\text{O}_4$ showing the hexagonal double layered arrangement of Lu (large dark-grey spheres), Fe (small black spheres), and oxygen (large white spheres) along the c-axis in the trigonal space group $R\bar{3}m$ . Right: The Fe double layers are shown with a triangular interconnectivity. The figures are adopted from Subramanian <i>et al.</i> (2006). . . . .	60
2.18	Two models describing the spin and charge ordering of the Fe double layer in $\text{LuFe}_2\text{O}_4$ . a) A frustrated spin configuration according to Nagano <i>et al.</i> (2007). b) A spin configuration without frustration according to Siratori <i>et al.</i> (1992); Ikeda <i>et al.</i> (2005b). The long red and blue arrows mark the spin direction of the $\text{Fe}^{3+}$ ions, while the shorter orange ones denote the direction of the $\text{Fe}^{2+}$ spins. Dotted circles represent frustrated $\text{Fe}^{2+}$ spins. . . . .	62
2.19	Fe 2p XAS measurements of $\text{LuFe}_2\text{O}_4$ in the TEY and TFY mode. The results are compared to crystal-field multiplet calculations with different $\text{Fe}^{2+}$ / $\text{Fe}^{3+}$ ratios. . . . .	63
2.20	Fe 2p XMCD measurements (panel (a)) and corresponding crystal-field multiplet calculations (panel (b) and (c)). . . . .	64
2.21	<b>Left:</b> Structure of the ferric star $\{Fe^{III}[Fe^{III}(L^1)_2]_3\}$ attached from Takacs (2005). Fe: Green; O: Red; C: Black; N: Blue; H: White. The Fe-ligand bondings are marked with dashed lines. <b>Right:</b> Illustration of the ferromagnetic ground state. . . . .	65
2.22	Fe 2p XAS and XMCD measurements of FeStar in comparison with CT multiplet calculations. . . . .	66
2.23	The integral of the Fe 2p XMCD measurement and XMCD CT multiplet calculations shown in figure 2.22. . . . .	68
2.24	Fe 2p XAS measurements of the ferric star. One spectrum shows an early measurement with a small beam exposure time and only 1% photon yield (light blue). The second spectrum was measured with the same yield but an exposure time of about 6 hours (violet). The third one, which was already discussed above, was measured with 100% photon yield (red). . . . .	69
2.25	Fe 2p XAS and XMCD measurement of a FeStar sample, which was exposed to the beam for a short time with only 1% undulator yield. The spectra are compared to CT multiplet calculations. . . . .	70

2.26	The integral of the Fe 2p XMCD measurement and XMCD CT multiplet calculations shown in figure 2.25. . . . .	71
2.27	<b>Left:</b> The molecular structure of the ferric star ( $\text{Fe}_4$ ) produced by Barra <i>et al.</i> (1999). The illustration is attached from Accorsi <i>et al.</i> (2006). Fe: Red; O: Yellow; C: Gray. <b>Right:</b> The molecular structure of the ferric star or FeStar produced by Saalfrank <i>et al.</i> (2001, 2006) attached from Takacs (2005). Fe: Green; O: Red; C: Black; N: Blue; H: White. . . . .	72
2.28	XAS and XMCD analysis on $\text{Fe}_4$ . Absorption spectra (white dots: $\mu^+$ ; black dots: $\mu^-$ ) and dichroic signal (black solid line) at $T = 0.75$ K and $B = 3.0$ T, along with simulated curves (gray solid lines) obtained using ligand field multiplet calculations. The figure is attached from Mannini <i>et al.</i> (2009b). . . . .	73
2.29	Ball-and-stick representation of the $\text{M}_{72}\text{Fe}_{30}$ ( $M = \text{Mo}, \text{W}$ ) cluster (Müller <i>et al.</i> , 2001). The ligand structure within the cluster is omitted for clarity. M: blue; Fe: yellow; O: red. . . . .	74
2.30	XAS and XMCD measurements of $\text{Mo}_{72}\text{Fe}_{30}$ (left, top and bottom) and $\text{W}_{72}\text{Fe}_{30}$ (right, top and bottom). In addition the spectra were simulated with charge transfer multiplet calculations (black line). For $\text{Mo}_{72}\text{Fe}_{30}$ the calculation assumes a $\text{Fe}^{2+} / \text{Fe}^{3+}$ ratio of about 45% / 55%, while for $\text{W}_{72}\text{Fe}_{30}$ a calculation with 100% $\text{Fe}^{3+}$ shows good agreement with the measurement. Finally also the integrated XMCD measurements are shown (red dotted line). . . . .	75
2.31	Comparison of the $L_3$ part of two Fe 2p XAS measurements of $\text{Mo}_{72}\text{Fe}_{30}$ taken at different times of the experiment. One spectrum was measured at the beginning of the experiment with a small exposure time of the sample to the photon beam (green line). The other was taken at the end of the measurement period (green dotted line). In addition also the photon energies of the $L_3$ line of divalent and trivalent Fe found by reference measurements are marked with dotted lines. . . . .	76
2.32	<b>Left, top:</b> Ball-and-stick representation of the $\text{W}_{72}\text{Fe}_{30}$ without the $\text{NH}_4^+$ ions but emphasising the 25 $\text{SO}_4^{2-}$ ligands coordinated in three different ways to the inner shell of the cluster and their disorder as a sign of the complexity. <b>Left, bottom:</b> One $\{\text{Fe}_3\text{W}_3\text{O}_6\}$ -type pore together with one $\{(W)\text{W}_5\}$ -type pentagonal unit and three different coordination types of the $\text{SO}_4^{2-}$ ligands. W: green; Fe: orange; O: red; $\text{SO}_4^{2-}$ ligands: yellow, lilac and turquoise. The disordered $\text{SO}_4^{2-}$ ligand positions are transparent for clarity. <b>Right, top:</b> Space-filling representation of $\text{W}_{72}\text{Fe}_{30}$ highlighting the affinity of the 20 $\{\text{Fe}_3\text{W}_3\text{O}_6\}$ -type pores for the 20 $\text{NH}_4^+$ cations located on the $C_3$ axes. <b>Right, bottom:</b> Two views of the pore situation (N blue, H light gray, other colors as in <b>left</b> ). The illustrations are taken from Todea <i>et al.</i> (2010). . . . .	77
3.1	The alternating $\text{FeO}_6$ and $\text{MoO}_6$ octahedra in the double perovskite structure of $\text{Sr}_2\text{FeMoO}_6$ attached from Tomioka <i>et al.</i> (2000). The Sr which is situated in-between the oxygen octahedra is omitted here for simplification. In addition the direction and strength of the ferrimagnetically coupled Fe and Mo spin magnetic moments are illustrated (blue arrows). . . . .	82

3.2	Fe 2p XAS and XMCD measurements of $\text{Sr}_2\text{FeMoO}_6$ together with multiplet calculations. One set of calculations is done for a mixed Fe valence state comprising 50% $\text{Fe}^{2+}$ and 50% $\text{Fe}^{3+}$ ions (left panel) the other for a 70% $\text{Fe}^{2+}$ / 30% $\text{Fe}^{3+}$ ratio (right panel). . . . .	84
3.3	XAS (upper panel) and XMCD (lower panel) measurements of $\text{Sr}_2\text{FeMoO}_6$ recorded in January 2004 (blue line) and August 2004 (red line). . . . .	85
3.4	An overview of several Fe 2p XAS measurements of the <i>same</i> $\text{Sr}_2\text{FeMoO}_6$ sample recorded over several years (black lines). It is attached from Kuepper <i>et al.</i> (2008). The date of each experiment is displayed. For one experiment a total fluorescence yield (TFY) spectrum has also been recorded (blue line). In addition CT multiplet calculations for different $\text{Fe}^{2+}$ and $\text{Fe}^{3+}$ ratios are shown (red lines). . . . .	86
4.1	The unit cell of the spinel $\text{Fe}_{1-x}\text{Cu}_x\text{Cr}_2\text{S}_4$ . The black and orange cubes all contain the same atomic structure. It is omitted here for simplification. The blue lines indicate the octahedral symmetry of the Cr-site and the tetrahedral symmetry of the mixed Cu-Fe site, respectively. . . . .	90
4.2	Illustration of a channel of the tripleexchange interaction in $\text{Fe}_{1-x}\text{Cu}_x\text{Cr}_2\text{S}_4$ . Here only the main part of the unit cell is shown. The spin direction is indicated by white arrows. . . . .	91
4.3	Tripleexchange process in $\text{Fe}_{1-x}\text{Cu}_x\text{Cr}_2\text{S}_4$ reproduced from Fritsch <i>et al.</i> (2003). The rough bandpositions are adopted from band-structure calculations of Park <i>et al.</i> (1999). The mobile electrons and empty states, in which they are hopping, are indicated by the violet spheres. . . . .	92
4.4	Cr 2p XPS spectra of $\text{Fe}_{1-x}\text{Cu}_x\text{Cr}_2\text{S}_4$ with different Cu concentrations. . .	95
4.5	Cu 3s XPS spectra of $\text{Fe}_{1-x}\text{Cu}_x\text{Cr}_2\text{S}_4$ with different Cu concentrations compared to ceramic $\text{Cu}_2\text{O}$ (formally $\text{Cu}^+$ ) and single crystalline $\text{CuO}$ (formally $\text{Cu}^{2+}$ ) reference spectra. . . . .	96
4.6	Cu 2p XAS spectrum of $\text{Fe}_{0.5}\text{Cu}_{0.5}\text{Cr}_2\text{S}_4$ (blue line) compared with a spectrum taken from Deb <i>et al.</i> (2003) (black line) and reference measurements of single crystalline $\text{Cu}_2\text{O}$ (formally $\text{Cu}^+$ ) and $\text{CuO}$ (formally $\text{Cu}^{2+}$ ). . . .	97
4.7	Cu 2p XAS spectra of in situ cleaned single crystalline $\text{Cu}_2\text{O}$ (formally $\text{Cu}^+$ )(red line) and $\text{CuO}$ (formally $\text{Cu}^{2+}$ )(green line) together with measurements of single crystalline $\text{Cu}_2\text{O}$ that was not cleaned and one that was cleaned inadequately (dotted lines). . . . .	98
4.8	Fe 2p XAS spectra of $\text{Fe}_{0.5}\text{Cu}_{0.5}\text{Cr}_2\text{S}_4$ cleaned in air (red line) and rasped in-situ (blue line) compared to reference measurements. The $\text{FeO}$ (formally $\text{Fe}^{2+}$ ) and the $\text{Fe}_2\text{O}_3$ (formally $\text{Fe}^{3+}$ ) spectra have been taken from Regan <i>et al.</i> (2001). . . . .	99
4.9	Fe 2p XAS spectra of $\text{Fe}_{0.5}\text{Cu}_{0.5}\text{Cr}_2\text{S}_4$ , obtained with the photon helicity parallel ( $\rho^+$ ) and antiparallel ( $\rho^-$ ) to the magnetisation, respectively. The XMCD spectrum (blue) corresponds to the difference between $\rho^+$ and $\rho^-$ ( $\text{XMCD} \equiv \rho^+ - \rho^-$ ). . . . .	100
4.10	Fe 2p XPS spectra of $\text{Fe}_{0.5}\text{Cu}_{0.5}\text{Cr}_2\text{S}_4$ cleaved in-situ (blue line), rasped in air (red line) and powdered in air (green line) compared to reference measurements of $\text{FeO}$ (formally $\text{Fe}^{2+}$ ) and $\text{Fe}_2\text{O}_3$ (formally $\text{Fe}^{3+}$ , taken from Moulder <i>et al.</i> (1992)). . . . .	101

4.11	Fe 2p XAS spectra of $\text{Fe}_{0.5}\text{Cu}_{0.5}\text{Cr}_2\text{S}_4$ cleaved in situ. Spectrum (a) was measured at the edge, (b) between the edge and the centre and (c) at the centre of the cleaved surface. This is also illustrated in the figure. . . . .	102
4.12	(a) Fe 2p XAS and XMCD measurement attached from Deb <i>et al.</i> (2003) measured at $T = 50$ K with $B = 1.4$ T. (b) Fe 2p XAS and XMCD of an in air cleaned $\text{Fe}_{0.5}\text{Cu}_{0.5}\text{Cr}_2\text{S}_4$ single crystal measured at $T = 80$ K with $B = 0.5$ T. Peak A origins from $\text{Fe}^{2+}$ , peak B from $\text{Fe}^{3+}$ ions on the surface. .	104
4.13	Measurements and multiplet calculations of Fe 2p XAS and XMCD spectra of single crystalline $\text{Fe}_{0.5}\text{Cu}_{0.5}\text{Cr}_2\text{S}_4$ . The Fe 2p XAS spectra of a sample cleaned in air (red dotted) and a sample cleaned in situ (red line) are compared to multiplet calculations of $\text{Fe}^{2+}$ (black line) and $\text{Fe}^{3+}$ (black dotted line). Below a measured Fe 2p XMCD spectrum (blue line) is compared to multiplet calculations of $\text{Fe}^{2+}$ (black line) and $\text{Fe}^{3+}$ (black dotted line). .	105
4.14	XMCD measurements of Fe (red line) and Cr (green line) in $\text{Fe}_{0.5}\text{Cu}_{0.5}\text{Cr}_2\text{S}_4$ . The XMCD signals are shown together with their integrals, violet dotted for Fe and dark green dotted for Cr. In addition a sketch of the direction of the spin magnetic moment is given. . . . .	106
4.15	Fe 2p XAS and XMCD spectra of $\text{Fe}_{0.5}\text{Cu}_{0.5}\text{Cr}_2\text{S}_4$ : (a) X-ray absorption spectra with photon helicity parallel ( $\mu^+$ ) and antiparallel ( $\mu^-$ ) to the magnetisation, respectively; (b) The sum of the absorption spectra ( $\mu^+ + \mu^-$ ) and its integral; (c) The XMCD spectrum ( $\mu^+ - \mu^-$ ) and its integral. The integrals needed for the sum rules are denoted by $r$ , $p$ and $q$ . . . . .	107
4.16	Illustration of an antisite process in which a Fe and Cr ion change positions. Here only the main part of the unit cell is shown. The spin direction is indicated by white arrows. . . . .	110
4.17	Field dependence of the magnetisation at $T = 4.2$ K for bulk and powdered $\text{FeCr}_2\text{S}_4$ poly- and single crystals attached from Tsurkan <i>et al.</i> (2005). The magnetisation of the samples at a magnetic field of $B = 0.5$ T and $B = 1.4$ T are stressed out. . . . .	111
4.18	Illustration of a surface anisotropy resulting in an easy axis of the surface layers (blue), which is non collinear with the bulk magnetisation (red). This causes a canting of the spins (black arrows) at the surface. . . . .	112
4.19	Illustration of two superexchange interactions in $\text{Fe}_{1-x}\text{Cu}_x\text{Cr}_2\text{S}_4$ . One is an antiferromagnetic interaction between Fe(A)–Cr(B), the other a ferromagnetic interaction between Cr(B)–Cr(B). Here only the main part of the unit cell is shown. The spin direction is indicated by white arrows. . . . .	114
4.20	Interacting orbitals of the $90^\circ$ $\text{Cr}^{3+}$ - anion - $\text{Cr}^{3+}$ superexchange interaction. . . . .	115
4.21	Resistivity and magnetoresistance versus temperature for $\text{FeCr}_2\text{S}_4$ (panel (a)) and $\text{Fe}_{0.5}\text{Cu}_{0.5}\text{Cr}_2\text{S}_4$ (panel (b)), attached from Ramirez <i>et al.</i> (1997) . Panel (c) illustrates the characteristics of the resistivity spectra. . . . .	117
4.22	In panel (a) the conduction band splitting and the charge carrier scattering is illustrated (attached from Haas <i>et al.</i> (1967)). Panel (b) also illustrates the donor level splitting (attached from Haas (1968)). . . . .	118

---

4.23	Calculation results of the band splitting model. Panel (a) shows the carrier concentration versus reciprocal temperature and the magnetoresistance versus temperature, in case of a field-independent mobility. In panel (b) the mobility and the MR versus temperature in case of a field-independent carrier concentration is shown. Spectra are attached from Bongers <i>et al.</i> (1969) . . . . .	119
4.24	Possible channels of the Fe(A)–Cr(B) antiferromagnetic superexchange interaction in $\text{Fe}_{1-x}\text{Cu}_x\text{Cr}_2\text{S}_4$ for different Cu concentrations. . . . .	123



# List of Tables

- 4.1 Here the measured spin ( $\mu_{spin}$ ) and orbital ( $\mu_{orb}$ ) magnetic moments for Fe and Cr in  $\text{Fe}_{0.5}\text{Cu}_{0.5}\text{Cr}_2\text{S}_4$  in units of  $\mu_B$  per atom are listed ( $B = 0.5$  T;  $T = 80$  K). In addition the magnetic moments measured by Deb *et al.* (2003) are shown ( $B = 1.4$  T;  $T = 50$  K). Finally also the theoretical  $\mu_{spin}$  and  $\mu_{orb}$  values for a  $\text{Fe}^{2+}$ ,  $\text{Fe}^{3+}$  and  $\text{Cr}^{3+}$  ion are given. For more details see the text.108





# Introduction

So called *advanced materials* (AM) play an important role in the advancement of present technologies and the development of future applications affecting every day life. Advanced materials are compounds showing unusual magnetic and/or electric behaviour, which opens new possibilities for circuitries and electric devices. For instance, in the so called spintronic not the charge of an electron will be used to store information, but its spin. This could lead to a huge increase of the capability of storage devices or further miniaturisation of existing products. In addition also completely new applications could be developed, like for instance quantum computing (Raekers (2009); Prinz (2009), and citations within). A present goal is to utterly understand the origin and characteristics that form the basis of AM properties. In the future this will make it possible to create materials with designed magnetic and electric behaviour most suitable for their purpose.

During this work the electronic and magnetic structure of the crystals  $\text{Sr}_2\text{FeMoO}_6$ ,  $\text{Fe}_{0.5}\text{Cu}_{0.5}\text{Cr}_2\text{S}_4$ ,  $\text{LuFe}_2\text{O}_4$  and the molecules FeStar,  $\text{Mo}_{72}\text{Fe}_{30}$ ,  $\text{W}_{72}\text{Fe}_{30}$  are investigated by means of X-ray spectroscopic techniques. These advanced materials exhibit very interesting properties like magnetoresistance or multiferroic behaviour. In case of the molecules they also could be used as spin model systems.

A long standing issue concerning the investigation of these materials are contradicting results found for the magnetic and electronic state of the iron (Fe) ions present in these compounds. Therefore this work focuses on the Fe state of these materials in order to elucidate reasons for these problems. Thereby the experimental results are compared to theoretical simulations. The presented thesis is structured as follows:

- In chapter 1 the reader is briefly introduced in the experimental techniques used in this work, namely X-ray photoelectron spectroscopy (XPS), X-ray absorption spectroscopy (XAS) and X-ray magnetic circular dichroism (XMCD). Furthermore a short introduction into multiplet calculations and magnetism is given.
- In chapter 2 XAS and XMCD measurements of various different chalcogenide systems are presented. Thereby the experimental results are compared to multiplet calculations. This reveals temporally changes of the Fe valence state to be present in the compounds. Possible reasons for this are described and discussed.
- Chapter 3 deals with the investigation of the valence state of Fe in the double perovskite  $\text{Sr}_2\text{FeMoO}_6$ . XAS and XMCD measurements on the same sample that recured over several years are presented and compared to multiplet calculations. Here first evidence of an ageing effect changing the Fe valence state of

an  $\text{Sr}_2\text{FeMoO}_6$  sample with time is found.

- A comprehensive study of the magnetic and electronic structure of the spinel system  $\text{Fe}_{1-x}\text{Cu}_x\text{Cr}_2\text{S}_4$  is given in chapter 4. XPS, XAS and XMCD measurements reveal changes of the Cu concentration  $x$  to have no influence on the Fe, Cu and Cr valence state in the sample bulk in contrast to theoretical predictions. In addition indications of an ageing effect changing the Fe valence state at the sample surface of  $\text{Fe}_{0.5}\text{Cu}_{0.5}\text{Cr}_2\text{S}_4$  are found, which could explain the contradicting results found in the attempt to determine the Fe valence state. Since the current model describing the anomalous magnetic and electric behaviour of this compound assumes a mixed iron valence state this finding leads to new explanations of the properties of  $\text{Fe}_{1-x}\text{Cu}_x\text{Cr}_2\text{S}_4$ . Appropriate models are introduced and described.
- Finally, in chapter 5 the main results achieved in the present work are summed up and an outlook is given, followed by the acknowledgement and a list containing the bibliographic references.

# Chapter 1

## History and Basics

### 1.1 The history of X-ray spectroscopy

In the following the important discoveries and developments that established the X-ray spectroscopy are summarised.

#### An effect was found



Figure 1.1: Heinrich Hertz (1857 - 1894) (left), Wilhelm Hallwachs (1859 - 1922) (middle) and Joseph Thomson (1856 - 1940) (right)

The German physicist **Heinrich Rudolf Hertz** (1857 - 1894) was the first to satisfactorily demonstrate the existence of electromagnetic waves by building an apparatus to produce and detect VHF and UHF radio waves, the first radio, which he was convinced was of no use (*"It's of no use whatsoever [...] this is just an experiment that proves Maestro Maxwell was right"* cited from Hebrew University of Jerusalem (2004)). During his research he also discovered the **external photoelectric effect**. He found out that with ultraviolet light illuminated charged objects lose their charge more readily (Hertz, 1887). Although he realised its significance he left his assistant Hallwachs to investigate and explain it.

The German physicist **Wilhelm Ludwig Franz Hallwachs** (1859 - 1922), Hertz's assistant, continued the investigation of the external photoelectric effect, which later

was also called **Hallwachs-effect** (Hallwachs, 1888), and became the leading scientist in the field of photoelectricity.

The third scientist, who has to be mentioned, is the British physicist **Sir Joseph John Thomson** (1856 - 1940). Due to his experimental findings he described "corpuscles" that are emitted by hot metals. Thomson noted "*Corpuscles are also given out by metals and other bodies, but especially by alkali metals, when these are exposed to light*" (Thomson, 1897). This was the discovery of the electron, or in this case photoelectron, for which Thomson was rewarded the 1906 Nobel Prize in Physics.

## A theory was formed

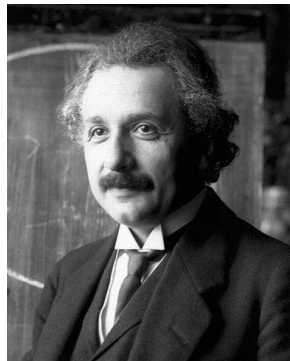


Figure 1.2: Albert Einstein (1879 - 1955)

**Albert Einstein** (1879 - 1955) was a theoretical physicist, who made many contributions to physics and is best known for his theories of special and general relativity. He is often regarded as the father of modern physics.

His many findings also include the **photon theory**. In a 1905 paper Einstein postulated that light itself consists of localised particles (quanta) (Einstein, 1905). Note that Einstein's paper on the light particles was almost entirely motivated by thermodynamic considerations. He was not at all motivated by the detailed experiments on the photoelectric effect done by Hertz, Hallwachs or Thomson, which could not confirm his theory. His considerations led him to conclude that each light wave of frequency  $\nu$  is associated with a collection of photons with energy  $h\nu$ , where  $h$  is Planck's constant. In his paper Einstein does not say much more, because he is not sure how the particles are related to the wave. But he does suggest that this idea would explain certain experimental results, notably the **photoelectric effect**.

Einstein's light quanta theory was nearly universally rejected by all physicists, including Max Planck and Niels Bohr.

## A theory was proven

The American experimental physicist **Robert Andrews Millikan** (1868 - 1953) was the first who measured the charge on the electron. He was also interested in photoelectricity and convinced that the particle light theory published by Einstein 1905 had to be wrong, due to the vast body of evidence that had already shown that light



Figure 1.3: Robert Millikan (1868 - 1953) (left) and Arthur Compton (1892 - 1962) (right)

was a wave. To test Einstein's theory, Millikan used an experimental setup in vacuum, in contrast to the photoelectric experiments of Hertz and Hallwachs. This was required to prepare a very clean metal surface and to measure excited photoelectrons, that were not inelastically scattered. The experiment was performed 1916 and it took Millikan by surprise that his results actually confirmed Einstein's photoelectric equation. He was rewarded with the 1923 Nobel Prize for the measurement of the electron charge and his work on the photoelectric effect.

Later the American physicist **Arthur Holly Compton** (1892 - 1962) discovered the so called *Compton effect*. He showed that the wavelength, thus the energy, of X-rays or gamma rays radiated onto a carbon target change with the scattering angle. This could no longer be explained by the universal view of light as a wave and also proofed Einstein's photon theory to be correct. For the discovery of the Compton effect he was rewarded with the 1927 Nobel Prize.

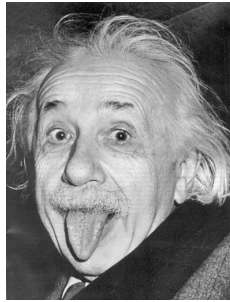


Figure 1.4: Albert Einstein (1879 - 1955)

In 1921, sixteen years after his light quanta paper, Einstein was rewarded with the Nobel Prize for the light quanta theory, although he was best known for his theory of relativity. This was due to a dispute in the Nobel Prize commission. Many members tended more to experimental physics than theoretical physics and also the accuracy of the gravitational lensing effect was doubted, with which the general relativity theory was confirmed. Therefore Einstein was not rewarded for the general relativity, for which he was nominated nearly every year since 1910 by Max Planck and Arnold Sommerfeld amongst others, but for the photon theory. However in his Nobel Prize speech Einstein exclusively spoke about his theory of relativity.

## A spectroscopy was invented

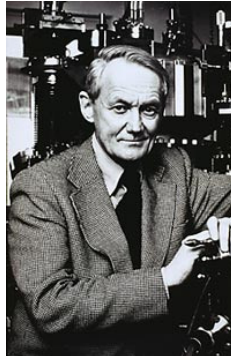


Figure 1.5: Kai Siegbahn (1918 - 2007)

For many years after its discovery the photoelectricity was disregarded, until the Swedish physicist **Kai Manne Börje Siegbahn** (1918 - 2007) substantially improved the energy resolution and sensitivity of  $\beta$ -spectrometers. Siegbahn et al. succeeded in enhancing the determination of electron binding energies in atoms by using X-rays ( $h\nu \approx 1500$  eV) and were able to detect chemical shifts of about 1 eV (Siegbahn *et al.*, 1967, 1969, 1972). The new high-resolution electron spectroscopy was named *Electron Spectroscopy for Chemical Analysis* (ESCA), now usually described as *X-ray photoelectron spectroscopy* (XPS). Siegbahn was rewarded with the 1981 Nobel Prize in Physics for his work. Later his development also led to other X-ray spectroscopic methods, like the *X-ray absorption spectroscopy* (XAS) and the *X-ray magnetic circular dichroism* (XMCD).

## 1.2 Experimental X-ray spectroscopic techniques

This section deals with the experimental techniques used in this work. Issues that are especially relevant in the present studies are emphasised.

### 1.2.1 X-ray Photoelectron Spectroscopy (XPS)

Figure 1.6 illustrates the principle of *photoelectron spectroscopy* (PES). Light is radiated onto a sample and excites electrons out of it. The light source, thus the energy of the photons, determines the energy level the electrons are excited out off, during this so called photoeffect. One possible light source is a helium discharge lamp, which provides photons with an energy in the ultra-violet region. This *Ultraviolet photoelectron spectroscopy* (UPS) excites mainly valence electrons and can give a lot of information about the electronic structure of a sample near the Fermi level. In *X-ray photoelectron spectroscopy* (XPS) normally the Bremsstrahlung of metal anodes, like aluminium or magnesium anodes, is used, which can also excite core level electrons as illustrated in figure 1.6. In addition synchrotrons, which provide photons with a tunable energy, are possible light sources for PES. The photoeffect was interpreted by Einstein (1905) with the light quantum hypothesis.

His thesis no longer describes light as a wave, but as a flow of particles, the photons, which hold a specific quantised amount of energy proportional to the Planck constant  $h$  and the frequency  $\nu$  of the light. For this work Albert Einstein was awarded with the Nobel price in 1921. According to the quantum light hypothesis the maximum kinetic energy of an emitted electron is given by

$$E_{kin,max} = h\nu - \Phi_{solid} \quad (1.1)$$

where  $h\nu$  denotes the energy of the exciting photon and  $\Phi_{solid}$  the work function of the solid. This material-specific function describes the energy an electron needs to leave the atom. Note that the equation 1.1 only applies for valence electrons located energetically close or at the Fermi energy  $E_F$  (dashed orange arrow in figure 1.6). Stronger bonded core level electrons also have to overcome their binding energy in order to leave the atom (orange arrow in figure 1.6), which leads to

$$E_{kin} = h\nu - E_{B,eff} - \Phi_{solid} \quad (1.2)$$

where  $E_{B,eff}$  is the effective binding energy of the emitted electron. If a conductive sample is connected to the spectrometer, the often unknown sample specific work function  $\Phi_{solid}$  can be replaced by the work function of the spectrometer  $\Phi_{spec}$ . Then one gets for the binding energy

$$E_{B,eff} = h\nu - E_{kin} - \Phi_{spec}. \quad (1.3)$$

Therefore if the energy of the radiated photons and the work function of the spectrometer is known, one can determine the binding energy of the excited electrons by measuring their kinetic energy. The number of excited photoelectrons with a specific kinetic energy is usually measured by a channeltron ( $Detector_{signal}$ ) and reveals the total density of electron occupied states (tDOS) shown as the intensity in the XPS spectrum (figure 1.6, green dotted line). Since the photoelectron can scatter easily inelastic on its way to the surface and lose its binding energy information, XPS is a very surface sensitive measurement. The emitted electrons in a solid state material have a mean free path depending on their kinetic energy of at most 100 Å. Thereby it has to be mentioned that a mean free path higher than 50 Å is only present for electrons with a very small kinetic energy (below 10 eV). Electrons with higher kinetic energies usually have a much shorter mean free path (below 20 Å) (Zangwill, 1988). Note that for the Fe 2p XPS spectra presented in this work photoelectrons with a kinetic energy of about 700 eV were detected. According to Zangwill (1988) these photoelectrons have a mean free path of about 10 Å.

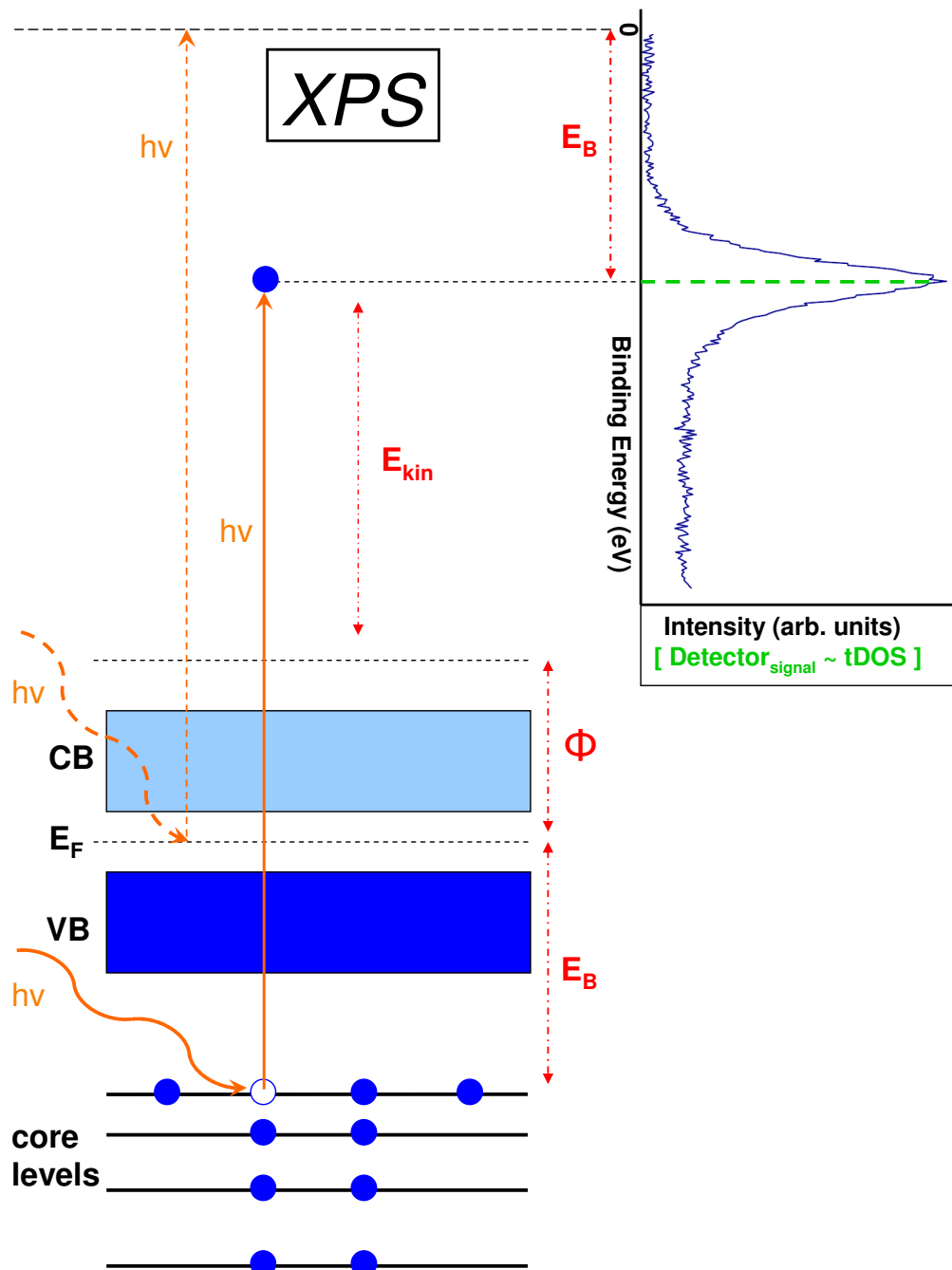


Figure 1.6: The principle of X-ray photoelectron spectroscopy (XPS). More details are given in the text.



### 1.2.1.1 Spectral characteristics

Although this method is based upon the photoeffect, the features in a photoelectric spectrum cannot be explained completely by this. Various side effects highly affect the measured spectra. Some of them modify the kinetic energy of the emitted electrons, like the *chemical shift* or the *spin-orbit coupling*, others compete with the photoelectric process by emitting additional electrons, like *satellites* or the *Auger-effect*. All these effects have to be completely understood in order to get correct information. Although this makes the interpretation of a PE spectrum more difficult, these additional effects are the main advantage of PES. Since they are element specific and highly influenced by the chemical environment of an atom, the resulting PE spectrum reveals a lot of information about the chemical and electronic structure of the measured sample. In the following a brief introduction of the basic side effects in PES is given.

### Chemical shift

Although valence electrons are involved in chemical bondings, core level electrons are affected by them. Due to a change of the electric environment, the electric potential changes and with it the binding energy of the core level electrons. For instance, if in a bonding the valence electrons of an atom migrate, like for the Fe atom in FeO, the core electrons feel a stronger Coulomb interaction with the nucleus. Therefore Fe 2p electrons in FeO and Fe<sub>2</sub>O<sub>3</sub> have a higher binding energy than in metallic Fe (figure 1.7). The magnitude of the energy shift depends on the type of binding and the neighbouring atoms. By comparing the binding energy shift of the core level electrons, the so called *chemical shift*, with reference measurements, one gets information about the bonding and the chemical environment of an atom in a sample. The theoretical approach of the *chemical shift* is difficult, because the influence of several factors can not be determined and calculated correctly. If only electrostatic considerations are taken into account, equation 1.3 can be modified in order to describe the changes of the effective binding energy in a chemical bonding:

$$E_{B,eff} = h\nu - E_{kin} - \Phi_{spec} + \Delta(E_{chem} + E_{Mod}); \quad (1.4)$$

$$\Delta E_{chem} = Kq_A; \quad (1.5)$$

$$\Delta E_{Mad} = \sum_{B \neq A} \left( \frac{q_B}{r_{AB}} \right) \quad (1.6)$$

$\Delta E_{chem}$  denotes the *chemical shift* in atom A relating to a reference, in which  $q_A$  describes the valency difference to the reference and  $K$  the interaction of the valence level electrons with the core level electrons. The latter is an empirical parameter. The Madelung term  $\Delta E_{Mad}$  considers the influence of the other atoms in a molecule or bulk. It is the sum of the effective charge  $q_B$  divided by the distance  $r_{AB}$  of every surrounding atom B to the atom A, where  $A \neq B$ .

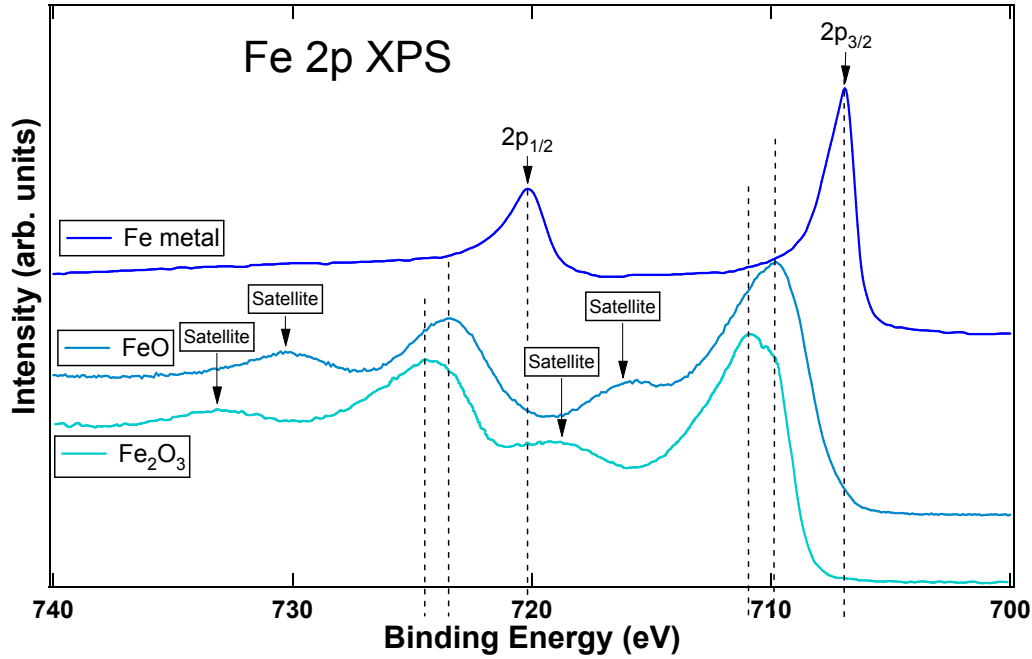


Figure 1.7: The *chemical shift* of the Fe 2p XPS spectrum of FeO and Fe<sub>2</sub>O<sub>3</sub> compared to metallic Fe. The origin of the line splitting and the satellites will be explained in the sections below.

### Spin-orbit coupling

To describe the way an electron is bound to an atom quantum numbers are used. The *principal quantum number*  $n$  ( $n = 1, 2, \dots$ ) denotes the atomic shell where the electron is located. The orbital of the electron is denoted by the *orbital quantum number*  $l$  ( $l = 0, 1, 2, \dots, n - 1$ ). Often the *orbital quantum number* is also described with characters, for example s ( $l = 0$ ), p ( $l = 1$ ), d ( $l = 2$ ). The third quantum number is the *spin*  $s$  ( $s = \frac{1}{2}$  for one electron).

In an atom the *spin* of an electron can interact with its *orbital momentum*, which results in different energetic states. This interaction is called *spin-orbit coupling*. When one takes the *spin-orbit coupling* into consideration the *total angular momentum quantum number*  $j$  is needed, which represents the sum of  $s$  and  $l$ . The possible values of  $j$  for one electron are thereby  $j = l \pm \frac{1}{2}$  with  $j > 0$ . It can be shown that the Hamiltonian describing the *spin-orbit interaction* is defined as follows,

$$\hat{H}_{SO} = \frac{1}{2m_e^2 c^2} \frac{1}{r} \left( \frac{\partial U}{\partial r} \right) \hat{L} \cdot \hat{S}, \quad (1.7)$$

where  $U$  denotes the potential energy of the electron in the field of the atom and  $\hat{L}$ ,  $\hat{S}$  the orbital and spin momentum operators, respectively. As can be seen the *spin-orbit interaction* is proportional to  $\hat{L} \cdot \hat{S}$ . This can be rewritten as  $\hat{L} \cdot \hat{S} = \frac{1}{2}(\hat{J}^2 - \hat{L}^2 - \hat{S}^2)$ , leading to

$$E_{SO} \sim \langle \hat{L} \cdot \hat{S} \rangle \sim \frac{\hbar^2}{2}(j(j+1) - l(l+1) - s(s+1)). \quad (1.8)$$

Here it is important to note that, due to the *spin-orbit coupling*, the total energy of a state depends on the value of the *total angular momentum quantum number*  $j$ . This means that for every electron state ( $nl$ ) with  $l \geq 1$  there are two different energy states  $nl_{l+\frac{1}{2}}$  and  $nl_{l-\frac{1}{2}}$ , thus a double-line (doublet) in the XPS spectrum. The relative intensities of the two lines are given by

$$\frac{I_{(l+\frac{1}{2})}}{I_{(l-\frac{1}{2})}} = \frac{l+1}{l}. \quad (1.9)$$

For example, for a p electron ( $l = 1$ ) the relative intensities of the corresponding doublet,  $p_{\frac{3}{2}}$  and  $p_{\frac{1}{2}}$ , are 2 : 1 (fig.1.7), whereas for a d electron ( $l = 2$ ) the ratio is  $\frac{I_{\frac{5}{2}}}{I_{\frac{3}{2}}} = \frac{3}{2}$ . In case of an s electron ( $l = 0$ ) there is no *spin-orbit coupling* present, since  $j$  cannot be negative and therefore has only one value  $j = \frac{1}{2}$ .

### Multiplet splitting

As described above for electrons with  $l = 0$  there is no *spin-orbit interaction* possible. Nevertheless often a splitting of an s electron line in the XPS spectrum occurs, for example in case of 3d transition metals. This so called *multiplet- or exchange splitting* is due to a spin-spin coupling of a core electron to the total valence electron spin ( $S$ ). Note that this is only possible, if the excited atom has unpaired valence electrons, thus a total valence electron spin exists. Then the spin  $s = \frac{1}{2}$  of the remaining unpaired s electron after the excitation process can couple parallel or antiparallel to  $S$ . This affects the binding energy of the excited photoelectron and splits the measured core line. The corresponding exchange splitting ( $\Delta E_s$ ) can be written according to the van Vleck theorem (van Vleck, 1934)

$$\Delta E_s = \frac{2S+1}{2l+1} G^2(3s, 3d), \quad (1.10)$$

where  $G^2(3s, 3d)$  is the Slater exchange integral and  $l$  the *orbital quantum number*. According to this theorem the binding energy of the state corresponding to  $(S + \frac{1}{2})$  is lower than the binding energy of the state corresponding to  $(S - \frac{1}{2})$ . The intensity ratio for the two peaks is given by

$$\frac{I_{S+\frac{1}{2}}}{I_{S-\frac{1}{2}}} = \frac{S+1}{S}. \quad (1.11)$$

Later it was found that there are *multiplet splittings*, which cannot be described by the van Vleck theorem correctly. The intensity ratio as well as the splitting value

were different from the calculated values (Fadley and Shirley, 1970; Galakhov *et al.*, 2002). This discrepancy was explained by intra-atomic near-degeneracy correlation effects (Bagus *et al.*, 1973). Intra-atomic correlation effects like charge transfer, which often dominate the electronic properties for instance in late transition metal compounds, are not considered in the van Vleck theorem. Due to this it fails to describe the XPS 3s spectra (Veal and Paulikas, 1983). Today the 3s *multiplet splitting* is treated with full multiplet calculations (Sangaletti *et al.*, 1995). Note that *multiplet splitting* also occurs for other core level lines ( $l \neq 0$ ). In this case the description is even more complex due to the additional spin-orbit splitting.

## Satellites

Due to the small timescale of the photoeffect the  $N - 1$  electron excited state caused by the photoemission process can affect the binding energy of the primary photoelectron. This leads to additional lines, the so called *satellites*, beside the main lines corresponding to the lowest excited state in the XPS spectra (fig. 1.7). Thereby one can distinguish between *extrinsic satellites*, which are due to *inter-atomic* excitations and *intrinsic satellites* caused by *intra-atomic* relaxations.

If an electron is emitted out of the sample during the photoemission process it is possible that a second electron is excited. The necessary energy is supplied by the kinetic energy of the primary photoelectron, which therefore will be measured with a lower kinetic energy, thus at higher binding energies in the spectrum. If the secondary electron is transferred to a higher energy orbit, the corresponding line is called *shake-up* satellite, if it is completely removed, it is called *shake-off* satellite (Hollas, 1998). Figure 1.8 shows the principle of a third kind of satellite, which is due to *charge transfer*. As one can see in contrast to the  $N$  electron ground state in the  $N - 1$  excited state electron states appear at the Fermi level of the ligand ( $L$ ) and metal ( $M$ ). This makes a charge transfer process possible, in which an electron is transferred from the ligand 2p to the metal 3d shell:  $3d^n L \rightarrow 3d^{n+1} L^{-1}(\underline{L})$  leading to the final state shown in figure 1.8. The energy required by this extrinsic charge transfer process ( $\Delta$ ) is simply

$$\Delta = E(3d^{n+1} L^{-1}) - E(3d^n L) \quad (1.12)$$

and taken from the primary photoelectron. This causes additional peaks accompanying the  $2p_{3/2}$  and  $2p_{1/2}$  lines at higher binding energies in spectra of many transition metal (TM) oxides like for instance NiO, FeO, Fe<sub>2</sub>O<sub>3</sub> (Uhlenbrock, 1994; Kuepper, 2005) (see also fig. 1.7). In case of Fe this can help to distinguish between divalent (FeO) and trivalent Fe (Fe<sub>2</sub>O<sub>3</sub>) ions.

Beside these *extrinsic satellites* in metallic samples *intrinsic satellites* occur due to quantified excitations in the conduction electron system caused by relaxation.

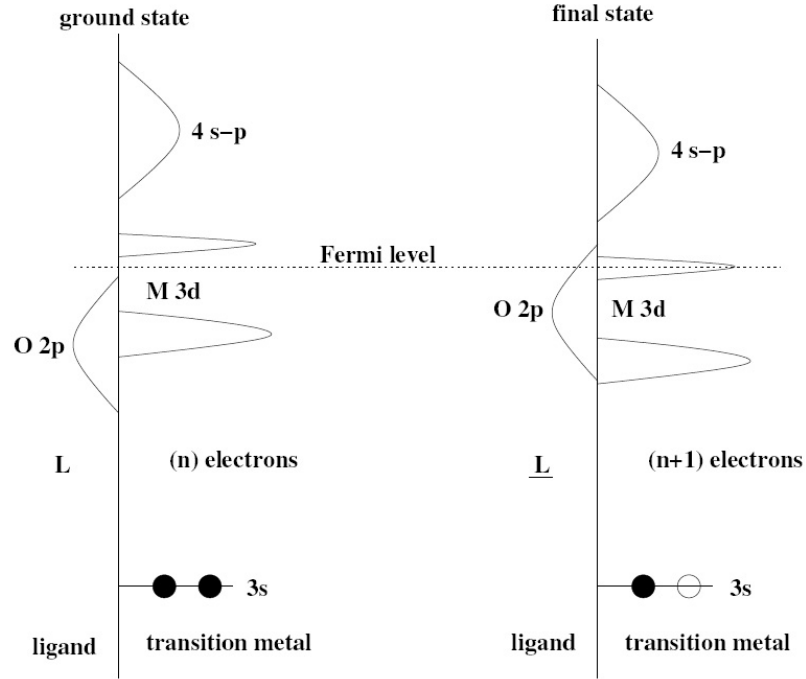


Figure 1.8: Illustration of a charge transfer excitation in a transition metal oxide (Kuepper, 2005).

### Auger electrons

After the photoemission process the remaining hole is filled with an electron of a higher energy level. This process releases energy, which is either radiated in the form of a photon or absorbed by an electron. This so called *Auger electron* is excited into the continuum and appears as an additional line in the spectrum (Auger, 1925). The timescale of this two-electron process is in the range of  $10^{-14}$  seconds. The approximated kinetic energy of the *Auger electron* is given by

$$E(ABC) \approx E(A) - E(B) - E(C) - \Phi, \quad (1.13)$$

where  $ABC$  denotes the Auger electron.  $A$  is the shell the first photoelectron was removed from,  $B$  the shell an electron is decaying from,  $C$  the shell the *Auger electron* is excited out of and  $\Phi$  the work function. Usually the  $ABC$  shells are named  $K$  for the  $1s$  levels,  $L_1, L_2$  and  $L_3$  for  $2s, 2p_{\frac{1}{2}}$  and  $2p_{\frac{3}{2}}$  as well as  $M_1, M_2, M_3, M_4$  and  $M_5$  for  $3s, 3p_{\frac{1}{2}}, 3p_{\frac{3}{2}}, 3d_{\frac{3}{2}}$  and  $3d_{\frac{5}{2}}$  energy levels, respectively. Thus, for instance an  $KL_1L_{23}$  Auger electron is formed due to a photoemission of an electron of the  $K$  shell ( $1s$  level), a decay of an electron from the  $L_1$  ( $2s$ ) level and an excitation of the Auger electron out of the  $L_{23}$  ( $2p_{\frac{1}{2}}$  or  $2p_{\frac{3}{2}}$ ) level. If the  $A$  and  $B$  hole states are on the same shell, but in different orbitals (for example,  $L_1L_3M_1$ ), then the process is of so called *Coster-Kronig* type (Kuzmany, 1998). Equation 1.13 shows that in contrast to the kinetic energy of the primary photoelectron the energy of an *Auger electron* is constant and does not depend on the energy of the radiated photon. The *Auger*

electron energy is determined exclusively by the energy difference of the involved electronic states. Therefore one can easily distinguish photoelectrons from *Auger electrons* by using different excitation energies. Then the lines of the photoelectrons will appear at the same binding energy while the Auger lines will occur shifted by  $|\hbar\nu_1 - \hbar\nu_2|$ . Note that relaxation effects and the reconfiguration of the excited state are not taken into account in equation 1.13.

### Inelastic background

Only photoelectrons that are excited out of surface layers maintain their primary kinetic energy. Electrons from deeper layers lose part of their kinetic energy due to inelastic scattering and end up at higher binding energies in the spectrum. This leads to a general rise of the background intensities with the detection of lower kinetic energies, which is called *inelastic background* or *secondary spectrum*. Therefore XPS is a surface sensitive measurement, since bulk photoelectrons lose their binding energy information due to the inelastic scattering. For quantitative analysis of the XPS spectra, the background has to be determined and subtracted. A very simple description of the *inelastic background* would be a linear function. More complex and appropriate background functions were proposed by Shirley (Shirley, 1972) and by Tougaard (Tougaard, 1990).

### 1.2.2 X-ray Absorption Spectroscopy (XAS)

In figure 1.9 the principle of *X-ray absorption spectroscopy* (XAS) is illustrated. In contrast to XPS in XAS a photon does not excite an electron completely out of the sample but into an unoccupied state of the conduction band (CB). Thus, XAS is a powerful probe of the unoccupied part of the electronic structure. Like in the photoemission, in the photoabsorption additional effects, for instance *chemical shift*, *spin-orbit coupling* and *multiplet interactions*, occur and affect the spectrum, which therefore can give valuable information about the chemical and electronic structure of the sample.

Due to the *dipole selection rules* only transitions, which change the angular momentum quantum number  $l$  by one,  $\Delta l = \pm 1$ , and conserve the spin,  $\Delta s = 0$ , occur in the XAS process. In particular, the z-components of the spin and orbital momentum have to change, such that  $\Delta m_s = 0$  and  $\Delta m_l = \pm 1, 0$ . While all of the possible transitions according to the dipole selection rules occur for linear polarised light, left circularly polarised light only initiate transitions with  $\Delta m_l = +1$ , whereas right circularly polarised light initiate  $\Delta m_l = -1$ . In addition so called *quadrupole transitions*, with  $\Delta l = \pm 2, 0$ , can occur in XAS spectra, but these transitions are hundred times weaker than the *dipole transitions*.

As illustrated in figure 1.9 the required energy  $E_{exc}$  to excite a core electron into an unoccupied state can simply be written as:

$$E_{exc} = E_{final} - E_{initial} \quad (1.14)$$

where  $E_{final}$  is the energy of the final state with the core electron excited into the conduction band and  $E_{initial}$  is the energy of the system before the excitation. The

energy  $E_{exc}$  is supplied by a photon (orange waved arrow) in a primary electron excitation process (orange arrow marked 1). Shortly after this due to relaxation the electron hole is filled by an energetically higher located electron and the excited electron falls back in lower energy levels (dashed orange arrows marked 2). This processes release energy, which causes either an Auger excitation (orange arrow marked 3) or the emission of photons (orange waved arrow marked 3).

The absorption of light, thus the intensity in the XAS spectrum, can be measured directly in transmission, but this is only possible for very thin samples. In case of bulk materials it is usual to measure the absorption indirectly by measuring a signal, which is proportional to the XAS signal. Such a signal is caused by the mentioned secondary processes due to the relaxation of the excited electron. This leads either to the emission of electrons or photons out of the sample (figure 1.9, orange arrow marked 3 and orange waved arrow marked 3, respectively). If the sample is conductive one can measure the drain current  $I_{drain}$  caused by the Auger emission. This is called the *total electron yield* (TEY). The TEY can also be measured by detecting the emitted electrons directly. If one measures only the amount of emitted electrons of a certain energy this is called the *partial electron yield* (PEY). Alternatively one can measure the intensity of the emitted photons after the absorption, for example with a CCD-detector ( $CCD_{signal}$ ). This method is called *total fluorescence yield* (TFY), or *partial fluorescence yield* (PFY) if only photons of a certain energy are counted. Since the escape depth of photons (about 1000 Å) is higher than the photoelectron escape depth (in the range of 20 Å – 100 Å) FY is less surface sensitive than EY (Zangwill, 1988; Nakajima *et al.*, 1999). However, XAS spectra recorded with FY often suffer due to strong saturating effects like self-absorption, which modify the spectral shape and falsify peak ratios (de Groot and Kotani, 2008; Stöhr and Siegmann, 2006). In addition in the soft X-ray region the intensity of measurements in the FY-mode is much weaker than in the EY-mode, since the Auger process dominates the decay in this energy region.

The XAS can be divided into two spectral regions. One is the so called *near edge X-ray absorption fine structure* (NEXAFS or XANES), which reflects excitations of the photoelectron into unoccupied states. The other is the so called *extended X-ray absorption fine structure* (EXAFS), where the photoelectron is excited into the continuum and its scattering with the environment of the absorber leads to characteristic features in the XAS spectrum. The EXAFS region is usually at photon energies well above the corresponding NEXAFS threshold. Please be referred to Stöhr (1992); Stöhr and Siegmann (2006); de Groot and Kotani (2008) for a more general and comprehensive treatment of *X-ray absorption spectroscopy*.

As shown in figure 1.9 in XAS the photon energy  $h\nu$  has to be changed in order to measure an absorption spectrum. Therefore XAS is usually performed with tunable synchrotron radiation.

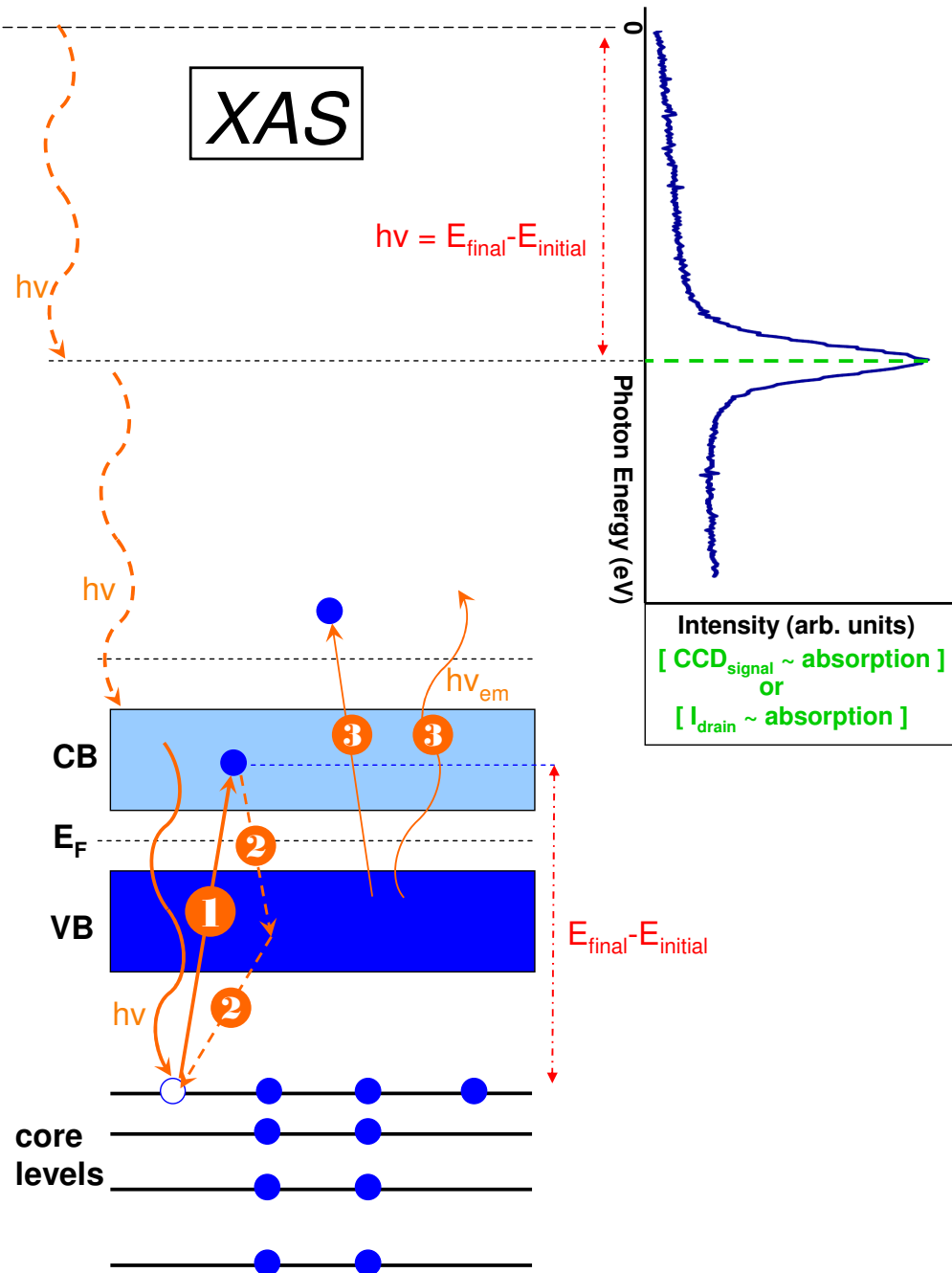


Figure 1.9: The principle of X-ray absorption spectroscopy (XAS). More details are given in the text.



### 1.2.2.1 X-ray Magnetic Circular Dichroism (XMCD)

Schütz *et al.* (1987) first verified a special XAS technique called *X-ray magnetic circular dichroism* (XMCD). In contrast to normal XAS in XMCD not linearly but circularly polarised light is radiated onto the sample. As already mentioned above this way not all possible transitions according to the dipole selection rules are initiated. Left and right circularly polarised light only initiate electron transitions with  $\Delta m_l = +1$  and  $\Delta m_l = -1$ , respectively. Note that here the magnetisation is assumed to be parallel to the photon wave vector. If the magnetisation is antiparallel to the photon wave vector the selection rules reverse. In combination with the spin-orbit split of the core levels ( $j = l \pm s$ ), preferentially either majority or minority spin carriers are excited to unoccupied electron states, depending on the light helicity (Ebert, 1996; Kapusta *et al.*, 1999). Phenomenologically this can be explained by the spin and orbital angular momentum coupling of the photon angular momentum  $L_{Ph} = \pm 1$  with the electron spins. In figure 1.10 for a  $2p \rightarrow 3d$  excitation with circularly polarised light the possible transitions and their probability are illustrated. As one can see while mainly spin down electrons are excited out of the  $2p_{\frac{1}{2}}$  levels, preferentially spin up electrons are excited out of the  $2p_{\frac{3}{2}}$  levels.

Note that in figure 1.10 XMCD transitions are shown for a d continuum. If the d band is partly filled the number of occupied spin states highly affect the possible transitions, and therefore the XMCD signal. According to Fermi's golden rule the absorption coefficients are proportional to the density of unoccupied states above the Fermi level. Thus, the photoelectron serves as a probe of the spin and orbital polarisation of these states, which is very important for the investigation and characterisation of magnetic materials and their magnetic moments. In the last decades this technique has become more and more widely used as probe for the *element-specific* characterisation of magnetic materials. Reasons for this are on the one hand the growing availability of tunable high brilliance X-rays (synchrotron), and on the other hand the unique possibility to analyse the magnetic moments element specifically as well as separated into their spin and orbital contributions.

Figure 4.9 in chapter 4 shows a typical XMCD spectrum of a transition metal L edge. As shown an XMCD measurement consists of 3 spectra. One spectrum is measured with photon helicity parallel ( $\rho^+$ , absorption coefficient  $\mu^+$ ), the other with photon helicity antiparallel ( $\rho^-$ , absorption coefficient  $\mu^-$ ) to the magnetisation, respectively. For the investigation of the magnetic moments the differences in the absorption coefficients  $\mu^+$  and  $\mu^-$  are of most interest and therefore the XMCD signal is formed, which is simply the subtraction of both spectra ( $\mu^+ - \mu^-$ ). The dependence of the XMCD signal on the experimental parameters is given in equation 1.15 (Stöhr and Siegmann, 2006).

$$I_{XMCD} \propto P_{circ} \cdot M \cdot L_{Ph} \propto P_{circ} \langle m \rangle \cos \theta \quad (1.15)$$

Here  $P_{circ}$  is the degree of circular photon polarisation,  $\langle m \rangle$  the expectation value of the magnetic moment and  $\theta$  the angle between the directions of the photon angular momentum  $L_{Ph}$  and the magnetisation  $M$ . As indicated by the formula in order to get a maximum XMCD signal one needs highly polarised light (synchrotron) and a magnetisation of the electron spins collinear to the photon angular momentum. The latter is done by an external magnetic field.

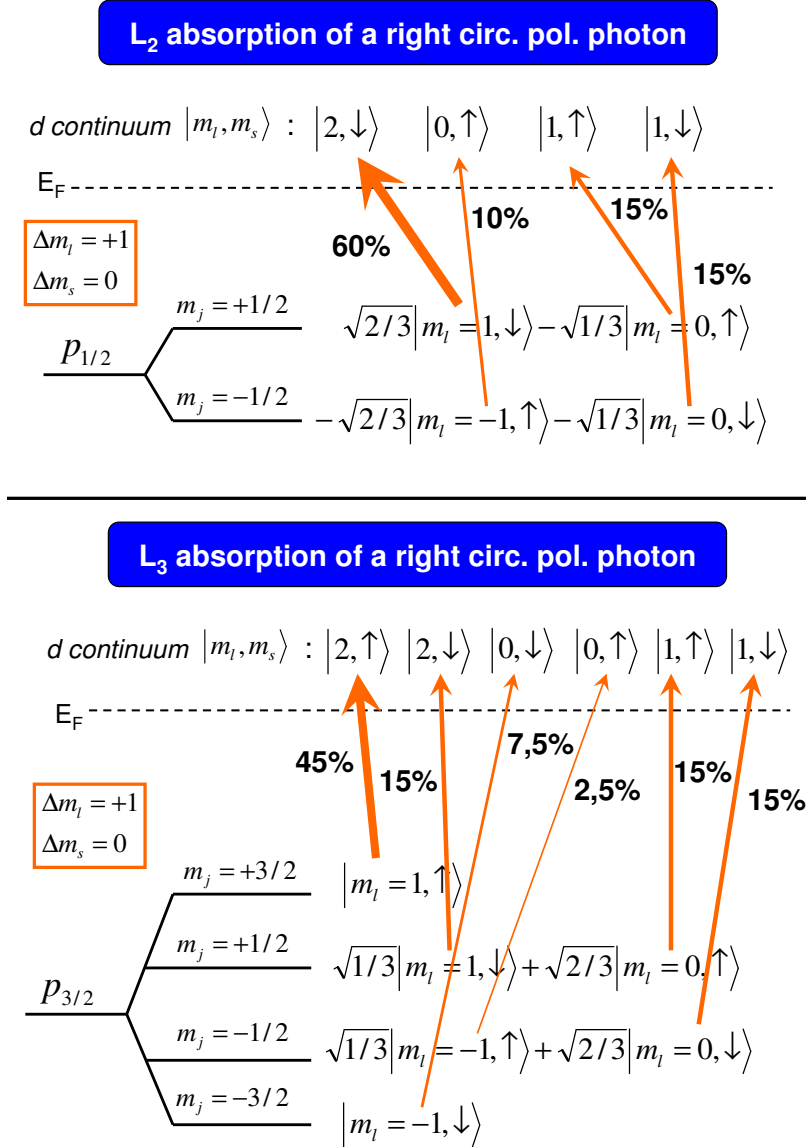


Figure 1.10: Illustration of a  $2p \rightarrow 3d$  excitation with right circularly polarised light to empty d-continuum states in a solid (according to Kapusta *et al.* (1999)). The excitation is separated in transitions from the core  $p_{1/2}$  (L<sub>2</sub>) levels (upper panel) and the ones from the  $p_{3/2}$  (L<sub>3</sub>) levels (lower panel). Note that here the magnetisation of the sample is assumed to be antiparallel to the photon wave vector ( $\Delta m_l = +1$ ).

To receive the spin and orbital magnetic moments from XMCD measurements of  $2p \rightarrow 3d$  transitions the so called *XMCD sum rules* are used. These were theoretically derived by Thole *et al.* (1992); Carra *et al.* (1993) and later reformulated by Chen *et al.* (1995). The modified sum rules are given in equations 1.16 and 1.17.

$$m_{orb} = - \frac{4 \int_{L_3+L_2} (\mu^+ - \mu^-) d\omega}{3 \int_{L_3+L_2} (\mu^+ + \mu^-) d\omega} (10 - n_{3d}), \quad (1.16)$$

$$m_{spin} = - \frac{6 \int_{L_3} (\mu^+ - \mu^-) d\omega - 4 \int_{L_3+L_2} (\mu^+ - \mu^-) d\omega}{\int_{L_3+L_2} (\mu^+ + \mu^-) d\omega} \times (10 - n_{3d}) \left( 1 + \frac{7 \langle T_z \rangle}{2 \langle S_z \rangle} \right)^{-1} \quad (1.17)$$

Here  $m_{orb}$  is the orbital magnetic moment and  $m_{spin}$  the spin magnetic moment in units of  $\mu_B/atom$ . The indices  $L_3$  and  $L_3 + L_2$  of the integrals refer to the integration over the whole  $L_3$  and  $L_3 + L_2$  peaks, respectively. As mentioned before  $(\mu^+ - \mu^-)$  is the XMCD spectrum, whereas  $(\mu^+ + \mu^-)$  is simply the sum of the absorption spectra measured with left and right circularly polarised light, respectively.  $n_{3d}$  stands for the number of 3d electrons in the corresponding ion.  $\langle T_z \rangle$  is the ground state expectation value of the magnetic dipole term originating from the expectation value of the magnetic dipole operator and  $\langle S_z \rangle$  is the corresponding spin operator. Usually for atoms in a cubic symmetry the term  $\frac{7 \langle T_z \rangle}{2 \langle S_z \rangle} \ll 1$  and can be omitted.

Note that within the sum rules several approximations were made. The  $2p \rightarrow 3d$  transitions are treated like in free atoms, so many-particle effects are neglected. Furthermore, the sum rules are derived for well separated core spin-orbit multiplets in the final state of X-ray absorption. In other words the  $L_3$  and  $L_2$  edges and the corresponding multiplets are assumed to be well separated, so that the integrals can be correctly performed. While this is the case for some late 3d transition metals like for example Ni and Co, Fe as well as Mn show a considerably high mixing of the  $L_3$  and  $L_2$  multiplets due to the Coulomb interactions between the electrons. This was shown by Teramura *et al.* (1996), who also derived correction factors  $C_{Teramura}$  for several transition metal ions in  $O_h$  symmetry to take the L edge mixing into account. Since only the sum rule of  $m_{spin}$  (1.17) needs a clear separation of the  $L_3$  and  $L_2$  edge the Teramura factors are only needed for the calculation of the spin magnetic moment ( $m_{spin}^{correct} = m_{spin}^{sum-rule} \times C_{Teramura}$ ).

As mentioned before the XMCD technique is element specific. So for instance the spin and orbital magnetic moments of the Fe and Cr ions in  $Fe_{1-x}Cu_xCr_2S_4$  can be derived separated from each other (see chapter 4), which in this case is very important, since the spin magnetic moments are aligned antiferromagnetically leading to a decreased magnetic moment in overall magnetic measurements.

## 1.3 Instrumentation

This section deals with the instrumentation necessary to perform the described X-ray spectroscopic techniques. Issues that are especially relevant in the present work are emphasised.

### 1.3.1 The photoelectron spectrometer PHI 5600ci

The XPS measurements presented in this work have been performed with a PHI 5600ci multitechnique spectrometer produced by the Perkin Elmer Cooperation (Chastain, 1992). Figure 1.11 shows the layout of the spectrometer.

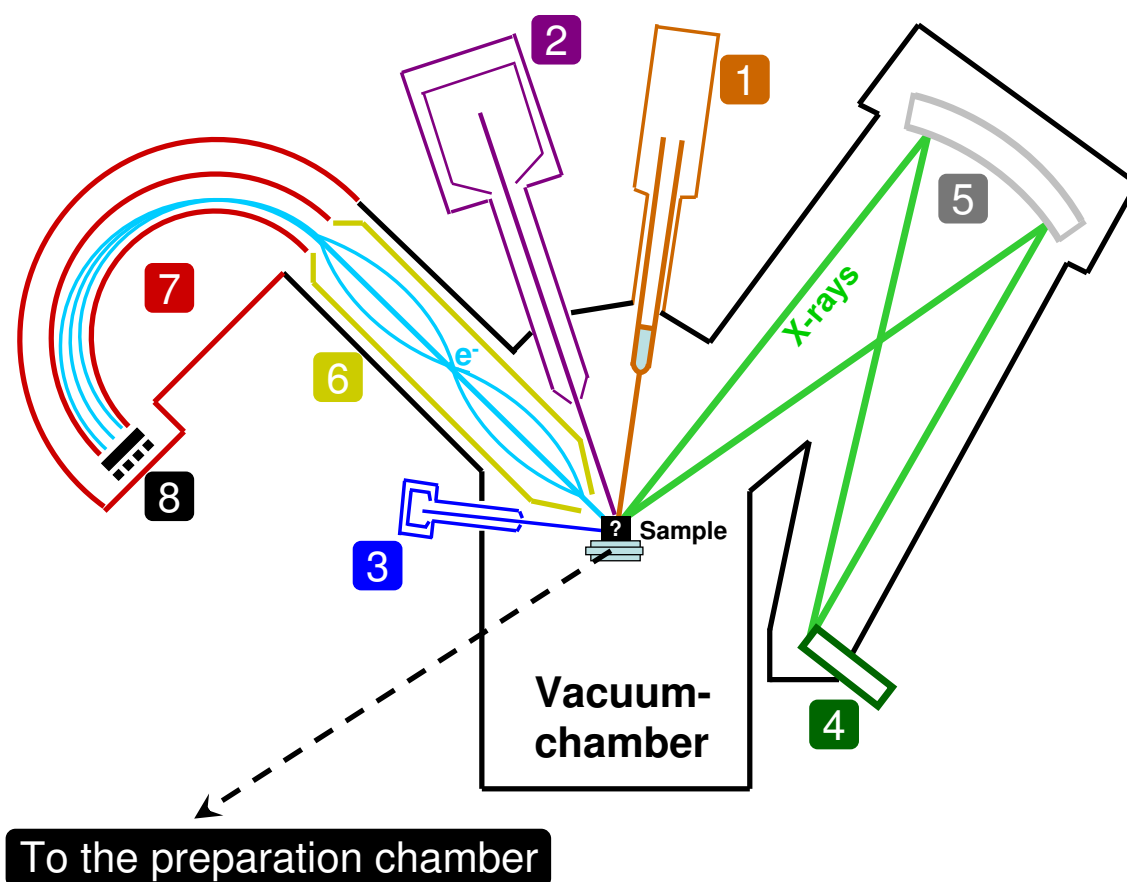


Figure 1.11: Layout of the PHI 5600ci multitechnique spectrometer. More details are given in the text.

The PHI 5600ci is equipped with a *dual Al/Mg X-ray anode* (number 1, orange), a *sputter ion gun* (number 2, violet), an *electron gun* (number 3, blue) and a *single Al X-ray anode* (number 4, dark green), which is monochromatised by a *quartz crystal monochromator* (number 5, grey) and was used for all XPS measurements presented in this work. The monochromatised X-ray source provides the Al  $K_{\alpha}$  radiation energy of 1486.6 eV with a energy half-width of  $\sim 0.3$  eV. The  $K_{\alpha}$  radiation is created in the Al anode due to a transition of an electron from the L shell to a hole in

the K shell, which was created due to a photoemission process. As illustrated in figure 1.11 the photoelectrons (light blue) excited out of the sample (black) by the monochromatised X-rays (green) are focussed with help of an electronic lens system (number 6, yellow). After that the kinetic energy of the electrons is measured with an 11 inches hemispherical analyser (number 7, red). The crystal-sample-analyser angle is fixed to  $90^\circ$ . Usually the analyser is operated in the so called *constant analyser transmission* (CAT) mode. This means the energy the electrons need to have in order to pass the analyser is always the same independent from the measured binding energy. This is possible with a bias, which increases or decreases the kinetic energy of the photoelectrons before their entrance in the analyser, so that only the electrons with the right binding energy have the necessary energy (so called *pass energy*  $E_p$ ) to reach the detector (number 8, black). Therefore the analyser only has to measure the *pass energy*  $E_p \pm \Delta E$ . The advantage of the CAT mode is that the *absolute energy resolution* denoted by  $\Delta E$  is constant for the whole spectrum. The usage of small pass energies decreases  $\Delta E$ , but also the overall intensity of the XPS signal is reduced. Usually a pass energy is chosen that gives an appropriate resolution while the intensity is preferably high.

Since the electrons, which leave the excited sample, shall reach the analyser without being scattered on a gas molecule the experiment has to be performed under *ultra high vacuum* (UHV). As mentioned before XPS is a rather surface sensitive technique and therefore the UHV is also required in order to keep the sample surface free of contamination. A pressure of about  $1 \times 10^{-9}$  mbar assures that XPS measurements can be performed for several hours without taking care of surface contamination. The UHV is achieved by a set of different vacuum pumps. At first rotation pumps create a pressure of about  $1 \times 10^{-6}$  mbar at which turbomolecular pumps can work. With these the pressure decreases to about  $1 \times 10^{-8}$  mbar. Finally an ion getter pump and a titanium sublimation pump are used to achieve a pressure of about  $1 \times 10^{-9}$  mbar. Often the sample surface is contaminated and has to be cleaned before the measurement. One method is the usage of a *sputter ion gun*, which bombards the sample with argon ions. Since in case of chalcogenides sputtering causes a dramatic change of the sample surface stoichiometry, this method could not be used in this work. An appropriate way to treat chalcogenides before the measurement is to scrape the sample with a diamond file in UHV or to cleave them in situ. This is done in a *preparation chamber* (black dashed arrow in figure 1.11), which was added to the spectrometer. If the sample is insulating the binding energy of the electrons changes during the XPS measurement due to charging of the sample. This leads to shifts in the spectrum, which can be prevented by a flow of electrons onto the sample surface provided by an *electron gun*.

### 1.3.2 Measurements at synchrotron endstations

As mentioned before tunable light sources are necessary in order to perform X-ray spectroscopic methods like XAS and XMCD. State of the art experiments are usually performed with the high brilliant light produced at synchrotron radiation (SR) facilities (Attwood, 1999). The measurements shown in this work were done at the Russian-German (RG)-beamline of the Berliner Elektronen-Speicherring Gesellschaft

für Synchrotronstrahlung (BESSY II) in Berlin, at the beamline 4.0.2 and 8.0.1 of the Advanced Light Source (ALS), Lawrence Berkeley National Laboratory in Berkeley (USA), at the Beamline of Advanced diCHroism (BACH) at ELETTRA in Trieste (Italy), at the National Synchrotron Radiation Research Center (NSRRC) in Taiwan and the Swiss Light Source (SLS) in Villigen (Switzerland) (figure 1.12).



Figure 1.12: Pictures of the BESSY II in Berlin (a), the NSRRC in Taiwan (b), the ALS in Berkeley (USA) (c), the ELETTRA in Trieste (Italy) (d) and the SLS in Villigen (Switzerland) (e).

### Storage ring and insertion devices

Today synchrotron facilities belong to the so called third-generation synchrotron sources, which appeared in the 1990s. Figure 1.13 shows a schematic plot of a synchrotron. At first electrons are generated and accelerated by a linear *accelerator*, or *linac* (1), which is an electromagnetic catapult that brings the electrons from a standing start to relativistic velocity near the speed of light. Note that a linac long enough to accelerate electrons to the energy needed for the synchrotron would usually not fit inside the building. Therefore the electrons are further accelerated by *radio frequency* (RF) cavities in the so called *booster synchrotron* (2). In less than a second inside the booster the electrons reach their target energy and are injected into the so called *storage ring* (3). In this ring the electrons are kept on a circular path for hours leading to an emission of light. It is possible to compensate the electron energy loss, which is due to the emitted radiation, by using RF cavities. Although linac, booster synchrotron and storage ring are kept under UHV, with time the electron current

in the ring decreases due to scattering of the electrons with air particles and a new injection has to be performed.

In order to keep the electrons on their orbital path in the storage ring so called *insertion devices* comprising different magnetic structures are used. Within their magnetic field the electrons are accelerated by the Lorentz force on their circular path. This acceleration causes the electrons to emit electromagnetic radiation, which is done in a narrow intense cone tangential to their trajectory, due to their relativistic velocity. This light is the synchrotron radiation (SR) used for various experimental setups like for example XAS and XMCD measurements. Different types of magnetic structures are available to bend the electron beam and subsequently to deviate the SR into the beamlines and experimental endstations. The two most common insertion devices are the *bending magnets* and the *undulators* (figure 1.13).

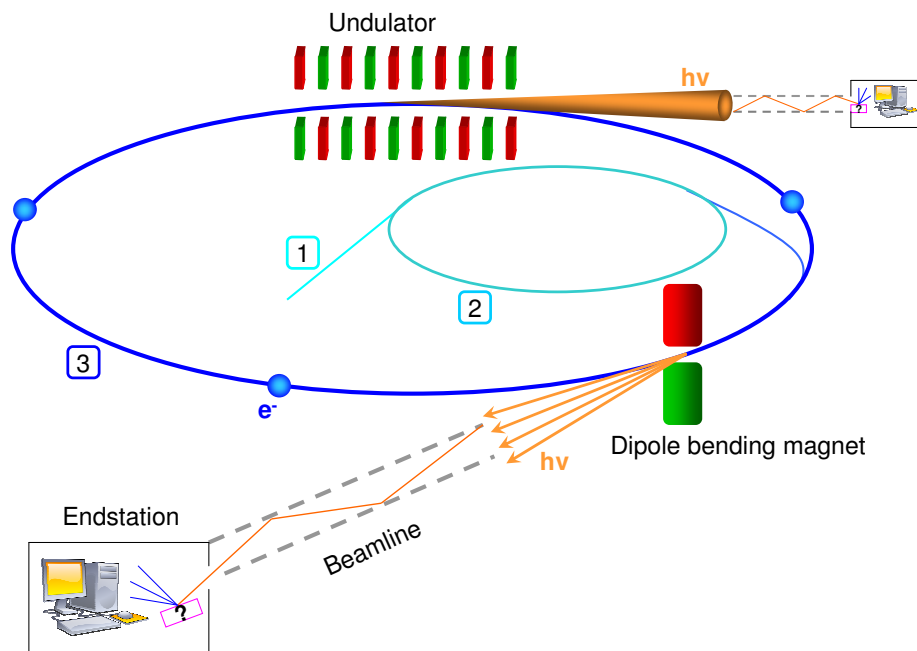


Figure 1.13: Schematic plot of a synchrotron. More details are given in the text.

A dipole, or bending magnet simply bends the electrons in a single curved trajectory producing a rather narrow cone of radiation. The spectrum is continuous over a wide energy range, for instance 100-1000 eV. An undulator comprises of a large number of strong permanent magnets with opposite polarisations (figure 1.14). The electrons oscillate through this periodic magnetic structure and emit coherent X-ray pulses leading to constructive interference. The overall emitted radiation is a very intense and narrow cone with small angular and spectral widths. Thus, the undulator spectrum consists of sharp peaks, called harmonics. The desired energy for the experiment can be chosen by varying the magnetic field strength between the poles. This is realised by changing the distance, or gap, between the upper and lower row of permanent magnets. Such a setup of an upper and lower row of permanent magnets leads to an almost 100% linearly and horizontally polarisation of the emitted light.

In order to perform experiments in dependence of the polarisation, especially if circularly polarised light is required as for instance in XMCD measurement, a combination of two undulators is necessary.

Alternatively one also uses so called *APPLE-type elliptical polarising insertion devices* (or APPLE-type undulators) comprising horizontally separated magnet rows (figure 1.14). By shifting these rows one can produce a helical field at the position of the electron beam causing an elliptical or even circular trajectory. Consequently, elliptically or circularly polarised light is emitted. To change the polarisation while staying at a fixed photon energy, both gap and shift have to be varied. In figure 1.14 one can see the APPLE-type undulator in the circular mode. The shift is set to the position with equal amplitudes of the horizontal and vertical magnetic fields.

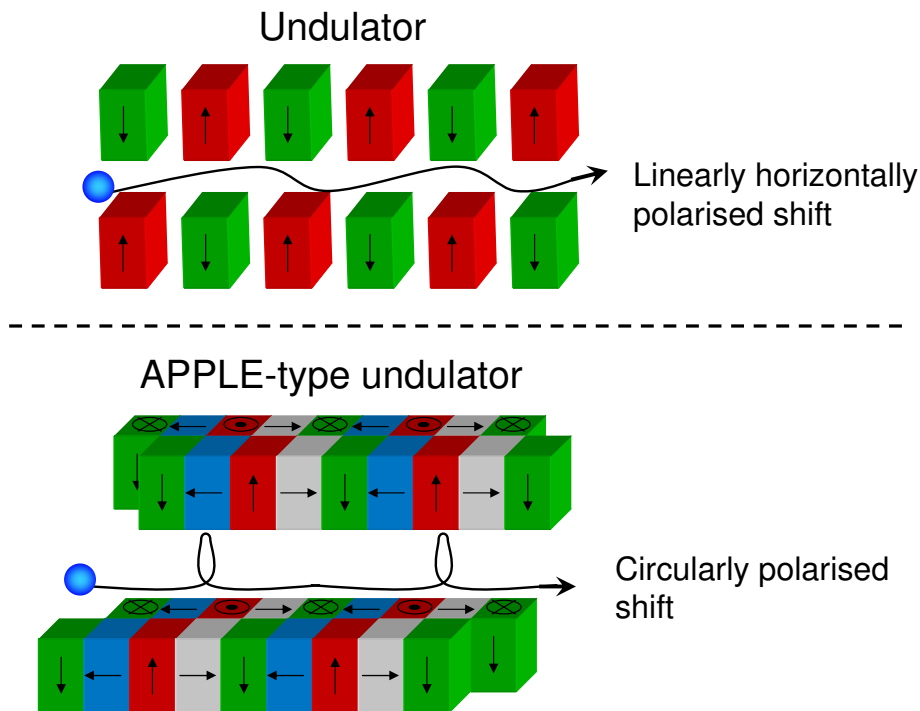


Figure 1.14: Illustration of the an undulator (top) and an APPLE-type undulator (bottom). More details are given in the text.

### Beamline and endstation

In order to use the synchrotron radiation generated by the insertion devices it has to be linked to the experiment. This is done by a so called *beamline*, which is an UHV arrangement of monochromators, slits and mirrors, as shown in figure 1.15. Firstly the desired excitation energy has to be adjusted. If the radiation was generated by an undulator this is done firstly by choosing the right arrangement of the magnetic rows. The produced light passes within the beamline a concrete wall, which is usually sealing the storage ring for safety reasons. Than inside the beamline it is further monochromatised by using a series of high precision optical elements,



for instance monochromators. In order to reflect the X-rays these gratings have to be aligned in very grazing incidence angles. Two different types of monochromators are widely used, the so called spherical grating monochromator (SGM) and the plane grating monochromator (PGM) (Peatman, 1997). In a beamline usually the radiation has to pass slits and mirrors before (vertical condensing mirror, entrance slit) and after (exit slit, refocusing mirror) it hits the monochromator to focus the beam onto the grating and refocus it afterwards onto the sample surface (figure 1.15).

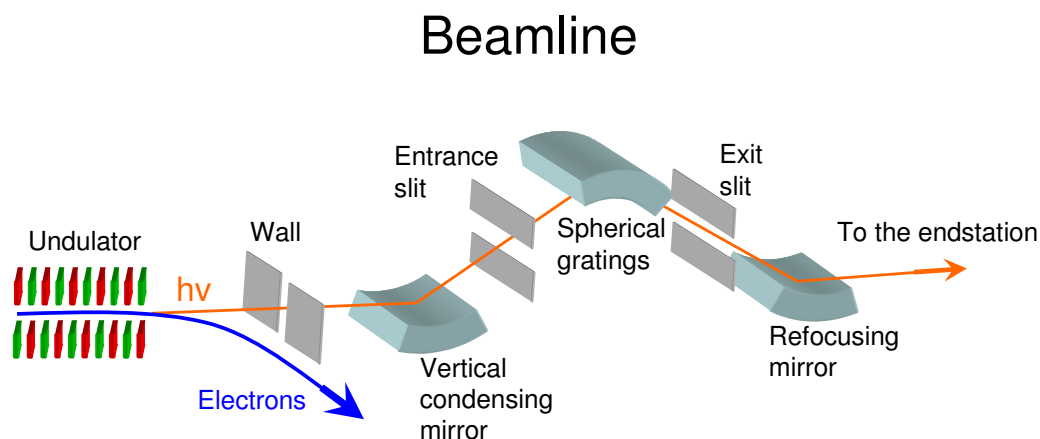


Figure 1.15: Schematic plot of a typical beamline setup.

The results presented in this work have been obtained by using a number of different beamlines equipped with complementary experimental endstations. For instance, XAS and XMCD measurements were performed at the beamlines 4.0.2 and 8.0.1 of the ALS. Beamline 8.0.1 is based upon a 50 mm period length undulator providing linearly polarized photons in the horizontal plane of the laboratory. The generated radiation can be monochromatised by three interchangeable SGMs. At beamline 4.0.2 radiation is generated by a 5.0-cm-period elliptical polarisation undulator (EPU5). Here the user can choose between linear polarisation, which is continuously variable from horizontal to vertical, and left or right elliptical (or circular) polarisation in an energy range of 50-1900 eV. The radiation is monochromatised with a variable-included-angle PGM. Beamline 4.0.2 has two interchangeable endstations. One comprises a fluid helium cooled cryostat enabling to perform measurements at low temperatures down to 2 K and magnetic fields up to 6 T. The measurements presented in this work were performed at the second endstation comprising of an octopole resistive magnet, which can create a magnetic field of 0.8 T tuneable in every spatial direction (Arenholz and Prestemon, 2005).

Furthermore XAS measurements were performed at the BACH beamline of ELETTRA in Trieste (Italy). Here two APPLE type helical undulators deliver X-rays over a wide range from 20-2000 eV with variable polarisation. The generated radiation can be monochromatised by four interchangeable SGMs.

XAS measurements were also performed at the Russian German beamline at BESSY II. Here radiation in a wide energy range of 30-1500 eV is produced by a dipole magnet, whereas the desired photon energies can be selected by two interchangeable PGMs.

Further information about the beamlines and endstations are provided in the internet on the homepages of the respective synchrotrons.

Note that most XAS and XMCD spectra presented in this work were recorded in the TEY-mode unless otherwise noted.

## 1.4 X-ray absorption in multiplet theory

In order to understand and proof X-ray absorption measurement results, in this work XAS and XMCD spectra are compared to so called *multiplet calculations*. For a better understanding of multiplet simulations in the following a brief introduction in the theoretical description of X-ray absorption is given (see also section 2.1.1).

### 1.4.1 Single-particle approximation

As described in section 1.2.2 in the X-ray absorption process, a core electron is excited to an empty state and, as such, XAS probes the unoccupied part of the electronic structure of the system. The resulting X-ray absorption spectrum can be described with the so called *Fermi Golden rule*

$$I_{XAS} \propto |\langle \Phi_f | \hat{e} \cdot r | \Phi_i \rangle|^2 \delta_{E_f - E_i - \hbar\omega} \quad (1.18)$$

According to this rule the absorption intensity  $I_{XAS}$  is proportional to a dipole matrix element ( $\hat{e} \cdot r$ ) coupling the initial state ( $\Phi_i$ ) and the final state ( $\Phi_f$ ). The delta function ( $\delta$ ) takes care of the conservation of energy.

Now one can make a so called *single-particle approximation*. Since in the final state a core electron has been excited, it can be described as the initial state with a continuum electron ( $\epsilon$ ) added and a core electron removed, i.e.,  $\Phi_f = \underline{c}\epsilon\Phi_i$  (equation 1.19). Furthermore one can assume that the matrix element can be rewritten into a single-electron matrix element by removing all electrons that are inactive in the transition itself. Thus only the excited core electron remains in the initial state and the continuum electron in the final state. The series of delta functions identifies with the density of states ( $\rho$ ) (equation 1.20) (Muller *et al.*, 1978).

$$I_{XAS} \propto |\langle \Phi_i \underline{c} \epsilon | \hat{e} \cdot r | \Phi_i \rangle|^2 \delta_{E_f - E_i - \hbar\omega} \quad (1.19)$$

$$I_{XAS} \propto |\langle \epsilon | \hat{e} \cdot r | c \rangle|^2 \cdot \rho \quad (1.20)$$

The dipole matrix element ( $\hat{e} \cdot r$ ) dictates that the density of states has an orbital moment that differs by 1 from the core state ( $\Delta L = \pm 1$ ), while the spin is conserved ( $\Delta S = 0$ ). Since in case of X-rays the quadrupole transitions are some hundred times weaker than the dipole transition, they can be neglected in most cases. Note that this single-particle approximation neglects all electron rearrangements that take place during the electron excitation process. Nevertheless single-particle methods within the so called density functional theorem (DFT) are very successful in describing for example metal and ligand 1s X-ray absorption (K-edge) (de Groot *et al.*, 1993).

Various methods exist to calculate the singel-particle density of states, for example, LMTO, LSW, LAPW and KKR (Zeller, 1992). Also real-space multiple scattering calculations, which are a formally closely related but conceptually different method, can be performed. For details please be refered to (Lytle and Gregor, 1988; Natoli *et al.*, 1986; Rehr *et al.*, 1998; Vvdensky, 1992).

### 1.4.2 The multiplet effect

The previously described singel-particle approximation breaks down in case of 2p X-ray absorption, due to a strong overlap of the p core wave functions with the d valence wave functions. This results in XAS structures that are strongly affected by the core hole wave function leading to so called *multiplet effects*, which the single-particle approximation is no longer appropriate to describe. The break down of the single-particle model is important for all systems with electrons in narrow bands, for example 3d metal and rare-earth metal compounds, which show a strong valence and core wave function overlap.

Within the multiplet theory, which is also based on the Fermi Golden rule, the core hole and free electron of equation 1.19 are rewritten to a 2p core hole ( $\underline{2p}$ ) and a 3d electron (equation 1.21). All valence electrons except the 3d electrons are omitted, and this yields equation 1.22, which is the starting point for all calculations.

$$I_{XAS} \propto \left| \langle \Phi_i \underline{2p} 3d | \hat{e} \cdot r | \Phi_i \rangle \right|^2 \delta_{E_f - E_i - \hbar\omega} \quad (1.21)$$

$$I_{XAS} \propto \left| \langle \underline{2p} 3d^{N+1} | \hat{e} \cdot r | 3d^N \rangle \right|^2 \delta_{E_f - E_i - \hbar\omega} \quad (1.22)$$

### Atomic multiplet theory

The basic starting point for a large part of the analysis of core-level spectra is atomic multiplet theory (Cowan, 1981; Weissbluth, 1978). Faced with the situation of a solid with its combination of extended valence states and a localised core hole, the problem is to find the best way to treat the X-ray absorption process. While a localised approach makes it possible to treat the core hole in detail, an itinerant approach is in most cases the best approach to the ground state of the solid. It has been shown over the last 30 years that a completely localised approach, based on atomic multiplet theory, can be very fruitful to core-level spectroscopy. In this section some aspects of atomic multiplet theory that are important for the analysis of X-ray absorption will be briefly introduced.

Within the atomic multiplet theory an  $N$ -electron atom is described by the Schrödinger equation for a free atom, thus the influence of the surrounding atoms is not taken into account. The overall Hamiltonian reads

$$H = \sum_N \frac{p_i^2}{2m} + \sum_N \frac{-Ze^2}{r_i} + \sum_{pairs} \frac{e^2}{r_{ij}} + \sum_N \zeta(r_i) l_i \cdot s_i \quad (1.23)$$

consisting of the kinetic energy of  $N$  electrons ( $\sum_N \frac{p_i^2}{2m}$ ), the electrostatic interaction of the  $N$  electrons with the nucleus of charge  $+Z$  ( $\sum_N \frac{-Ze^2}{r_i}$ ), the electron-electron repulsion ( $H_{ee} = \sum_{pairs} \frac{e^2}{r_{ij}}$ ), and the spin-orbit coupling of each electron ( $H_{ls} = \sum_N \zeta(r_i) l_i \cdot s_i$ ). Since the kinetic energy and the interaction with the nucleus are the same for all electrons in a certain atomic configuration, they define the average energy of a certain state ( $H_{av}$ ). So the important interactions to be solved are  $H_{ee}$  and  $H_{ls}$ . The basic difficulty when solving the Schrödinger equation is that  $H_{ee}$  is too large to be treated as a perturbation. This problem has been solved with the *central field approximation* by separating the spherical average of the electron-electron interaction ( $\langle H_{ee} \rangle$ ) from the nonspherical part. In the modified electron-electron Hamiltonian  $H'_{ee}$ , the spherical average has been subtracted (equation 1.24) and added to ( $H_{av}$ ), giving a simplified Hamiltonian (equation 1.25).

$$H'_{ee} = H_{ee} - \langle H_{ee} \rangle = \sum_{pairs} \frac{e^2}{r_{ij}} - \left\langle \sum_{pairs} \frac{e^2}{r_{ij}} \right\rangle \quad (1.24)$$

$$H = H_{av} + H'_{ee} + H_{ls} \quad (1.25)$$

This leaves the two interactions  $H'_{ee}$  and  $H_{ls}$  to determine the energies of the various electronic symmetry configurations within the atomic configuration. In the following the 2p X-ray absorption of  $\text{Ti}^{4+}$  will be used as a simple example to make the calculation process more clear.  $\text{Ti}^{4+}$  has a  $2p^6 3d^0$  electron configuration in the initial state and a  $2p^5 3d^1$  configuration in the final state (equation 1.26). To understand the multiplet calculation one has to use so called *term symbols* to describe the various electronic symmetry configurations. These are indicated with their orbital moment  $L$ , spin moment  $S$ , and total moment  $J$  (see also section 1.2.1.1). Together, these three quantum numbers, summerised in the term symbol  $^{2S+1}L_J$ , indicate a certain state and determine its specific energy. In case of  $\text{Ti}^{4+}$  the initial state has only filled or empty shells, which results in  $S = 0$ ,  $L = 0$  and  $J = 0$  described by the term symbol  $^1S_0$ . In the final state the 2p level is occupied by five electrons, which is equivalent to one p-electron ( $S = \frac{1}{2}$ ,  $L = 1$ ), denoted by two term symbols  $^2P_{\frac{1}{2}}$  and  $^2P_{\frac{3}{2}}$  ( $^2P_{\frac{1}{2}, \frac{3}{2}}$ ). The 3d level is occupied by one electron ( $S = \frac{1}{2}$ ,  $L = 2$ ) giving  $^2D_{\frac{3}{2}, \frac{5}{2}}$ . Now within the multiplet theory the 2p and 3d symmetry configurations of the final state are multiplied ( $^2P \otimes ^2D$ ), due to the overlap of the core wave functions with the valence wave functions. This results in new configurations with  $L = 3, 2, 1$  and  $S = 1, 0$  namely  $^1P_1$ ,  $^1D_2$ ,  $^1F_3$ ,  $^3P_{012}$ ,  $^3D_{123}$ ,  $^3F_{234}$ . The X-ray absorption transition matrix elements to be calculated are given in equation 1.27.

$$I_{XAS} \propto |\langle 2p^5 3d^1 | p | 3d^0 \rangle|^2 \quad (1.26)$$

$$I_{XAS} \propto |\langle ^1, ^3PDF | ^1P_1 | ^1S_0 \rangle|^2 \quad (1.27)$$

In 1.27 the symmetry of the dipole transition is given as  $^1P_1$ , according to the dipole selection rules ( $\Delta J = +1, 0, -1$ ;  $\Delta S = 0$ ;  $\Delta L = 1$ ). This reduces the number of final states that can obtain finite intensity, thus the number of lines in the spectrum,

since from a ground state with  $J = 0$  only final states with  $J = 1$  can be reached. Three final state configurations fulfil this condition, namely  $^1P_1$ ,  $^3P_1$  and  $^3D_1$ . So, the problem of calculating the 2p absorption spectrum is reduced to solving the  $3 \times 3$  energy matrix of the  $J = 1$  final states to get the energy positions of the absorption lines (equation 1.29). The energy matrix of the initial state (equation 1.28) is zero, since in  $^1S_0$  neither a spin-orbit coupling nor a nonspherical electron-electron interaction is present.

$$H_{INIT} = \langle 3d^0 | H'_{ee} + H_{ls} | 3d^0 \rangle = \left\langle ^1S_0 \left| \frac{e^2}{r_{12}} + \zeta_d l_d \cdot s_d \right| ^1S_0 \right\rangle \quad (1.28)$$

$$\begin{aligned} H_{FINAL} &= \langle 2p^5 3d^1 | H'_{ee} + H_{ls} | 2p^5 3d^1 \rangle \\ &= \left\langle ^{1,3}P_1 ^{3D}_1 \left| \frac{e^2}{r_{12}} + \zeta_p l_p \cdot s_p + \zeta_d l_d \cdot s_d \right| ^{1,3}P_1 ^{3D}_1 \right\rangle \end{aligned} \quad (1.29)$$

The resulting lines are broadened with a lorentzian and a gaussian function to account for the lifetime broadening and the broadening due to the experiment. This results in a 2p XAS spectrum (figure 1.16). Note that in the single electron picture the Ti 2p absorption spectrum would only have two lines due to the spin-orbit coupling.

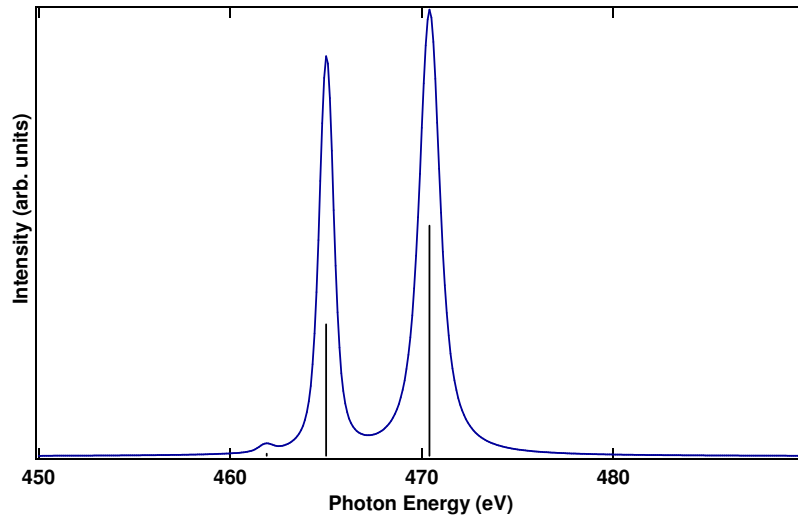


Figure 1.16: Atomic multiplet calculation of a  $\text{Ti}^{4+}$  XAS spectrum.

### Ligand-field multiplet theory

If one wants to calculate XAS spectra for a solid state one has to consider two additional aspects, one is the different local symmetry, the other the different more itinerant electronic features. The first aspect is taken care of with the ligand-field (or crystal-field) multiplet theory described in this section, the second is treated with the charge transfer multiplet approach, which is introduced in the next section.

For core spectroscopy the ligand-field theory has been developed by Thole and co-workers (Thole *et al.*, 1988). The dominant symmetry effect in solids is the cubic

ligand-field. The strength of this operator is usually denoted as the ligand-field splitting (10Dq). The ligand-field multiplet theory now simply extends the atomic multiplet theory by incorporation of the ligand-field splitting. A good overview about the crystal field theory is given by Moffit and Ballhausen (1956). In for instance an octahedral environment, the field of the neighbouring atoms on the central atom has cubic ( $O_h$ ) symmetry, which divides the 5-fold-degenerate 3d orbitals into two distinct representations of  $T_{2g}$  and  $E_g$  symmetry. These states are energetically separated due to the fact that the 2-fold-degenerate  $E_g$  state contains orbitals that point toward the centre of the cube face, thus the position of the ligands, while the three  $t_{2g}$  orbitals point toward the corners of the cube. Therefore the  $E_g$  states interact stronger, electrostatically as well as covalently, with the ligands. The effect of the cubic ligand-field on the energies of the atomic states has been described in the textbooks of Butler (1981); Fontaine (1995) and Sugano *et al.* (1970). It is found that the degeneracy of the atomic states is partially lifted and the D, F and higher states are split into a series of representations in cubic symmetry (see figure 1.17). Note that also the number of multiplet states is considerably larger ( $2p^53d^1(\text{atomic})$ : 12 multiplet states ;  $2p^53d^1(O_h)$ : 25 multiplet states).

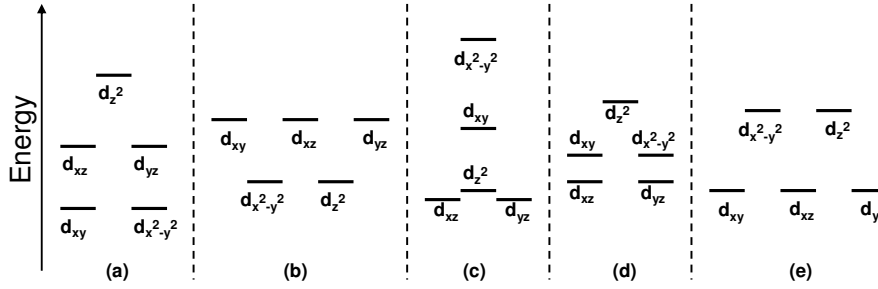


Figure 1.17: Splitting patterns of d orbitals in ligand fields for (a) linear  $ML_2$ , (b) tetrahedral  $ML_4$ , (c) square planar  $ML_4$ , (d) trigonal-bipyramidal  $ML_5$  and (e) octahedral  $ML_6$ .

The transition probability for the  $3d^0$  systems in cubic symmetry is given in equation 1.30. As denoted by  $p[T_1]$  from the  $A_1$  initial state all final states of  $T_1$  symmetry are allowed and have a finite transition probability. In contrast to the atomic multiplet theory this includes in addition to the atomic states with  $J = 1$  the states with  $J = 3$  and  $J = 4$ . These are the seven states  $^1P_1$ ,  $^3P_1$ ,  $^3D_1$ ,  $^1F_3$ ,  $^3D_3$ ,  $^3F_3$  and  $^3F_4$ . In order to calculate the proper spectrum, for these final states and the initial state the atomic plus ligand-field Hamiltonian are solved (equation 1.31, 1.32).

$$I_{XAS,1} \propto |\langle 2p^53d^1[T_1] | p[T_1] | 3d^0[A_1] \rangle|^2 \quad (1.30)$$

$$\begin{aligned} H_{INIT,1} &= \langle 3d^0 | H'_{ee} + H_{ls} + H_{LFM} | 3d^0 \rangle \\ &= \left\langle {}^1S_0 \left| \frac{e^2}{r_{12}} + \zeta_d l_d \cdot s_d + H_{LFM} \right| {}^1S_0 \right\rangle \end{aligned} \quad (1.31)$$

$$H_{FINAL,1} = \langle 2p^5 3d^1 | H'_{ee} + H_{ls} + H_{LFM} | 2p^5 3d^1 \rangle$$

$$= \left\langle {}^{1,3}P_1 {}^3D_{13} {}^{1,3}F_{34} \left| \frac{e^2}{r_{12}} + \zeta_p l_p \cdot s_p + \zeta_d l_d \cdot s_d + H_{LFM} \right| {}^{1,3}P_1 {}^3D_{13} {}^{1,3}F_{34} \right\rangle \quad (1.32)$$

In figure 1.18 the effects of an increasing cubic ligand-field on the atomic multiplet spectrum (figure 1.16) are shown. As one can see for small ligand-fields the spectrum is hardly modified, since the four additional transitions have not gained enough intensity to be detectable in the spectrum. But for higher ligand-fields the additional lines are clearly visible.

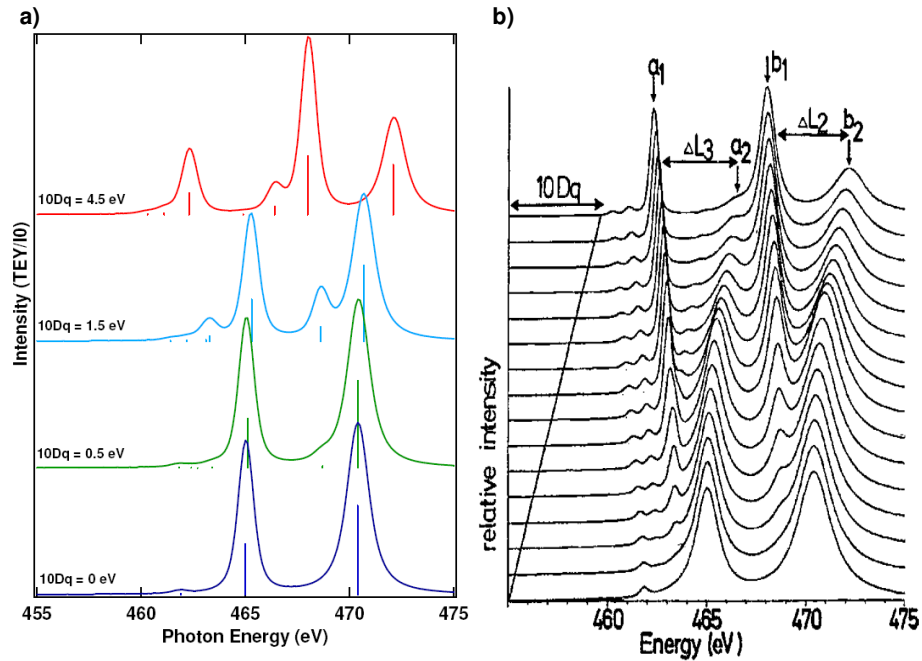


Figure 1.18: Ligand-field multiplet calculations of  $\text{Ti}^{4+}$  XAS spectra with different cubic crystal-field values. a) selected calculations together with their unbroadened lines. b) calculation overview attached from de Groot (2001) in steps of 0.3 eV. Bottom spectrum has a crystal-field of 0.0 eV, top spectrum of 4.5 eV.

Note that although the peak splitting in the spectra is related to the value of  $10Dq$ , it is not a direct measure of it. So 2p X-ray absorption cannot be used to directly measure the crystal-field splitting.

Nevertheless ligand-field multiplet calculations can be directly compared with experiments and show very good results (de Groot *et al.*, 1990a,b). The high resolution of soft X-ray edges, due to the long lifetime of the core states, makes the spectra sensitive to details of the electronic structure, such as the valence, symmetry, spin state, and crystal-field value (Cramer *et al.*, 1991; de Groot, 1994).

### Charge-Transfer multiplet theory

The charge-transfer multiplet calculation is similar to a ligand-field multiplet calculation but it uses more than one configuration. In case of  $\text{Ti}^{4+}$  at first the matrixes of the ligand-field approach (equation 1.30, 1.31 and 1.32) are solved. The charge-transfer model now adds a  $3d^{N+1} \underline{L}$  initial state plus the corresponding changes in the final states. In case of a transition-metal oxide, in a  $3d^{N+1} \underline{L}$  configuration an electron has been moved from the oxygen 2p valence band to the metal 3d band. This adds a second initial state, final state and dipole transition. For  $\text{Ti}^{4+}$  this gives (here the term symbols are omitted for clarity):

$$I_{XAS,2} \propto |\langle 2p^5 3d^2 \underline{L} | p | 3d^1 \underline{L} \rangle|^2 \quad (1.33)$$

$$H_{INIT,2} = \left\langle 3d^1 \underline{L} \left| \frac{e^2}{r_{12}} + \zeta_d l_d \cdot s_d + H_{LFM} \right| 3d^1 \underline{L} \right\rangle \quad (1.34)$$

$$H_{FINAL,2} = \left\langle 2p^5 3d^2 \underline{L} \left| \frac{e^2}{r_{12}} + \zeta_p l_p \cdot s_p + \zeta_d l_d \cdot s_d + H_{LFM} \right| 2p^5 3d^2 \underline{L} \right\rangle \quad (1.35)$$

Finally the two initial states and two final states are coupled by monopole transitions, i.e., configuration interaction.

$$H_{MIX \ I1,I2} = \langle 3d^0 | t/\Delta | 3d^1 \underline{L} \rangle \quad (1.36)$$

$$H_{MIX \ F1,F2} = \langle 2p^5 3d^1 | t/\Delta | 2p^5 3d^2 \underline{L} \rangle \quad (1.37)$$

Here  $t$  denotes the mixing parameter, which couples both configurations. The charge transfer energy ( $\Delta$ ) is the energy difference between the  $3d^N$  and  $3d^{N+1} \underline{L}$  configurations. Therefore the Hamiltonian is indicated with  $t/\Delta$ . The spectrum is calculated by solving the equations 1.30 - 1.37. Note that here the 3d states are described in a correlation fashion, while all other electrons are described in a band-like fashion (Zaanen *et al.*, 1985). This is essentially the Anderson impurity model. In the final state of the X-ray absorption process a 2p electron is annihilated, and a 3d electron is created leading to the configurations  $2p^5 3d^{N+1}$  and  $2p^5 3d^{N+2} \underline{L}$ . The energy difference between these configurations is given as  $\Delta + U - Q$ , where  $U$  is the 3d3d correlation energy and  $Q$  the core hole potential. The formal definition of  $U$  is the energy difference one obtains when an electron is transferred from one metal site to another, i.e.  $U = E(3d^{N+1}) + E(3d^{N-1}) - E(3d^N) - E(3d^N)$ . The number of interactions of two  $3d^N$  configurations is one more than the number of interactions of  $3d^{N+1}$  plus  $3d^{N-1}$ , implying that this energy difference is equal to the correlation energy between two 3d electrons. The core hole potential  $Q$  is due to a not 100% filled core state in the final state of the XAS process. This creates an additional attraction to all the core and valence levels that lie above it. The most important core hole potentials are the effects on the 3d states. Thus, in our case  $Q$  identifies with the 2p3d correlation energy. From the systematic analysis of core-level photoemission spectra, it has been found that  $Q$  is slightly larger than  $U$ . Typical values are 9 eV



for  $Q$  and 7-8 eV for  $U$ . Due to this only small charge-transfer satellites are visible in X-ray absorption (de Groot, 1994; de Groot and Kotani, 2008).

Figure 1.19 shows the effects of the charge-transfer energy on divalent nickel. The top spectrum has a  $\Delta$  of +10 eV and is essentially the ligand-field multiplet spectrum of  $\text{Ni}^{2+}$  ( $3d^8$ ). The spectrum at the bottom uses  $\Delta = -10$  eV, thus the ground state is almost a pure  $3d^9\bar{L}$  configuration.

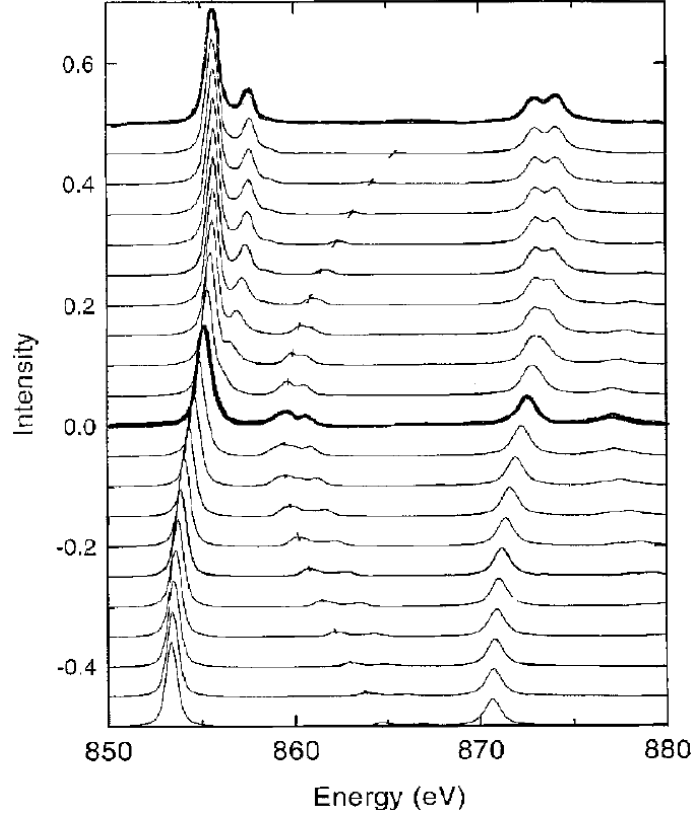


Figure 1.19: Series of charge-transfer multiplet calculations for the ground state  $3d^8 + 3d^9\bar{L}$ , attached from de Groot (2001).

As can be seen the effects of charge transfer on the ligand-field X-ray absorption spectral shape are (1) the contraction of the multiplet structures and (2) the formation of small satellites. This is in agreement with experimental results (Okada and Kotani, 1992a,b; Okada *et al.*, 1992; Okada and Kotani, 1993; van der Laan *et al.*, 1986). It is found that for many systems charge-transfer multiplet calculations are important, since no good comparison with ligand-field multiplet spectra can be made (Hu *et al.*, 1998b,a). Note that one can also continue with this procedure and add a  $3d^{N+2}\bar{L}^2$  configuration etc., but in many cases two configurations will be enough to explain the spectral shape.

For further information about multiplet calculations please be referred to de Groot (2001) and de Groot and Kotani (2008) and citations within.

## 1.5 Magnetism

Magnetism is a physical phenomenon which manifest itself in an action of force between magnets, magnetic materials and moved charges. Although the scientific research and understanding of magnetism started not until the modern age with the systematic analysis of William Gilbert, an english physician and physicist, in 1600, the phenomenon is known for a much longer time. Legend has it that an old grecian shepherd, called magnes, was the first human who experienced magnetism about 4000 years ago. He grazed his sheep in magnesia a region in northern greece and it is said that his cleats and the thorn of his hiking pole stuck to a big black stone. This stone was named magnetit according to magnesia or magnus. The first known chronicle of magnetic stones was done by Thales of Miletus (about 634-546 BC) (Stöhr and Siegmann, 2006). Although known for such a long time and researched scientifically for hundreds of years there are still a lot of questions concerning the magnetic behaviour of materials. In physics one tries to understand and describe how a material responds on the microscopic level to an applied magnetic field. Here the spin of an electron plays an important role. In this work new advanced magnetic materials were investigated in order to understand their anomalous electric and magnetic properties.

### 1.5.1 Magnetism in solids

This section deals with the different types of magnetism in a solid. Figure 1.20 shows an overview of various magnetic ground states. The direction and strength of the spontaneous magnetisation as well as the induced magnetisation by an external magnetic field in a compound (pale blue square) are illustrated. In the following a brief description of the different types of magnetism is given.

#### Diamagnetism

All materials are diamagnetic, which means they have a tendency to oppose an applied magnetic field and therefore to be repelled by it. However the diamagnetic behaviour is usually very weak and is clearly dominated by other magnetic behaviours like para- or ferromagnetism. Thus, although present in all materials, diamagnetism is only observed in a purely diamagnetic material. As illustrated in figure 1.20 in a diamagnetic material the atoms have no unpaired electrons and therefore no atomic spin magnetic moments are present (diamagnetism, left panel). These materials do not show a spontaneous magnetisation. If an external magnetic field is applied, magnetic moments appear, which are aligned antiparallel to the direction of the magnetic field. These moments arise from the orbital motions of the electrons and can be understood classically as follows. The external magnetic field causes the electrons circling the nucleus to experience a Lorentz force. This effect systematically increases the orbital magnetic moments that were aligned opposite to the field, and decreases the ones aligned parallel to the field (in accordance with Lenz's law). This results in a small bulk magnetic moment, with an opposite direction to the applied field (diamagnetism, right panel).

Here it has to be mentioned that this description is meant only as an heuristic. A proper understanding requires a quantum-mechanical description.

## Paramagnetism

A paramagnetic material consists of atoms with unpaired electrons and therefore has atomic spin magnetic moments. In an ideal paramagnet these moments are isolated from each other and can align in any direction (figure 1.20, paramagnetism, left panel). Thus, there is no spontaneous magnetisation. In the presence of an external magnetic field the magnetic moments tend to align themselves parallel to it, which reinforces the field (figure 1.20, paramagnetism, right panel). Since the atomic magnetic moments are isolated from each other, the magnetisation vanishes when the external magnetic field is removed due to the thermal agitation. Accordingly the paramagnetism decreases with increasing temperature.

## Ferromagnetism

Like a paramagnet a ferromagnetic material consists of atoms with unpaired electrons. But the resulting atomic spin magnetic moments do not only tend to align themselves with an external magnetic field, there is also a tendency of the moments to align themselves parallel to each other. This coupling does not reach throughout the material. The spin magnetic moments form small regions, called *Weiss domains* or magnetic domains, in which they align more or less uniform. As illustrated in figure 1.20 (ferromagnetism, left panel) the direction of the spin magnetic moments between the *Weiss domains* can be very different resulting in a small or even no spontaneous magnetisation. If an external magnetic field is applied the spin magnetic moments tend to align themselves parallel to the magnetic field and the domain boundaries vanish (figure 1.20, ferromagnetism, right panel). After that, when the magnetic field is removed, the magnetic moments may stay in the same direction resulting in a magnetised ferromagnetic material.

Every ferromagnet has its own individual temperature, called *Curie temperature*, above which it loses its ferromagnetic properties showing only paramagnetic behaviour. This is because of the thermal energy which overwhelms the energy-lowering due to ferromagnetic order and disorders the spin magnetic moments.

## Antiferromagnetism

In contrast to the ferromagnet in an antiferromagnetic material the neighbouring atomic spin magnetic moments of unpaired electrons try to align themselves antiparallel to each other. This results in a zero spontaneous magnetisation (see figure 1.20, antiferromagnetism, left panel). In a strong magnetic field and/or at higher temperatures the antiferromagnetic coupling weakens leading to a not vanishing net magnetic moment (figure 1.20, antiferromagnetism, right panel).

Like every ferromagnet also every antiferromagnet has its own individual temperature above which it loses its antiferromagnetic order, due to the thermal energy. This temperature is called the *Néel temperature*.

## Ferrimagnetism

In ferrimagnets like in antiferromagnets the neighbouring atomic spin magnetic moments align themselves antiparallel to each other. But in contrast to antiferromagnets there are two different kind of magnetic sublattices, which align parallel among themselves indicated by black and green arrows in figure 1.20. Since one magnetic sublattice has a higher magnetic moment than the other, this often results in a spontaneous magnetisation similar to a ferromagnet (figure 1.20, ferrimagnetism, left panel). If an external magnetic field is applied the spin magnetic moments try to align parallel respectively antiparallel to the direction of the field resulting in a net magnetic moment that points in the direction of the magnetic field (figure 1.20, ferrimagnetism, right panel). Like in a ferromagnet the spin magnetic moments in a ferrimagnet may retain their direction when the magnetic field is removed resulting in a magnetised ferrimagnetic material.

The individual temperature above which a ferrimagnet loses its spin magnetic order due to the thermal energy is referred to as *Curie temperature* similar to ferromagnets.

## Antiferromagnetism

The term antiferromagnetism is sometimes used to describe a special form of antiferromagnetism in which a parasitic ferromagnetism occurs. This is explained by a canting of the antiferromagnetically coupled spin magnetic moments resulting in a non collinear ordering of neighbouring magnetic moments, like for example in haematite (Dzyaloshinsky, 1958). This leads to a not vanishing net magnetic moment. Like ferromagnets antiferromagnetic materials can show a spontaneous magnetisation. The net magnetic moment aligns parallel to an applied magnetic field. After removal of the magnetic field the material shows a weak but very stable magnetisation (Tarling and Hrouda, 1993).

Note that there are also antiferromagnetic spin systems, so called frustrated systems, which are geometrically unable to form an antiferromagnetic ground state (Nagano *et al.*, 2007; Schnalle *et al.*, 2009).

The individual temperature above which a canted antiferromagnet loses its spin magnetic order due to the thermal energy is usually referred to as *Néel temperature* similar to antiferromagnets.

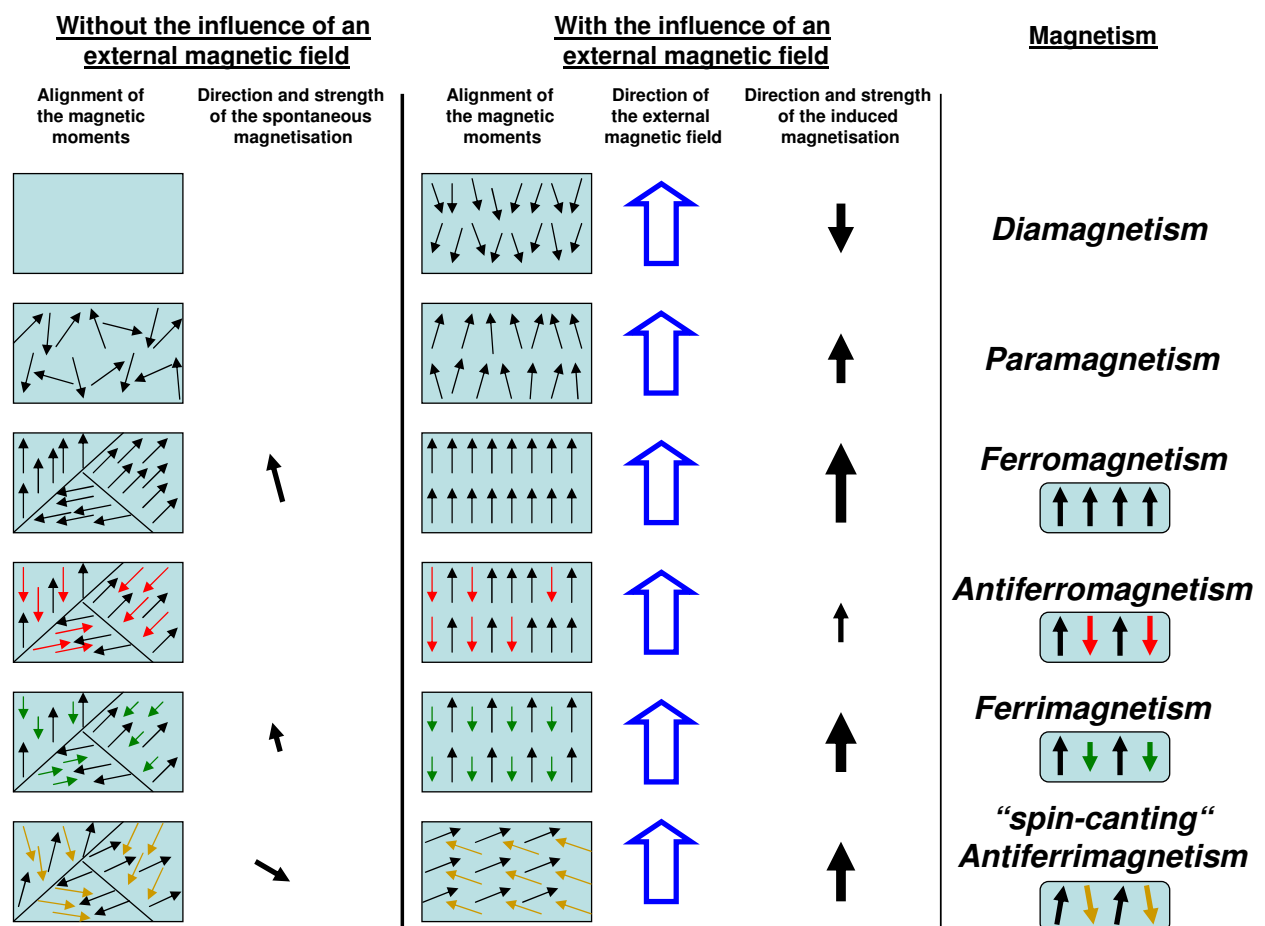


Figure 1.20: An overview of different types of magnetism. The strength and direction of the spontaneous magnetisation and the induced magnetisation by an external magnetic field are illustrated (below the Curie temperature and Néel temperature, respectively). Inspired by Günther (2003).

### 1.5.2 Magnetism in theory

As shown in the previous section the different types of magnetism in a solid originate from unpaired electron spins and their alignment with and without an external magnetic field. This section deals with the microscopic origin of magnetism, thus with the quantum mechanical reason for the alignment of spins. Note that here only a small selection of laws and concepts describing magnetism can be given. Issues that are important for the present work are emphasised. For further studies please be referred to appropriate literature like for example Stöhr and Siegmann (2006).

#### The Pauli exclusion principle and the exchange interaction

Although an electron spin can be seen as a small elementary magnet the alignment of spins cannot be caused by a magnetic interaction between spins. The direct magnetic interaction between a pair of electrons is negligibly small compared to the electric interaction. In fact the cause of the spin alignment is pure quantum mechanical. Its origin is the *Pauli exclusion principle* found by Wolfgang Ernst Pauli (1900 - 1958) in 1925 and the *exchange interaction* discovered by Werner Heisenberg (1901 - 1976) and P.A.M. Dirac (1902 - 1984) in 1926.

The Pauli exclusion principle states that *the total wavefunction of a system of  $N$  identical fermions (half integer spin particles, like electrons) is antisymmetric concerning the permutation of two particles*. To illustrate the consequence of this one can consider a system of two electrons. In many cases it is possible to separate the total wavefunction in the position-space wavefunction and the spin wavefunction. If one now assumes a symmetric position-space wavefunction, thus allows the electrons to be located at the same position, the spin wavefunction has to be antisymmetric in order to get an antisymmetric total wavefunction. This means the spins of the two electrons are aligned antiparallel. In case of an antisymmetric position-space wavefunction, which makes the location of the electrons at the same position impossible, the spin wavefunction has to be symmetric, thus the spins are aligned parallel. In other words the Pauli exclusion principle states that two electrons are not allowed to be identical in their position and spin direction, thus in all their quantum numbers.

A logical consequence of the Pauli principle is the exchange interaction. The wavefunctions of identical neighbouring particles can overlap. Although the Pauli principle shows that two electrons align either parallel or antiparallel subject to the symmetry of the position-space wavefunction, it does not favour one constellation. But due to the Coulomb repulsion the systems energetically prefers a constellation in which the average distance between the electrons is higher. This is the case for an antisymmetric position-space wavefunction causing a parallel alignment of the spins. Therefore the exchange interaction cannot be understood as a force, but as a quantum mechanical effect. It directly causes the Hund's rules and in many cases ferromagnetism.

Note that in solids also exchange interactions can exist that prefer antiferromagnetic ordering of the electron spins. One possible reason for this can be the distance between the atomic nuclei. If the atomic distances are very small it is energetically preferable if the electrons are located between the atomic cores to decrease the repulsive force of the positive nuclei. This makes a symmetric position-space wavefunction necessary and therefore an antiferromagnetic ordering of the spins. In general the

influence of the exchange interaction on the spins is highly dependent on the concrete wavefunction in a solid. Also other additional effects like for instance the *superexchange* or the *double-exchange* can affect or dominate the spin alignment in a solid. These mechanisms are introduced briefly in the following.

### Superexchange and double-exchange mechanism

Kramers (1934) noticed that the Mn atoms in MnO manage to interact with each other despite having nonmagnetic oxygen atoms between them. He proposed an exchange interaction that takes place over a nonmagnetic ligand, the so called *superexchange interaction*. Later the superexchange interaction was formulated by Anderson (1950). As shown by Kanamori (1959) the sign of the superexchange interaction is closely connected with the cation orbital state, when the cation is subject to the crystalline field arising from octahedrally or tetrahedrally surrounding anions. In a crystal the orbital of the cation and that of the anions overlap each other considerably, but due to certain different symmetry properties some orbitals can be considered as orthogonal. This leads to ferromagnetic or antiferromagnetic superexchange interactions in dependence on the number of 3d electrons of the interacting cations, the angle between the cations and the ligand field symmetry. For instance a  $\text{Cr}^{3+} - \text{Cr}^{3+}$  ( $d^3-d^3$ ) interaction via oxygen in an octahedral site would be ferromagnetic in  $90^\circ$  interaction, while it would be antiferromagnetic in  $180^\circ$  interaction. In the presented work evidence was found that superexchange interaction dominates the ferrimagnetic ordering in  $\text{Fe}_{1-x}\text{Cu}_x\text{Cr}_2\text{S}_4$  (see chapter 4).

Beside the direct exchange and superexchange interaction also a different mechanism, the so called *double-exchange* can affect the spin alignment. It was first proposed by Zener (1951) and is related to the electron exchange between two atomic species. The double-exchange predicts that electron movement from one species to another will be facilitated more easily if the electrons do not have to change spin direction in order to conform with Hund's rules. The resulting ability to hop (to delocalise) reduces the kinetic energy and therefore can lead to ferromagnetic alignment of neighbouring ions. A related process the tripleexchange was introduced by Palmer and Greaves (1999). Basically similar to the double-exchange the tripleexchange involves a third metallic ion in the hopping process leading to antiferromagnetic or ferrimagnetic alignment (see also chapter 4).

Note that the direct exchange and superexchange effect align spins of atoms with the same valence, while double- and tripleexchange can only occur between atoms with different valence states. In direct exchange and superexchange also the electrons do not actually move between the cations in contrast to the double- and tripleexchange mechanism.

### The spin and orbital magnetic moment

To investigate the magnetic properties of a solid its reaction to an external magnetic field, thus its magnetic moment is measured. The magnetic moment of a solid is the sum of its atomic magnetic moments, which is the total magnetic dipole moment of its electrons.

As already mentioned electrons have an intrinsic angular momentum, the spin. This

leads to a *spin magnetic moment*:

$$\vec{\mu}_S = -g_S \mu_B \left( \frac{\vec{S}}{\hbar} \right) \quad (1.38)$$

with the z component:

$$(\vec{\mu}_S)_z = -g_S \mu_B m_S \quad (1.39)$$

Here  $\vec{S}$  is the electron spin angular momentum and  $m_S$  the spin quantum number.  $\mu_B$  is the Bohr magneton and  $\hbar$  the reduced Planck constant. The spin  $g$ -factor  $g_S \sim 2$  comes from the Dirac equation, a fundamental equation connecting the electron spin with its electromagnetic properties. According to this the electron spin is twice as effective in producing a magnetic moment as it would be as a classical spin of a charged body. Therefore the spin can not be understood as a rotation of an electron. Beside the spin angular momentum also the orbital motion of an electron in a solid produces a magnetic moment, the so called *orbital magnetic moment*:

$$\vec{\mu}_L = -g_L \mu_B \left( \frac{\vec{L}}{\hbar} \right) \quad (1.40)$$

$$(\vec{\mu}_L)_z = -g_L \mu_B m_L \quad (1.41)$$

$\vec{L}$  is the orbital angular momentum and  $m_L$  the orbital quantum number. The orbital  $g$ -factor  $g_L$  is exactly equal to one. Note that  $\vec{\mu}_S$  and  $\vec{\mu}_L$  are negative constants multiplied by the spin and orbital angular momentum, respectively. So the magnetic moment is antiparallel to the angular momentum.

Many experimental methods measure the *total magnetic moment* resulting from both the spin and orbital angular momenta. It is related to the total angular momentum  $\vec{J} = \vec{L} + \vec{S}$ :

$$\vec{\mu}_J = -g_J \mu_B \left( \frac{\vec{J}}{\hbar} \right) \quad (1.42)$$

$$(\vec{\mu}_J)_z = -g_J \mu_B m_J \quad (1.43)$$

The  $g$ -factor  $g_J$  is known as the Lande  $g$ -factor, which can be related to  $g_L$  and  $g_S$  by quantum mechanics. As mentioned in section 1.2.2.1 one big advantage of XMCD measurements is that one can measure the magnetic moment of a solid separated in its spin and orbital magnetic moment. Note that in many crystals the orbital magnetic moment is exactly or very close to zero (quenched), due to the crystal field which lifts the degeneracy of the electron valence states and annuls the Hund's rules.



# Chapter 2

## Fe in different molecules and chalcogenide systems

### 2.1 Introduction

In a chemical point of view iron is a group 8 and period 4 metallic element with the symbol Fe (latin: ferrum), which is also classified as a transition metal. It has the atomic number 26 and the electron configuration  $3d^6 4s^2$ . Iron is one of the most common metals and ferromagnetic materials in everyday use. Pure iron single crystals are soft (softer than aluminium) and are allotropic. As molten iron cools down it crystallises at 1538 °C into its so called  $\delta$  allotrope, which has a body-centred cubic (bcc) crystal structure. With further decreasing temperature the crystal structure changes to face-centred cubic (fcc) at 1394 °C ( $\gamma$ -iron) and becomes bcc again at 912 °C ( $\alpha$ -iron). At 770 °C (Curie temperature,  $T_C$ ) iron becomes magnetic (see also figure 2.1).

Although pure iron is a metallic ferromagnet, it also can be present in various other compounds exhibiting completely different properties. For instance, Fe can be present in insulators (e.g. FeO), half-metals (e.g.  $\text{Sr}_2\text{FeMoO}_6$ ) or semiconductors (e.g.  $\text{FeCr}_2\text{S}_4$ ); in ferrimagnetic (e.g.  $\text{Fe}_3\text{O}_4$ ) or antiferromagnetic (e.g. FeO,  $\text{Fe}_2\text{O}_3$ ) materials. In a compound Fe can be metallic or it can be present in so called ionic valence states like for instance  $\text{Fe}^{2-}$ ,  $\text{Fe}^{2+}$ ,  $\text{Fe}^{3+}$  or  $\text{Fe}^{6+}$ . Note that in chalcogenide systems Fe mainly occurs in a divalent or trivalent valence state ( $\text{Fe}^{2+}$ ,  $\text{Fe}^{3+}$ ), like also in the compounds investigated in this work.

Many so called advanced materials, which show very interesting magnetic and electric behaviour, contain Fe. Therefore the investigation of the electronic and magnetic structure of Fe in these compounds is of high importance in order to understand the origin of their interesting properties. In this chapter an overview of various different electronic and magnetic Fe states found in advanced materials will be given. Thereby XAS and XMCD measurements are compared to multiplet calculations in order to understand and confirm the results. The following section gives a short overview of Fe 2p XAS and XMCD multiplet calculations and the influence of crystal field, charge transfer and temperature on the spectra (see also section 1.4).

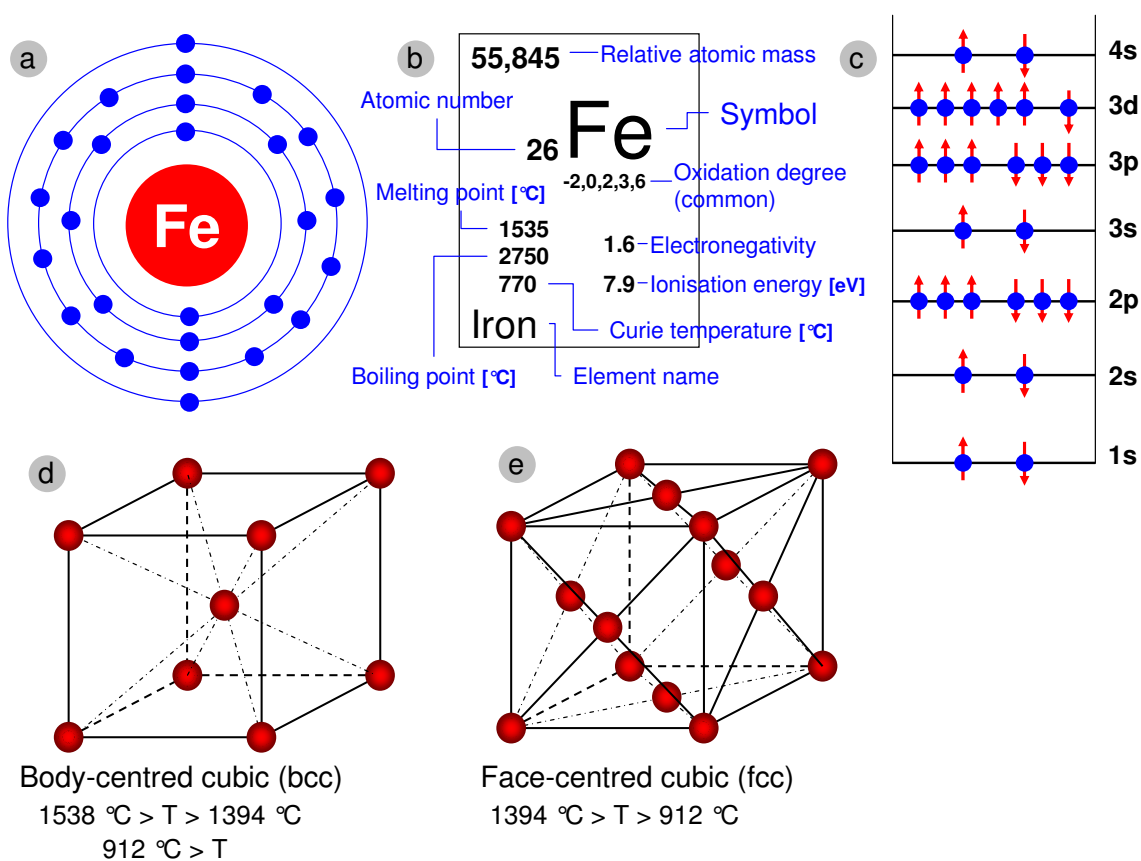


Figure 2.1: Overview of Fe properties: a) the classic electron shell, b) information about Fe in a periodic table, c) the atomic electron configuration, d) and e) the two possible crystal structures.

### 2.1.1 Calculation overview

In all the chalcogenide systems investigated in this work Fe appeared in a divalent or trivalent valence state. Therefore in the following an overview of multiplet calculations for  $\text{Fe}^{2+}$  and  $\text{Fe}^{3+}$  will be presented (see also de Groot *et al.* (1990a)). In figure 2.2 atomic multiplet calculations of the Fe 2p XAS spectrum are presented. Here all solid-state effects, like for instance the crystal-field, are neglected. As one can see in contrast to  $\text{Ti}^{4+}$  ( $3d^0$ ) (figure 1.16) for  $\text{Fe}^{2+}$  ( $3d^6$ ) and  $\text{Fe}^{3+}$  ( $3d^5$ ) a rich multiplet structure with many lines is present in the absorption spectrum, due to the big variety of initial and final multiplet states. In order to compare the calculations with experiments the spectra have to be broadened. For all the calculations presented here a Lorentzian broadening with  $\sigma = 0.4$  eV at the  $L_3$  part and  $\sigma = 0.6$  eV at the  $L_2$  part is used. In addition the spectra are convoluted with a Gaussian broadening with  $\sigma = 0.2$  eV. These values showed good agreement with measurement results. Also the calculated intensity and energy scale is used. Note that these calculations are not suited for the calculation of the absolute energy positions. Therefore in order to compare the calculations with the experiment the spectra simply have to be shifted. In the next sections the influence of the crystal field, charge transfer and temperature on the calculated Fe multiplet structure will be shown.

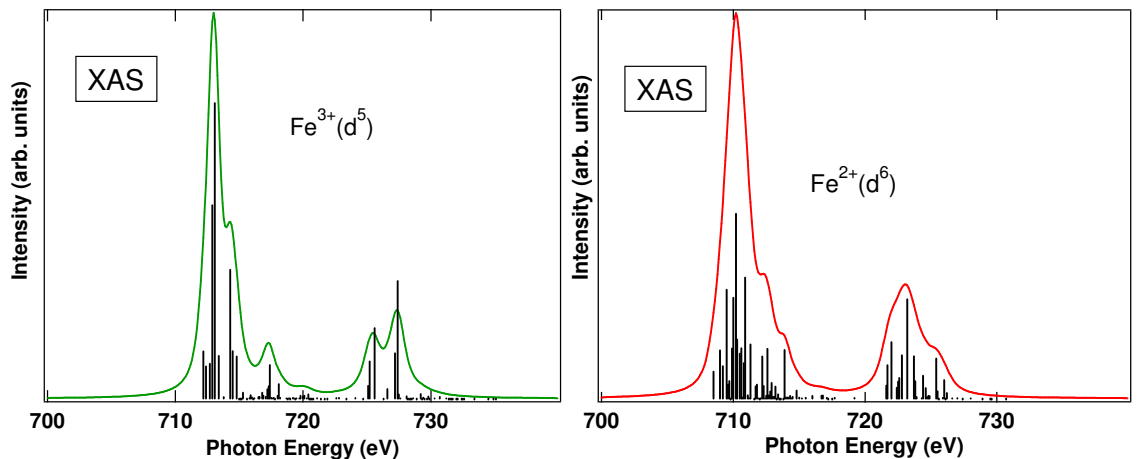


Figure 2.2: Fe 2p XAS atomic multiplet calculation for  $\text{Fe}^{2+}$  and  $\text{Fe}^{3+}$ .

### Influence of the crystal field

Since most of the compounds investigated during this work contain Fe atoms surrounded by ligands in an octahedral ( $O_h$ ) or tetrahedral ( $T_d$ ) symmetry, here an overview of crystal-field (CF) multiplet calculations for both symmetries is given. In figure 2.3 Fe 2p XAS and XMCD CF multiplet calculations for  $\text{Fe}^{3+}$  are shown. The crystal-field strength (also denoted as  $10Dq$ ) is changed from 0 eV to 3.6 eV with an increment of 0.3 eV. In the left panel the calculation results are shown for a  $O_h$  symmetry, in the right panel for a  $T_d$  symmetry. All calculations are performed without the influence of temperature and charge transfer. As can be seen for both

symmetries the increase of the crystal-field from 0 eV to 3.0 eV leads to the appearance of a  $L_3$  pre-peak at about 710 eV photon energy, while the  $L_3$  main peak is shifted slightly to higher photon energies. At the  $L_2$  part of the spectra the clearly defined double peak structure broadens resulting in a triple peak like structure. For crystal fields above 3.0 eV all spectra show a sudden change in their spectral shape, which is pointed out by a color change from black to red. The reason for this will be discussed below. The comparison of the  $O_h$  symmetry calculations with the  $T_d$  ones reveals that for small crystal-fields the calculated spectra are nearly the same, while for higher fields the spectra start to show differences.

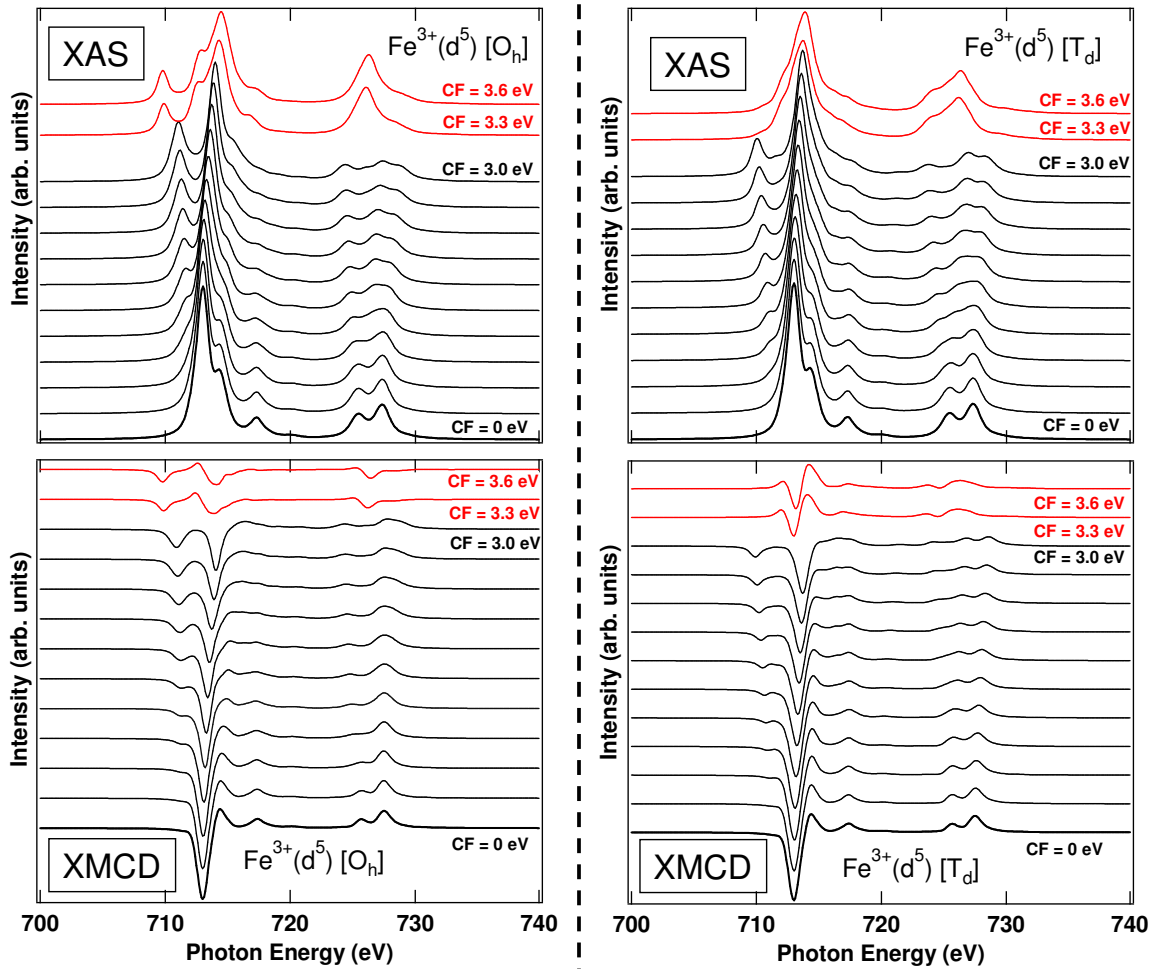


Figure 2.3: Fe 2p XAS and XMCD multiplet calculations for  $\text{Fe}^{3+}$  in  $O_h$  (left panel) and  $T_d$  (right panel) symmetry with different crystal-field (CF) values. The crystal-field is changed from 0 eV to 3.6 eV with an increment of 0.3 eV. For all calculations the influence of the temperature and charge transfer is neglected. More details are given in the text.

In figure 2.4 the CF calculations for  $O_h$  symmetry with a crystal field of 0.3 eV and 1.5 eV are directly compared to the corresponding  $T_d$  calculations. Like displayed for a  $T_d$  crystal-field of 1.5 eV the pre-peak structure of the  $L_3$  and the  $L_2$  part of the XAS spectrum becomes less pronounced and appears at lower photon energies

than for the  $O_h$  symmetry. The XMCD spectra show even more differences. At the  $L_3$  as well as at the  $L_2$  part of the spectrum with  $CF = 1.5$  eV differences in peak intensities and positions clearly occur.

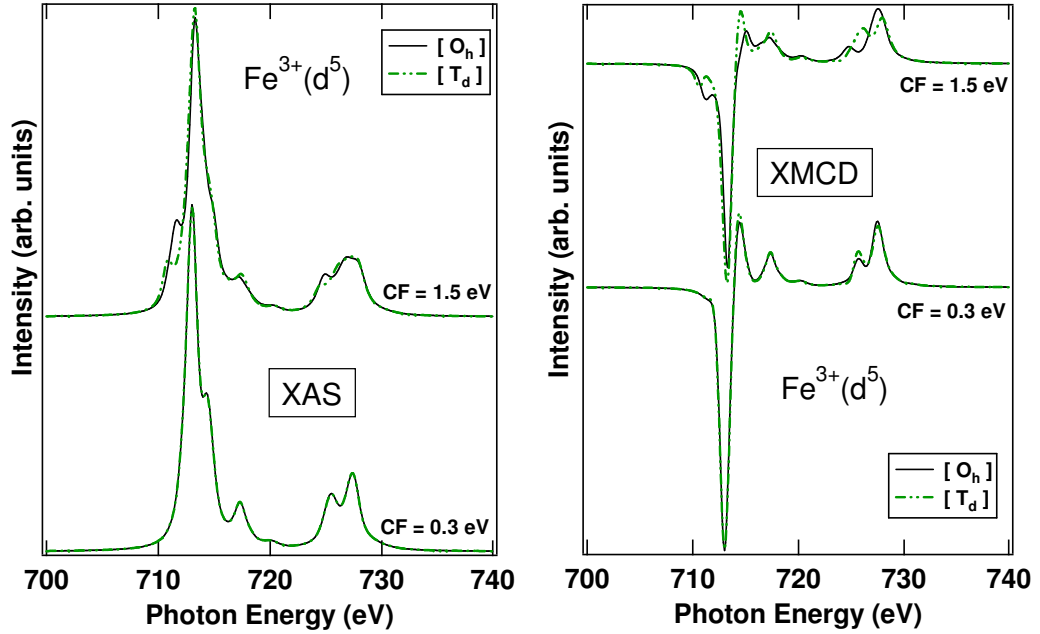


Figure 2.4: Comparison of the  $Fe^{3+}$  XAS and XMCD multiplet calculations in  $O_h$  symmetry with the ones in  $T_d$  symmetry. The crystal-field was set to 0.3 eV and 1.5 eV.

As mentioned before for crystal-fields above 3.0 eV all XAS and XMCD CF multiplet calculations show a sudden change of the spectral shape (see figure 2.3). This is due to the fact that a strong crystal-field can lead to a change in the spin character of the ground state. For small crystal-fields, the ground state does not change character and originates from the atomic ground state according to Hund's rules. In this state the electrons firstly occupy the spin up states, which leads to a ground state with the maximum overall spin. This state is called *high spin*. For strong crystal-fields the Hund's rules can be disabled and additional spin down states appear in the ground state, which is also called *low spin*. The  $Fe^{3+}$  high spin and low spin ground states are illustrated in figure 2.5 for a  $O_h$  and  $T_d$  ligand field symmetry. As shown for both symmetries the overall spin magnetic moment changes from  $5 \mu_B$  (high spin) to  $1 \mu_B$  (low spin). Note that this illustration is a one-electron picture, which cannot be compared to the results of the multiplet calculations in detail. But the decrease of the spin magnetic moment with the change of the spin character of the ground state can clearly be seen in the XMCD spectra (figure 2.3). Above  $CF = 3.0$  eV the  $O_h$  as well as the  $T_d$  calculations show a similar decrease of the XMCD signal. Investigation of the XMCD integrals reveals that the signal decrease is in the same dimension as predicted by the illustration in figure 2.5.

Note that the crystal-field also splits the final state multiplet. If the ground state is not changed and still high spin, the same final states are reached. In this case

the changes in the spectra with increasing crystal field are only due to the crystal-field effect on the final state. This leads to level splitting and/or shifting, and a modification of the transition matrix elements due to changes in the final state wave functions. In the  $\text{Fe}^{3+}$  CF multiplet calculations shown in figure 2.3 this is the case for  $\text{CF} \leq 3.0$  eV. Above 3.0 eV a change of the ground state character to low spin occurs, which makes dipole transitions to a totally new set of final states possible resulting in a complete change of the spectral shape.

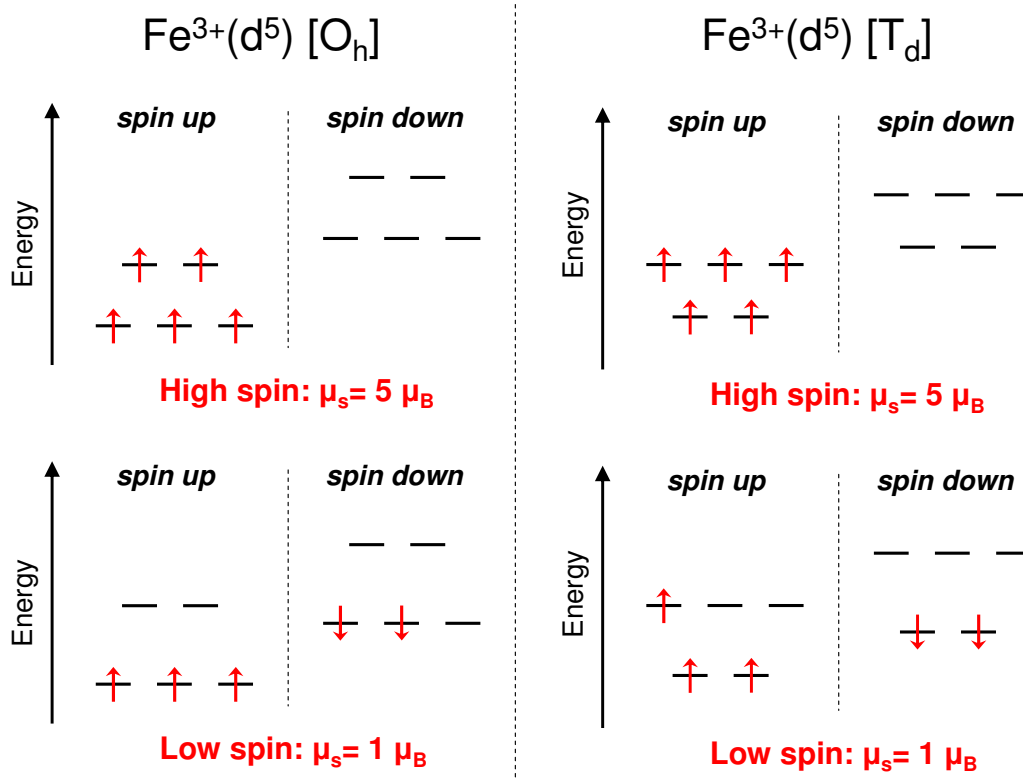


Figure 2.5: Illustration of the high-spin and low-spin ground states for  $\text{Fe}^{3+}$  in  $O_h$  (left panel) and  $T_d$  (right panel) ligand field symmetry.

In figure 2.6 Fe 2p XAS and XMCD CF multiplet calculations for  $\text{Fe}^{2+}$  are shown. The crystal-field strength is changed from 0 eV to 3.0 eV with an increment of 0.3 eV. In the left panel the calculation results are shown for a  $O_h$  symmetry, in the right panel for a  $T_d$  symmetry. Again all calculations are performed without the influence of temperature and charge transfer. As displayed for both symmetries the increase of the crystal field leads to a broadening of the  $L_3$  and  $L_2$  part of the spectra showing a rich multiplet structure. Like in the  $\text{Fe}^{3+}$  calculations a sudden change of the spectral shape occurs at higher crystal field values, pointed out by a color change from black to red. But compared to  $\text{Fe}^{3+}$  for  $\text{Fe}^{2+}$  this happens for lower crystal fields and there are clear differences between the  $O_h$  and  $T_d$  symmetry. This will be discussed below. Like for  $\text{Fe}^{3+}$  the comparison of the  $O_h$  symmetry calculations with the  $T_d$  ones reveals that for small crystal-fields the calculated spectra are nearly the same, while for higher fields the spectra start to show differences.

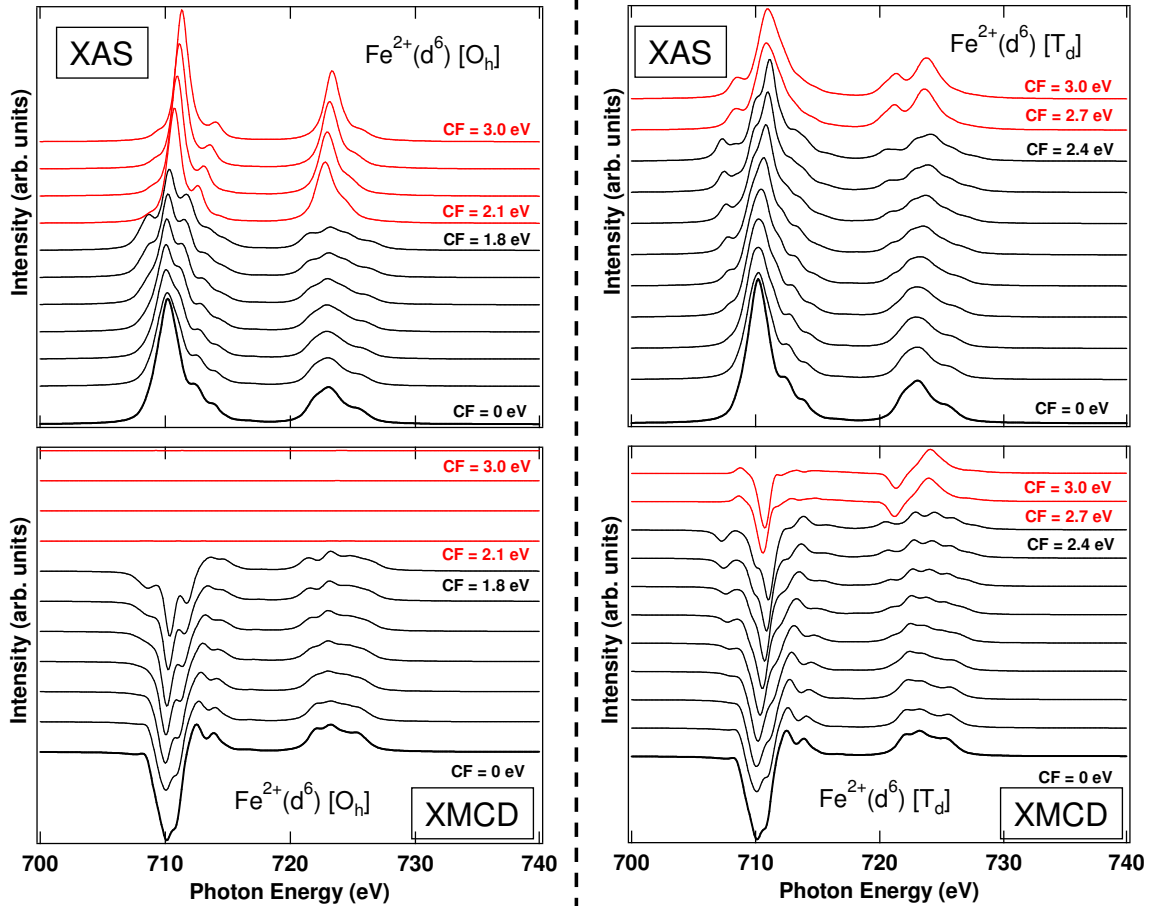


Figure 2.6: Fe 2p XAS and XMCD multiplet calculations for  $\text{Fe}^{2+}$  in  $\text{O}_h$  (left panel) and  $\text{T}_d$  (right panel) symmetry with different crystal-field (CF) values. The crystal-field is changed from 0 eV to 3.0 eV with an increment of 0.3 eV. For all calculations the influence of the temperature and charge transfer is neglected. More details are given in the text.

In figure 2.7 the CF calculations for  $O_h$  symmetry with a crystal field of 0.3 eV and 1.5 eV are directly compared to the corresponding  $T_d$  calculations. Similar to the  $Fe^{3+}$  findings also in case of  $Fe^{2+}$  calculations with a  $T_d$  crystal-field of 1.5 eV the pre-peak structure of the  $L_3$  and the  $L_2$  part of the XAS spectrum becomes less pronounced and appears at lower photon energies than for the  $O_h$  symmetry. But in addition also changes in the post-peak structure occur. The XMCD spectra again show more differences. At the  $L_3$  as well as at the  $L_2$  part of the CF = 1.5 eV spectrum differences in peak intensities and positions clearly occur.

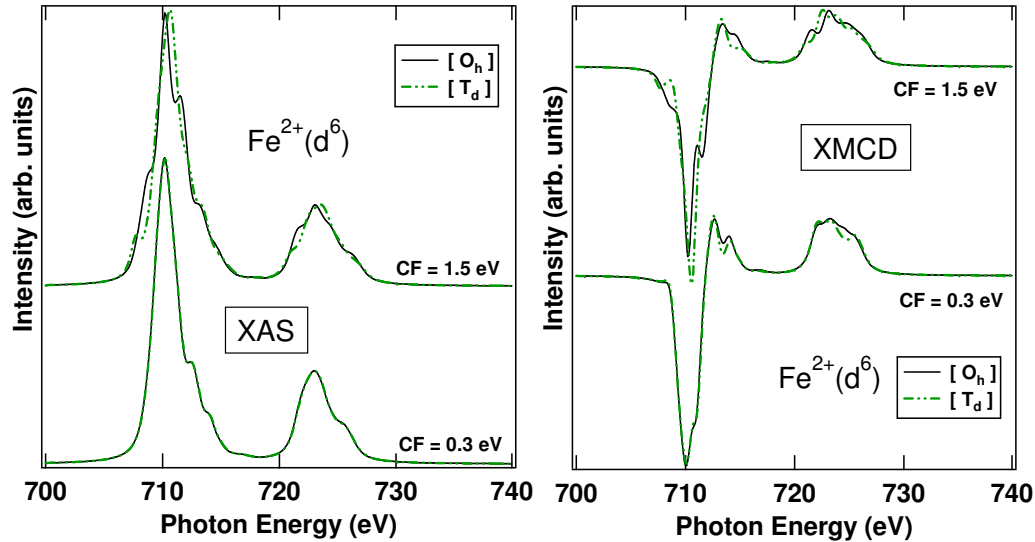


Figure 2.7: Comparison of the  $Fe^{2+}$  XAS and XMCD multiplet calculations in  $O_h$  symmetry with the ones in  $T_d$  symmetry. The crystal-field was set to 0.3 eV and 1.5 eV.

As already mentioned in contrast to  $Fe^{3+}$  for the  $Fe^{2+}$  XAS and XMCD CF multiplet calculations the sudden change in the spectral shape, originating from a change of the ground state character, occurs at different crystal-fields depending on the ligand field symmetry (figure 2.6). In  $O_h$  symmetry the new spectral shape appears at a crystal-field of about 2.1 eV, while for the  $T_d$  symmetry the change occurs at a higher value of about 2.7 eV. This indicates that the new ground state differs between  $O_h$  and  $T_d$  symmetry. A look at the XMCD spectra supports this. The low spin ground state for  $O_h$  seems to have no XMCD signal and therefore no overall spin magnetic moment, while for  $T_d$  the low spin state still consists of an overall spin magnetic moment, which nevertheless is reduced. Investigation of the integrals reveals that for  $CF \geq 2.7$  eV the XMCD signal decreases about 50%. In figure 2.8 the  $Fe^{2+}$  ( $d^6$ ) high and low spin ground states for a  $O_h$  and  $T_d$  ligand field symmetry are illustrated. Again it has to be mentioned that this one-electron picture cannot be compared in detail to the multiplet calculation results. But in consistence with the findings of the multiplet calculations also the illustration in figure 2.8 shows different ground states for the  $O_h$  and  $T_d$  symmetry. It also gives an explanation for the vanishing overall spin magnetic moment of the  $O_h$  symmetry. As one can see for an octahedral crystal field in the low spin ground state spin up and down states are occupied equally resulting in a reduction of the overall spin magnetic moment from



$4 \mu_B$  to  $0 \mu_B$ . In contrast to this for a  $T_d$  symmetry the low spin state only consists of one additional spin down state leading to a reduction of the overall spin magnetic moment from  $4 \mu_B$  to  $2 \mu_B$ . As mentioned before also the XMCD CF multiplet calculations in  $T_d$  symmetry reveal a reduction of the overall spin magnetic moment of about 50% supporting the illustration in figure 2.8.

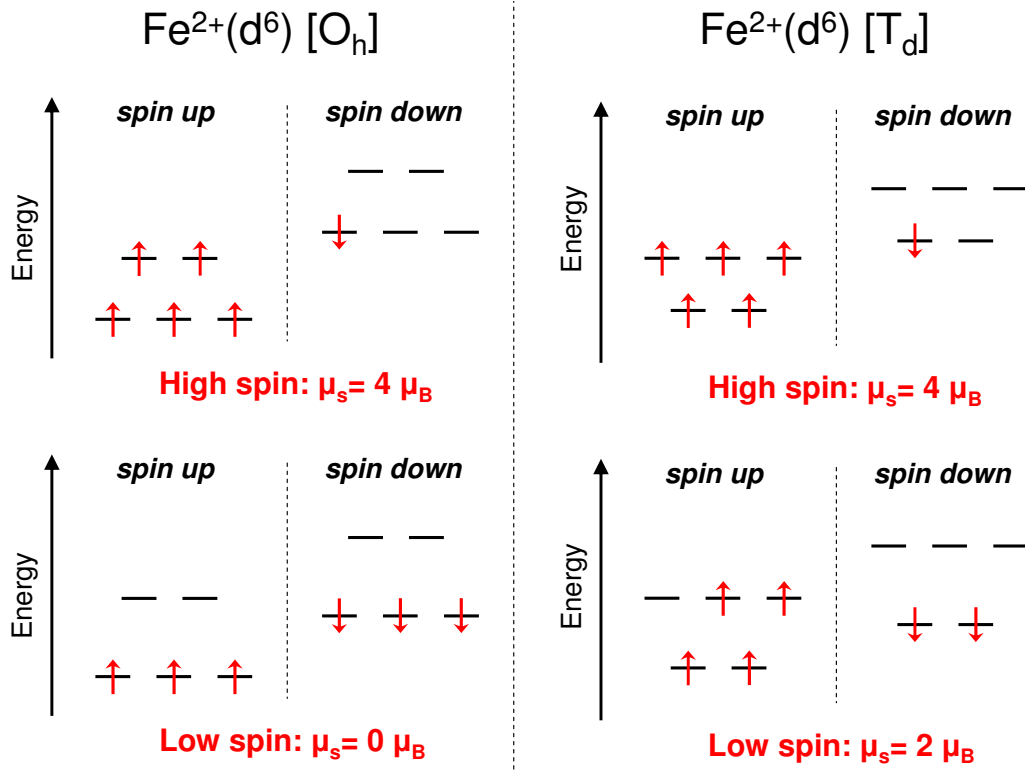


Figure 2.8: Illustration of the high spin and low spin states for  $\text{Fe}^{2+}$  in  $O_h$  (left panel) and  $T_d$  (right panel) ligand field symmetry.

### Influence of the charge transfer

In this section the influence of a ligand to metal charge transfer on the  $\text{Fe}^{2+}$  and  $\text{Fe}^{3+}$  multiplet calculations will be shown. For all calculations the influence of the temperature and crystal field is neglected.

As described in section 1.4.2 in the charge transfer multiplet calculation a second configuration is added to the ligand field multiplet calculation, in which an electron has moved from a filled oxygen 2p-band to a metal 3d-band. This leads to the new ground state configuration  $3d^6\bar{L}$  and  $3d^7\bar{L}$  for  $\text{Fe}^{3+}$  and  $\text{Fe}^{2+}$ , respectively. Here  $\bar{L}$  stands for a hole on the oxygen ligand. After performing two dipole transition calculations, from  $3d^N$  to  $2p^5 3d^{N+1}$  and from  $3d^{N+1}\bar{L}$  to  $2p^5 3d^{N+2}\bar{L}$  ( $\text{Fe}^{3+}$ :  $N=5$ ;  $\text{Fe}^{2+}$ :  $N=6$ ), the configurations are mixed. This is done by a monopole transition between the two ground and final state configurations. The mixing is controlled by the charge transfer energy  $\Delta$ .

In figure 2.9 charge transfer (CT) multiplet calculations of the Fe 2p XAS and XMCD

spectrum for  $\text{Fe}^{3+}$  with different  $\Delta$  values are shown. The charge transfer energy  $\Delta$  is changed from 12 eV to -12 eV with an increment of 3 eV. Beside the calculated spectra the used  $\Delta$  value, in brackets, as well as the resulting mixing of the ground state is denoted. Like shown for  $\Delta = 12$  eV the ground state is almost of pure  $3d^5$  character with only 4%  $3d^6\bar{L}$  character. The reduction of the charge transfer energy to  $\Delta = 6$  eV seems to have no big influence on the mixing. Here still 90% of the ground state is of  $3d^5$  character. With further reduction of  $\Delta$  the mixing becomes stronger resulting in a ground state comprising 30%  $3d^6\bar{L}$  character for  $\Delta = 0$  eV. For negative  $\Delta$  values the charge transfer character of the ground state becomes dominant. Finally for  $\Delta = -12$  eV only 9% of the ground state is due to the  $3d^5$  configuration resulting in XAS and XMCD spectra very similar to the ones calculated for  $\text{Fe}^{2+}$ . Here it has to be pointed out that, although for high positive and negative  $\Delta$  values the spectrum is very similar to respectively a pure  $\text{Fe}^{3+}$  and  $\text{Fe}^{2+}$  spectrum, for small  $\Delta$  values the spectrum is not just a mixture of both. As shown in figure 2.9 for  $-3 \text{ eV} \leq \Delta \leq 3 \text{ eV}$  additional satellite structures appear between the  $L_3$  and  $L_2$  part of the spectra. These would not be present in a simple mixture of a calculated  $\text{Fe}^{3+}$  and  $\text{Fe}^{2+}$  spectrum.

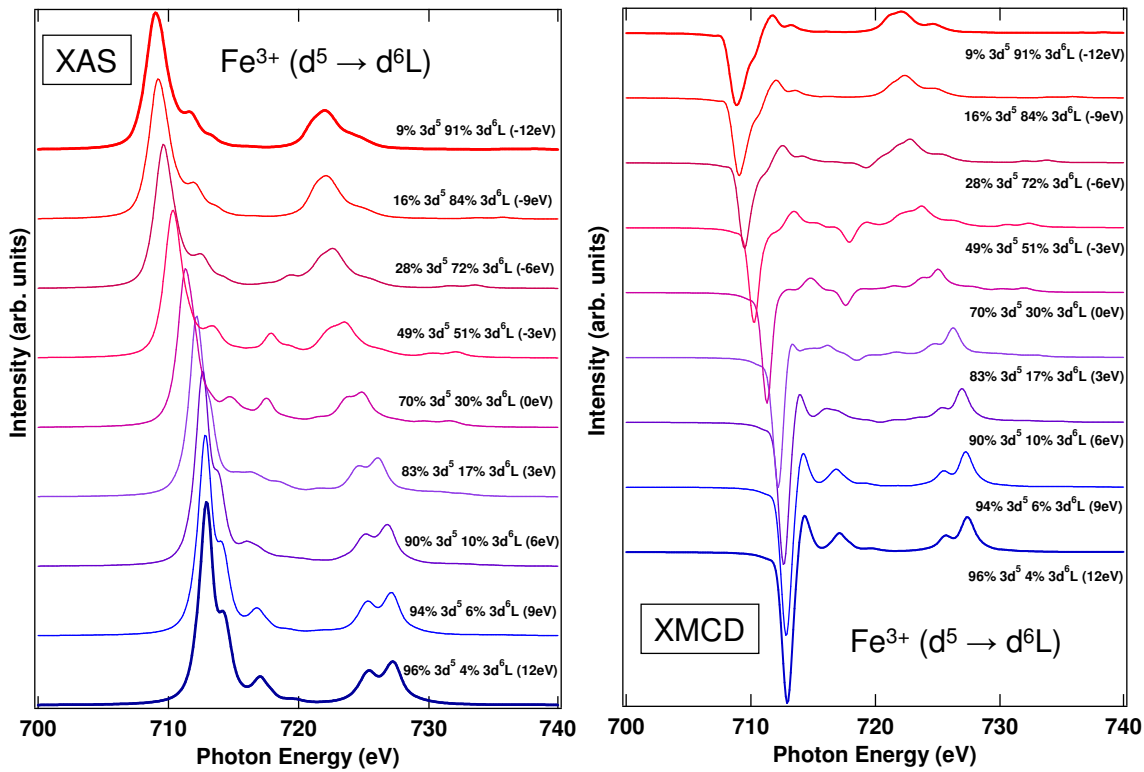


Figure 2.9: Fe 2p XAS and XMCD charge transfer multiplet calculations for  $\text{Fe}^{3+}$  with the  $\Delta$  value changed from 12 eV to -12 eV with an increment of 3 eV. For all calculations the influence of the temperature and crystal field is neglected. More details are given in the text.

In figure 2.10 charge transfer multiplet calculations of the Fe 2p XAS and XMCD spectrum for  $\text{Fe}^{2+}$  with different  $\Delta$  values are shown. Again the charge transfer energy

$\Delta$  is changed from 12 eV to -12 eV with an increment of 3 eV. The resulting mixing of the ground state is similar to the one found for  $\text{Fe}^{3+}$ , although it is not exactly the same. Here for  $\Delta = 12$  eV the ground state is almost of pure  $3d^6$  character, while for  $\Delta = -12$  eV it is dominated by the  $3d^7\bar{L}$  character. Similar to the  $\text{Fe}^{3+}$  calculations for small values of  $\Delta$  satellite structures appear between the  $L_3$  and  $L_2$  part of the XAS and XMCD spectra of  $\text{Fe}^{2+}$ . But compared to  $\text{Fe}^{3+}$  they are less pronounced.

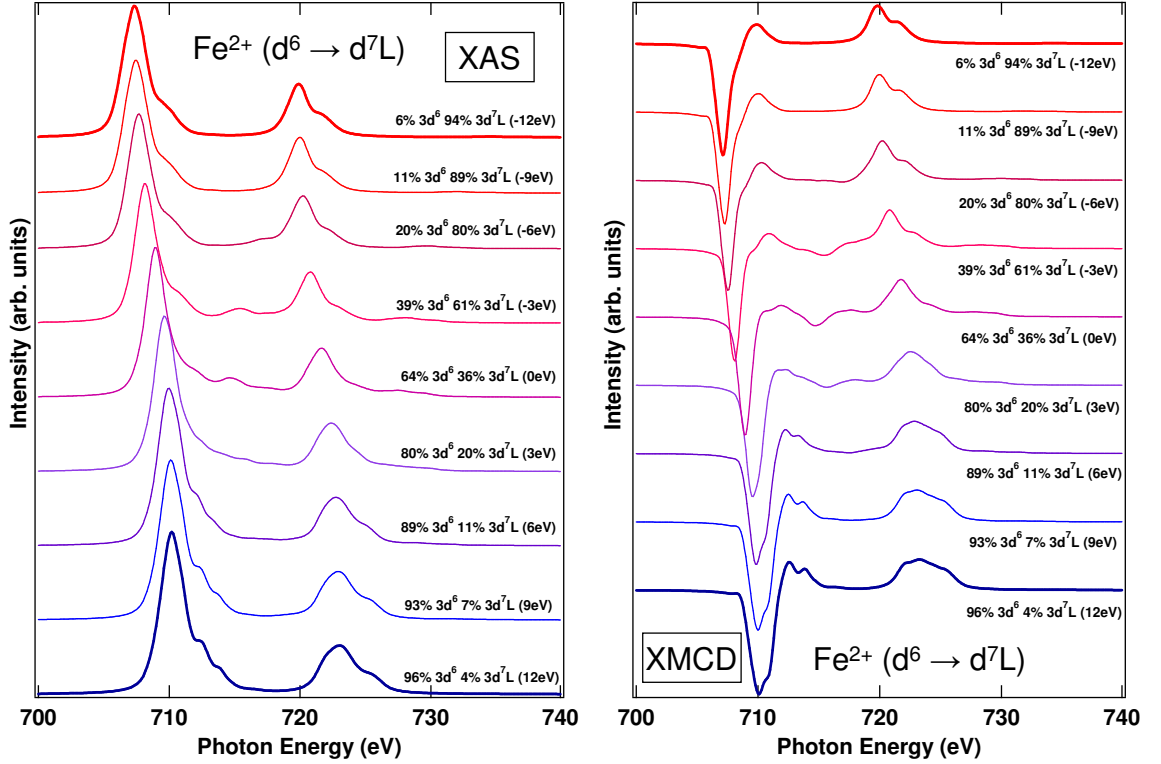


Figure 2.10: Fe 2p XAS and XMCD charge transfer multiplet calculations for  $\text{Fe}^{2+}$  with the  $\Delta$  value changed from 12 eV to -12 eV with an increment of 3 eV. For all calculations the influence of the temperature and crystal field is neglected. More details are given in the text.

### Influence of the temperature

In this section the influence of temperature on the  $\text{Fe}^{2+}$  and  $\text{Fe}^{3+}$  multiplet calculations will be shown. For all calculations the influence of charge transfer and crystal field is neglected.

In figure 2.11 XAS and XMCD atomic multiplet calculations for  $\text{Fe}^{3+}$  and  $\text{Fe}^{2+}$  with  $T = 0$  K are compared to those with  $T = 400$  K. As one can see for both valence states the increase of the thermal energy results in an increase of the XAS signal, while the XMCD signal is reduced. Normalising of the  $T = 0$  K spectra with the  $T = 400$  K ones reveals that there is no change in the spectral shape. The reason for the increase of the XAS signal and the decrease of the XMCD signal are additional

ground and final state configurations that become available with higher temperature. This is further discussed below.

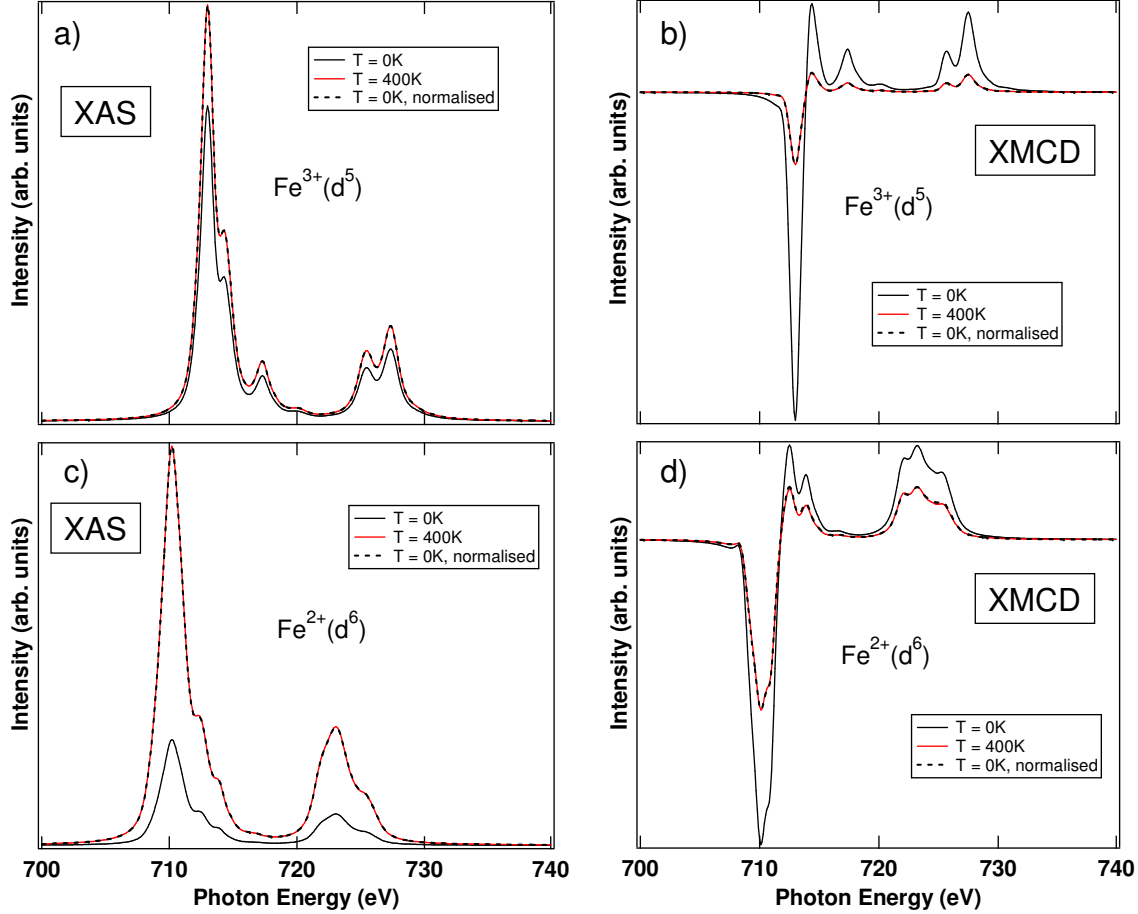


Figure 2.11: Fe 2p XAS and XMCD multiplet calculations for Fe<sup>3+</sup> (panel a), b)) and Fe<sup>2+</sup> (panel c), d)) with the temperature set to T = 0 K and T = 400 K. For all calculations the influence of charge transfer and crystal field is neglected. More details are given in the text.

Figure 2.12 shows the calculated XAS and XMCD spectra for both valence states with T = 0 K and T = 400 K together with the corresponding  $\mu^+$ ,  $\mu^-$  and  $\mu^0$  spectra. The XAS spectrum is simply the sum of the  $\mu^+$ ,  $\mu^-$  and  $\mu^0$  spectra, while the XMCD spectrum results from the difference of  $\mu^-$  and  $\mu^+$ . As displayed for both valence states in the T = 0 K spectra there are clear differences between the  $\mu^-$  and the  $\mu^+$  spectra resulting in a big XMCD signal. For T = 400 K the  $\mu^0$  spectral shape does not change, but both the  $\mu^-$  and  $\mu^+$  spectra change drastically revealing a shape similar to  $\mu^0$ . Due to the resulting smaller differences between  $\mu^-$  and  $\mu^+$  the XMCD signal decreases. Note that as shown before the shape of the XMCD signal does not change. Therefore one can conclude, that due to the temperature in the  $\mu^-$  and  $\mu^+$  spectra additional states with  $\mu^0$  character occur. This results in an increase of the XAS signal and simultaneously a decrease of the corresponding XMCD signal.

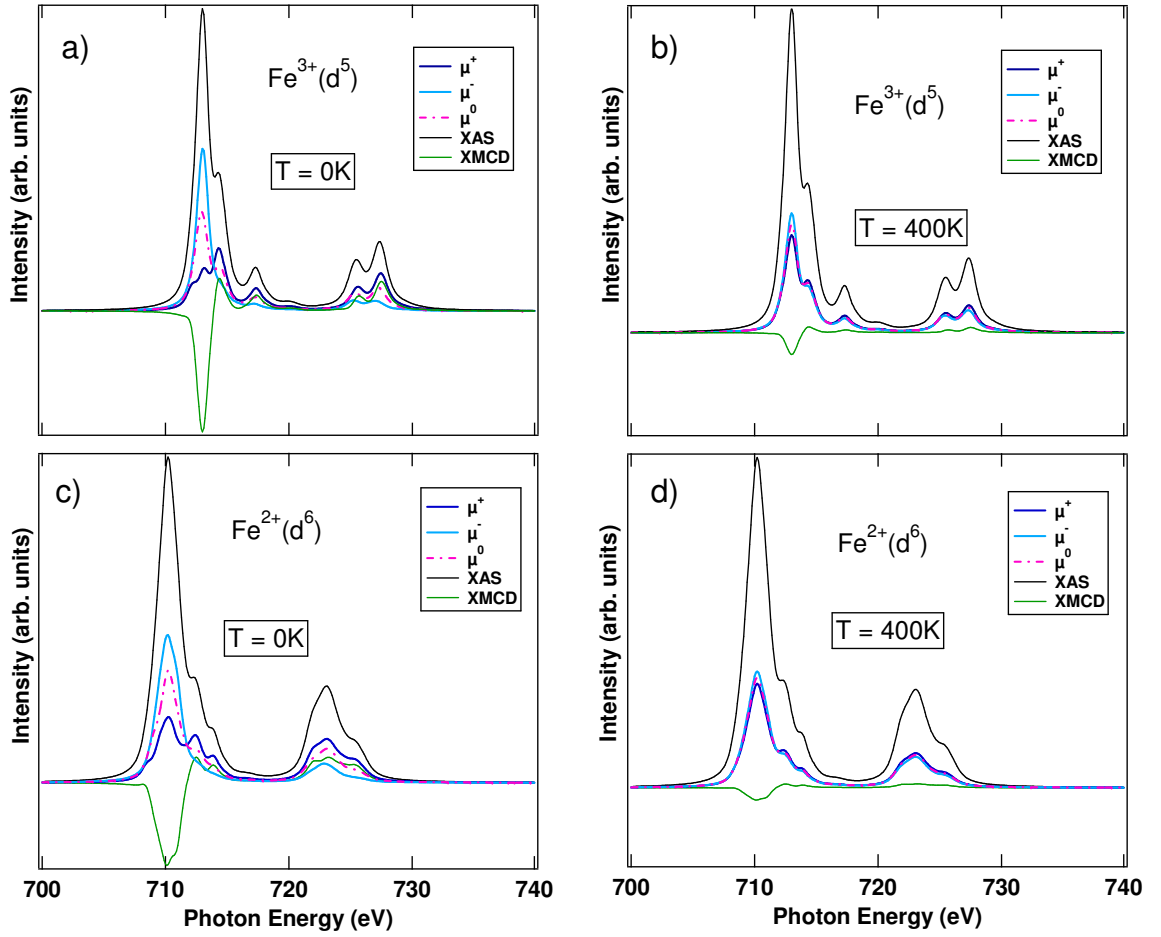


Figure 2.12: The calculated  $\mu^+$ ,  $\mu^-$  and  $\mu^0$  Fe 2p spectra for  $\text{Fe}^{3+}$  (panel a), b)) and  $\text{Fe}^{2+}$  (panel c), d)) together with the corresponding XAS and XMCD spectra. The temperature was set to  $T = 0\text{ K}$  and  $T = 400\text{ K}$ , respectively. The influence of charge transfer and crystal field is neglected. More details are given in the text.

## 2.2 Results

This section gives an overview of Fe 2p XAS and XMCD measurements of various chalcogenide systems. After that the different compounds are shortly introduced and their electronic and magnetic Fe state is discussed, based on the measurement results. The investigated compounds are crystals like  $\text{Fe}_{0.5}\text{Cu}_{0.5}\text{Cr}_2\text{S}_4$ ,  $\text{Sr}_2\text{FeMoO}_6$  and  $\text{LuFe}_2\text{O}_4$  as well as molecules like the ferric star,  $\text{Mo}_{72}\text{Fe}_{30}$  and  $\text{W}_{72}\text{Fe}_{30}$ . In figure 2.13 Fe 2p XAS measurements of the various chalcogenide compounds are shown. The photon energies of the  $L_3$  line of divalent and trivalent Fe found by reference measurements are marked with dotted lines. The XAS spectra are ordered by the amount of the  $\text{Fe}^{2+}$  and  $\text{Fe}^{3+}$  contribution to the spectral shape.

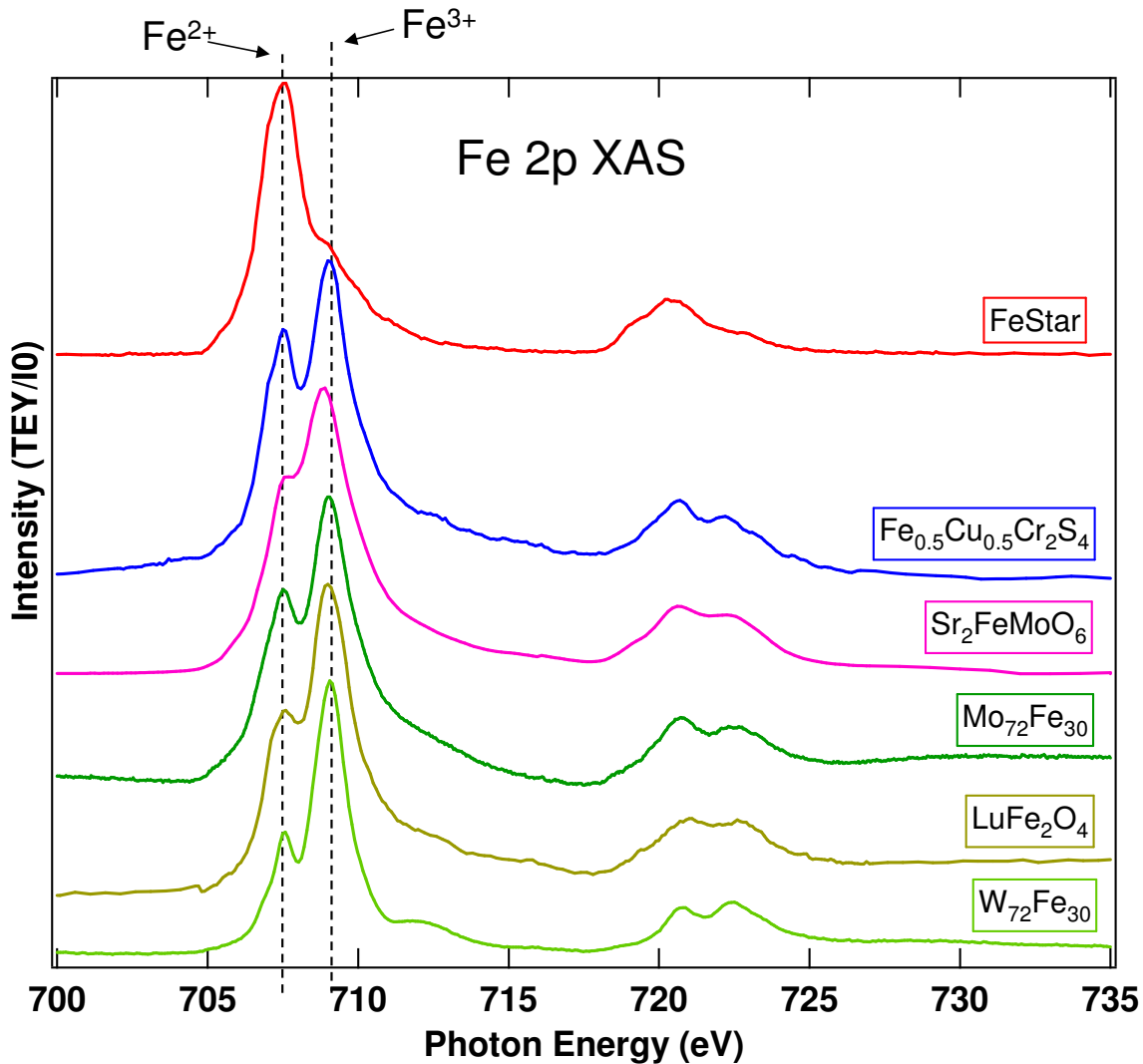


Figure 2.13: Overview of Fe 2p XAS measurements of various chalcogenide systems.

As one can see in case of the FeStar the  $L_3$  line is located at the  $\text{Fe}^{2+}$  energie position. In addition the spectral shape is similar to the one found by multiplet calculations for divalent Fe (see section 2.1.1) and the shape measured for FeO (formally  $\text{Fe}^{2+}$ ) (see figure 4.8). Therefore at this point it is reasonable to conclude that in the FeStar molecule most of the Fe ions have a divalent valence state. For  $\text{Fe}_{0.5}\text{Cu}_{0.5}\text{Cr}_2\text{S}_4$  the Fe 2p XAS spectrum seems to be a mixture of  $\text{Fe}^{2+}$  and  $\text{Fe}^{3+}$  features. In the spectrum of  $\text{Sr}_2\text{FeMoO}_6$  the amount of the trivalent Fe part rises. For  $\text{Mo}_{72}\text{Fe}_{30}$  and  $\text{LuFe}_2\text{O}_4$  the trivalent Fe features become dominant and finally in case of  $\text{W}_{72}\text{Fe}_{30}$  the spectrum is equal to that of pure trivalent Fe. This can be seen by comparison with multiplet calculations (see section 2.1.1) and reference measurements, for instance of  $\text{Fe}_2\text{O}_3$  (formally  $\text{Fe}^{3+}$ ) (see figure 4.8).

Thus at this point it is reasonable to conclude that, while in FeStar divalent iron is present,  $\text{Fe}_{0.5}\text{Cu}_{0.5}\text{Cr}_2\text{S}_4$ ,  $\text{Sr}_2\text{FeMoO}_6$ ,  $\text{Mo}_{72}\text{Fe}_{30}$  and  $\text{LuFe}_2\text{O}_4$  contain a mixture of  $\text{Fe}^{2+}$  and  $\text{Fe}^{3+}$  ions with different ratios. In  $\text{W}_{72}\text{Fe}_{30}$  all Fe ions seem to be trivalent. However comparison with the XMCD measurements contradict parts of this conclusion.

In figure 2.14 Fe 2p XMCD measurements of  $\text{Fe}_{0.5}\text{Cu}_{0.5}\text{Cr}_2\text{S}_4$ ,  $\text{Sr}_2\text{FeMoO}_6$ ,  $\text{LuFe}_2\text{O}_4$ , FeStar,  $\text{Mo}_{72}\text{Fe}_{30}$  and  $\text{W}_{72}\text{Fe}_{30}$  are shown. Again the  $L_3$  photon energies of divalent and trivalent Fe found by reference measurements are marked with dotted lines and the spectra are ordered by their amount of  $\text{Fe}^{2+}$  and  $\text{Fe}^{3+}$  features. As displayed the order is surprisingly different from that of the XAS spectra.

Here  $\text{Fe}_{0.5}\text{Cu}_{0.5}\text{Cr}_2\text{S}_4$  shows an XMCD signal with a photon energy typical for divalent Fe. Also the shape is similar to the one found by multiplet calculations for pure  $\text{Fe}^{2+}$  (see figure 4.13). Thus according to the XMCD signal  $\text{Fe}_{0.5}\text{Cu}_{0.5}\text{Cr}_2\text{S}_4$  seems only to contain divalent Fe, despite the considerably high amount of trivalent Fe found in the XAS measurements (figure 2.13). Possible reasons for this are discussed below and in chapter 4.

The second spectrum from above showing small  $\text{Fe}^{3+}$  features beside  $\text{Fe}^{2+}$  in the XMCD signal is  $\text{LuFe}_2\text{O}_4$ . This is also a surprise, since according to the absorption spectrum one would expect that this compound would show mostly trivalent Fe features in the XMCD signal. Further below this and the fact that the  $\text{Fe}^{3+}$  part of the spectrum is oriented in the opposite direction compared to  $\text{Fe}^{2+}$  is discussed and explained.

The third spectrum is the one measured for the FeStar molecule. Here the XMCD signal shows unexpectedly high  $\text{Fe}^{3+}$  features, since the XAS spectrum resembled that of pure  $\text{Fe}^{2+}$  (see figure 2.13). At this point it also has to be mentioned that due to Basic magnetochemical investigations and magnetic measurements the Fe ions in FeStar are predicted to be purely trivalent, which is clearly in contradiction with the presented measurements. Possible explanations are given below.

The spectrum of  $\text{Sr}_2\text{FeMoO}_6$  shows an XMCD signal, which comprises  $\text{Fe}^{2+}$  and  $\text{Fe}^{3+}$  features in a ratio of 70%  $\text{Fe}^{2+}$  to 30%  $\text{Fe}^{3+}$  according to multiplet calculations. However the XAS spectrum could be best fitted by multiplet calculations with a ratio of 50%  $\text{Fe}^{2+}$  to 50%  $\text{Fe}^{3+}$  (see figure 3.2). This discrepancy is further discussed below and in chapter 3.

The  $\text{Mo}_{72}\text{Fe}_{30}$  molecule shows an XMCD signal with dominant  $\text{Fe}^{3+}$  features in consistency with its absorption spectrum. The  $\text{W}_{72}\text{Fe}_{30}$  molecule shows an XMCD signal

typical for pure  $\text{Fe}^{3+}$  also in agreement with its XAS spectrum. However the clear differences in the spectra between  $\text{Mo}_{72}\text{Fe}_{30}$  and  $\text{W}_{72}\text{Fe}_{30}$  are surprising since both molecules have a similar structure and are predicted to contain pure trivalent Fe. This is further discussed in the following sections.

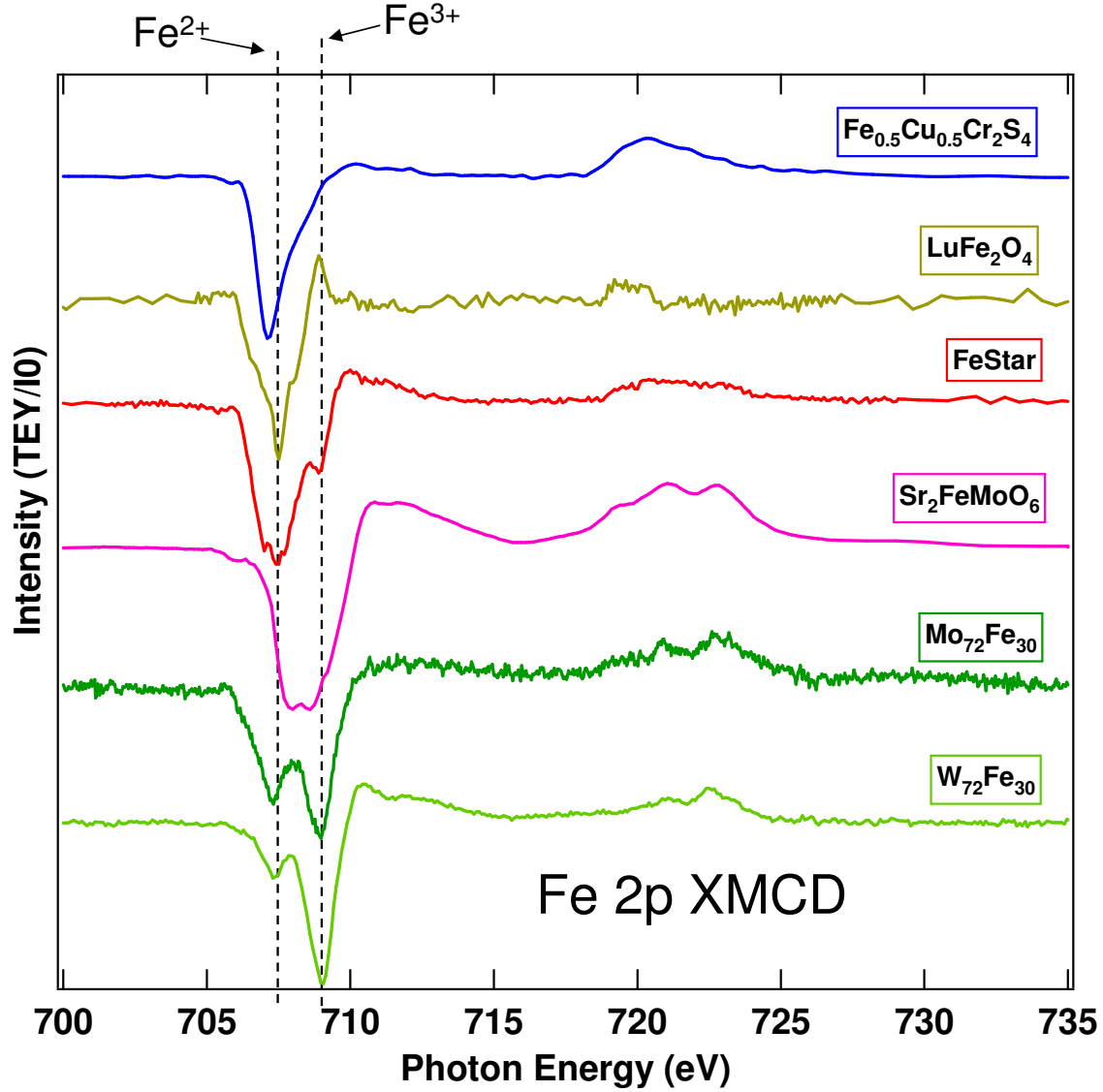


Figure 2.14: Overview of Fe 2p XMCD measurements of various chalcogenide systems.

### 2.2.1 Fe in $\text{Sr}_2\text{FeMoO}_6$

The starting point of the presented investigation of the magnetic and electronic Fe state in different chalcogenide systems was the investigation of the double perovskite  $\text{Sr}_2\text{FeMoO}_6$ . In this crystalline structure Fe is surrounded by oxygen (O) octahedral (see figure 3.1). To calculate the XAS and XMCD measurements charge



transfer multiplet calculations were performed. As shown in figure 2.15 in order to calculate the spectral shape a  $\text{Fe}^{2+}$  (red line) and a  $\text{Fe}^{3+}$  (green line) CT multiplet calculation is mixed. Both calculations were performed in an octahedral ( $O_h$ ) symmetry with a crystal field of  $10Dq = 0.8$  eV and a  $\Delta$  value mixing the two ground state configurations in a ratio of 85%  $3d^n$  / 15%  $3d^{n+1}\underline{L}$ . Then all spectra were broadened with a Lorentzian and a Gaussian function to account for the lifetime broadening and the broadening due to the experiment. After that the resulting spectra were calibrated according to reference measurements. Finally the  $\text{Fe}^{2+}$  and  $\text{Fe}^{3+}$  spectra were summed up in different ratios (for instance 50% / 50% as shown in figure 2.15) (black line).

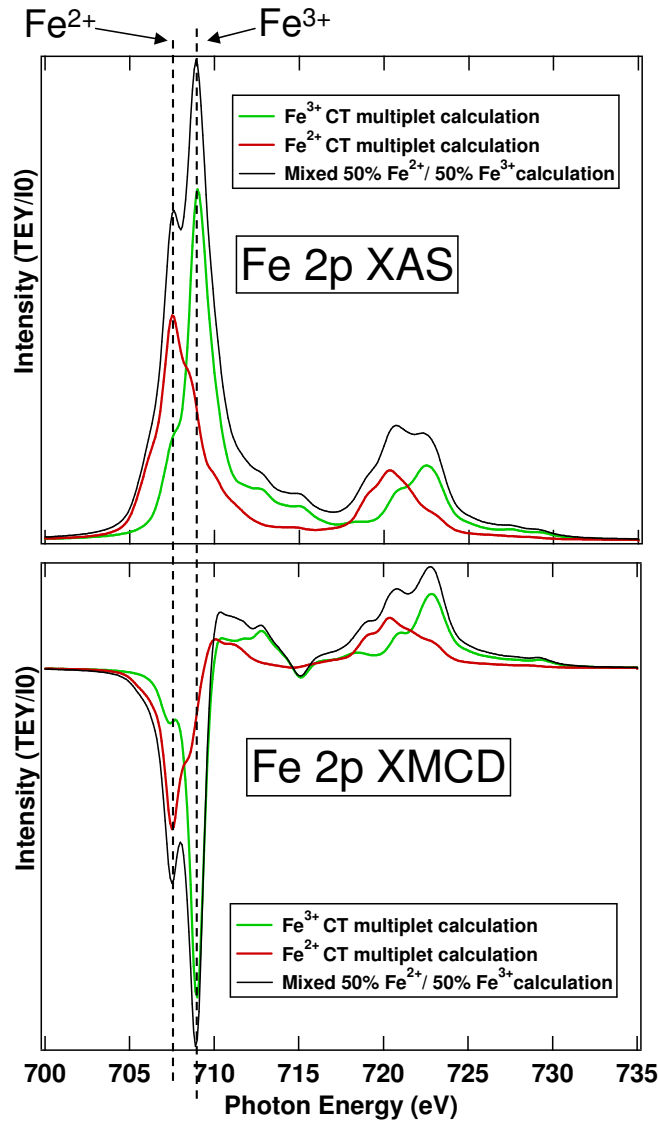


Figure 2.15: Fe 2p XAS (upper panel) and XMCD (lower panel) CT multiplet calculation of a mixed 50%  $\text{Fe}^{2+}$  / 50%  $\text{Fe}^{3+}$  valence state. In addition to the mixed spectra (black line) also the separated  $\text{Fe}^{2+}$  (red line) and  $\text{Fe}^{3+}$  (green line) calculations are shown.

As shown in chapter 3 (figure 3.2) for the XAS measurement of  $\text{Sr}_2\text{FeMoO}_6$  the best calculated fit was found with an  $\text{Fe}^{2+} / \text{Fe}^{3+}$  ratio of about 50% / 50%. Surprisingly the spectral shape of the XMCD measurement could not be calculated with this ratio. In case of the XMCD signal a considerably smaller  $\text{Fe}^{3+}$  amount had to be assumed in the calculation. This discrepancy could only be explained by the fact that part of the trivalent Fe present in  $\text{Sr}_2\text{FeMoO}_6$  showed no macroscopic magnetic behaviour during the XMCD experiment.

This finding led to an overall investigation of XAS and XMCD measurements performed on  $\text{Sr}_2\text{FeMoO}_6$  during several years and the discovery of an ageing effect, which was found to increase the  $\text{Fe}^{3+}$  features in the Fe 2p XAS spectrum. More details are given in chapter 3 and in Kuepper *et al.* (2008).

### 2.2.2 Fe in $\text{Fe}_{0.5}\text{Cu}_{0.5}\text{Cr}_2\text{S}_4$

$\text{Fe}_{0.5}\text{Cu}_{0.5}\text{Cr}_2\text{S}_4$  crystallises in a spinel structure where Fe is surrounded by sulphur (S) tetrahedral (see figure 4.1). In figure 2.16 the Fe 2p XAS measurement is compared to charge transfer multiplet calculations. Like for the  $\text{Sr}_2\text{FeMoO}_6$  also the calculation for  $\text{Fe}_{0.5}\text{Cu}_{0.5}\text{Cr}_2\text{S}_4$  is a mixture of a  $\text{Fe}^{2+}$  and a  $\text{Fe}^{3+}$  multiplet calculation. The simulations were performed in tetrahedral ( $T_d$ ) symmetry with a crystal field of  $10Dq = 0.5$  eV and broadened with a Lorentzian and a Gaussian function. Shown are a crystal-field (CF) multiplet calculation in comparison to a charge transfer (CT) multiplet calculation with a  $\Delta$  value mixing the two ground state configurations in a ratio of 82%  $3d^n$  / 18%  $3d^{n+1}\underline{L}$ . In case of the CF multiplet calculation the best fit was found for an  $\text{Fe}^{2+} / \text{Fe}^{3+}$  ratio of about 60% / 40%, while for the CT multiplet calculation the measurement could be best fitted with a ratio of 55% / 45%.

As illustrated without charge transfer there are clear differences between the measurement and calculation. The double peak structure of the  $L_3$  line is not well reproduced and the calculation shows a shoulder at higher photon energies that is absent in the measurement. In addition the calculated  $L_2$  line is broader than in the measurement and has a different shape. The calculation also clearly shows a satellite at about 713 eV photon energy, which is not visible in the XAS measurement. The decay of the calculated intensity between the  $L_3$  and  $L_2$  line is much stronger than in the measurement, as well.

In contrast to the CF calculation the charge transfer multiplet calculation shows a much better consistency with the measurement. The double peak structure of the  $L_3$  line is well reproduced and only a small shoulder is visible at higher photon energies in agreement with the measurement. The calculated  $L_2$  line is less broad and resembles the measurement much better, although there are still differences in the spectral shape. The satellite found in the crystal-field calculation vanishes in the charge transfer calculation and the spectral shape between the  $L_3$  and  $L_2$  line is in good agreement with the experimental result. Therefore one can conclude that charge transfer effects are most likely present in  $\text{Fe}_{0.5}\text{Cu}_{0.5}\text{Cr}_2\text{S}_4$ .

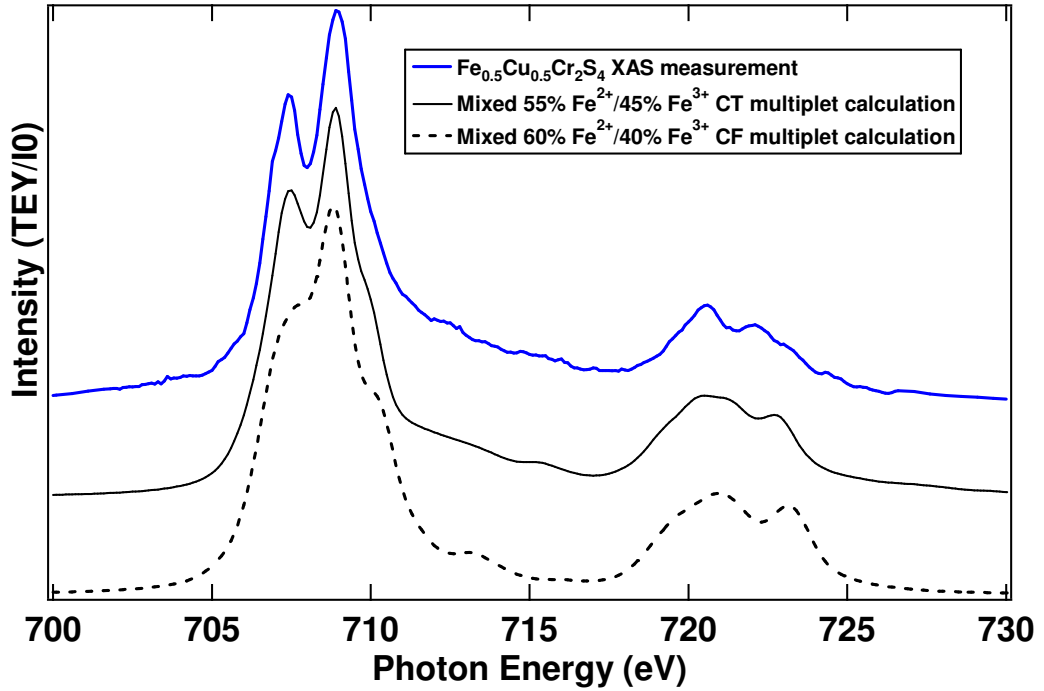


Figure 2.16: Fe 2p XAS measurement of  $\text{Fe}_{0.5}\text{Cu}_{0.5}\text{Cr}_2\text{S}_4$  and corresponding crystal-field (CF) and charge transfer (CT) multiplet calculations.

As mentioned above in contrast to the XAS results the XMCD signal only shows  $\text{Fe}^{2+}$  features, which could be confirmed by CT multiplet calculations (see chapter 4, figure 4.13). Due to the findings for the  $\text{Sr}_2\text{FeMoO}_6$  where an ageing effect was discovered leading to additional  $\text{Fe}^{3+}$  features in the XAS spectrum with no contribution to the XMCD signal, it could be concluded that for  $\text{Fe}_{0.5}\text{Cu}_{0.5}\text{Cr}_2\text{S}_4$  a similar process occurs. Since in case of the spinel there is no  $\text{Fe}^{3+}$  contribution to the XMCD spectrum the whole trivalent Fe amount measured in the XAS seems to be due to such a chemical change at the surface. This could be confirmed by measurements of  $\text{Fe}_{0.5}\text{Cu}_{0.5}\text{Cr}_2\text{S}_4$  samples that were treated differently. The findings led to new explanations for the magnetic, electric and magnetoresistive behaviour in  $\text{Fe}_{0.5}\text{Cu}_{0.5}\text{Cr}_2\text{S}_4$  and are described and discussed in detail in chapter 4.

### 2.2.3 Fe in $\text{LuFe}_2\text{O}_4$

$\text{LuFe}_2\text{O}_4$  crystallises in a rhombohedral crystal structure (space group  $R\bar{3}m$ ). The underlying layered structure consists of W-like hexagonal  $\text{Fe}_2\text{O}_{2.5}$  and U-like  $\text{LuO}_{1.5}$  layers (Isobe *et al.*, 1990). In the U layer Lu is surrounded by O octahedral. The W layers comprise two triangular nets of Fe ions surrounded by O trigonal bipyramidal (see figure 2.17).

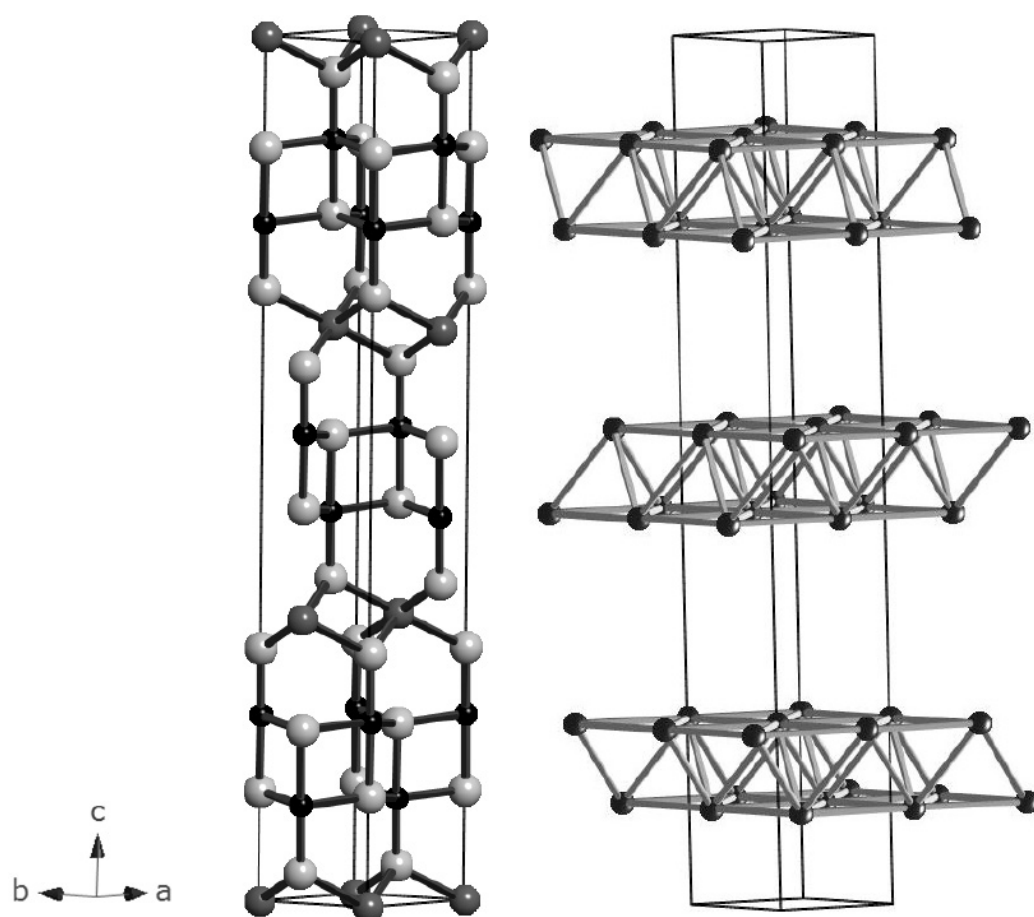


Figure 2.17: Left: Crystal structure of LuFe<sub>2</sub>O<sub>4</sub> showing the hexagonal double layered arrangement of Lu (large dark-grey spheres), Fe (small black spheres), and oxygen (large white spheres) along the c-axis in the trigonal space group  $R\bar{3}m$ . Right: The Fe double layers are shown with a triangular interconnectivity. The figures are adopted from Subramanian *et al.* (2006).

$\text{LuFe}_2\text{O}_4$  is a so called multiferroic transition metal oxide and has attracted intense interest due to its fascinating ferroelectric and magnetoelectric properties (Ikeda *et al.*, 2005a; Subramanian *et al.*, 2006). Multiferroic denotes the fact that in  $\text{LuFe}_2\text{O}_4$  more than one ferroic phase coexists, namely ferroelectricity and ferrimagnetism. Below 330 K an electric polarisation is induced via a frustrated charge ordering (CO) of  $\text{Fe}^{2+}$  and  $\text{Fe}^{3+}$  ions on the resulting honeycomb lattice (Kim *et al.*, 2009; Yamada *et al.*, 2000; Ikeda *et al.*, 2005b). Below 240 K a long-range ferrimagnetic order sets in (Ikeda *et al.*, 2005b). Since the ferroelectricity is caused by correlated electrons from the Fe ions,  $\text{LuFe}_2\text{O}_4$  shows unusual properties and unique capabilities (Subramanian *et al.*, 2006; Zeng *et al.*, 2008; Li *et al.*, 2008).

An intricate interplay between charge and spin degrees of freedom with the crystal lattice and external electrical and magnetic fields to some extent on a short-range order is assumed to be responsible for the large magnetoelectric coupling (Angst *et al.*, 2008; Xu *et al.*, 2008; Wu *et al.*, 2008; Li *et al.*, 2009; Wen *et al.*, 2009). However, there is still some confusion about the nature of the spin-charge coupling in  $\text{LuFe}_2\text{O}_4$ . In particular a model finding a  $\sqrt{3} \times \sqrt{3}$  CO ground state (Xiang and Whangbo, 2007; Xiang *et al.*, 2009) is challenged by simulations implying that the electrical polarisation in  $\text{LuFe}_2\text{O}_4$  is due to spin-charge coupling and a spin frustrated magnetic ground state in a chain CO state (Nagano *et al.*, 2007; Naka *et al.*, 2008). On the other hand the first model finds a ferrimagnetic spin ground state where  $\text{Fe}^{2+}$  and 1/3 of  $\text{Fe}^{3+}$  make up the majority spin, and 2/3 of  $\text{Fe}^{3+}$  make up the minority spin (Ikeda *et al.*, 2005b) (see also figure 2.18). Note that in both models a  $\text{Fe}^{2+} / \text{Fe}^{3+}$  ratio of 50% / 50% is expected.

In order to investigate the magnetic ground state of the Fe ions in  $\text{LuFe}_2\text{O}_4$  XAS and XMCD measurements were done. In figure 2.19 Fe 2p XAS measurements of  $\text{LuFe}_2\text{O}_4$  are shown together with crystal-field (CF) multiplet calculations. The calculations were done in trigonal bipyramidal symmetry ( $c_{3i}$ ). The presented calculations are mixtures of  $\text{Fe}^{2+}$  and  $\text{Fe}^{3+}$  CF calculations with different ratios. More details are given in Raekers (2009). In order to check if this compound is also affected by an ageing effect like  $\text{Sr}_2\text{FeMoO}_6$  and  $\text{Fe}_{0.5}\text{Cu}_{0.5}\text{Cr}_2\text{S}_4$  the absorption measurements were done in the total electron yield (TEY) and the more bulk sensitive total fluorescence yield (TFY) mode. As one can see there are clear differences between the TEY and TFY XAS spectrum. Note that due to self absorption effects the  $L_3 / L_2$  ratio is different in the TFY spectrum compared to the TEY one. However the spectral shape is comparable between the two measurement modes. The  $L_3$  spectral shape reveals that in the TEY mode a considerably higher  $\text{Fe}^{3+}$  signal is detected than in the TFY mode. This clearly indicates that also in  $\text{LuFe}_2\text{O}_4$  a chemical process is present at the surface affecting the Fe valence. Like shown in figure 2.19 the CF calculation with a  $\text{Fe}^{2+} / \text{Fe}^{3+}$  ratio of 50% / 50%, as expected for  $\text{LuFe}_2\text{O}_4$ , resembles the spectral shape of the TFY XAS spectrum quite good. In contrast to this the TEY spectrum could only be simulated with a much higher  $\text{Fe}^{3+}$  amount leading to a  $\text{Fe}^{2+} / \text{Fe}^{3+}$  ratio of about 25% / 75%.

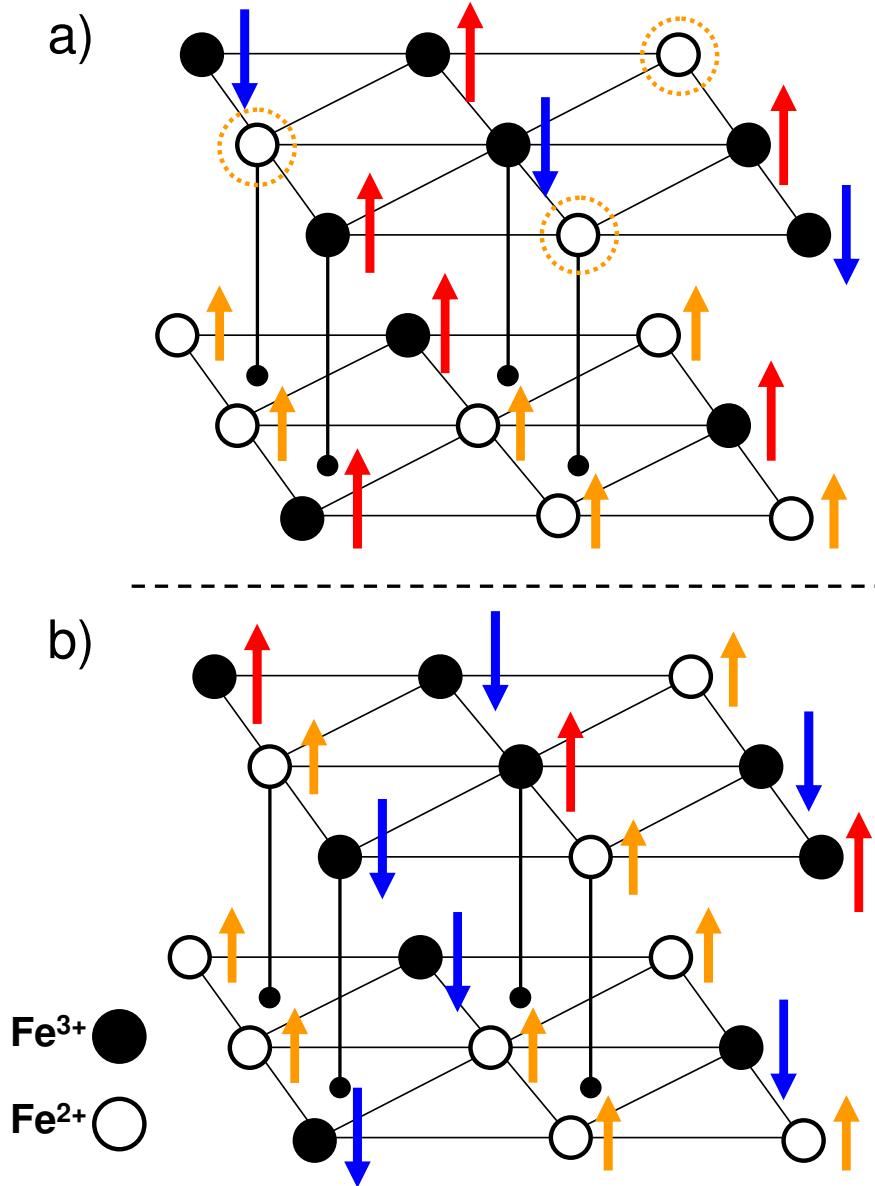


Figure 2.18: Two models describing the spin and charge ordering of the Fe double layer in  $\text{LuFe}_2\text{O}_4$ . a) A frustrated spin configuration according to Nagano *et al.* (2007). b) A spin configuration without frustration according to Siratori *et al.* (1992); Ikeda *et al.* (2005b). The long red and blue arrows mark the spin direction of the  $\text{Fe}^{3+}$  ions, while the shorter orange ones denote the direction of the  $\text{Fe}^{2+}$  spins. Dotted circles represent frustrated  $\text{Fe}^{2+}$  spins.

Therefore it can be concluded that in the TEY mode only about 25% of the detected  $\text{Fe}^{3+}$  signal is due to the sample bulk, while the rest is due to an additional  $\text{Fe}^{3+}$  amount at the sample surface. This signal is assumed not to contribute to the XMCD signal like found for  $\text{Sr}_2\text{FeMoO}_6$  and  $\text{Fe}_{0.5}\text{Cu}_{0.5}\text{Cr}_2\text{S}_4$ . The clear differences in the  $L_3$  spectral shape between the measurements and the calculations can be due to charge transfer effects, which are not taken into account in the CF calculations. As mentioned before the much higher signal at the  $L_2$  line in the TFY spectrum in comparison to the TEY mode and the calculations is due to self absorption effects.

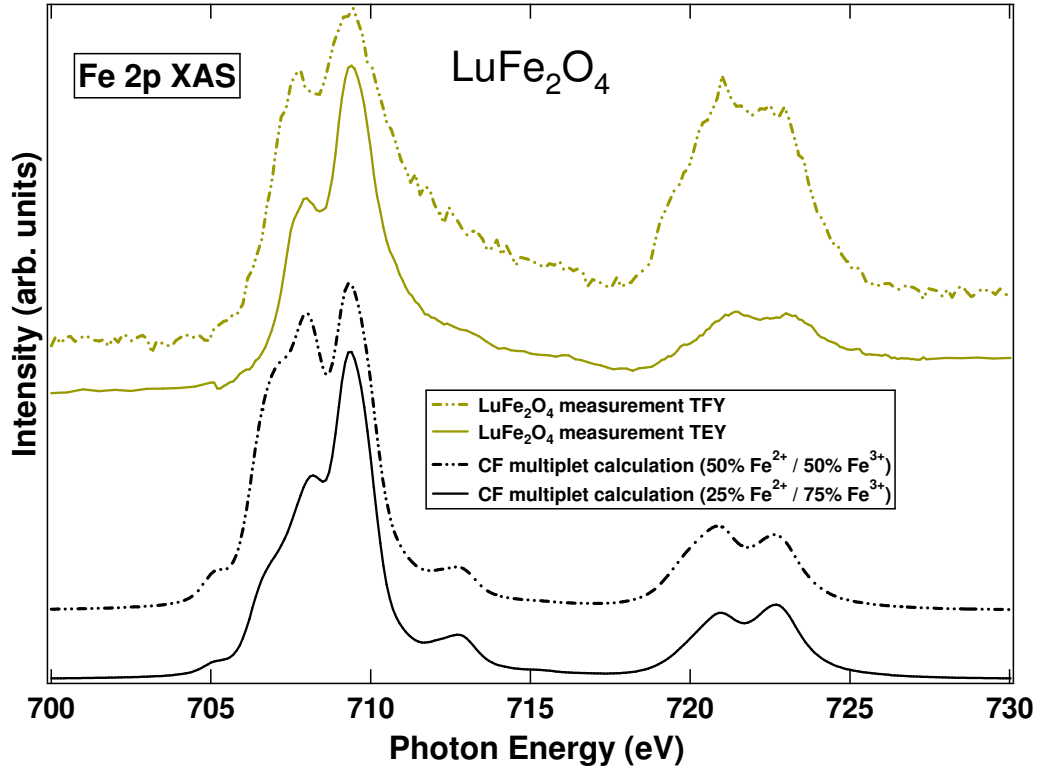


Figure 2.19: Fe 2p XAS measurements of  $\text{LuFe}_2\text{O}_4$  in the TEY and TFY mode. The results are compared to crystal-field multiplet calculations with different  $\text{Fe}^{2+} / \text{Fe}^{3+}$  ratios.

In figure 2.20 a Fe 2p XMCD TEY measurement of  $\text{LuFe}_2\text{O}_4$  is presented together with corresponding CF multiplet calculations. The measurement was performed at the Advanced Light Source (ALS) in Berkeley (California) at a temperature of about 80 K and an external applied magnetic field of 6 T. More details are given in Kuepper *et al.* (2009). As mentioned above XAS measurements indicate that in the TEY mode about 50% of the  $\text{Fe}^{3+}$  signal is due to a chemical change at the sample surface, which most likely will not contribute to the XMCD signal according to the results found for  $\text{Sr}_2\text{FeMoO}_6$  and  $\text{Fe}_{0.5}\text{Cu}_{0.5}\text{Cr}_2\text{S}_4$ . This was taken into account in the CF multiplet calculations shown in figure 2.20. The calculation shown in panel (b) simulates a spin magnetic ground state as predicted by Ikeda *et al.* (2005b) (see also figure 2.18 (b)). In panel (c) a frustrated spin magnetic ground state is assumed according to Nagano *et al.* (2007) (see also figure 2.18 (a)). As can be seen both calculations resemble the experimental result. But a more detailed look reveals that the spectral

shape of the unfrustrated system resembles the measurement much better than the one calculated for the frustrated system. As pointed out by the vertical black line, at the  $L_3$  part of the experiment as well as in the unfrustrated calculation the dichroic signal ( $\mu_+ - \mu_-$ ) changes its sign at about 709 eV. This is a clear indication of all  $\text{Fe}^{2+}$  sites being in the majority-spin state, while  $1/3$  of the  $\text{Fe}^{3+}$  spin being in majority and  $2/3$  in minority. The change of sign at 709 eV is absent in the calculation for the frustrated system. In addition also the  $L_2$  part of the measurement shows clear differences to the frustrated calculation. Although the dichroic signal at  $L_2$  is small in the measurement, it clearly resembles the calculation of the unfrustrated system. Therefore one can conclude that the Fe ions in  $\text{LuFe}_2\text{O}_4$  are not in a spin frustrated ground state.

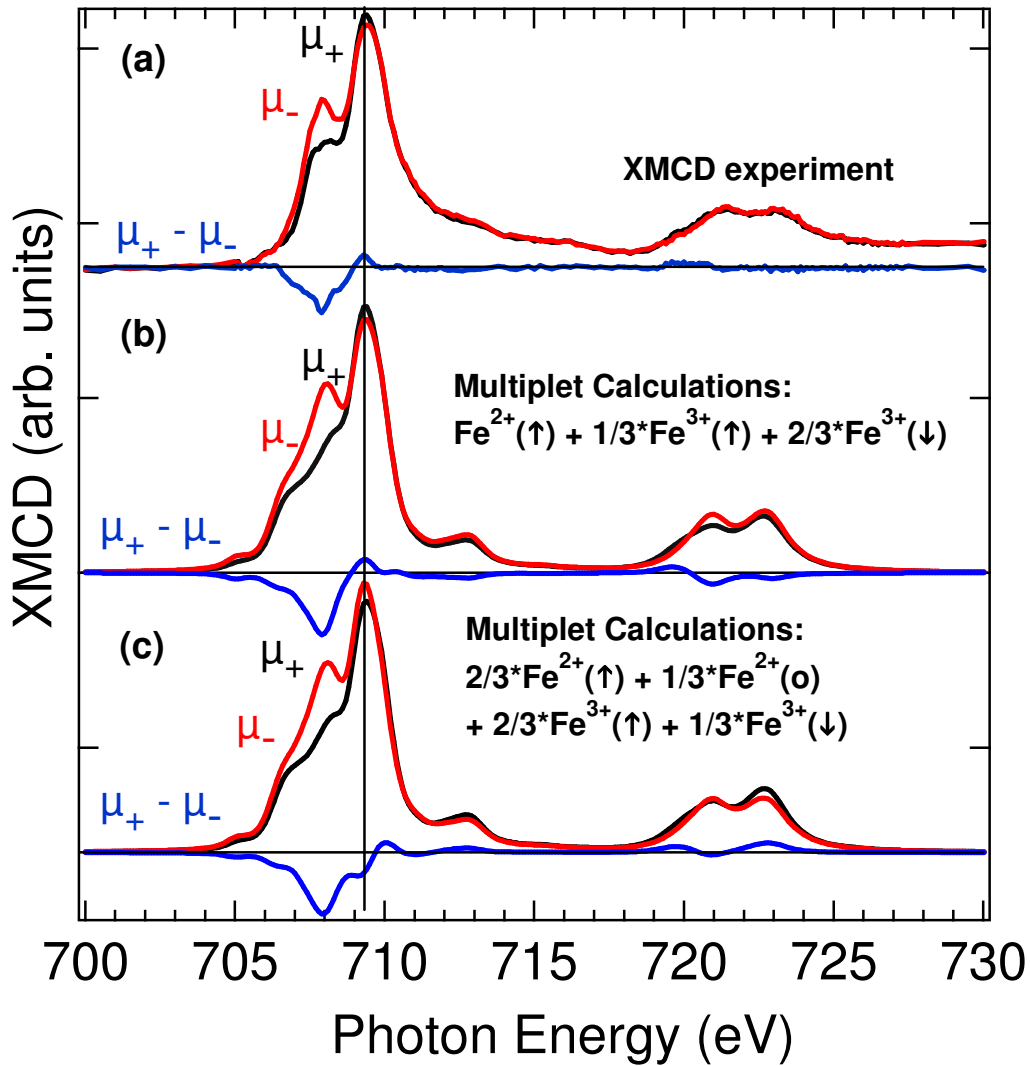


Figure 2.20: Fe 2p XMCD measurements (panel (a)) and corresponding crystal-field multiplet calculations (panel (b) and (c)).



### 2.2.4 Fe in the Ferric star

The star-shaped complex  $\{Fe^{III}[Fe^{III}(L^1)_2]_3\} \cdot 4CHCl_3$ , also called ferric star or FeStar, is shown in figure 2.21. Here  $L^1 = CH_3N(CH_2CH_2O)_2^-$ . For more details concerning the structure and synthesis please be referred to Takacs *et al.* (2006); Saalfrank *et al.* (2001, 2006). This trigonal, metal-centered  $\{FeFe_3\}$  complex is one of the simplest inorganic systems showing single-molecule magnet (SMM) behaviour and therefore has been extensively studied as a model system. As indicated by the formula of the complex, in the FeStar the four Fe ions are expected to be trivalent. Mössbauer measurements revealed that the Fe ions are octahedrally surrounded by ligands with some deviation from the perfect surrounding at the peripheral Fe ions (Saalfrank *et al.*, 2006) (see also figure 2.21). Note also that in contrast to the centered Fe ion the peripheral ions are not only surrounded by oxygen, but also by two nitrogen ions, respectively. Basic magnetochemical investigations and magnetic measurements of the ferric star reveal the three spins with  $S = \frac{5}{2}$  of the peripheral Fe ions at the star edges to couple antiferromagnetic with the central ion leading to a ferrimagnetic ground state with  $\mu_s = 10 \mu_B$  / molecule (Barra *et al.*, 1999; Saalfrank *et al.*, 2006) (see also figure 2.21).

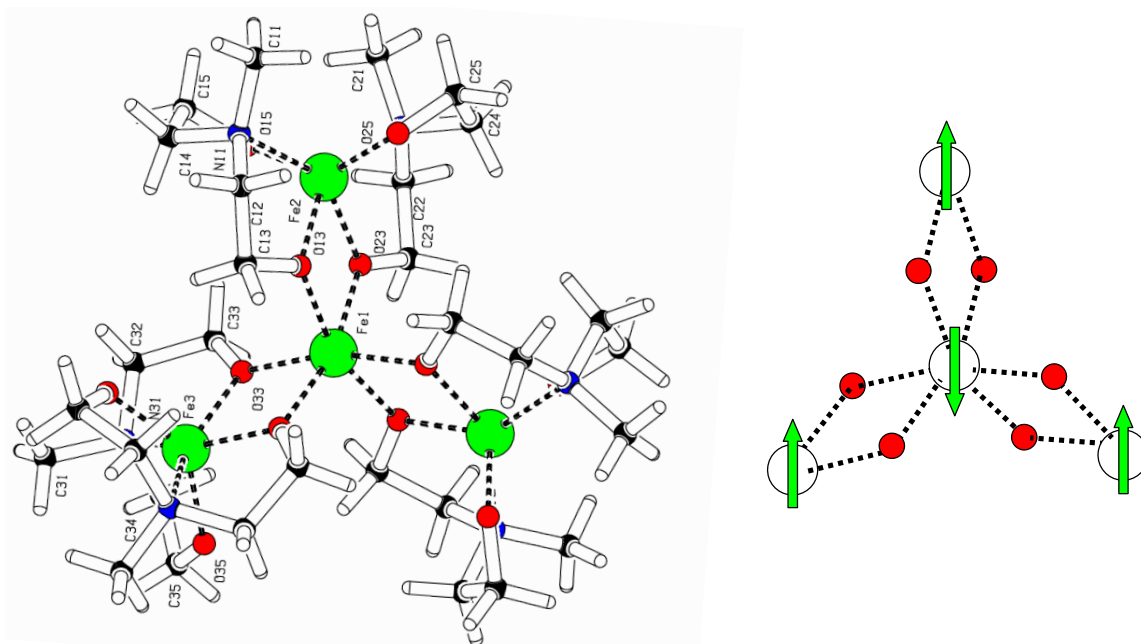


Figure 2.21: **Left:** Structure of the ferric star  $\{Fe^{III}[Fe^{III}(L^1)_2]_3\}$  attached from Takacs (2005). Fe: Green; O: Red; C: Black; N: Blue; H: White. The Fe-ligand bondings are marked with dashed lines. **Right:** Illustration of the ferrimagnetic ground state.

In figure 2.22 Fe 2p XAS and XMCD measurements of the ferric star are presented together with charge transfer (CT) multiplet calculations. As mentioned before in contrast to the expected Fe valence state the XAS and XMCD spectral shape indicate the Fe ions to be nearly completely divalent. This is also confirmed by the multiplet simulations. The calculations were done with a crystal field of  $10Dq = 0.8$  eV and a charge transfer mixing the ground state in a ratio of about 82%  $3d^n$  / 18%  $3d^{n+1}\underline{L}$ .

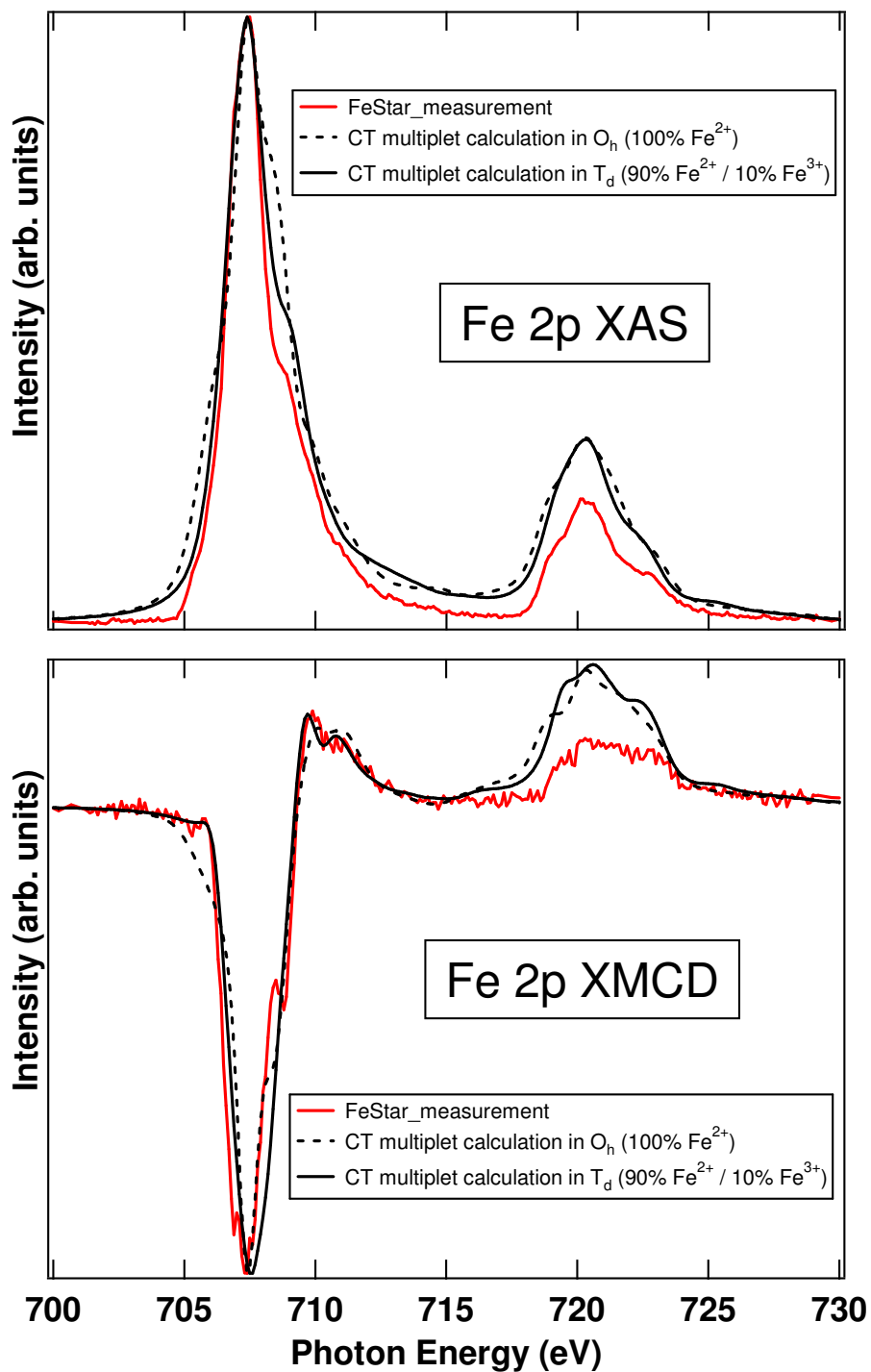


Figure 2.22: Fe 2p XAS and XMCD measurements of FeStar in comparison with CT multiplet calculations.

If one assumes an octahedral symmetry for the Fe ions the best fit of the spectral shape is found for Fe in a complete divalent valence state (see figure 2.22, dashed line). However the simulation differs considerably from the measurement. For instance the  $L_3$  part of the XAS spectrum is broader in the calculation than in the measurement. Also the simulated shoulder at higher photon energies appears at higher intensity compared to the measurement. The spectral shape of the measurement between  $L_3 - L_2$  and the  $L_2$  part itself is quite similar to the calculation but the measurement shows a different background. Note that a two step function with a 2/3 ( $L_3$ ) to 1/3 ( $L_2$ ) ratio was assumed as background and subtracted from the measurement. Due to multiplet mixing the actual background can differ from this simple model, which could cause the found difference in background between the calculation and the measurement. This problem is not present for the XMCD measurement since the background is deleted by the subtraction of the  $\mu^-$  and  $\mu^+$  absorption spectra. Nevertheless again the calculation (dashed line) differs from the measurement. The  $L_3$  part of the XMCD calculation shows multiplet states at lower photon energies than found in the measurement. Also the calculated  $L_3$  spectral shape differs from the measurement. At the  $L_2$  part the calculation and measurement show even more differences. A possible reason for this will be discussed below.

Beside the calculation assuming an octahedral symmetry for the Fe ions, according to the molecular structure, also CT multiplet calculations assuming a tetrahedral symmetry were compared to the XAS and XMCD measurements (figure 2.22, black line). Here the best fit was found for Fe in a mixed  $Fe^{2+} / Fe^{3+}$  valence state with a ratio of about 90% / 10%. As one can see there are still differences between the calculation and the measurement, but surprisingly the spectral shape is much better simulated. Especially the  $L_3$  part of the calculation resembles the absorption measurement much better. Most of the remaining differences can be due to problems with the background subtraction already mentioned before. This becomes even more clear by looking at the XMCD results. Although the measured  $L_3$  spectral shape still differs from the calculation its shape at low photon energy (about 705 eV) and at higher photon energy (about 710 eV) is much better reproduced by the tetrahedral simulation compared to the octahedral one. Again the  $L_2$  part is not well simulated. On the one hand the better consistency of the tetrahedral simulation could be explained by the deviation of the peripheral Fe ligand structure, which shows some tetrahedral character (figure 2.21). On the other hand this finding could be an indication for a change of the FeStar molecular structure. This is also supported by the fact that at least 90% of the Fe ions seem to be in a divalent valence state in the measurement, while according to magnetochemical investigations and magnetic measurements only  $Fe^{3+}$  ions should be present (Barra *et al.*, 1999; Saalfrank *et al.*, 2006). With Fe becoming divalent the Fe-ligand binding could weaken, which would make a structural change possible. Finally also the considerable difference between the  $L_2$  part of the XMCD measurement and the one of the calculations is a clear evidence for a distortion of the Fe surrounding. In a perfect octahedral or tetrahedral surrounding the Hund's rules are annulled leading to the quenching of the orbital magnetic moment. As shown in figure 2.23 the overall integral of the calculation is about zero for the octahedral as well as the tetrahedral symmetry. According to the sum rules (see section 1.2.2.1) this would lead to a quenched orbital magnetic moment.

However for the measured XMCD signal the integral is different due to the smaller signal at the  $L_2$  part (see figure 2.22). Therefore the overall integral of the XMCD measurement does not become zero leading to an orbital magnetic moment (see figure 2.23). This clearly indicates a greater distortion of the Fe surrounding possibly due to a structural change.

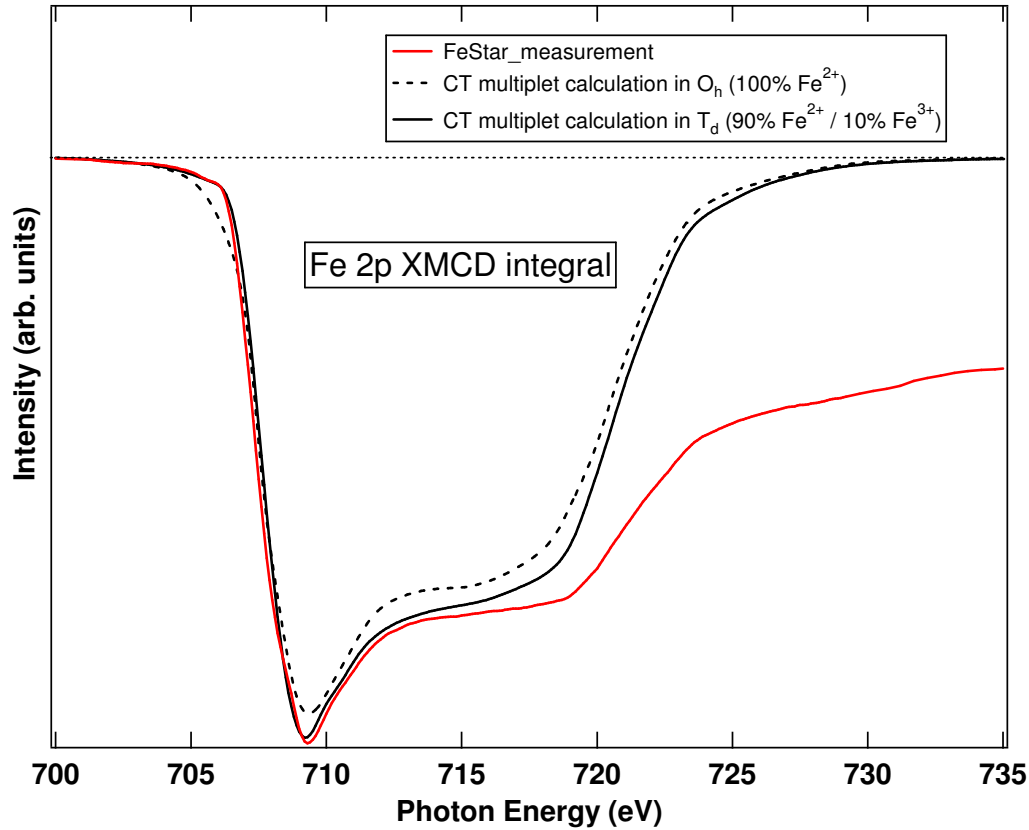


Figure 2.23: The integral of the Fe 2p XMCD measurement and XMCD CT multiplet calculations shown in figure 2.22.

In order to proof the assumption of a structural and/or valence instability in the ferric star and to find a possible reason for this, Fe 2p XAS and XMCD measurements with only 1% undulator yield were performed. Figure 2.24 presents a Fe 2p XAS spectrum of an early measurement in comparison with a measurement done after the sample was exposed to the beam for about 6 hours. In addition also the spectrum discussed above measured with 100% photon yield is shown. As displayed there is a clear change of the spectral shape. The early measurement done with 1% undulator yield reveals trivalent Fe ions to be present. After 6 hours beam exposure time there seems to be an increase of the  $\text{Fe}^{2+}$  amount in the sample. With further progress this would lead to an  $\text{Fe}^{2+}$  spectrum as found for the sample measured with 100% photon yield. This clearly indicates that the synchrotron beam radiated onto the sample is responsible for the found changes in the FeStar.

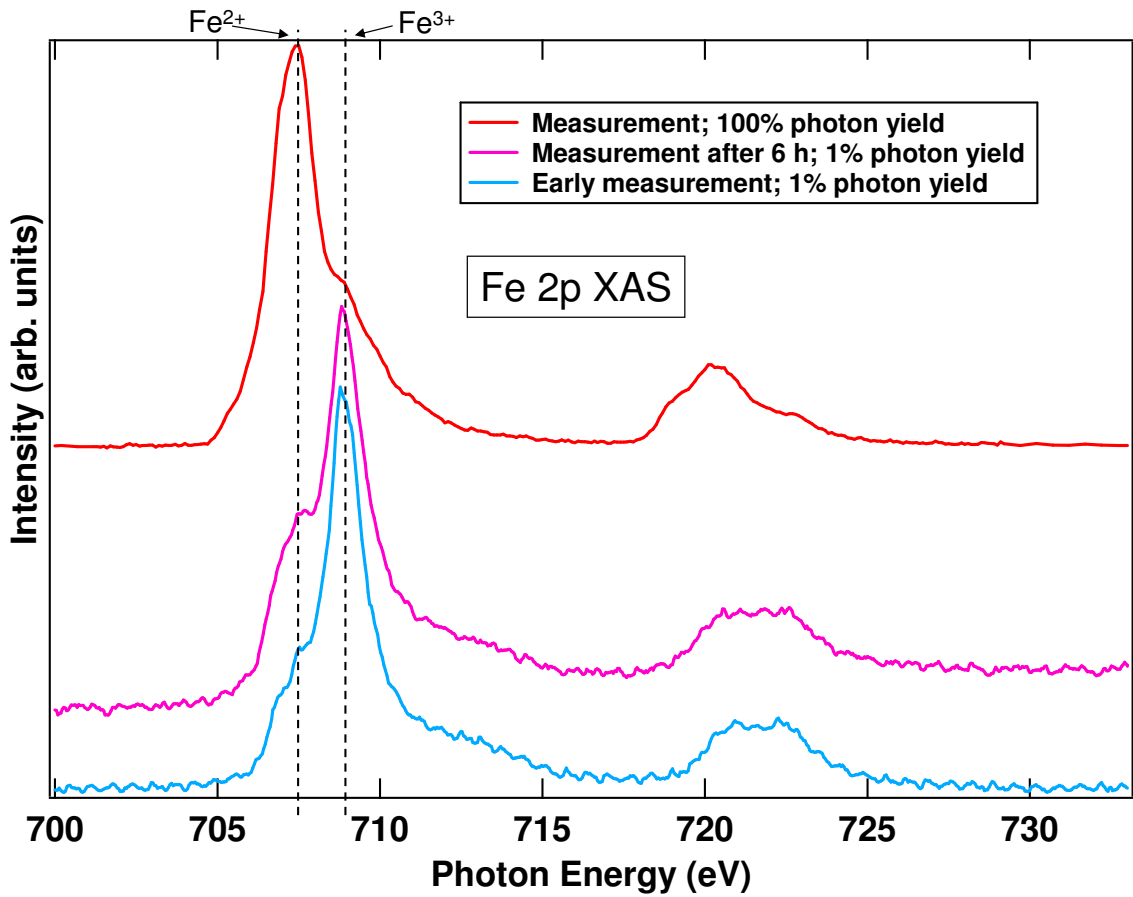


Figure 2.24: Fe 2p XAS measurements of the ferric star. One spectrum shows an early measurement with a small beam exposure time and only 1% photon yield (light blue). The second spectrum was measured with the same yield but an exposure time of about 6 hours (violet). The third one, which was already discussed above, was measured with 100% photon yield (red).

In figure 2.25 the early measured Fe 2p XAS and XMCD spectrum with 1% undulator yield is presented together with  $\text{Fe}^{3+}$  CT multiplet calculations done in  $O_h$  and  $T_d$  symmetry, respectively. The same crystal field and charge transfer values were used as for the calculations discussed above. As can be seen in contrast to the measurement shown in figure 2.22, this one can be well reproduced with a simulation assuming all Fe ions to be in a trivalent valence state surrounded octahedrally by their ligands. Note that the tetrahedral simulation also reproduces the spectral shape quite good, but there are more differences visible. Surprisingly by looking at the Fe 2p XMCD spectrum there is better consistency with the  $O_h$  calculation at about 707 eV photon energy, while the  $T_d$  simulation clearly better reproduces the measurement at higher photon energies of about 710 eV - 713 eV. This could be an indication of a structural change. However this also can be explained by the mentioned deviation from the perfect octahedral surrounding of the peripheral Fe ligand structure (see figure 2.21).

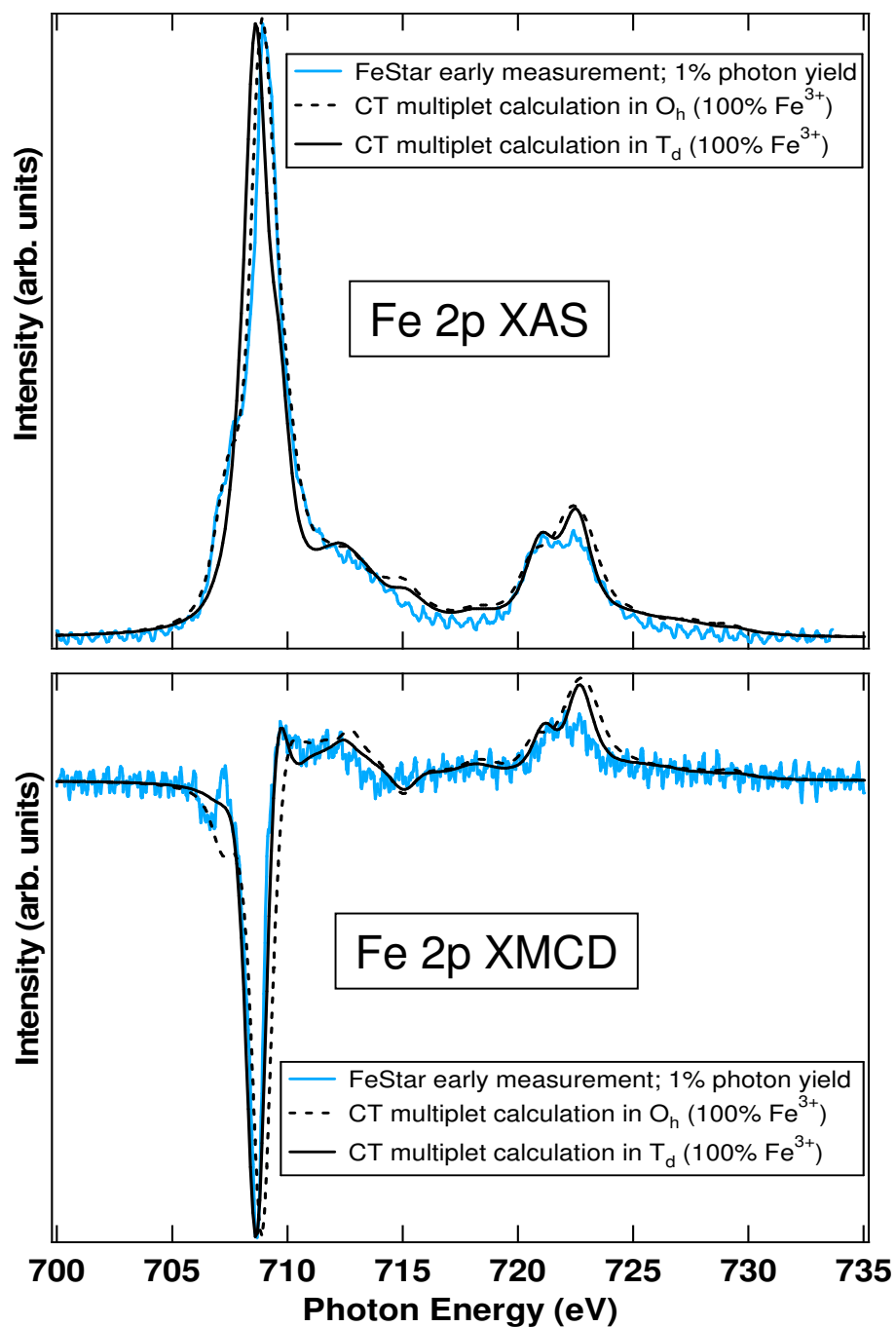


Figure 2.25: Fe 2p XAS and XMCD measurement of a FeStar sample, which was exposed to the beam for a short time with only 1% undulator yield. The spectra are compared to CT multiplet calculations.

The latter is supported by investigation of the integrated XMCD spectra, which are shown in figure 2.26. As can be seen the measurement shows a decreased integral, which is due to the noise in the spectrum. Nevertheless in contrast to the measurement performed with 100% photon yield (figure 2.23), here the overall integral clearly becomes zero, indicating a quenched orbital moment. Thus it seems like the deviation of the peripheral Fe ligand structure does not have a big influence on the orbital magnetic moment.

Therefore it can be concluded that for the ferric star sample irradiated with 100% photon yield indications for a considerable structure and valence change have been found that are absent in a sample irradiated for a short time with only 1% photon yield.

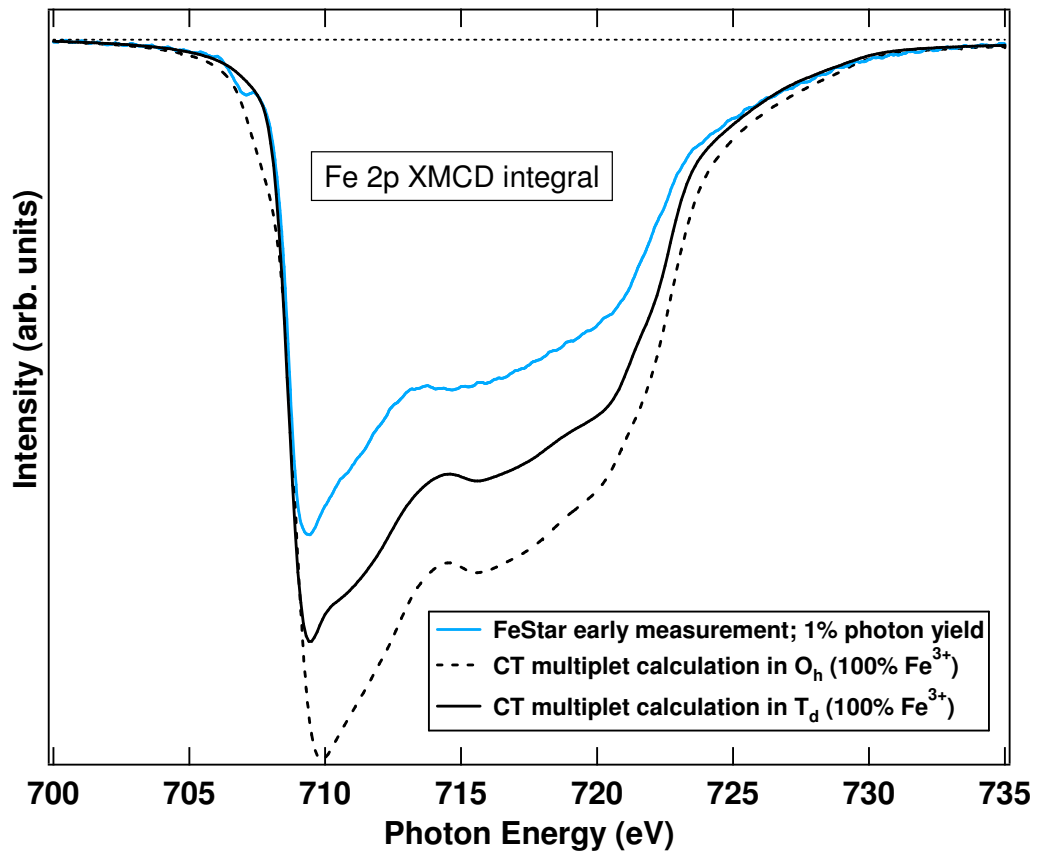


Figure 2.26: The integral of the Fe 2p XMCD measurement and XMCD CT multiplet calculations shown in figure 2.25.

The findings of Mannini *et al.* (2009a,b) give evidence that the changes in the ferric star activated by the beam radiated onto the sample could be related to the molecular structure.

In figure 2.27 (left) the structure of a ferric star molecule produced by Barra *et al.* (1999) is illustrated. In the following this molecule will be denoted as  $\text{Fe}_4$ . As shown the  $\text{Fe}_4$  structure differs from the one of the ferric star produced by Saalfrank *et al.* (2001, 2006) (see figure 2.27, right). In contrast to the ferric star in the  $\text{Fe}_4$  there seems

to be no connection of the oxygen ligands of the centered Fe ion to the ones of the peripheral Fe ions via a carbon chain. Also in the  $\text{Fe}_4$  all the Fe ions are surrounded by oxygen atoms, while in the ferric star the peripheral Fe ions are surrounded by four oxygen and two nitrogen atoms. In addition the octahedral symmetry of the peripheral Fe ions in the  $\text{F}_4$  seem to be less distorted than in the ferric star.

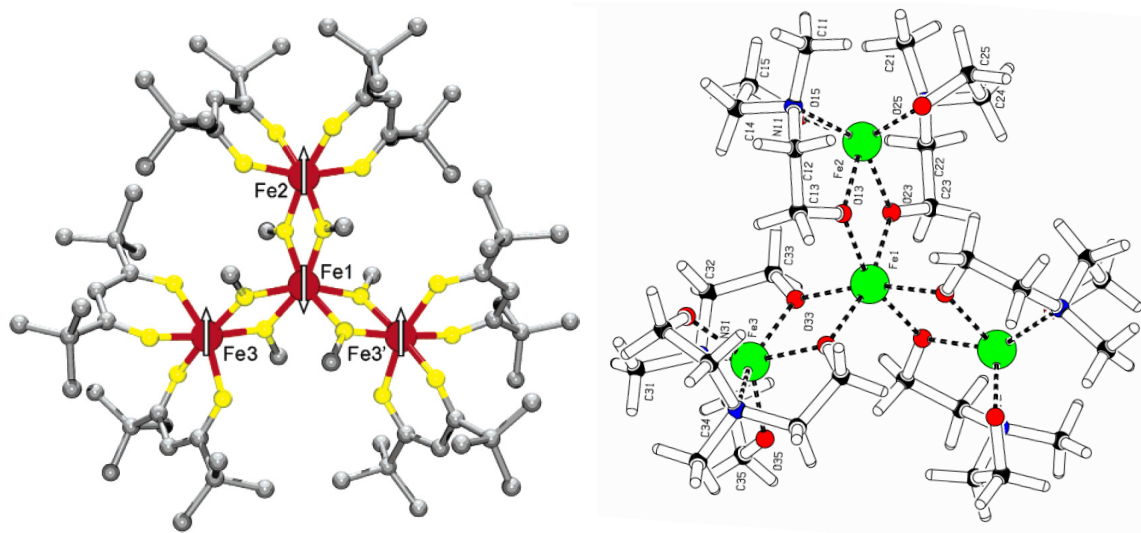


Figure 2.27: **Left:** The molecular structure of the ferric star ( $\text{Fe}_4$ ) produced by Barra *et al.* (1999). The illustration is attached from Accorsi *et al.* (2006). Fe: Red; O: Yellow; C: Gray. **Right:** The molecular structure of the ferric star or FeStar produced by Saalfrank *et al.* (2001, 2006) attached from Takacs (2005). Fe: Green; O: Red; C: Black; N: Blue; H: White.

The  $\text{Fe}_4$  molecule was investigated with XAS and XMCD by Mannini *et al.* (2009a,b). The results are shown in figure 2.28 together with corresponding ligand and field multiplet calculations. It becomes obvious that the measured spectra differ significantly from the measurement results of the FeStar using 100% undulator yield. The ones using 1% undulator yield show more consistence with the results found for the  $\text{Fe}_4$ , although there are still clear differences. Multiplet calculations assuming all Fe ions to be present in a trivalent valence state reveal that in the  $\text{Fe}_4$  the octahedral crystal field seems to be higher than in the FeStar. Ligand field multiplet calculations with a crystal field of  $10Dq = 1.5$  eV show a good consistence with the measured results (figure 2.28). The smaller average crystal field ( $10Dq = 0.8$  eV) for the  $\text{Fe}^{3+}$  ions found in the ferric star measured using 1% undulator yield could be explained by the reduced symmetry of the peripheral Fe ligand structure (see figure 2.27). Surprisingly no change of the spectral shape due to the synchrotron beam is reported for the  $\text{Fe}_4$ .

These results indicate that, beside a higher average crystal field of the four Fe ions, the different ligand structure of the  $\text{Fe}_4$  molecule seems to lead to the absence of a valence or structure instability. Therefore it can be concluded that the ligand structure in the ferric star molecule is most likely responsible for the found changes activated by the photon radiation.



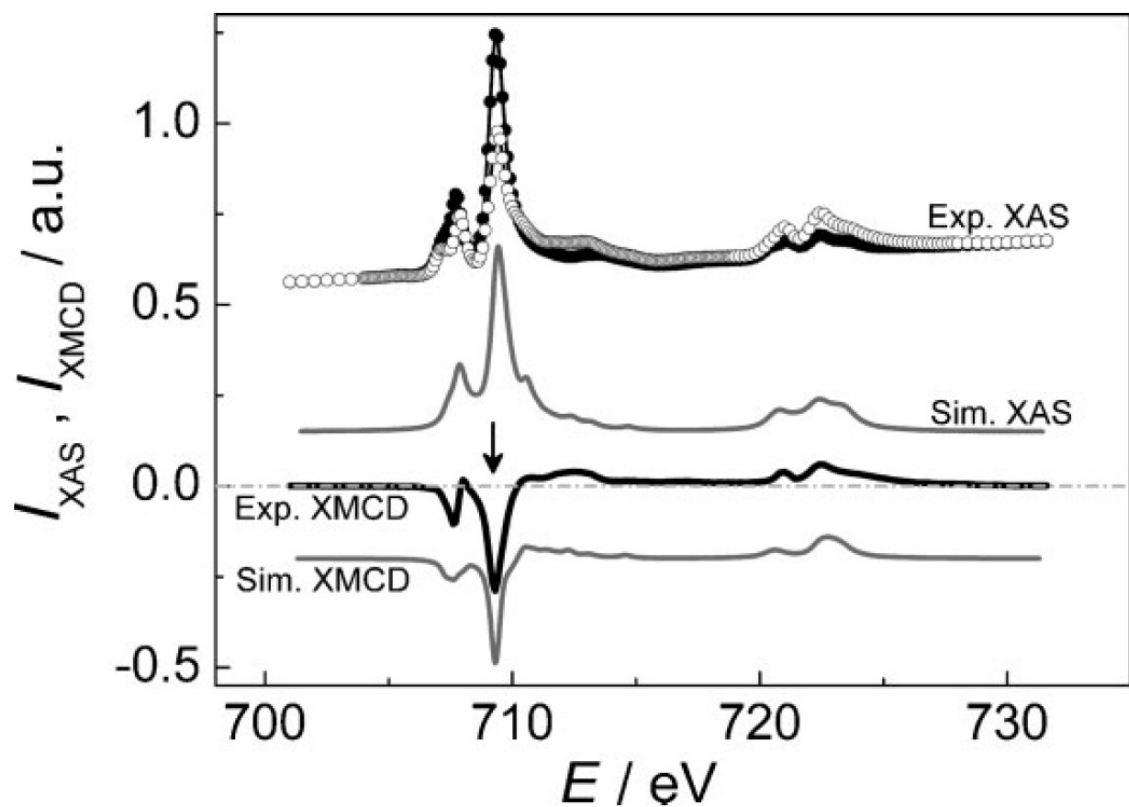


Figure 2.28: XAS and XMCD analysis on Fe<sub>4</sub>. Absorption spectra (white dots:  $\mu^+$ ; black dots:  $\mu^-$ ) and dichroic signal (black solid line) at  $T = 0.75$  K and  $B = 3.0$  T, along with simulated curves (gray solid lines) obtained using ligand field multiplet calculations. The figure is attached from Mannini *et al.* (2009b).

### 2.2.5 Fe in $\text{Mo}_{72}\text{Fe}_{30}$ and $\text{W}_{72}\text{Fe}_{30}$

$\text{Mo}_{72}\text{Fe}_{30}$  and  $\text{W}_{72}\text{Fe}_{30}$  are spherical molecules containing 30  $\text{Fe}^{3+}$  ( $S=\frac{5}{2}$ ) ions surrounded octahedrally by oxygen (see figure 2.29). To date this is the largest number of paramagnetic ions that have successfully been incorporated in the diamagnetic framework of a synthetic molecule. Since there is negligible intermolecular interaction  $\text{Mo}_{72}\text{Fe}_{30}$  and  $\text{W}_{72}\text{Fe}_{30}$  are promising model systems to study the behaviour of  $N = 30$  interacting paramagnetic ions (Schnack and Luban, 2000). For more details about the structure and synthesis of  $\text{Mo}_{72}\text{Fe}_{30}$  and  $\text{W}_{72}\text{Fe}_{30}$  please be referred to Müller *et al.* (1999) and Todea *et al.* (2010), respectively.

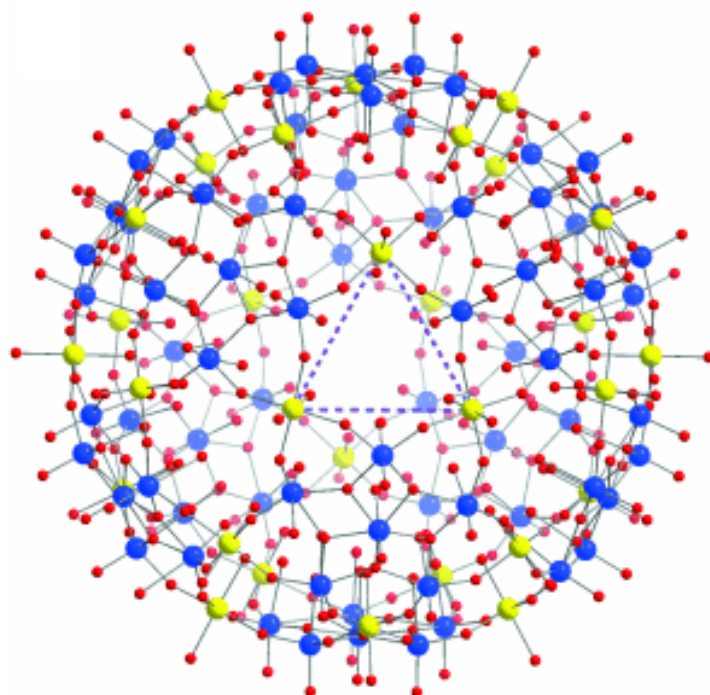


Figure 2.29: Ball-and-stick representation of the  $\text{M}_{72}\text{Fe}_{30}$  ( $\text{M} = \text{Mo}, \text{W}$ ) cluster (Müller *et al.*, 2001). The ligand structure within the cluster is omitted for clarity. M: blue; Fe: yellow; O: red.

As already mentioned before and shown in figure 2.13 and 2.14 for  $\text{M}_{72}\text{Fe}_{30}$  ( $\text{M} = \text{Mo}, \text{W}$ ) the results of the XAS and XMCD measurement are in agreement. In case of  $\text{Mo}_{72}\text{Fe}_{30}$  the XAS and XMCD measurement show Fe to be in a mixed valence state, while for the  $\text{W}_{72}\text{Fe}_{30}$  both measurements show Fe to be purely trivalent. This is also supported by charge transfer multiplet calculations, done with an octahedral ( $\text{O}_h$ ) crystal field of  $10\text{Dq} = 1.5 \text{ eV}$  and a charge transfer value mixing the ground state in a ratio of about 82%  $3\text{d}^n$  / 18%  $3\text{d}^{n+1}\underline{\text{L}}$ . As shown in figure 2.30 for  $\text{Mo}_{72}\text{Fe}_{30}$  the spectral shape could be simulated assuming a mixed  $\text{Fe}^{2+}$  /  $\text{Fe}^{3+}$  valence state with a ratio of about 45% / 55%. In case of  $\text{W}_{72}\text{Fe}_{30}$  the best fit was found for CT multiplet calculations assuming only trivalent Fe ions to be present.

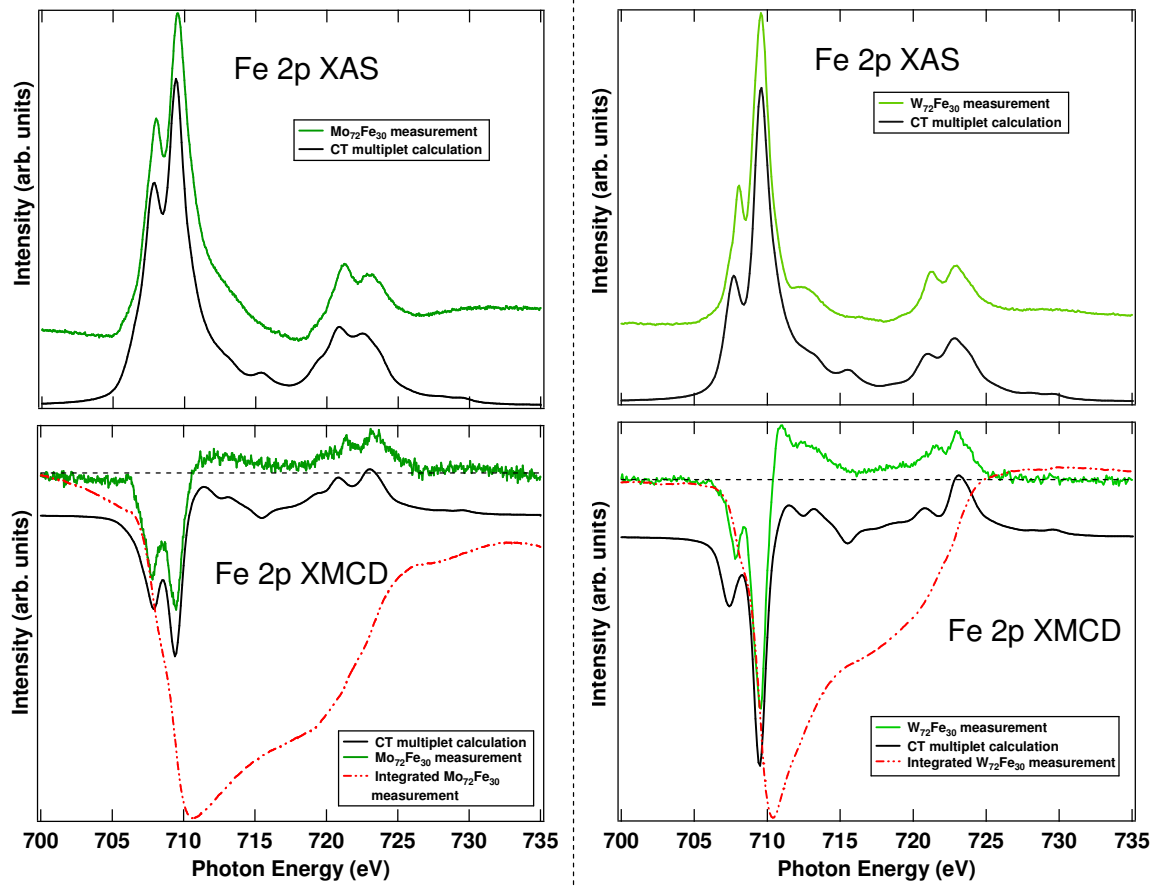


Figure 2.30: XAS and XMCD measurements of  $\text{Mo}_{72}\text{Fe}_{30}$  (left, top and bottom) and  $\text{W}_{72}\text{Fe}_{30}$  (right, top and bottom). In addition the spectra were simulated with charge transfer multiplet calculations (black line). For  $\text{Mo}_{72}\text{Fe}_{30}$  the calculation assumes a  $\text{Fe}^{2+} / \text{Fe}^{3+}$  ratio of about 45% / 55%, while for  $\text{W}_{72}\text{Fe}_{30}$  a calculation with 100%  $\text{Fe}^{3+}$  shows good agreement with the measurement. Finally also the integrated XMCD measurements are shown (red dotted line).

Since in both compounds only  $\text{Fe}^{3+}$  ions are expected to be present the found difference in the Fe valence state is quite surprising. As shown in figure 2.31 comparison of the  $L_3$  line of an early XAS measurement of  $\text{Mo}_{72}\text{Fe}_{30}$  and a measurement done at the end of the experiment reveals the  $\text{Fe}^{2+}$  features in the spectrum to increase temporally.

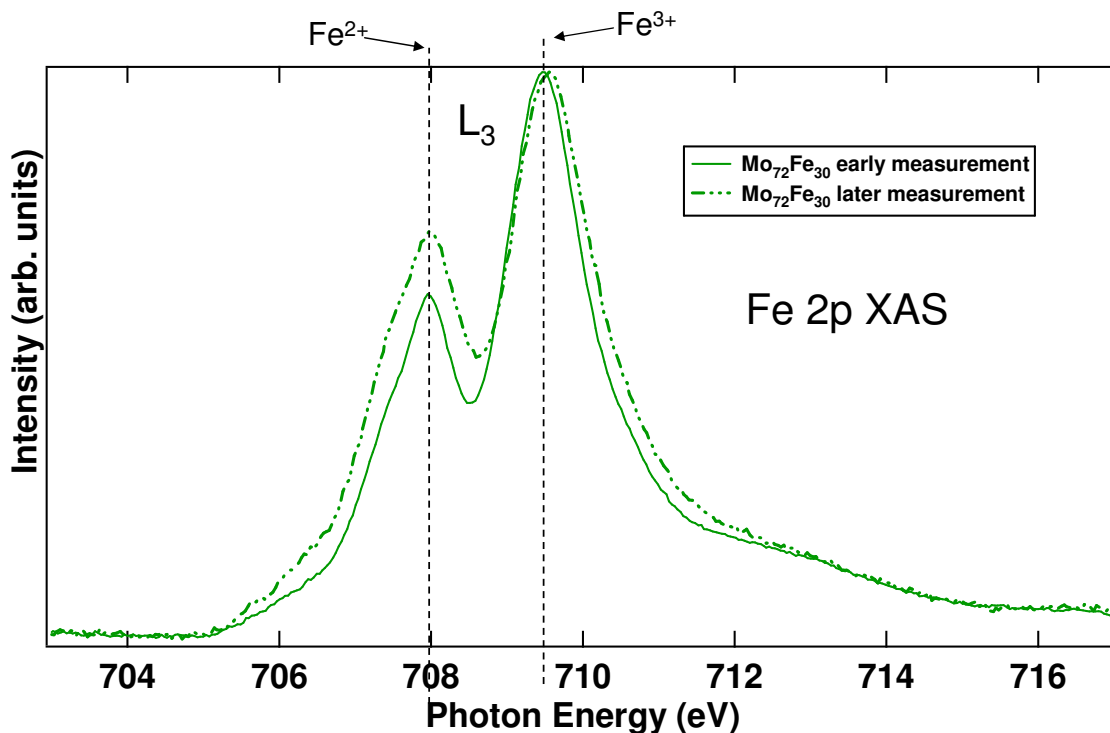


Figure 2.31: Comparison of the  $L_3$  part of two Fe 2p XAS measurements of  $\text{Mo}_{72}\text{Fe}_{30}$  taken at different times of the experiment. One spectrum was measured at the beginning of the experiment with a small exposure time of the sample to the photon beam (green line). The other was taken at the end of the measurement period (green dotted line). In addition also the photon energies of the  $L_3$  line of divalent and trivalent Fe found by reference measurements are marked with dotted lines.

Therefore with a view to the findings for the ferric star molecule it seems possible that also in case of  $\text{Mo}_{72}\text{Fe}_{30}$  a valence instability is present leading to the appearance of divalent Fe ions. Like for the FeStar also in case of this spherical molecules differences in the ligand structure can be an explanation for the Fe valence change. The  $\text{Mo}_{72}\text{Fe}_{30}$  ball contains acetate ligands and is practically neutral (Müller *et al.*, 1999; Todea *et al.*, 2010). In contrast to this 25 sulfate ligands ( $\text{SO}_4^{2-}$ ) are present inside the cavity of the  $\text{W}_{72}\text{Fe}_{30}$  molecule causing a considerable negative charge (see figure 2.32, left). This leads to the fixing of  $\text{NH}_4^+$  ions through hydrogen bonds to the  $\text{Fe}_3\text{W}_3\text{O}_6$  pores (figure 2.32, right) (Todea *et al.*, 2010). It is possible that this considerable difference in the molecular structure can cause a valence and/or structure instability in the  $\text{Mo}_{72}\text{Fe}_{30}$  leading to the appearance of divalent Fe ions. Indication for a structure instability is found by investigation of the integral of the XMCD measurement. Like shown in figure 2.30 in case of  $\text{W}_{72}\text{Fe}_{30}$  the overall integral of the XMCD signal is

close to zero, indicating a quenched orbital magnetic moment and therefore a nearly perfect octahedral surrounding of the Fe ions. For the  $\text{Mo}_{72}\text{Fe}_{30}$  the overall integral remains negativ, which indicates a distortion of the Fe ligand structure.

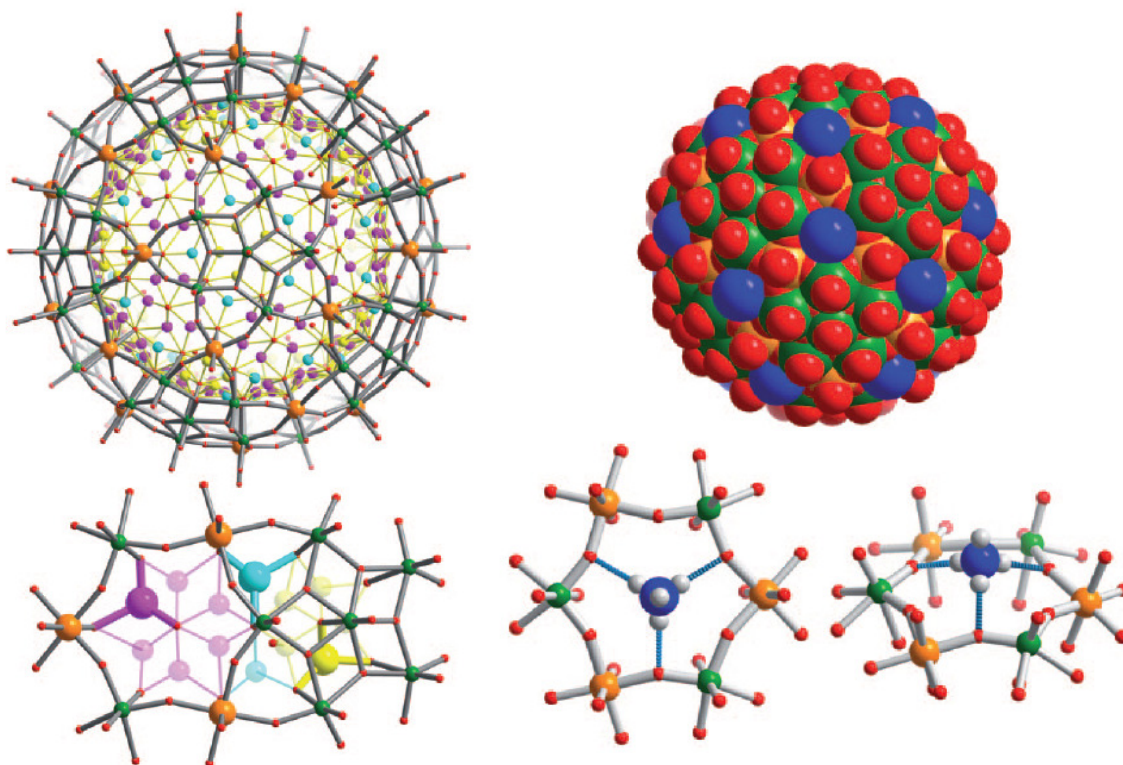


Figure 2.32: **Left, top:** Ball-and-stick representation of the  $\text{W}_{72}\text{Fe}_{30}$  without the  $\text{NH}_4^+$  ions but emphasising the 25  $\text{SO}_4^{2-}$  ligands coordinated in three different ways to the inner shell of the cluster and their disorder as a sign of the complexity. **Left, bottom:** One  $\{\text{Fe}_3\text{W}_3\text{O}_6\}$ -type pore together with one  $\{(W)W_5\}$ -type pentagonal unit and three different coordination types of the  $\text{SO}_4^{2-}$  ligands. W: green; Fe: orange; O: red;  $\text{SO}_4^{2-}$  ligands: yellow, lilac and turquoise. The disordered  $\text{SO}_4^{2-}$  ligand positions are transparent for clarity. **Right, top:** Space-filling representation of  $\text{W}_{72}\text{Fe}_{30}$  highlighting the affinity of the 20  $\{\text{Fe}_3\text{W}_3\text{O}_6\}$ -type pores for the 20  $\text{NH}_4^+$  cations located on the  $C_3$  axes. **Right, bottom:** Two views of the pore situation (N blue, H light gray, other colors as in **left**). The illustrations are taken from Todea *et al.* (2010).

## 2.3 Conclusion

In this chapter multiplet simulations for the Fe 2p XAS and XMCD spectra were introduced and the influence of crystal field, charge transfer and temperature on the spectral shape were shown.

Then an overview of Fe 2p XAS and XMCD measurements of different compounds is given. On the basis of the XAS measurements first predictions for the Fe valence state in the different compounds could be made. Thereby the Fe ions seem mostly

to be present in a mixed  $\text{Fe}^{2+} / \text{Fe}^{3+}$  valence state with different ratios. Comparison with the XMCD measurements revealed that the results found with XAS seem to be affected by temporally effects. These effects seem to differ between the crystalline materials on the one hand and the molecular materials on the other.

For the crystalline materials ( $\text{Sr}_2\text{FeMoO}_6$ ,  $\text{Fe}_{0.5}\text{Cu}_{0.5}\text{Cr}_2\text{S}_4$ ,  $\text{LuFe}_2\text{O}_4$ ) an ageing effect was discovered leading to an increase of the  $\text{Fe}^{3+}$  contribution to the absorption spectrum with no contribution to the XMCD signal. First of all measurements of  $\text{Sr}_2\text{FeMoO}_6$  indicated a change of the mixed Fe valence state with time (see also chapter 3 and Kuepper *et al.* (2008)). Here an increase of the  $\text{Fe}^{3+}$  contribution to the XAS spectrum was observed, which could not be seen in the XMCD spectral shape. This indicated the absence of a macroscopic magnetic ordering or an anti-ferromagnetic alignment of the additional  $\text{Fe}^{3+}$  ions leading to the assumption of a chemical change most likely at the sample surface. Later for  $\text{Fe}_{0.5}\text{Cu}_{0.5}\text{Cr}_2\text{S}_4$  a similar effect was found (see also chapter 4 and Taubitz *et al.* (2009)). Here the whole  $\text{Fe}^{3+}$  amount visible in the XAS measurement showed no XMCD signal at all. Further investigations revealed that the  $\text{Fe}^{3+}$  ions are present in the surface layers, while only  $\text{Fe}^{2+}$  ions can be found in the bulk. Since the current model describing the magnetoresistance (MR) assumes a mixed Fe valence state present in  $\text{Fe}_{0.5}\text{Cu}_{0.5}\text{Cr}_2\text{S}_4$ , this finding led to different explanations for the MR in this spinel system (see chapter 4). Finally for  $\text{LuFe}_2\text{O}_4$  a difference between the  $\text{Fe}^{3+}$  contribution to the Fe 2p XAS spectrum measured in the TEY-mode and the one measured in the TFY-mode was detected. The surface sensitive TEY-mode showed a considerable higher amount of trivalent Fe ions than the more bulk sensitive TFY-mode. Since again there seems to be no contribution of the additional  $\text{Fe}^{3+}$  ions to the XMCD signal a similar effect like found for  $\text{Sr}_2\text{FeMoO}_6$  and  $\text{Fe}_{0.5}\text{Cu}_{0.5}\text{Cr}_2\text{S}_4$  could be assumed. This was considered in multiplet calculations simulating the XAS and XMCD measurements of  $\text{LuFe}_2\text{O}_4$ , which revealed the Fe ions to be in a magnetic ground state without frustration (see also Kuepper *et al.* (2009)).

In case of the molecules (FeStar,  $\text{Mo}_{72}\text{Fe}_{30}$  and  $\text{W}_{72}\text{Fe}_{30}$ ) no chemical change like found for the crystalline materials seems to occur, but the measurements revealed a different temporally effect affecting the XAS and XMCD results. Thereby the molecular structure seems to cause a structure and/or valence instability activated by a photon beam radiated onto the sample. Note that in contrast to the valence instability of the crystalline materials this effect seems to increase the  $\text{Fe}^{2+}$  amount in the measurement, which shows a contribution to the XMCD signal, thus a macroscopic magnetic ordering. The measurements of the FeStar molecule, which was predicted to contain only trivalent Fe ions, showed at least 90% of the Fe ions to be in a divalent valence state. In addition evidence of a distortion of the ligand structure was found. Further investigations revealed that measurements done with only 1% undulator yield showed only  $\text{Fe}^{3+}$  ions to be present in the FeStar with no or only a small distortion. This indicated a structure and/or valence instability caused by the light radiated onto the sample. Surprisingly measurements of a similar molecule, which only differs in its ligand structure ( $\text{Fe}_4$ ), does not show such an instability. Therefore it can be concluded that the ligand structure seems to be responsible for the found changes of FeStar caused by light radiation. The measurements of  $\text{Mo}_{72}\text{Fe}_{30}$

and  $\text{W}_{72}\text{Fe}_{30}$  revealed a similar behaviour. In both compounds all Fe ions are predicted to be trivalent. While for the  $\text{W}_{72}\text{Fe}_{30}$  this could be confirmed by the XAS and XMCD measurements in case of  $\text{Mo}_{72}\text{Fe}_{30}$  about 45% of the Fe ions seem to be divalent. In addition the XMCD integral indicates a distortion of the ligand surrounding in  $\text{Mo}_{72}\text{Fe}_{30}$ . Again the ligand structures of  $\text{Mo}_{72}\text{Fe}_{30}$  and  $\text{W}_{72}\text{Fe}_{30}$  differ considerably. This supports the assumption that the ligand structure is responsible for the Fe valence and structure change in  $\text{Mo}_{72}\text{Fe}_{30}$  most likely caused by the photon radiation.





## Chapter 3

# Investigation of the Fe valence state in $\text{Sr}_2\text{FeMoO}_6$

### 3.1 Introduction

$\text{Sr}_2\text{FeMoO}_6$  has an ordered double perovskite structure  $\text{A}_2\text{B}'\text{B}''\text{O}_6$  comprising alternating  $\text{AB}'\text{O}_3$  and  $\text{AB}''\text{O}_3$  perovskite units. The A site is occupied by Sr and the B' and B'' site by Fe and Mo, respectively. This compound crystallises in the tetragonal  $I4/mmm$  space group. As shown in figure 3.1 Fe and Mo are surrounded by oxygen in an octahedral symmetry.  $\text{Sr}_2\text{FeMoO}_6$  is ferrimagnetic, since the spin magnetic moment of Fe is coupled antiferromagnetically to the smaller spin moment at the Mo site (Besse *et al.*, 2002). In addition evidence for a half metallic character of this material was found (Park *et al.*, 1998; Kuepper *et al.*, 2005).

With the discovery of room-temperature low field magneto resistance (LFMR) an intensified study of the magnetic and electric properties of  $\text{Sr}_2\text{FeMoO}_6$  started, since the high Curie temperature of about 420 K and the magnetoresistance (MR) make this material a promising compound for future applications in magnetoelectronics (Kobayashi *et al.*, 1998).

However, despite a lot of theoretical and experimental studies essential properties of  $\text{Sr}_2\text{FeMoO}_6$  are still under discussion, for instance the valence state of iron. The direct measurement of valence states is important, since results of other methods like magnetometry are strongly influenced by structural effects such as antisites or antiphase boundaries (Sanchez *et al.*, 2002; Fang, 2005). Probed by various techniques such as Mössbauer spectroscopy (Linden *et al.*, 2000; Balcells *et al.*, 2001; Raekers *et al.*, 2006), X-ray photoelectron (Moreno *et al.*, 2001; Kuepper *et al.*, 2004), and X-ray absorption spectroscopy (Kuepper *et al.*, 2004; Ray *et al.*, 2001; Besse *et al.*, 2002; di Trolio *et al.*, 2006), or theoretical electronic structure calculations (Kang *et al.*, 2002; Kuepper *et al.*, 2005; Kanchana *et al.*, 2007), the results for the iron valence state in  $\text{Sr}_2\text{FeMoO}_6$  differ a lot. To give just a few examples, Martinez *et al.* (2000) report the Fe valence state to be closer to  $\text{Fe}^{2+}$ , while other works determine the Fe valency to be close to  $\text{Fe}^{2+}$  with essential amounts of  $\text{Fe}^{3+}$  (Kuepper *et al.*, 2004; Besse *et al.*, 2002; Kang *et al.*, 2002; Garcia-Landa *et al.*, 1999). Then also a mixed 50%  $\text{Fe}^{2+}$ , 50%  $\text{Fe}^{3+}$  valence state is reported (Linden *et al.*, 2000; Raekers *et al.*, 2006). Finally, a large number of works measure a nearly or complete trivalent Fe valence state (Ray

*et al.*, 2001; di Trolio *et al.*, 2006; Kanchana *et al.*, 2007).

A quite complex intra- and intergrain structure on the surface of  $\text{Sr}_2\text{FeMoO}_6$  could be a reason for this discrepancies (Moreno *et al.*, 2001; Ray *et al.*, 2001; di Trolio *et al.*, 2006; Kanchana *et al.*, 2007). Also a gradual decomposition of  $\text{Sr}_2\text{FeMoO}_6$  with time into  $\text{SrMoO}_4$  has been reported, leading to a structural transformation of the system (Navarro *et al.*, 2003).

In the following Fe 2p XAS and XMCD multiplet calculations are presented and discussed together with measurements, revealing an additional ageing effect of  $\text{Sr}_2\text{FeMoO}_6$ , which could explain the various different results concerning the Fe valence state. The TT-multiplets program was used, which is based upon the methods described by Thole, van der Laan and de Groot (de Groot *et al.*, 1990a; de Groot, 2001; van der Laan *et al.*, 1992).

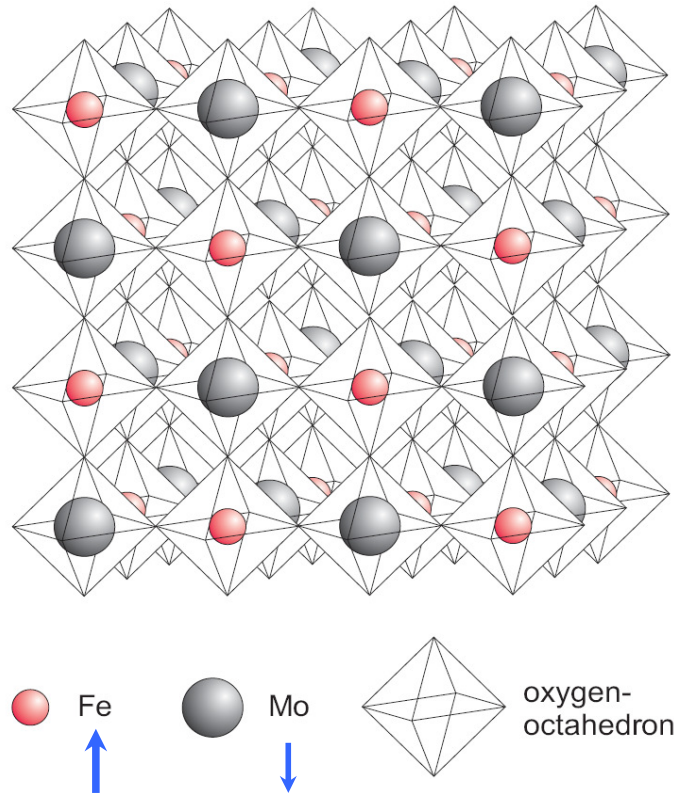


Figure 3.1: The alternating  $\text{FeO}_6$  and  $\text{MoO}_6$  octahedra in the double perovskite structure of  $\text{Sr}_2\text{FeMoO}_6$  attached from Tomioka *et al.* (2000). The Sr which is situated in-between the oxygen octahedra is omitted here for simplification. In addition the direction and strength of the ferrimagnetically coupled Fe and Mo spin magnetic moments are illustrated (blue arrows).

## 3.2 Results

High quality  $\text{Sr}_2\text{FeMoO}_6$  polycrystalline samples were produced by standard solid state reaction, in which powder was annealed at  $1200^\circ\text{C}$  in 99% Ar/1%  $\text{H}_2$ . The structural and chemical properties were probed directly after production by means of X-ray diffraction and XPS revealing a very low concentration of antisite defects ( $\approx 3\%$ ). In addition a mixed Fe valence state was found to be present in the samples comprising 70%  $\text{Fe}^{2+}$  and 30%  $\text{Fe}^{3+}$  ions (Kuepper *et al.*, 2004).

After this charge transfer multiplet calculations were done in order to confirm the metal valence state. A cubic crystal field ( $\text{O}_h$  symmetry) with a strength of  $10Dq = 0.8 \text{ eV}$  was assumed. In case of the charge transfer (CT) calculations a ligand-to-metal charge transfer between the oxygen ligands and the Fe ions is considered with a ground state containing about 85%  $3d^n$  and 15%  $3d^{n+1}\underline{L}$  character. Here  $3d^n$  stands for the occupation of the Fe 3d level and  $\underline{L}$  for an oxygen hole. All spectra were broadened with a lorentzian and a gaussian function to account for the lifetime broadening and the broadening due to the experiment. As already shown and described in chapter 2 (figure 2.15) the Fe 2p XAS and XMCD measurements were simulated by a mixture of CT multiplet calculations for  $\text{Fe}^{2+}$  and  $\text{Fe}^{3+}$  ions in different ratios.

In figure 3.2 XAS and XMCD measurements of  $\text{Sr}_2\text{FeMoO}_6$  recorded in August 2004 are presented together with calculations of two differently mixed Fe valence states. One set of spectra simulates a 70%  $\text{Fe}^{2+}$ /30%  $\text{Fe}^{3+}$  ratio, the other a valence state comprising 50%  $\text{Fe}^{2+}$  and 50%  $\text{Fe}^{3+}$  ions. The spectra are calculated with and without charge transfer (CT), respectively.

As one can see the calculations done without charge transfer (dotted lines) fit the spectra less accurate than the ones done with CT (black lines). In the XAS as well as in the XMCD calculations without CT features at about 710 eV and 723 eV photon energy occur that are not present in the measurements. These features are absent in the CT multiplet calculations, which simulate the spectra quite well. Therefore one can conclude that there is a ligand-to-metal charge transfer present in  $\text{Sr}_2\text{FeMoO}_6$ .

Furthermore as expected the shapes of the XAS and XMCD measurements reveal a mixed Fe valence state. The double peak structure of the  $\text{L}_3$ -edge clearly indicates  $\text{Fe}^{2+}$  and  $\text{Fe}^{3+}$  ions to be present (see also figure 2.15). Interestingly as can be seen in figure 3.2 the calculation of the expected 70%  $\text{Fe}^{2+}$  / 30%  $\text{Fe}^{3+}$  ratio simulates the XMCD spectrum quite well, while in case of the XAS measurement the simulated spectrum differs considerably (right panel). Here a much higher  $\text{Fe}^{3+}$  contribution is necessary to calculate the spectral shape. A XAS calculation simulating a 50%  $\text{Fe}^{2+}$  / 50%  $\text{Fe}^{3+}$  mixed valence state shows good consistency with the spectrum (figure 3.2, left panel). Therefore it seems like part of the  $\text{Fe}^{3+}$  signal visible in the XAS measurement does not contribute to the XMCD spectrum. This could be explained by an additional  $\text{Fe}^{3+}$  containing phase present in the sample that shows no macroscopic magnetic ordering or an antiferromagnetic behaviour.

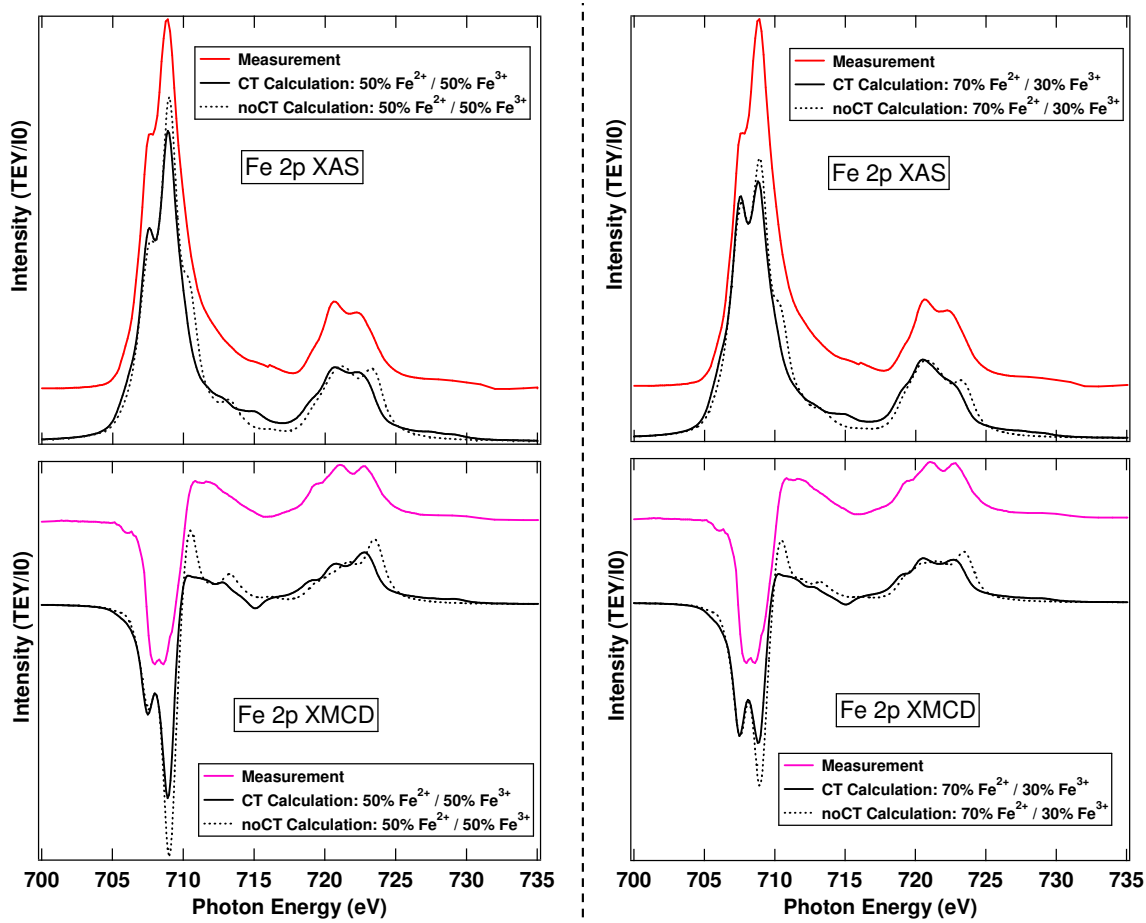


Figure 3.2: Fe 2p XAS and XMCD measurements of  $\text{Sr}_2\text{FeMoO}_6$  together with multiplet calculations. One set of calculations is done for a mixed Fe valence state comprising 50%  $\text{Fe}^{2+}$  and 50%  $\text{Fe}^{3+}$  ions (left panel) the other for a 70%  $\text{Fe}^{2+}$  / 30%  $\text{Fe}^{3+}$  ratio (right panel).

In figure 3.3 XAS and XMCD measurements of  $\text{Sr}_2\text{FeMoO}_6$  recorded in January 2004 are compared to those done in August 2004. This reveals that there is a clear temporally increase of the overall maximum at about 709 eV visible in the XAS spectrum. Comparison with figure 2.15 and 3.2 reveals that this increase can be attributed to an increase of the  $\text{Fe}^{3+}$  amount in the sample. However in the XMCD measurements no considerable change of the spectral shape is visible, which confirms the appearance of an additional non magnetic or antiferromagnetic  $\text{Fe}^{3+}$  phase in  $\text{Sr}_2\text{FeMoO}_6$ , as already assumed from multiplet calculations.

Based on these findings Kuepper *et al.* (2008) started an overwiewing investigation of XAS measurements that recured over several years. The measurements done in January 2004 and May 2005 were carried out at the Beamline for Advanced Dichroism (BACH) at Elettra, Italy. All other spectra were measured at beamlines 4.0.2 and 8.0.1 of the Advanced Light Source (ALS), Berkeley, USA. Most of the experiments were recorded in total electron yield (TEY) and therefore are to a considerable extent surface sensitive. For transition metals an electron escape depth of around 5 nm was reported (Gota *et al.*, 2000). Before every measurement a fresh piece of the same  $\text{Sr}_2\text{FeMoO}_6$ -pellet was scraped ex situ, thus the experimental conditions were

comparable for all experiments.

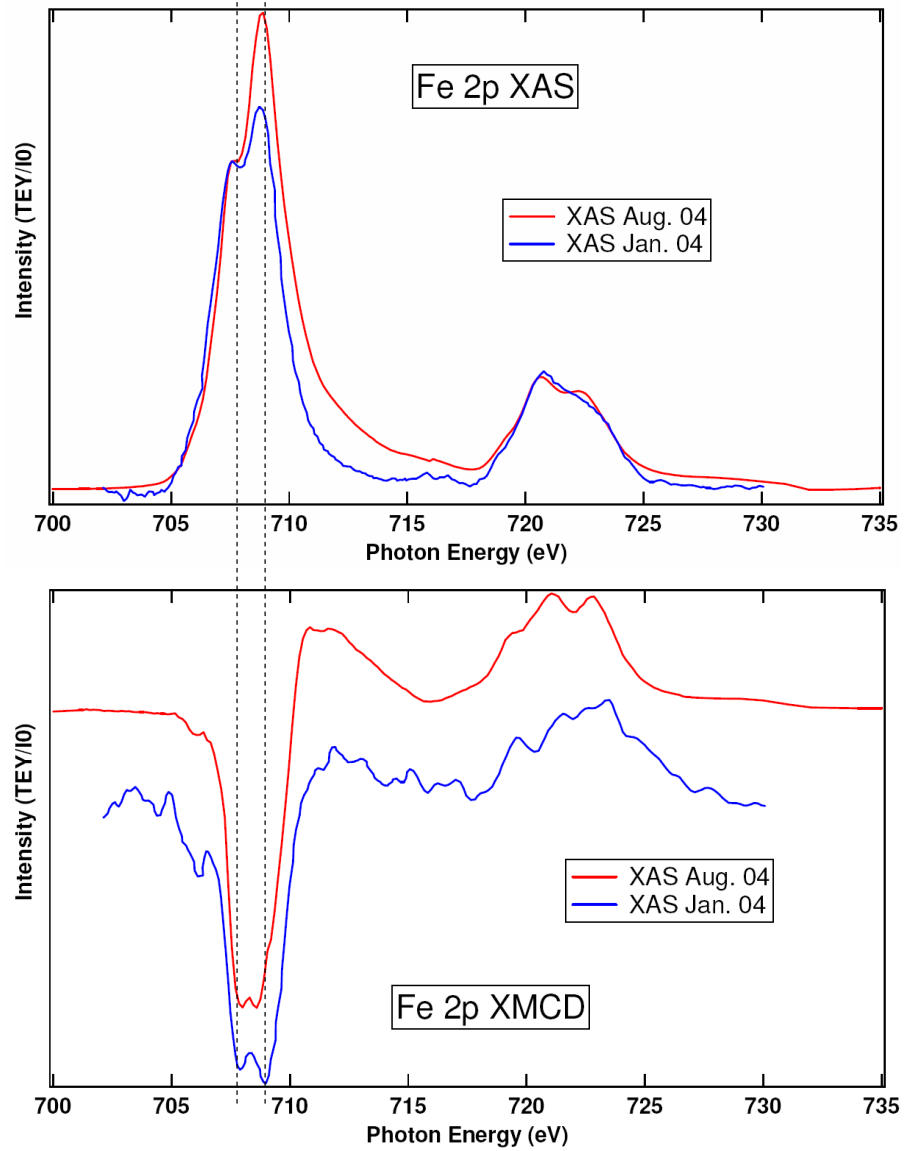


Figure 3.3: XAS (upper panel) and XMCD (lower panel) measurements of  $\text{Sr}_2\text{FeMoO}_6$  recorded in January 2004 (blue line) and August 2004 (red line).

In figure 3.4, attached from Kuepper *et al.* (2008), an overview of the XAS measurements is given. In addition to the measurements also CT multiplet calculations for different  $\text{Fe}^{2+}$  and  $\text{Fe}^{3+}$  ratios are shown. This reveals that there is a clear change in the spectral shape with time. The intensity of the total maximum at about 709 eV increases in comparison to the prepeak located around 708 eV. As already mentioned before this can be attributed to an temporally increase of the  $\text{Fe}^{3+}$  amount in the sample. This is also confirmed by the multiplet calculations, which simulate the spectra with an increase of the  $\text{Fe}^{3+}$  amount from 35% for the first measurements to 60% for the latest ones.

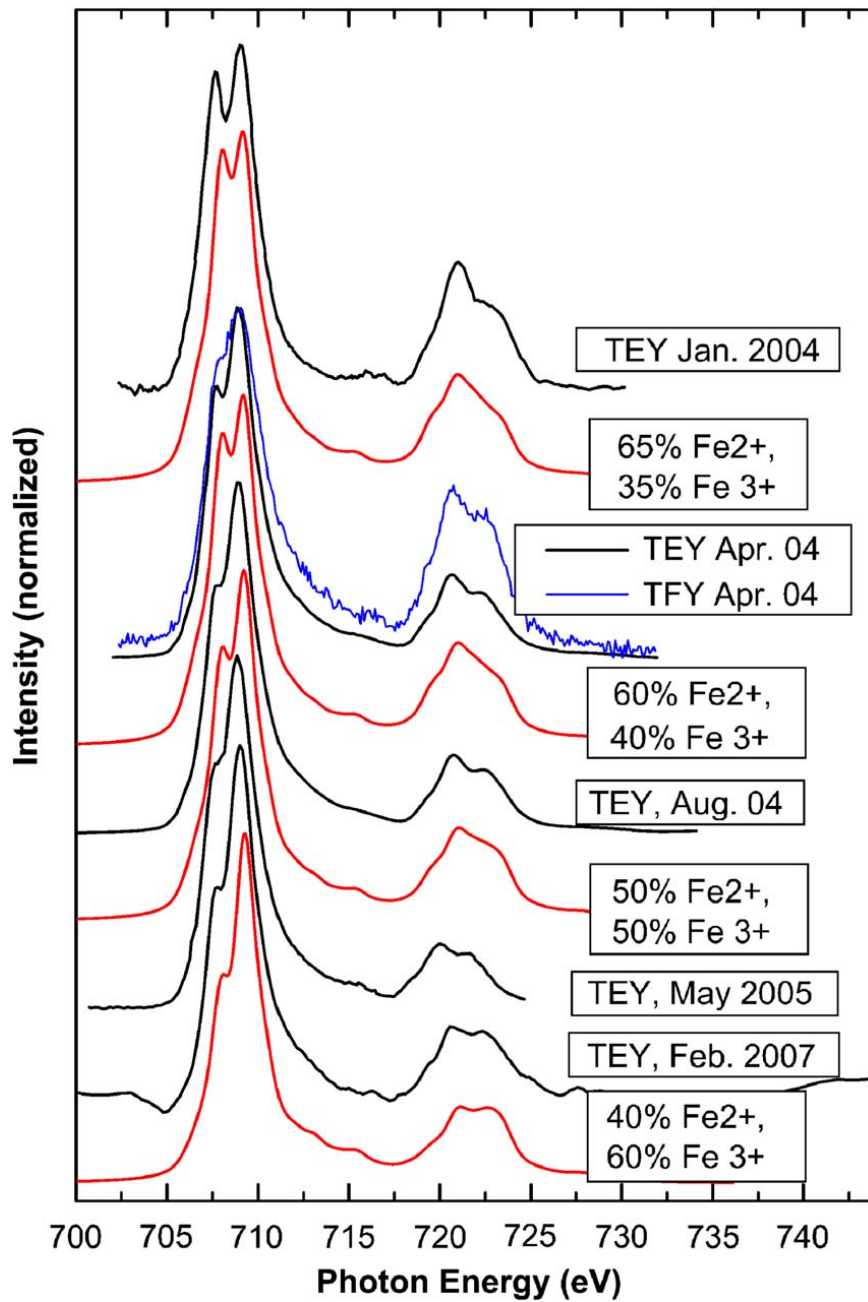


Figure 3.4: An overview of several Fe 2p XAS measurements of the *same*  $\text{Sr}_2\text{FeMoO}_6$  sample recorded over several years (black lines). It is attached from Kuepper *et al.* (2008). The date of each experiment is displayed. For one experiment a total fluorescence yield (TFY) spectrum has also been recorded (blue line). In addition CT multiplet calculations for different  $\text{Fe}^{2+}$  and  $\text{Fe}^{3+}$  ratios are shown (red lines).

Thus, an ageing effect is found changing the Fe valence state of  $\text{Sr}_2\text{FeMoO}_6$ . Note that the spectrum measured in the total fluorescence yield (TFY) mode in April 2004 seems to be less influenced by the found ageing process (figure 3.4, blue line). This indicates that the temporally changes primarily affect the surface layers of  $\text{Sr}_2\text{FeMoO}_6$ , since the TFY mode is more bulk sensitivity, with a probing depth of a few hundred nm (note that the difference in the  $L_2/L_3$  branching ratio is due to self absorption effects). Therefore in Kuepper *et al.* (2008) it was concluded that the ageing process could be due to water and oxygen. Navarro *et al.* (2003) reported a structural decomposition of polycrystalline  $\text{Sr}_2\text{FeMoO}_6$  with time into  $\text{SrMoO}_4$ . In addition  $\text{SrFeO}_{3-x}$  particles have been found in somewhat lower layers of the polycrystalline grains (Kim *et al.*, 2004), which could also explain the Fe deficiency found at  $\text{Sr}_2\text{FeMoO}_6$  surfaces (Fix *et al.*, 2007). Note that in  $\text{SrFeO}_3$  nominally  $\text{Fe}^{4+}$  ions are present. However a high amount of charge transfer  $3d^5\bar{L}$  states and the tendency to form oxygen deficient  $\text{SrFeO}_{3-x}$  could explain the enhancement of  $\text{Fe}^{3+}$ -like features in the XAS. The fact that in the XMCD measurement the increase of the  $\text{Fe}^{3+}$ -features is not visible, see figure 3.2, can be explained by the antiferromagnetic behaviour of  $\text{SrFeO}_3$  (Abbate *et al.*, 2002). An antiferromagnetic ordering would lead to the absence of an overall net-magnetic moment, which therefore would not contribute to the XMCD signal.

Interestingly evidence was found that in  $\text{Sr}_2\text{FeMoO}_6$  not a double-exchange induced colossal magnetoresistance (CMR) process is responsible for the LFMR but a tunnelling-type magnetoresistance (TMR) process through tunnel barriers formed by impurities (Kobayashi *et al.*, 1998; Saitoh *et al.*, 2002; Deb *et al.*, 2004). It is reasonable to assume that the ageing effect found here will influence the magneto resistive properties of the compound (Yuan *et al.*, 2003). Of course this has to be considered for potential future applications of  $\text{Sr}_2\text{FeMoO}_6$ .

### 3.3 Conclusion

Fe 2p XAS and XMCD multiplet calculations of the double perovskite  $\text{Sr}_2\text{FeMoO}_6$  were compared to measurements that recurred over several years. This revealed an ageing effect involving the Fe valence state. It was found that the  $\text{Fe}^{3+}$  amount in the sample seems to increase significantly with time. Since this increase is not visible in the XMCD spectra it can be assumed that the appearing  $\text{Fe}^{3+}$  phase exhibits no macroscopic magnetic ordering or is antiferromagnetic. A possible explanation could be the appearance of  $\text{SrFeO}_{3-x}$  particles in the sample (Kim *et al.*, 2004).

In  $\text{Sr}_2\text{FeMoO}_6$  not a double-exchange process is assumed to cause the LFMR, but an impurity induced tunnelling-type magnetoresistance (TMR) process (Kobayashi *et al.*, 1998; Saitoh *et al.*, 2002; Deb *et al.*, 2004). It is reasonable to assume that the ageing effect found here will have a major influence on the magnetoresistive properties of  $\text{Sr}_2\text{FeMoO}_6$  (Yuan *et al.*, 2003). Therefore this has to be considered for potential future applications. Note that also in other MR-materials impurity conduction is assumed to be present and a key property, like for example in the spinel system  $\text{Fe}_{1-x}\text{Cu}_x\text{Cr}_2\text{S}_4$  (see chapter 4).





# Chapter 4

## Valence states in $\text{Fe}_{1-x}\text{Cu}_x\text{Cr}_2\text{S}_4$

### 4.1 Introduction

The Cr based chalcogenide system  $\text{Fe}_{1-x}\text{Cu}_x\text{Cr}_2\text{S}_4$  has a normal spinel structure  $\text{AB}_2\text{X}_4$  in which X represents the sulfur, the B site is occupied by chromium and the A site a mixture of iron and copper in different concentrations. The Cr is surrounded by sulfur in an octahedral symmetry while Fe and Cu are surrounded tetrahedral. The unit cell is basically consisting of two atomic structures indicated by the black and the orange cubes in figure 4.1. The shown arrangement of four of these structures, respectively, represents the unit cell. The Fe and Cr spin magnetic moments couple ferromagnetic among themselves, while they are antiferromagnetic coupled between each other. The latter can for example be proven with a XMCD measurement. In figure 4.14 this is shown for  $\text{Fe}_{0.5}\text{Cu}_{0.5}\text{Cr}_2\text{S}_4$ , but can also be seen for other Cu substitutions (Han *et al.*, 2006).

During the last years  $\text{Fe}_{1-x}\text{Cu}_x\text{Cr}_2\text{S}_4$  ( $0 \leq x \leq 1$ ) has attracted considerable attention due to a variety of interesting electronic and magnetic properties including colossal negative magnetoresistance, semiconducting behaviour, and room temperature spontaneous magnetism (Ramirez *et al.*, 1997).

For  $x = 0$  and  $0.5$  the materials are respectively p- and n-type semiconducting ferromagnets (Lotgering *et al.*, 1969), whereas  $\text{CuCr}_2\text{S}_4$  ( $x = 1$ ) is a ferromagnetic metal (Haacke and Beegle, 1967). A very large negative magnetoresistance (MR) effect comparable to the colossal magnetoresistance (CMR) in perovskites was reported in  $\text{Fe}_{1-x}\text{Cu}_x\text{Cr}_2\text{S}_4$  ( $x = 0, 0.5$ ). This effect occurs together with a metal-to-insulator (M–I) crossover near the magnetic transition temperature  $T_C$ . On further cooling the resistivity  $\rho(T)$  recovers the insulating behaviour far below  $T_C$  (Ramirez *et al.*, 1997; Watanabe and Nakada, 1978). The temperature range of the metallic features of  $\rho(T)$  is wider for  $x = 0.5$  than for  $x = 0$ . The M–I crossover occurs together with the magnetic transition also for  $0.1 \leq x < 0.5$ . With increasing substitution  $x$  in  $\text{Fe}_{1-x}\text{Cu}_x\text{Cr}_2\text{S}_4$ , the value of  $T_C$  increases monotonically, whereas the room temperature resistivity and the MR change non-monotonously exhibiting a minimum near  $x = 0.2$  and maximum at  $x = 0.5$  (Lotgering *et al.*, 1969; Haacke and Beegle, 1967; Ando *et al.*, 1979; Fritsch *et al.*, 2003). For  $x > 0.5$  both the resistivity and the MR decrease monotonically.  $\text{CuCr}_2\text{S}_4$  shows a ferromagnetic order with a Curie temperature of 377 K well above the room temperature (Kimura *et al.*, 2001).

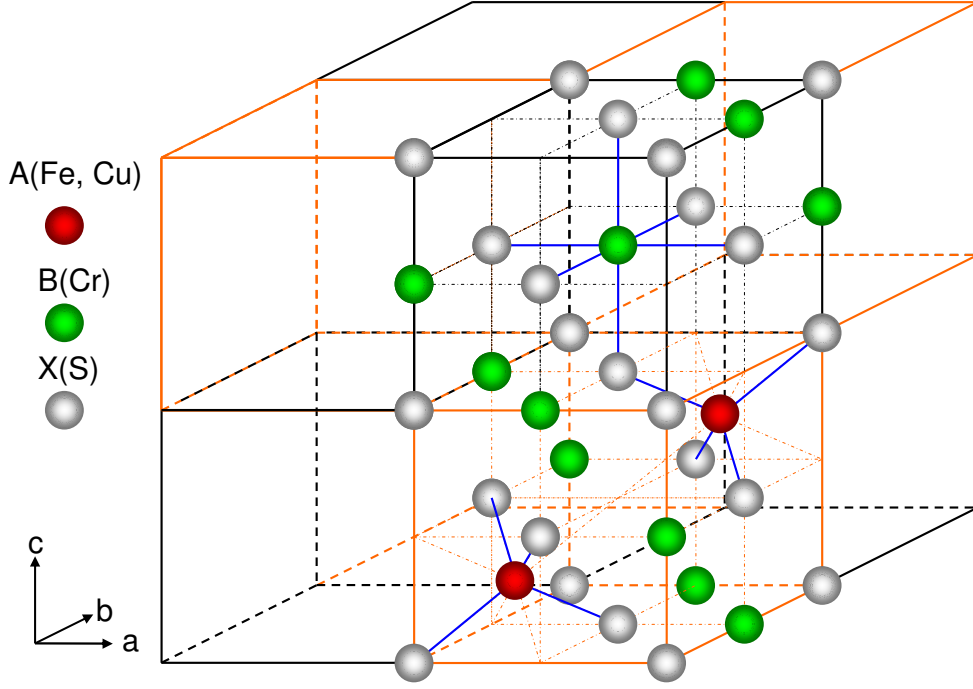


Figure 4.1: The unit cell of the spinel  $\text{Fe}_{1-x}\text{Cu}_x\text{Cr}_2\text{S}_4$ . The black and orange cubes all contain the same atomic structure. It is omitted here for simplification. The blue lines indicate the octahedral symmetry of the Cr-site and the tetrahedral symmetry of the mixed Cu-Fe site, respectively.

One of the long-standing problems in  $\text{Fe}_{1-x}\text{Cu}_x\text{Cr}_2\text{S}_4$  that is under continuous debates is related to the charge and valence state of the Fe and Cu ions. To get a clear answer on this problem is very important in view of elucidating the origin of the colossal magnetoresistance and the M–I transition found in these materials. While for  $x = 0$  the nominal valence state is considered as  $\text{Fe}^{2+}\text{Cr}_2^{3+}\text{S}_4^{2-}$ , for  $\text{CuCr}_2\text{S}_4$  ( $x = 1$ ) two competing models have been proposed. In the model of Goodenough (1969) divalent Cu ions and trivalent Cr ions are suggested. In contrast, in the Lotgering–van Stapele model (Lotgering and van Stapele, 1967) the Cu ions are expected to be monovalent and the Cr ions to be in a mixed valence state:

$$\text{Goodenough model : } \text{Cu}^{2+}\text{Cr}_2^{3+}\text{S}_4^{2-} \quad (4.1)$$

$$\text{Lotgering model : } \text{Cu}^+[\text{Cr}^{3+}\text{Cr}^{4+}]\text{S}_4^{2-} \quad (4.2)$$

Later on, Lotgering et al. (Lotgering *et al.*, 1969) also postulated  $\text{Cu}^+$  ions to be present in  $\text{Fe}_{1-x}\text{Cu}_x\text{Cr}_2\text{S}_4$  ( $0 \leq x \leq 1$ ) leading to the following valence configurations:

$$\text{Fe}_{1-2x}^{2+}\text{Fe}_x^{3+}\text{Cu}_x^+[\text{Cr}_2^{3+}]\text{S}_4^{2-} \quad \text{for} \quad 0 \leq x \leq \frac{1}{2} \quad (4.3)$$

$$\text{Fe}_{1-x}^{3+}\text{Cu}_x^+[\text{Cr}_2^{3+}]\text{S}_{5-2x}^{2-}\text{S}_{2x-1}^- \quad \text{for} \quad \frac{1}{2} \leq x \leq \frac{1+\delta_0}{2} \quad (4.4)$$

$$\text{Fe}_{1-x}^{3+}\text{Cu}_x^+[\text{Cr}_{3-2x+\delta_0}^{3+}\text{Cr}_{2x-1-\delta_0}^{4+}]\text{S}_{4-\delta_0}^{2-}\text{S}_{\delta_0}^- \quad \text{for} \quad \frac{1+\delta_0}{2} \leq x \leq 1 \quad (4.5)$$

Here  $S^-$  represents a hole in the valence band and  $\delta_0$  an unknown parameter. The Lotgering model starts at  $x = 0$  with the valence state  $\text{Fe}^{2+}\text{Cr}_2^3+\text{S}_4^{2-}$ . With increase of the monovalent Cu concentration  $x$  the Fe ions are expected to change their valence state gradually to  $\text{Fe}^{3+}$ . For  $x = 0.5$  all Fe ions are predicted to be trivalent (equation 4.3). If the Cu concentration increases further ( $x > 0.5$ ) S is expected to exhibit holes in the 3p band ( $S^-$ ) to achieve charge neutrality (equation 4.4). At last for very high Cu concentrations that exceed an unknown threshold ( $\frac{1+\delta_0}{2}$ ), the Cr ions are predicted to become partially  $\text{Cr}^{4+}$  (equation 4.5).

To explain the magnetoresistance in  $\text{Fe}_{1-x}\text{Cu}_x\text{Cr}_2\text{S}_4$  one can consider the double-exchange (DE) interaction mechanism like in colossal magnetoresistive (CMR) perovskite manganites. But unlike in manganites, magnetic ions in spinels occupy two different sites, tetrahedral ( $T_d$ ) and octahedral ( $O_h$ ). Therefore the DE process in spinels has to be modified. This problem was discussed by Palmer and Greaves (1999) within the so called tripleexchange (TE) model. The TE process considers a mixed Fe valence state to be present in the chalcogenide system. In figure 4.2 a channel of the tripleexchange interaction between  $\text{Fe}^{2+}$  and  $\text{Fe}^{3+}$  ions in  $\text{Fe}_{1-x}\text{Cu}_x\text{Cr}_2\text{S}_4$  is illustrated.

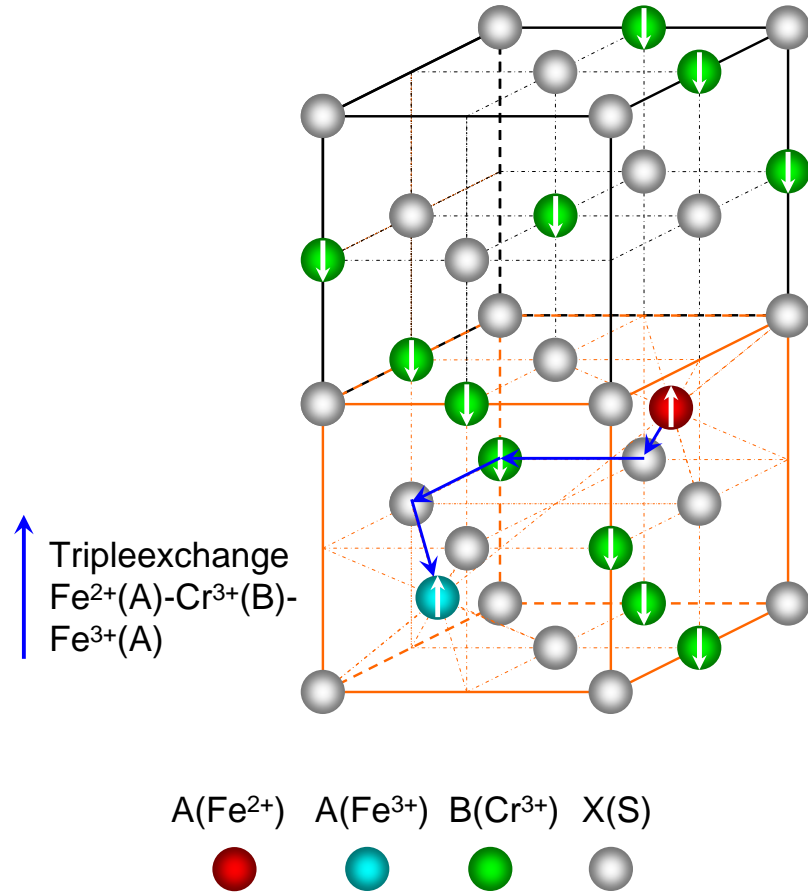


Figure 4.2: Illustration of a channel of the tripleexchange interaction in  $\text{Fe}_{1-x}\text{Cu}_x\text{Cr}_2\text{S}_4$ . Here only the main part of the unit cell is shown. The spin direction is indicated by white arrows.

A band-structure picture of the TE reproduced from Fritsch *et al.* (2003) is shown in figure 4.3. Like the double-exchange the TE process consists of an electron hopping between metallic ions over a non-metallic ligand. But in contrast to the DE in the TE also a third metallic ion is involved. As can be seen in figure 4.3 in the for  $\text{Fe}_{1-x}\text{Cu}_x\text{Cr}_2\text{S}_4$  assumed tripleexchange process a single electron from the  $\text{Fe}^{2+}$  spin-up  $e_g$  band is transferred via a p-orbital of the sulphur to an empty spin-up  $e_g$  band of the  $\text{Cr}^{3+}$ . From the temporary divalent Cr the electron proceeds via a second S to an empty spin-up  $e_g$  state of the  $\text{Fe}^{3+}$ . The antiferromagnetic alignment of the Cr and Fe spin magnetic moments is essential for the TE, since otherwise the opposite spin directions of the mobile Fe electron and the empty state of Cr would make a hopping impossible.

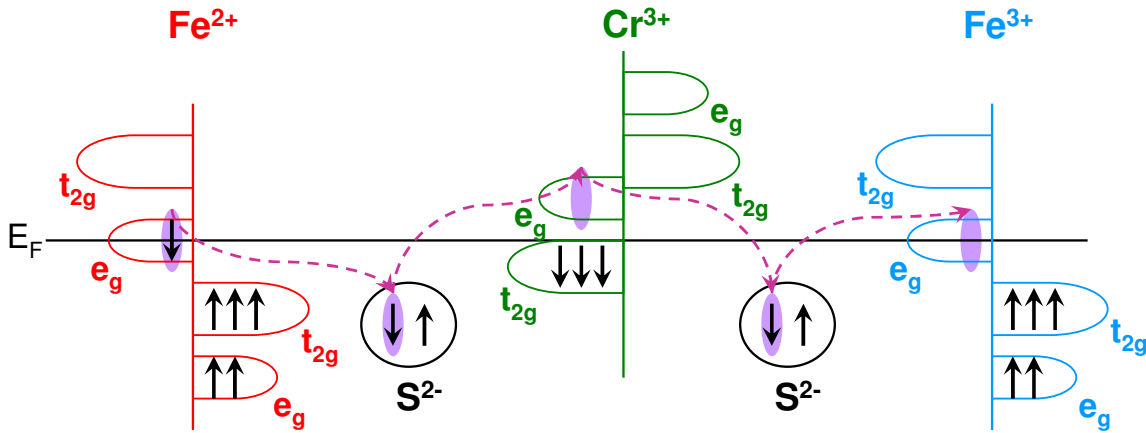


Figure 4.3: Tripleexchange process in  $\text{Fe}_{1-x}\text{Cu}_x\text{Cr}_2\text{S}_4$  reproduced from Fritsch *et al.* (2003). The rough bandpositions are adopted from band-structure calculations of Park *et al.* (1999). The mobile electrons and empty states, in which they are hopping, are indicated by the violet spheres.

In another model exchange interactions are assumed to be the dominant magnetic interaction and responsible for the magnetism in  $\text{Fe}_{1-x}\text{Cu}_x\text{Cr}_2\text{S}_4$  (Kim *et al.*, 1993; Son *et al.*, 2005; Kim *et al.*, 2002; Tsurkan *et al.*, 2005). Here the Fe ions are not expected to be in a mixed valence state, but either in a  $\text{Fe}^{3+}$  or in a  $\text{Fe}^{2+}$  state. Concerning the M-I crossover and MR of chalcogenide spinels beside the tripleexchange model various other models are introduced in the literature involving interactions of local magnetic moments and charge carriers, which alter the carrier density and/or mobility. Again a mixed Fe valence state is not necessary in these models, which will be discussed in the section 4.4 below in more detail.

Here it becomes clear that the determination of the ion valence states in  $\text{Fe}_{1-x}\text{Cu}_x\text{Cr}_2\text{S}_4$  is essential in order to elucidate the magnetism, conductivity and MR behaviour of this chalcogenide system. The valence state of the constituent elements in  $\text{Fe}_{1-x}\text{Cu}_x\text{Cr}_2\text{S}_4$  was investigated by many authors using various methods. However, many controversial results were reported and interpreted within the mutual exclusive models.

Yokoyama *et al.* (1967) investigated the NMR spectra of  $\text{CuCr}_2\text{S}_4$  ( $x = 1$ ) and concluded that all Cr ions are in a trivalent state. Magnetic and XPS measurements

of the single crystalline  $\text{CuCr}_2\text{Se}_4$ , very similar to  $\text{CuCr}_2\text{S}_4$ , support this conclusion (Nakatani *et al.*, 1978; Tsurkan *et al.*, 2000). In addition, neutron diffraction measurements indicate the presence of  $\text{Cr}^{3+}$  and  $\text{Cu}^+$  ions in the crystal (Colominas, 1967; Robbins *et al.*, 1967). At the same time, the NMR measurements performed by Kovtun *et al.* (1977, 1978) were interpreted assuming a mixed tetra- and trivalent valence state of chromium, supported by investigations of cation–anion distances (Riedel and Horvath, 1973). Neutron diffraction studies of  $\text{CuCr}_2\text{Se}_4$  (Yamashita *et al.*, 1979) also revealed the presence of monovalent Cu ions, while the Cr ions were shown to be in a mixed valence state. Kimura *et al.* (2001) found an indication of a small amount of  $\text{Cu}^{2+}$  in this compound. Finally, a temperature dependence of the Cu and Cr valences was suggested by neutron diffraction studies (Kovtun *et al.*, 1979).

In case of pure  $\text{FeCr}_2\text{S}_4$  ( $x = 0$ ) the experimental results are quite consistent. XPS (Tsurkan *et al.*, 2000; Kurmaev *et al.*, 2000), Mössbauer (van Diepen and van Staple, 1973; Spender and Morrish, 1972; Klencsar *et al.*, 2002), and XAS measurements of  $\text{Fe}_{0.9}\text{Cu}_{0.1}\text{Cr}_2\text{S}_4$  with composition close to stoichiometric  $\text{FeCr}_2\text{S}_4$  (Han *et al.*, 2006) revealed the presence of  $\text{Fe}^{2+}$  and  $\text{Cr}^{3+}$  ions. This is supported by neutron powder diffraction (Kim *et al.*, 2002; Kurmaev *et al.*, 2000; Shirane *et al.*, 1964) and magnetic measurements (Haacke and Beegle, 1967; Shirane *et al.*, 1964). The fact that the results of neutron diffraction show strong variations and the saturation magnetic moment is lower than the theoretically expected value of  $2\mu_B$  for the antiferromagnetic arrangement of spins of the  $\text{Cr}^{3+}$  and  $\text{Fe}^{2+}$  ions is explained by covalent bonding or hybridization effects (Han *et al.*, 2006; Nath *et al.*, 2002).

For  $\text{Fe}_{0.5}\text{Cu}_{0.5}\text{Cr}_2\text{S}_4$  ( $x = 0.5$ ) the situation is even more different. While the Mössbauer experiments revealed the Fe ions to be completely in a trivalent state (Son *et al.*, 2005; Klencsar *et al.*, 2005), the X-ray absorption (XAS) and X-ray emission (XPS) studies showed that the Fe ions remain divalent (Kurmaev *et al.*, 2000; Han *et al.*, 2006). Only Deb *et al.* (2003) reported the XAS spectrum for  $\text{Fe}^{3+}$  ions. Furthermore, XPS and XAS experiments suggest a trivalent state for the Cr ions and a monovalent state for the Cu ions (Tsurkan *et al.*, 2000; Kurmaev *et al.*, 2000; Han *et al.*, 2006). X-ray magnetic circular dichroism (XMCD) measurements of  $\text{Fe}_{0.5}\text{Cu}_{0.5}\text{Cr}_2\text{S}_4$  confirm an antiferromagnetic coupling of the Fe and Cr ions, revealing the spectra typical for divalent Fe ions (Han *et al.*, 2006; Deb *et al.*, 2003; Kang *et al.*, 2007). Neutron powder diffraction (Palmer and Greaves, 1999; Son *et al.*, 2005; Lang *et al.*, 2000) and magnetic measurements (Son *et al.*, 2005; Tsurkan *et al.*, 2005; Deb *et al.*, 2002) support the presence of  $\text{Cr}^{3+}$  and  $\text{Fe}^{3+}$  ions in  $\text{Fe}_{0.5}\text{Cu}_{0.5}\text{Cr}_2\text{S}_4$ , but again the results vary significantly. Their variation is explained by strong covalent bonding, metallic hybridized state or spin canting of the Fe ions (Palmer and Greaves, 1999; Han *et al.*, 2006; Deb *et al.*, 2003; Lang *et al.*, 2000). In addition, due to deviation from the stoichiometry often observed in ternary chalcogenides, certain sample dependence cannot be excluded. Palmer and Greaves (1999) determined from the neutron diffraction that the Fe and Cu ions order over the tetrahedral sites in the space group  $F\bar{4}3m$ . Later on, Lang *et al.* (2000) were unable to establish such ordering and suggested that it could depend on the sample preparation. Furthermore, Tsurkan *et al.* (2005) showed that the significant differences between the properties of the single and polycrystalline samples of  $\text{Fe}_{1-x}\text{Cu}_x\text{Cr}_2\text{S}_4$  concerning their Curie temperature and saturation magnetization are related to deviation from the stoichiometry.

Summarizing, one can state that the experimental results are rather contradictory, sometimes even when they are obtained with the same methods. In order to understand the reason for these discrepancies and to get reliable information about the valence states in  $\text{Fe}_{1-x}\text{Cu}_x\text{Cr}_2\text{S}_4$  single crystalline samples of various composition and different treatment were studied.

In the following XAS, XPS and XMCD measurements of single crystalline  $\text{Fe}_{0.5}\text{Cu}_{0.5}\text{Cr}_2\text{S}_4$  grown by bromine and XPS measurements of single crystalline  $\text{Fe}_{1-x}\text{Cu}_x\text{Cr}_2\text{S}_4$  ( $x = 0.2, 0.5, 0.6, 0.9$ ) grown using chlorine are presented and discussed. The results indicate that over the whole substitution range in the  $\text{Fe}_{1-x}\text{Cu}_x\text{Cr}_2\text{S}_4$  system, the Cu ions stay mainly monovalent and the Cr ions remain trivalent. Furthermore, a comparison with literature data reveals that a small amount of  $\text{Cu}^{2+}$  found in  $\text{Fe}_{0.5}\text{Cu}_{0.5}\text{Cr}_2\text{S}_4$  is sample dependent and therefore is most likely related to an impurity phase. In addition, it is shown that an impurity phase containing  $\text{Fe}^{3+}$  is present in air treated  $\text{Fe}_{0.5}\text{Cu}_{0.5}\text{Cr}_2\text{S}_4$ , while only the lines attributed to  $\text{Fe}^{2+}$  remain in vacuum cleaned samples.

## 4.2 Experimental Details

Single crystals of  $\text{Fe}_{1-x}\text{Cu}_x\text{Cr}_2\text{S}_4$  were grown by the chemical transport reactions method with chlorine (using anhydrous  $\text{CrCl}_3$  or ultra-dry  $\text{TeCl}_4$  compounds) and bromine as the transport agents. The polycrystalline  $\text{Fe}_{1-x}\text{Cu}_x\text{Cr}_2\text{S}_4$  prepared by solid state reaction from the high-purity elements (99.99% and 99.999%) was used as a starting material for the single crystal growth. The composition and phase homogeneity of the samples was checked by the wave-length dispersive electron-probe microanalysis (EPMA) and X-ray diffraction. EPMA studies of the crystals prepared by chlorine revealed a small amount of the halogen which substitutes the sulfur ions due to close ionic radius of these anions (Tsurkan *et al.*, 2005). No halogen contamination was detected in crystals grown with bromine. The X-ray photoemission spectra were measured in ultra-high vacuum (UHV) at the University of Osnabrück with a PHI 5600ci multitechnique spectrometer. The samples were radiated with monochromatic Al  $K_\alpha$  radiation giving an overall resolution of about 0.4 eV. The X-ray magnetic circular dichroism spectrum was measured at beamline 4.0.2 of the Advanced Light Source (ALS) in Berkeley, USA, at a temperature of 80 K and a magnetic field of 0.5 T. The X-ray absorption measurements were performed at beamline 4.0.2 of the ALS and the RG-beamline at the BESSY II in Berlin. Furthermore the XAS spectra presented in figure 4.11 were measured in cooperation with the working group of Prof. Dr. Tjeng from the University of Köln at the NSRRC in Taiwan. All the following spectra were measured in the total electron yield (TEY) mode. To get a surface free of contamination, the samples were fractured in-situ directly prior to the experiment unless otherwise noted.

## 4.3 Results

This section deals with the results found during the investigation of the Cr-, Cu- and Fe-valence states in the chalcogenide spinel system  $\text{Fe}_{1-x}\text{Cu}_x\text{Cr}_2\text{S}_4$ . As

mentioned before Lotgering (equation 4.2) and Goodenough (equation 4.1) presented two contrary models describing the valence states in  $\text{CuCr}_2\text{S}_4$ . In addition Lotgering predicted valence state changes in  $\text{Fe}_{1-x}\text{Cu}_x\text{Cr}_2\text{S}_4$  with increasing Cu substitution  $x$  (equation 4.3 - 4.5). In the following these models will be compared to measurement results, literature data and calculations in order to solve the long-standing valence problem.

### 4.3.1 Investigation of the Cr valence

Goodenough predicted  $\text{Cr}^{3+}$  ions to be present in  $\text{CuCr}_2\text{S}_4$  (equation 4.1), while Lotgering assumed the Cr-ions to be in a mixed  $\text{Cr}^{3+}$  -  $\text{Cr}^{4+}$  state (equation 4.2). According to Lotgering with increasing Cu substitution  $x$  in  $\text{Fe}_{1-x}\text{Cu}_x\text{Cr}_2\text{S}_4$  the Cr valence will change from  $\text{Cr}^{3+}$  at lower  $x$  to a  $\text{Cr}^{3+}$  -  $\text{Cr}^{4+}$  mixing for high Cu concentrations (equation 4.3 - 4.5).

In Fig. 4.4 Cr 2p XPS spectra of  $\text{Fe}_{1-x}\text{Cu}_x\text{Cr}_2\text{S}_4$  ( $x = 0.2, 0.5, 0.6, 0.9$ ) are given. As can be seen neither the spectral shape nor the binding energy of the Cr 2p lines change with the Cu substitution, indicating the Cr ions to stay in the same valence state.

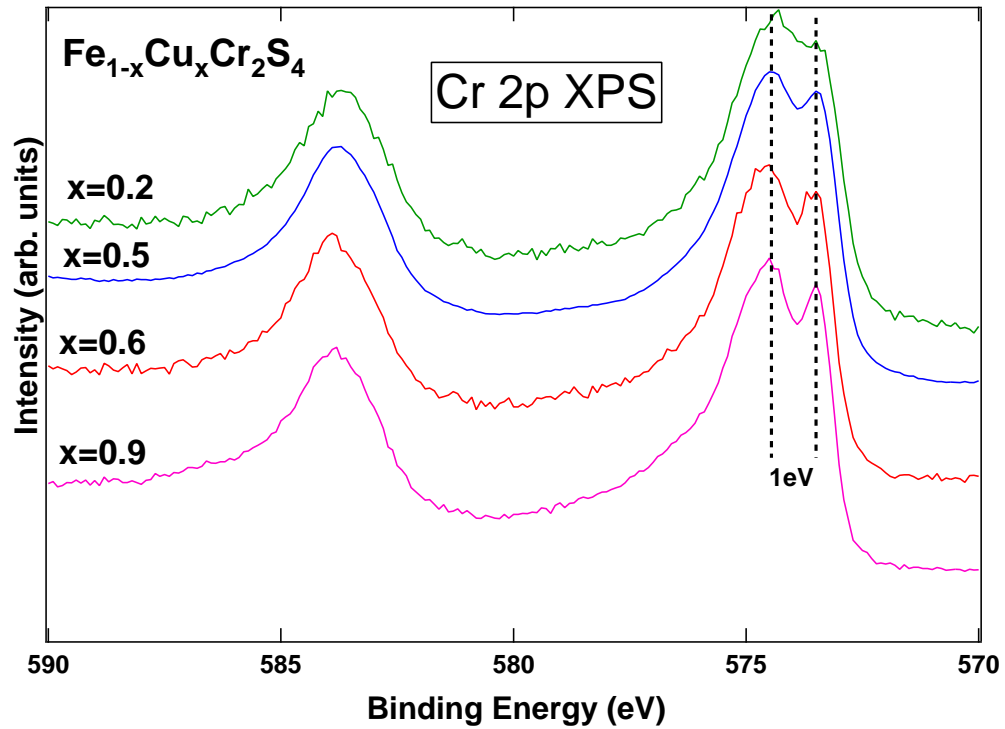


Figure 4.4: Cr 2p XPS spectra of  $\text{Fe}_{1-x}\text{Cu}_x\text{Cr}_2\text{S}_4$  with different Cu concentrations.

In addition in all spectra a clear splitting of the Cr  $2p_{3/2}$  line can be observed. This splitting is considered to be proportional to the local magnetic moment (Tsurkan *et al.*, 2000). The Cr  $2p_{3/2}$  splitting is about 1 eV for all  $x$ , which is attributed to a local Cr magnetic moment of about  $3\mu_B$  ( $\text{Cr}^{3+}$ ). Since also for  $\text{CuCr}_2\text{S}_4$  ( $x = 1$ )

many investigations show Cr to be in a trivalent valence state (Yokoyama *et al.*, 1967; Nakatani *et al.*, 1978; Tsurkan *et al.*, 2000; Colominas, 1967; Robbins *et al.*, 1967), one can conclude that in contrast to the Lotgering model the Cr ions stay trivalent for all Cu substitutions. Here the Goodenough model seems to be correct.

### 4.3.2 Investigation of the Cu valence

According to Goodenough the Cu ions in  $\text{CuCr}_2\text{S}_4$  are divalent (equation 4.1), while Lotgering predicted monovalent Cu to be present (equation 4.2). Furthermore in the Lotgering model Cu stays monovalent in  $\text{Fe}_{1-x}\text{Cu}_x\text{Cr}_2\text{S}_4$  for all Cu substitutions  $x$  (equation 4.3 - 4.5).

Figure 4.5 shows the Cu 3s XPS spectra of  $\text{Fe}_{1-x}\text{Cu}_x\text{Cr}_2\text{S}_4$  ( $x = 0.2, 0.5, 0.6, 0.9$ ) together with reference spectra of single crystalline CuO (formally  $\text{Cu}^{2+}$ ) and ceramic  $\text{Cu}_2\text{O}$  (formally  $\text{Cu}^+$ ). It is found that for different concentrations  $x$  the spectral shape does not change, indicating that the Cu ions stay in the same valence state. It is well established that the spectral splitting of the 3s XPS corelevel spectra of transition metals originates from the exchange coupling between the 3d electrons and the 3s hole created in the photoemission process. The 3s splitting is related to the total spin of the 3d electrons (van Vleck, 1934) and therefore from its value one can get information about the electronic configuration of the transition metal. Since there is no Cu 3s exchange splitting visible, one can conclude that most of the Cu ions are in a diamagnetic  $3d^{10}$  ( $\text{Cu}^+$ ) electronic configuration.

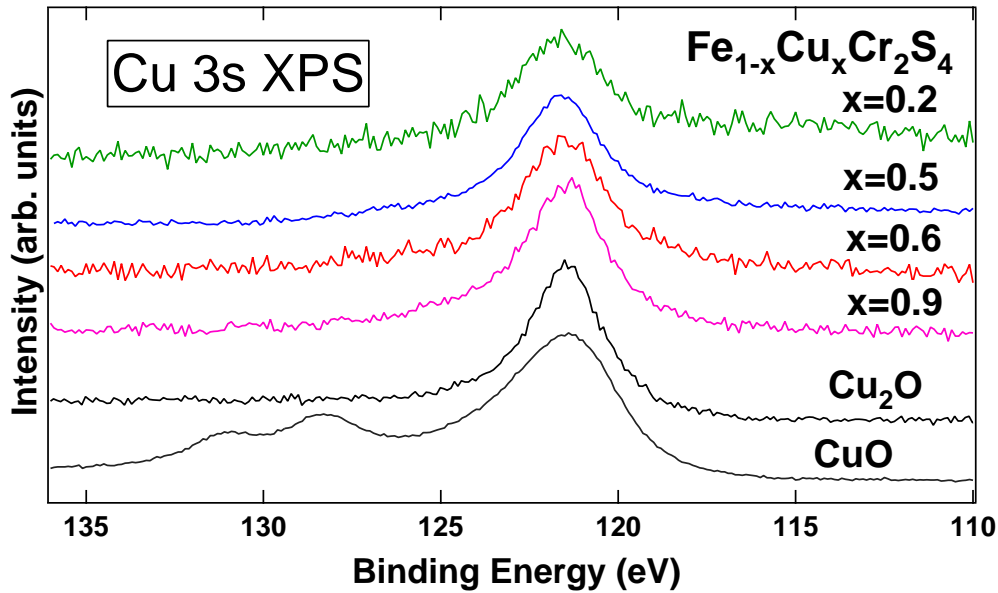


Figure 4.5: Cu 3s XPS spectra of  $\text{Fe}_{1-x}\text{Cu}_x\text{Cr}_2\text{S}_4$  with different Cu concentrations compared to ceramic  $\text{Cu}_2\text{O}$  (formally  $\text{Cu}^+$ ) and single crystalline  $\text{CuO}$  (formally  $\text{Cu}^{2+}$ ) reference spectra.

In spite of this there are hints that a small amount of  $\text{Cu}^{2+}$  can be present in this spinel system. Figure 4.6 compares a measured Cu 2p XAS spectrum of



$\text{Fe}_{0.5}\text{Cu}_{0.5}\text{Cr}_2\text{S}_4$  to those of reference compounds, namely single crystalline  $\text{CuO}$  (formally  $\text{Cu}^{2+}$ ) and  $\text{Cu}_2\text{O}$  (formally  $\text{Cu}^+$ ). In addition, another  $\text{Cu}$  2p XAS spectrum of a  $\text{Fe}_{0.5}\text{Cu}_{0.5}\text{Cr}_2\text{S}_4$  single crystal taken from Deb *et al.* (2003) is shown. The comparison of the measured spectrum with the reference measurements reveals that most of the  $\text{Cu}$  ions are monovalent as indicated by the large peak B in the  $\text{Cu}$  2p XAS spectrum of  $\text{Fe}_{0.5}\text{Cu}_{0.5}\text{Cr}_2\text{S}_4$ . Peaks C and D are considered to originate from hybridized ground and final states of the  $\text{Cu}^+$  ions (Han *et al.*, 2006; van der Laan *et al.*, 2002). At the same time, a small peak at lower photon energies is observed (peak A). This peak can be assigned to a small amount of  $\text{Cu}^{2+}$  ions. Comparison with the data measured by Deb *et al.* (2003) suggests that peak A is sample dependent. This peak is much weaker in the measured spectrum than in the measurement presented by Deb *et al.* (2003), indicating a lower amount of  $\text{Cu}^{2+}$  ions in the investigated sample. Therefore peaks C and D are increased in the present measurement due to the higher amount of  $\text{Cu}^+$  ions in the sample. The fact that peak A shows a small XMCD signal (Deb *et al.*, 2003) supports the assumption that it represents divalent  $\text{Cu}$  ions. The difference of the  $\text{Cu}^{2+}$  amount in the two measurements could be explained by an additional impurity phase, possibly due to oxidation. Thus, the formation of this phase could be dependent on the sample age and/or treatment.

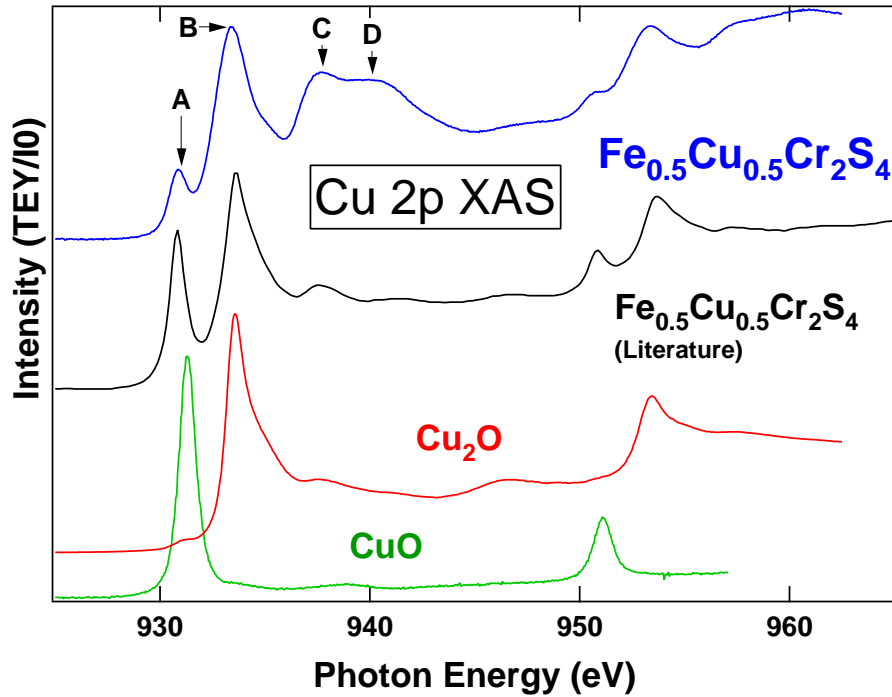


Figure 4.6:  $\text{Cu}$  2p XAS spectrum of  $\text{Fe}_{0.5}\text{Cu}_{0.5}\text{Cr}_2\text{S}_4$  (blue line) compared with a spectrum taken from Deb *et al.* (2003) (black line) and reference measurements of single crystalline  $\text{Cu}_2\text{O}$  (formally  $\text{Cu}^+$ ) and  $\text{CuO}$  (formally  $\text{Cu}^{2+}$ ).

Such an impurity phase containing divalent  $\text{Cu}$  in a monovalent  $\text{Cu}$  system could be verified for  $\text{Cu}_2\text{O}$ , which supports the assumptions above. Single crystalline  $\text{Cu}_2\text{O}$

samples subjected to different treatment were investigated by means of X-ray absorption. Figure 4.7 shows Cu 2p XAS spectra of in situ cleaned  $\text{Cu}_2\text{O}$  (formally  $\text{Cu}^+$ ) and  $\text{CuO}$  (formally  $\text{Cu}^{2+}$ ) together with measurements of  $\text{Cu}_2\text{O}$  single crystals in different states of the cleaning process. One sample was not cleaned in situ prior to the measurement, the other one was cleaned inadequately. The spectra of these samples show prepeaks A and A\* that decrease with further cleaning of the samples. Comparison with the  $\text{CuO}$  measurement reveals that these features result from an  $\text{Cu}^{2+}$  phase, that most likely form on the sample surface due to oxidation. It is possible that such a valence instability of the Cu-ions is also present in  $\text{Fe}_{0.5}\text{Cu}_{0.5}\text{Cr}_2\text{S}_4$ .

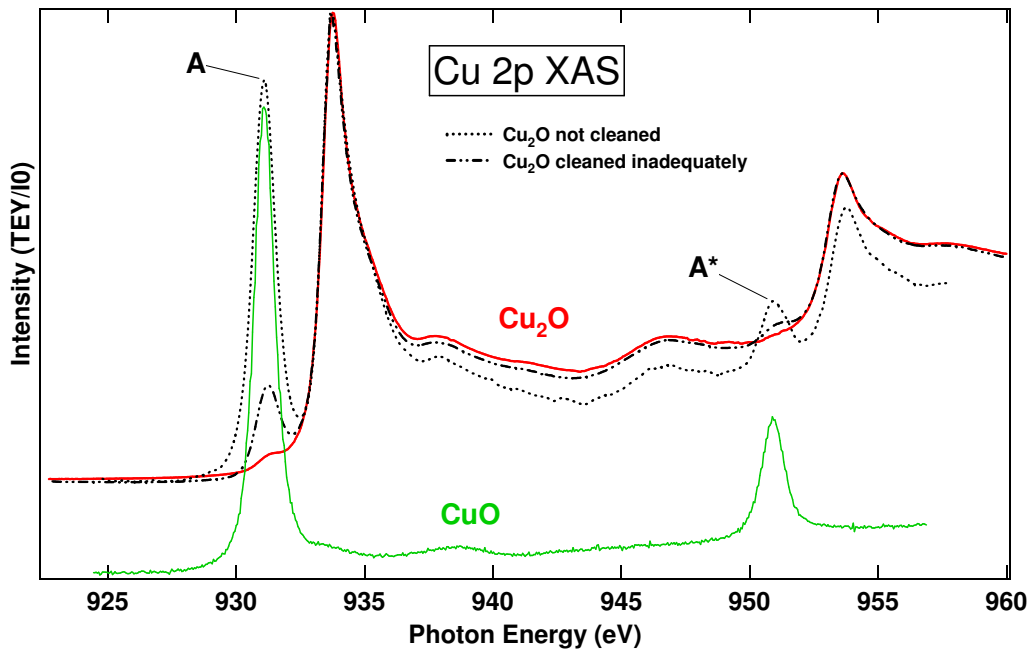


Figure 4.7: Cu 2p XAS spectra of in situ cleaned single crystalline  $\text{Cu}_2\text{O}$  (formally  $\text{Cu}^+$ ) (red line) and  $\text{CuO}$  (formally  $\text{Cu}^{2+}$ ) (green line) together with measurements of single crystalline  $\text{Cu}_2\text{O}$  that was not cleaned and one that was cleaned inadequately (dotted lines).

Since also measurements of the mothercompound  $\text{CuCr}_2\text{S}_4$  show  $\text{Cu}^+$  ions (Colomina, 1967; Robbins *et al.*, 1967; Yamashita *et al.*, 1979), one can conclude that in contrast to the Goodenough model in the bulk of  $\text{Fe}_{1-x}\text{Cu}_x\text{Cr}_2\text{S}_4$  Cu stays monovalent for all  $x$ .  $\text{Cu}^{2+}$  seems to be present in this chalcogenide system only as an impurity phase most likely due to oxidation. Therefore here the Lotgering model seems to be the appropriate model.

### 4.3.3 Investigation of the Fe valence

According to Lotgering the Fe ions in  $\text{Fe}_{1-x}\text{Cu}_x\text{Cr}_2\text{S}_4$  change their valence state with increasing Cu substitution  $x$  (equation 4.3 - 4.5). While for  $x = 0$  only  $\text{Fe}^{2+}$  should be present Lotgering predicts the Fe ions to become gradually trivalent with increasing  $x$ . For  $x \geq 0.5$  all Fe ions are expected to be trivalent. Figure 4.8 compares the Fe 2p XAS spectra of  $\text{Fe}_{0.5}\text{Cu}_{0.5}\text{Cr}_2\text{S}_4$  with those of  $\text{FeO}$

(formally  $\text{Fe}^{2+}$ ) and  $\text{Fe}_2\text{O}_3$  (formally  $\text{Fe}^{3+}$ ) taken from Regan *et al.* (2001). The upper spectrum (red line) was measured on the sample cleaned in air with acetone without subsequent cleaning in vacuum. The other Fe 2p XAS spectrum was measured after rasping the sample with a diamond file in-situ (blue line). A striking difference of the spectral shape between these two measurements is clearly seen. The comparison with the reference measurements suggests that a mixture of  $\text{Fe}^{2+}$  and  $\text{Fe}^{3+}$  ions is present in the sample not cleaned in vacuum. For this sample in the Fe 2p XAS spectrum in addition to peak A attributed to  $\text{Fe}^{2+}$  there also appears a large peak at higher photon energies (peak B). Since the position and the shape of this peak is very similar to that of  $\text{Fe}_2\text{O}_3$ , peak B can be associated with trivalent Fe ions. After rasping the sample in-situ the peak B completely disappears indicating that the  $\text{Fe}^{3+}$  ions represent an additional phase on the surface. Appearance of this phase can be attributed to oxidation of the material at the surface (Regan *et al.*, 2001). As introduced and discussed in chapter 3 Kuepper *et al.* (2008) observed a similar increase of the  $\text{Fe}^{3+}$  contribution in the Fe 2p XAS spectrum of polycrystalline  $\text{Sr}_2\text{FeMoO}_6$  related to an ageing process involving water and oxygen.

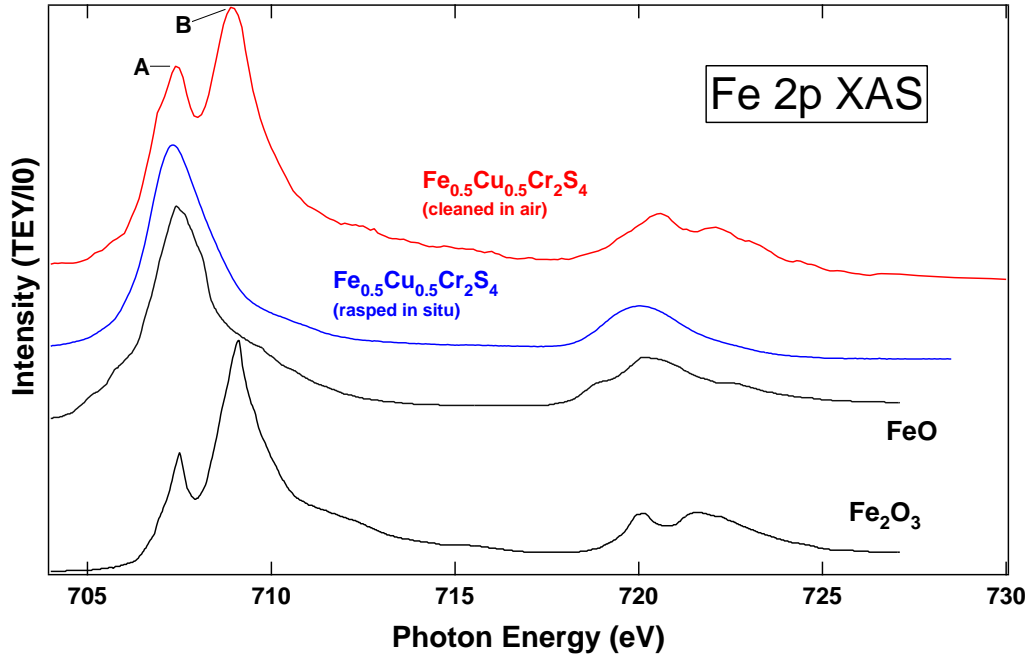


Figure 4.8: Fe 2p XAS spectra of  $\text{Fe}_{0.5}\text{Cu}_{0.5}\text{Cr}_2\text{S}_4$  cleaned in air (red line) and rasped in-situ (blue line) compared to reference measurements. The FeO (formally  $\text{Fe}^{2+}$ ) and the  $\text{Fe}_2\text{O}_3$  (formally  $\text{Fe}^{3+}$ ) spectra have been taken from Regan *et al.* (2001).

Figure 4.9 presents the Fe 2p XMCD measurement of a sample that was not cleaned in-situ. It can be seen that the part of the spectrum associated with  $\text{Fe}^{3+}$  (peak B) does not contribute to the XMCD signal. The absence of a macroscopic spontaneous magnetic order of the  $\text{Fe}^{3+}$  phase is a further indication of  $\text{Fe}^{3+}$  being part of an impurity phase. As mentioned before after rasping the sample in-situ the Fe 2p XAS spectrum shows only one peak A which can be attributed to divalent Fe

and within the experimental resolution no evidence for the peak B associated with  $\text{Fe}^{3+}$  can be found (Figure 4.8).

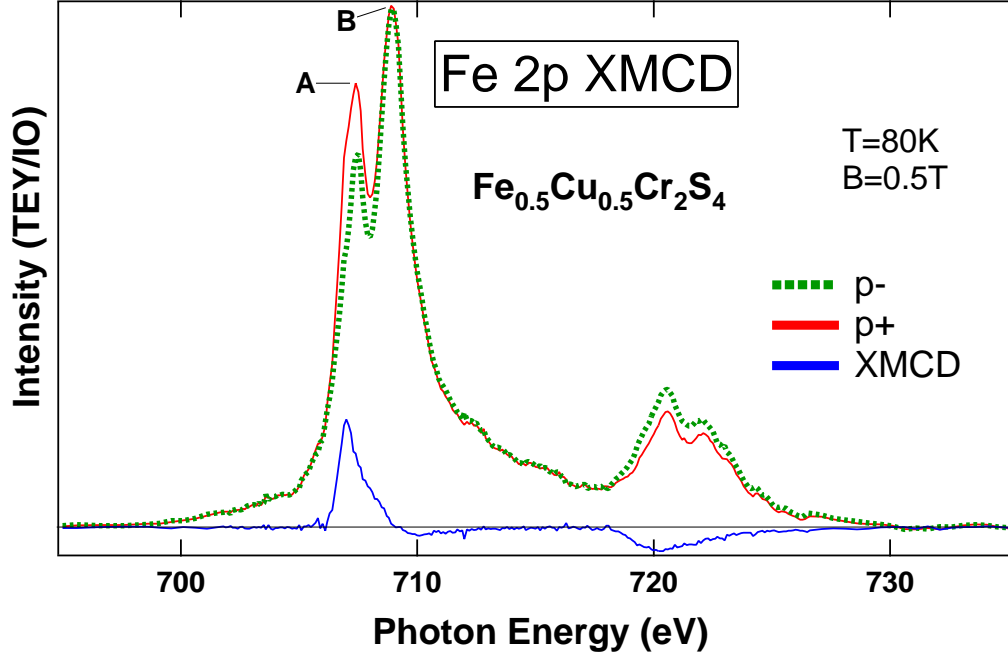


Figure 4.9: Fe 2p XAS spectra of  $\text{Fe}_{0.5}\text{Cu}_{0.5}\text{Cr}_2\text{S}_4$ , obtained with the photon helicity parallel ( $\rho^+$ ) and antiparallel ( $\rho^-$ ) to the magnetisation, respectively. The XMCD spectrum (blue) corresponds to the difference between  $\rho^+$  and  $\rho^-$  ( $\text{XMCD} \equiv \rho^+ - \rho^-$ ).

To investigate how the sample preparation can affect the ageing process, thus the Fe valence change, Fe 2p XPS spectra of single crystalline  $\text{Fe}_{0.5}\text{Cu}_{0.5}\text{Cr}_2\text{S}_4$  subjected to different treatment were performed. In Fig. 4.10 the results are presented. The spectra show the Fe 2p spectrum of a sample powdered in air (green line), rasped in air (red line) and cleaved in-situ (blue line) together with reference measurements of FeO (formally  $\text{Fe}^{2+}$ ) and  $\text{Fe}_2\text{O}_3$  (formally  $\text{Fe}^{3+}$ , taken from Moulder *et al.* (1992)). The measurements of the samples treated in air clearly show a shift to higher binding energies, especially the spectrum of the powdered sample, indicating the appearance of a considerable amount of trivalent Fe ions. Therefore it can be concluded that the Fe valence change is rather sensitive to the sample preparation.

In order to find out if the Fe valence change can also reach deeper into the bulk material a small piece of single crystalline  $\text{Fe}_{0.5}\text{Cu}_{0.5}\text{Cr}_2\text{S}_4$  was investigated. In Fig. 4.11 XAS spectra of the sample that was cleaved in situ are presented. The spectra were measured at three different beampositions on the cleaved sample surface. Spectrum (a) was measured at the edge, (b) between the edge and the centre and (c) at the centre of the cleaved surface. As one can see the peak B, associated with an  $\text{Fe}^{3+}$  containing oxidation phase, dominates the Fe 2p XAS spectrum (a). Spectra (b) and (c) clearly show a decrease of the  $\text{Fe}^{3+}$  features and a spectral shape similar to divalent Fe. This confirms that the edge of the sample, thus the uncleaned surface, contains a high amount of trivalent Fe.

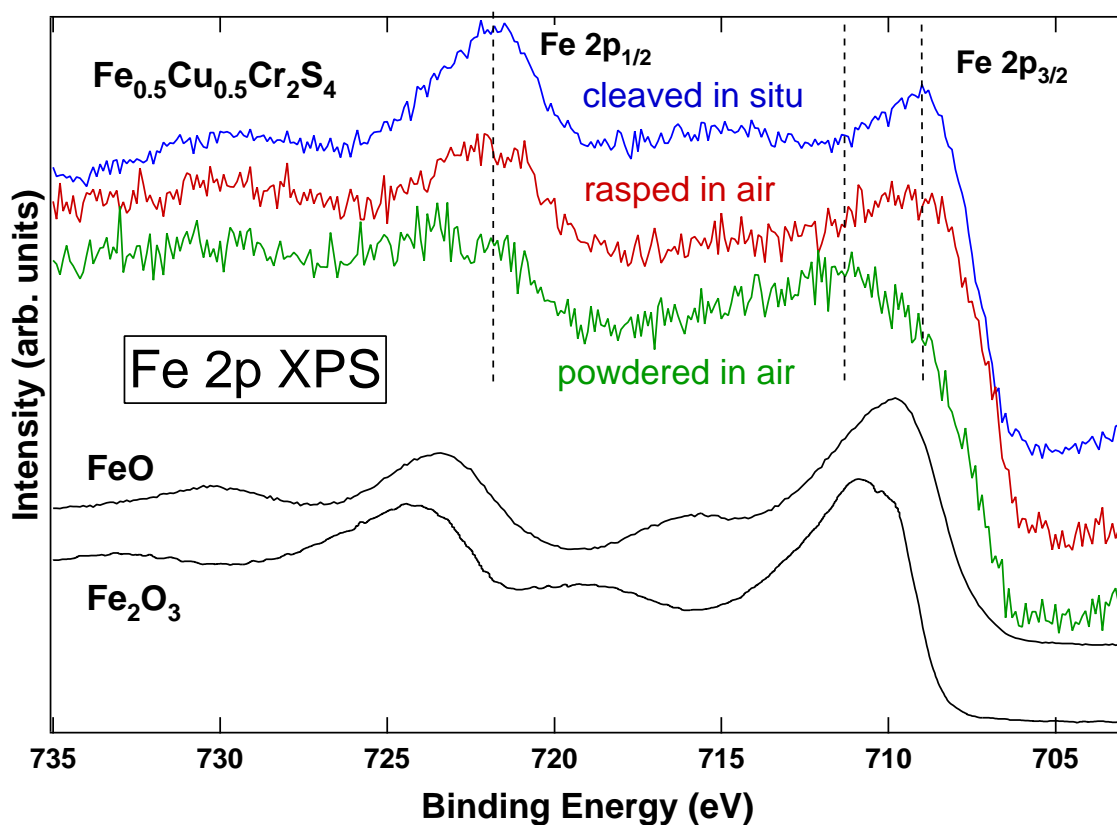


Figure 4.10: Fe 2p XPS spectra of  $\text{Fe}_{0.5}\text{Cu}_{0.5}\text{Cr}_2\text{S}_4$  cleaved in-situ (blue line), rasped in air (red line) and powdered in air (green line) compared to reference measurements of FeO (formally  $\text{Fe}^{2+}$ ) and  $\text{Fe}_2\text{O}_3$  (formally  $\text{Fe}^{3+}$ , taken from Moulder *et al.* (1992)).

The decrease of the  $\text{Fe}^{3+}$  features in the more centered measurements of the cleaved sample surface indicates that in the bulk the trivalent Fe ions vanish, thus only divalent Fe ions are present. The fact that even in spectrum (c)  $\text{Fe}^{3+}$  features are visible can be explained by the dimensions of the beam and the sample. The cleaved surface size was about 1x1 mm while the beamsize was about 0.8x0.7 mm. So also in the measurement (c) Fe-ions of the surface region contribute to the spectrum. However these measurements show that the Fe valence change reaches surprisingly deep into the bulk of the  $\text{Fe}_{0.5}\text{Cu}_{0.5}\text{Cr}_2\text{S}_4$  single crystal. Therefore it is possible that in a powdered sample of  $\text{Fe}_{0.5}\text{Cu}_{0.5}\text{Cr}_2\text{S}_4$  a considerable high amount of Fe ions change their valence state from a divalent to a trivalent character explaining the differing results published in the literature.

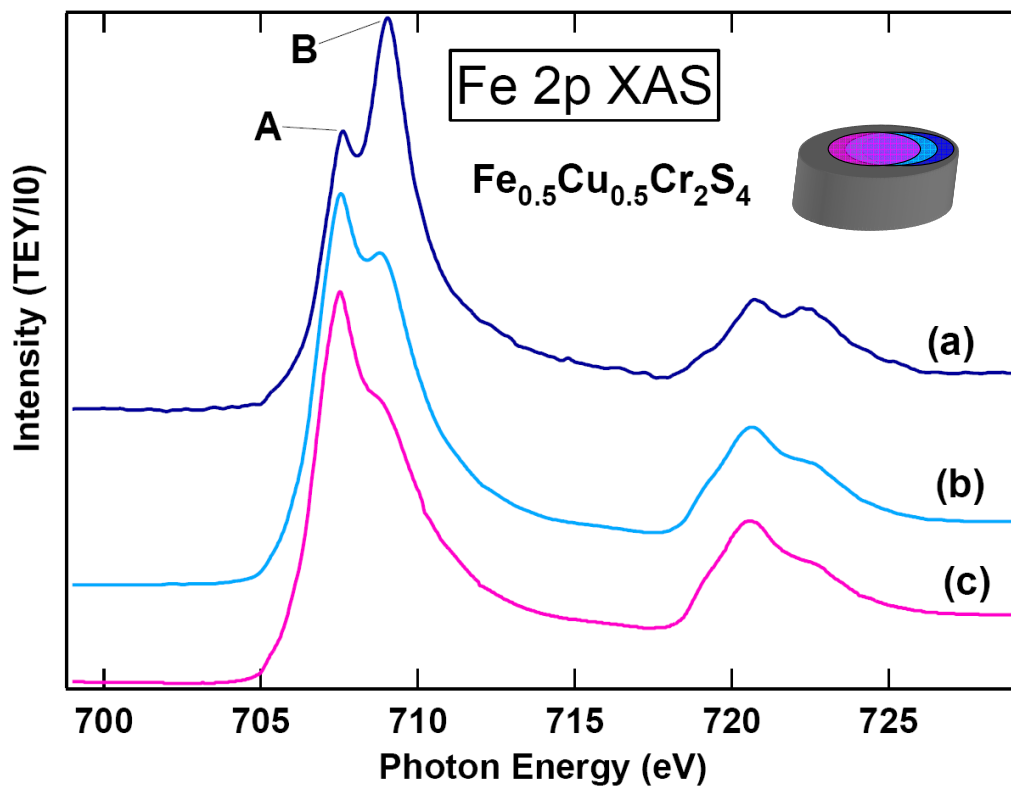


Figure 4.11: Fe 2p XAS spectra of  $\text{Fe}_{0.5}\text{Cu}_{0.5}\text{Cr}_2\text{S}_4$  cleaved in situ. Spectrum (a) was measured at the edge, (b) between the edge and the centre and (c) at the centre of the cleaved surface. This is also illustrated in the figure.

### Comparison with literature results

Han *et al.* (2006) measured Fe 2p XAS spectra of  $\text{Fe}_{1-x}\text{Cu}_x\text{Cr}_2\text{S}_4$  ( $0.1 \leq x \leq 0.5$ ). It was found that for all different Cu concentrations  $x$  the spectral shape does not change indicating that  $x$  does not affect the Fe valence state. All the presented spectra show a striking consistency with the Fe 2p XAS spectrum of an in situ rasped  $\text{Fe}_{0.5}\text{Cu}_{0.5}\text{Cr}_2\text{S}_4$  sample presented in figure 4.8 (blue line). As described above this spectrum reveals

Fe to be divalent. In addition XPS measurements of  $\text{Fe}_{0.5}\text{Cu}_{0.5}\text{Cr}_2\text{S}_4$  were presented by Kurmaev *et al.* (2000). The spectra clearly exhibit a spectral shape similar to divalent Fe.

These results confirm the ones presented in this work, but are in contradiction with the Lotgering model that predicts Fe to become trivalent in  $\text{Fe}_{0.5}\text{Cu}_{0.5}\text{Cr}_2\text{S}_4$  (Lotgering *et al.*, 1969), as well as with the results of Mössbauer investigations (Son *et al.*, 2005; Klencsar *et al.*, 2005).

Han *et al.* (2006) explained the fact that the Fe 2p XAS measurements do not show trivalent Fe ions with a metallic like bonding between Fe and S ions, indicated by the absence of multiplet features in the Fe 2p XAS spectrum. The strong hybridisation of the Fe and S states is assumed to be responsible for the similar shape of the Fe 2p XAS spectra of  $\text{FeCr}_2\text{S}_4$  ( $\text{Fe}^{2+}$ ) and  $\text{Fe}_{0.5}\text{Cu}_{0.5}\text{Cr}_2\text{S}_4$ . But a metallic state of Fe could not be detected with XPS. As discussed before in Fig. 4.10 a Fe 2p XPS spectrum of the single crystalline  $\text{Fe}_{0.5}\text{Cu}_{0.5}\text{Cr}_2\text{S}_4$  cleaved in-situ is presented (upper spectrum, blue line). Metallic Fe is expected to have a  $2p_{3/2}$  binding energy of about 707 eV. But the maximum of the Fe 2p  $L_3$  line of the in-situ cleaved  $\text{Fe}_{0.5}\text{Cu}_{0.5}\text{Cr}_2\text{S}_4$  crystal appears at a binding energy of about 709 eV, which can be attributed to  $\text{Fe}^{2+}$  state when compared with FeO (formally  $\text{Fe}^{2+}$ ) (see also figure 1.7).

In case of XPS measurements the fact that the Fe 2p spectrum shows  $\text{Fe}^{2+}$  instead of  $\text{Fe}^{3+}$  ions in  $\text{Fe}_{0.5}\text{Cu}_{0.5}\text{Cr}_2\text{S}_4$  is explained by a charge transfer from the  $\text{S}^{2-}$  to the  $\text{Fe}^{3+}$  ions during the photoemission excitation process (Kurmaev *et al.*, 2000). However, this effect can not occur in XAS measurements, which also show divalent Fe ions as discussed before. Thus, both XAS and XPS measurements reveal Fe to be in a divalent state in the bulk material.

The fact that XAS and XPS are relatively surface sensitive compared to other methods might be a reason for the different results concerning the Fe valence. However, for the samples cleaned in-situ one can definitely exclude surface contamination and in this case both XAS and XPS probe the bulk properties.

One must also note that XAS and XPS studies are performed on single crystalline material in ultra-high vacuum whereas other techniques use powdered samples and measure in air or low vacuum. As already shown in Fig. 4.10 the treatment of  $\text{Fe}_{0.5}\text{Cu}_{0.5}\text{Cr}_2\text{S}_4$  in air highly affects the Fe valence state leading to the appearance of trivalent Fe ions. This change can reach deeper into the sample bulk as shown in figure 4.11, which could affect the Fe valence state in the whole powdered sample.

As mentioned before Deb *et al.* (2003) reported an XAS measurement of trivalent Fe in a  $\text{Fe}_{0.5}\text{Cu}_{0.5}\text{Cr}_2\text{S}_4$  single crystal, that was cleaned in situ. In figure 4.12 Fe 2p XAS and XMCD measurements attached from Deb *et al.* (2003) are compared to the Fe 2p XMCD measurement also shown in figure 4.9. The XMCD signal was inverted for better comparison. It can be seen that the two XMCD measurements show a remarkable similarity. As described before only the features belonging to the  $\text{Fe}^{2+}$  contribute to the XMCD signal. Therefore it is likely that in fact  $\text{Fe}^{2+}$  was measured by Deb *et al.* (2003).

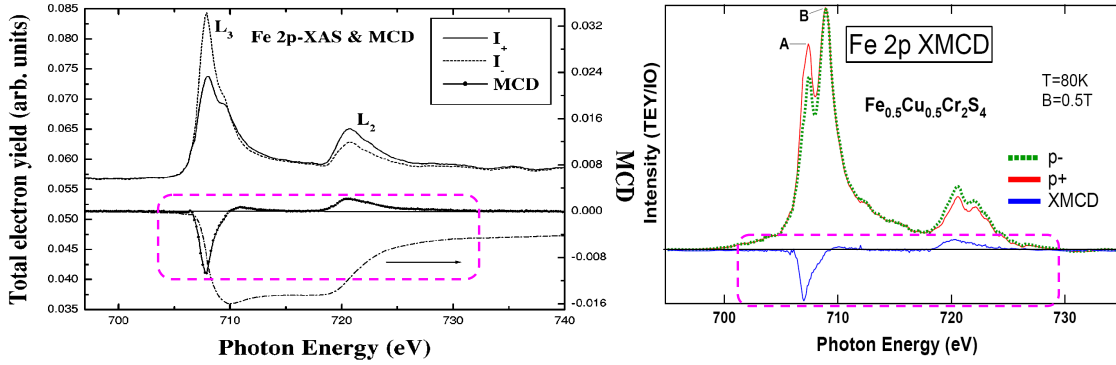


Figure 4.12: (a) Fe 2p XAS and XMCD measurement attached from Deb *et al.* (2003) measured at  $T = 50$  K with  $B = 1.4$  T. (b) Fe 2p XAS and XMCD of an in air cleaned  $\text{Fe}_{0.5}\text{Cu}_{0.5}\text{Cr}_2\text{S}_4$  single crystal measured at  $T = 80$  K with  $B = 0.5$  T. Peak A originates from  $\text{Fe}^{2+}$ , peak B from  $\text{Fe}^{3+}$  ions on the surface.

In addition charge transfer (CT) multiplet calculations were performed to support this assumption. The TT-multiplets program was used, which is based upon the methods described by Thole, van der Laan and de Groot (de Groot *et al.*, 1990a; de Groot, 2001; van der Laan *et al.*, 1992)(see also section 1.4.2). In figure 4.13 Fe 2p XAS and XMCD measurements are compared to CT multiplet calculations of  $\text{Fe}^{2+}$  and  $\text{Fe}^{3+}$  ions. The Fe 2p calculations were performed in  $T_d$  (tetrahedral) symmetry with a crystal field of  $10Dq = 0.5$  eV like done by Deb *et al.* (2003). Within the CT model best agreement with the experimental results were found by setting the DELTA value to 3 eV leading to a ground state containing about 83%  $3d^n$  and about 17%  $3d^{n+1}\underline{L}$  character. Here  $3d^n$  stands for the occupation of the metal 3d level and  $\underline{L}$  for an oxygen hole. The spectra were broadened with a Lorentzian and a Gaussian function to account for the lifetime broadening and the broadening due to the experiment. The calculations are calibrated and normalised on the experimental peaks. Above Fe 2p XAS spectra of a sample cleaned in air (red dotted line) and a sample cleaned in situ (red line) are compared to calculations of  $\text{Fe}^{2+}$  (black line) and  $\text{Fe}^{3+}$  (black dotted line). As can be seen there is a nice agreement between the measured Fe 2p spectrum of the sample cleaned in situ and the  $\text{Fe}^{2+}$  calculation. Furthermore it becomes clear that the spectrum of the sample not treated in situ can be described as a mixture of the  $\text{Fe}^{2+}$  and  $\text{Fe}^{3+}$  calculation. A good agreement with the measurement is achieved with a  $\text{Fe}^{2+}/\text{Fe}^{3+}$  ratio of about 55/45.

Below the XMCD measurement (blue line) is compared to  $\text{Fe}^{2+}$  (black line) and  $\text{Fe}^{3+}$  (black dotted line) calculations. Again there is a nice agreement between the  $\text{Fe}^{2+}$  calculation and the measured XMCD signal. As mentioned before the same signal was measured by Deb *et al.* (2003) interpreted and calculated as  $\text{Fe}^{3+}$ . Although similar in shape at the  $2p_{3/2}$  features the Fe 2p XAS and XMCD  $\text{Fe}^{2+}$  and  $\text{Fe}^{3+}$  calculations show clear differences at the  $2p_{1/2}$  features. In XAS as well as in XMCD the measured spectra show good agreement with the  $2p_{1/2}$  line of the divalent Fe calculation while there is a clear difference compared to the trivalent Fe calculation. The same can also be seen in the calculations done by Deb *et al.* (2003). Therefore one can conclude that also Deb *et al.* (2003) measured most likely divalent Fe in  $\text{Fe}_{0.5}\text{Cu}_{0.5}\text{Cr}_2\text{S}_4$ .



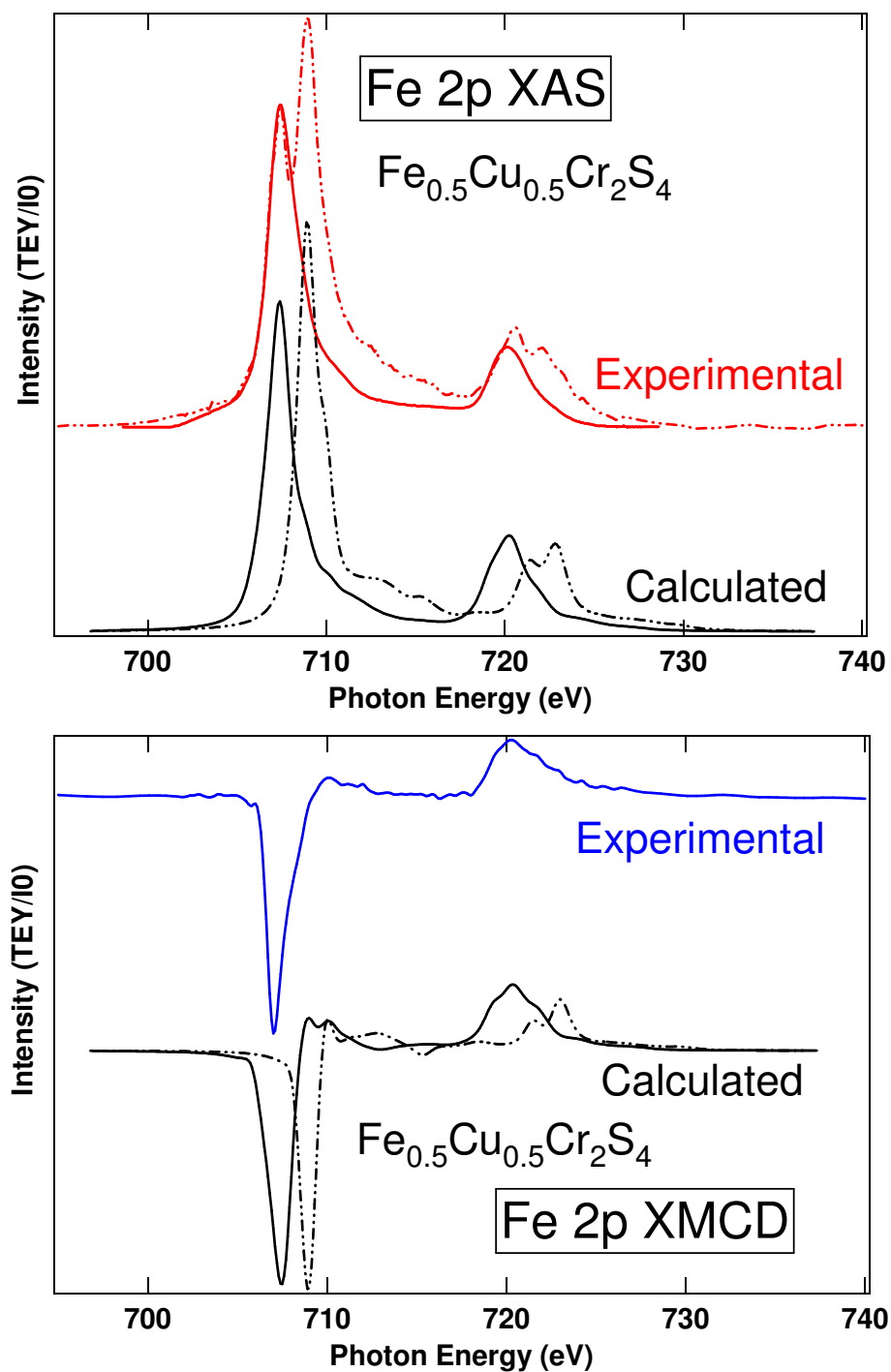


Figure 4.13: Measurements and multiplet calculations of Fe 2p XAS and XMCD spectra of single crystalline  $\text{Fe}_{0.5}\text{Cu}_{0.5}\text{Cr}_2\text{S}_4$ . The Fe 2p XAS spectra of a sample cleaned in air (red dotted) and a sample cleaned in situ (red line) are compared to multiplet calculations of  $\text{Fe}^{2+}$  (black line) and  $\text{Fe}^{3+}$  (black dotted line). Below a measured Fe 2p XMCD spectrum (blue line) is compared to multiplet calculations of  $\text{Fe}^{2+}$  (black line) and  $\text{Fe}^{3+}$  (black dotted line).

In summary one can say that in contrast to the Lotgering model the Fe ions seem to stay in a divalent valence state in the bulk of  $\text{Fe}_{0.5}\text{Cu}_{0.5}\text{Cr}_2\text{S}_4$ . However a considerably high amount of trivalent Fe was found on the surface of untreated samples and in samples powdered in air. In addition it was shown that this trivalent Fe site can reach surprisingly deep into the sample bulk. Therefore, since many experimental methods differ significantly in the sample treatment, this Fe valence instability in  $\text{Fe}_{0.5}\text{Cu}_{0.5}\text{Cr}_2\text{S}_4$  might explain the differing results found by various other experiments concerning the Fe valence.

#### 4.3.4 Investigation of the XMCD measurements

In this section the XMCD measurements of  $\text{Fe}_{0.5}\text{Cu}_{0.5}\text{Cr}_2\text{S}_4$  are analysed. As discussed above evidence was found that the measurements presented in this work were performed on a sample that was affected by a chemical process changing its Fe valence state in the surface layers and therefore most likely also its magnetic properties. However the investigation of the XMCD signal can give valuable information about the sample surface.

Despite the changes at the sample surface the XMCD spectra of  $\text{Fe}_{0.5}\text{Cu}_{0.5}\text{Cr}_2\text{S}_4$  clearly show a ferrimagnetic ground state. In figure 4.14 the Fe 2p and Cr 2p XMCD measurements and their integrals are presented. As one can see the XMCD signals of Cr and Fe are opposite to each other, which especially becomes visible by comparison of the integrals. Since the Cr amount is four times higher than the Fe amount in  $\text{Fe}_{0.5}\text{Cu}_{0.5}\text{Cr}_2\text{S}_4$  the antiferromagnetic alignment between Cr and Fe leads to a ferrimagnetic ground state.

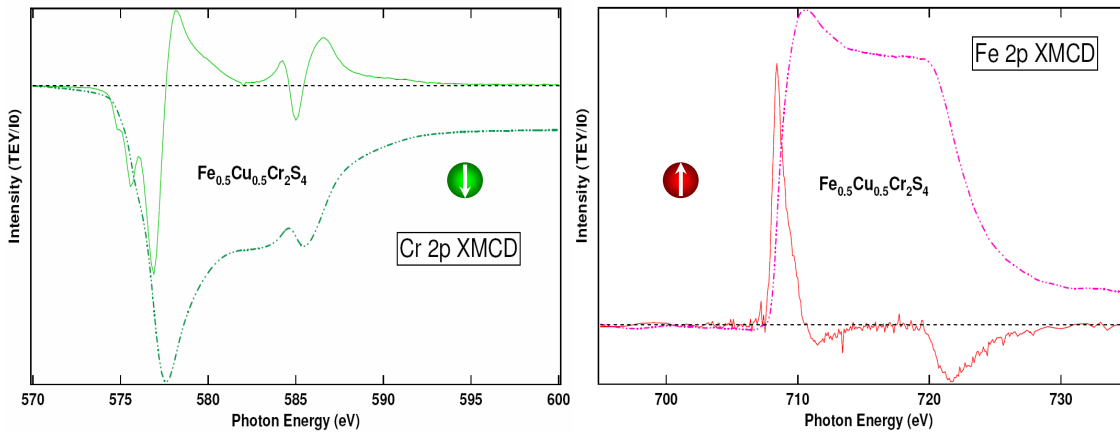


Figure 4.14: XMCD measurements of Fe (red line) and Cr (green line) in  $\text{Fe}_{0.5}\text{Cu}_{0.5}\text{Cr}_2\text{S}_4$ . The XMCD signals are shown together with their integrals, violet dotted for Fe and dark green dotted for Cr. In addition a sketch of the direction of the spin magnetic moment is given.

As described in section 1.2.2.1 it is possible to achieve the spin and orbital magnetic moments from the XMCD signal by calculating the sum rule equations. In figure 4.15 all the spectra and integrals that are necessary to calculate the Fe and

Cr magnetic moments in  $\text{Fe}_{0.5}\text{Cu}_{0.5}\text{Cr}_2\text{S}_4$  are shown on the basis of the Fe 2p lines. Basically the integrals of two spectra are needed. One is the integral of the sum of the XAS spectra taken with left and right circularly polarised light, respectively (graph (b), blue line). The integral is calculated over the hole  $L_3+L_2$  lines (parameter  $r$ ). The other is the integral of the XMCD signal (graph (c), violet line). Note that the sum rule equation for the spin magnetic moment needs two XMCD integrals. One over the  $L_3$  (parameter  $p$ ) and one integral over the hole  $L_3+L_2$  lines (parameter  $q$ ) (see equation 1.17).

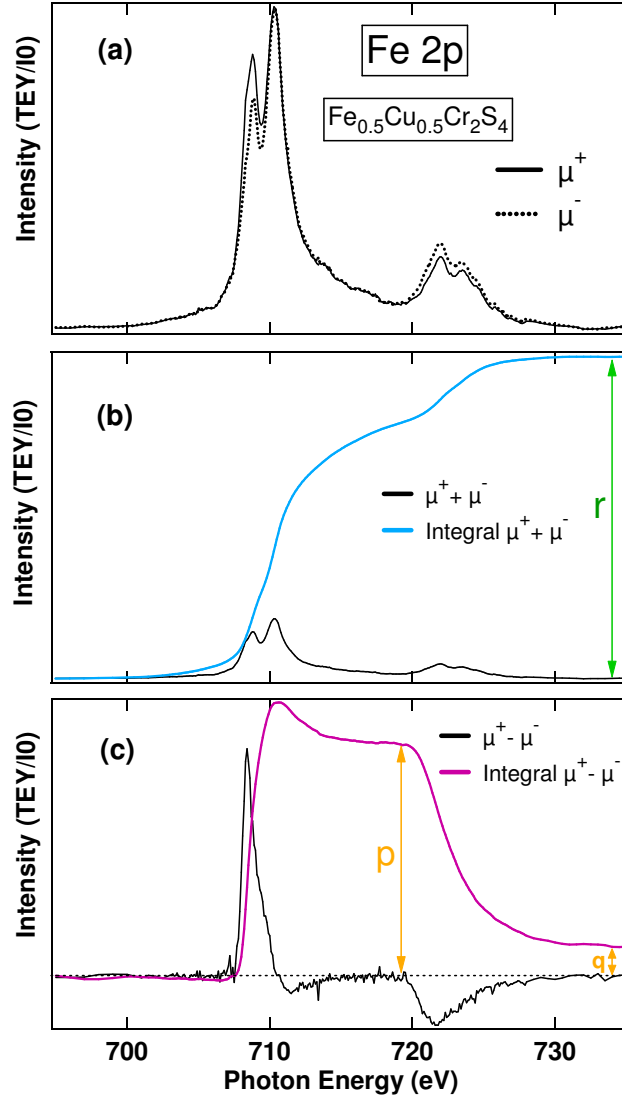


Figure 4.15: Fe 2p XAS and XMCD spectra of  $\text{Fe}_{0.5}\text{Cu}_{0.5}\text{Cr}_2\text{S}_4$ : (a) X-ray absorption spectra with photon helicity parallel ( $\mu^+$ ) and antiparallel ( $\mu^-$ ) to the magnetisation, respectively; (b) The sum of the absorption spectra ( $\mu^+ + \mu^-$ ) and its integral; (c) The XMCD spectrum ( $\mu^+ - \mu^-$ ) and its integral. The integrals needed for the sum rules are denoted by  $r$ ,  $p$  and  $q$ .

The exact equations used to calculate the spin and orbital magnetic moments are the following:

$$m_{orb} = - \frac{4q}{3r} \cdot (10 - n_{3d}) \cdot C_{pol} , \quad (4.6)$$

$$m_{spin} = - \frac{6p - 4q}{r} \cdot (10 - n_{3d}) \cdot C_{pol} \cdot C_{Teramura} \quad (4.7)$$

Here the parameters shown in figure 4.15 are used. In addition to the sum rules established by Chen *et al.* (1995) a factor  $C_{pol}$  is considered, which takes into account the quality of the light polarisation. In case of  $m_{spin}$  a second factor  $C_{Teramura}$  is multiplied, which represents the Teramura factor (see also section 1.2.2.1). As already mentioned the  $\text{Fe}^{3+}$  ions do not contribute to the XMCD signal and therefore the equations 4.6 - 4.7 are calculated for a  $\text{Fe}^{2+}$  and a  $\text{Cr}^{3+}$  ion, respectively. In case of  $\text{Fe}^{2+}$  ( $n_{3d} = 6$ ) a Teramura factor of  $C_{Teramura} = 1.14$  was used (Teramura *et al.*, 1996) and a light polarisation of 90% was assumed ( $C_{pol} = 1.1$ ). Note that in contrast to XMCD in XAS the trivalent Fe is visible and therefore contributes to its integral  $r$ . This has to be considered in the calculation. As described before multiplet calculations revealed a  $\text{Fe}^{2+}/\text{Fe}^{3+}$  ratio of about 55/45 (figure 4.13). Since the XAS integral contributes to the denominator in the sum rules the spin and orbital magnetic moments calculated for Fe have to be multiplied by a factor of 1.82. For  $\text{Cr}^{3+}$  ( $n_{3d} = 3$ ) the Teramura factor was set to  $C_{Teramura} = 1.0$ , since no factor is available. Therefore the spin magnetic moment calculated by equation 4.7 is most likely underestimated for the  $\text{Cr}^{3+}$ , due to the strong multiplet mixing between the  $L_2$  and  $L_3$  lines. All the results are listed in table 4.1 and compared to the spin and orbital magnetic moments published by Deb *et al.* (2003) as well as theoretical values. Note that the signs of the published values are reversed for a better comparison.

Atom	magnetic moment	XMCD exp. ( $\mu_B/\text{atom}$ )	XMCD exp. [Deb] ( $\mu_B/\text{atom}$ )	ion <sup>2+</sup> ( $\mu_B/\text{atom}$ )	ion <sup>3+</sup> ( $\mu_B/\text{atom}$ )
Fe	$\mu_{spin}$	$-0.98 \pm 0.02$	$-3.28 \pm 0.02$ (for $\text{Fe}^{3+}$ ) $-2.62 \pm 0.02$ (for $\text{Fe}^{2+}$ )	-4	-5
	$\mu_{orb}$	$-0.03 \pm 0.02$	$-0.24 \pm 0.02$ (for $\text{Fe}^{3+}$ ) $-0.19 \pm 0.02$ (for $\text{Fe}^{2+}$ )	-2	0
Cr	$\mu_{spin}$	$0.62 \pm 0.02$	$2.33 \pm 0.03$		3
	$\mu_{orb}$	$0.02 \pm 0.02$	$-0.09 \pm 0.03$		3

Table 4.1: Here the measured spin ( $\mu_{spin}$ ) and orbital ( $\mu_{orb}$ ) magnetic moments for Fe and Cr in  $\text{Fe}_{0.5}\text{Cu}_{0.5}\text{Cr}_2\text{S}_4$  in units of  $\mu_B$  per atom are listed ( $B = 0.5$  T;  $T = 80$  K). In addition the magnetic moments measured by Deb *et al.* (2003) are shown ( $B = 1.4$  T;  $T = 50$  K). Finally also the theoretical  $\mu_{spin}$  and  $\mu_{orb}$  values for a  $\text{Fe}^{2+}$ ,  $\text{Fe}^{3+}$  and  $\text{Cr}^{3+}$  ion are given. For more details see the text.

In table 4.1 two values are given for the Fe spin and orbital magnetic moments measured by Deb *et al.* (2003). This is due to the expected Fe valence state. Deb *et al.* (2003) assumed Fe to be completely in a trivalent valence state. Therefore the magnetic moments  $\mu_{spin}$  and  $\mu_{orb}$  were calculated with  $n_{3d} = 5$  giving the upper values. Since the findings in this work give rise to the assumption that Fe is nearly completely divalent in a vacuum cleaned  $\text{Fe}_{0.5}\text{Cu}_{0.5}\text{Cr}_2\text{S}_4$  sample, thus also in the measurements done by Deb *et al.* (2003), the values were recalculated with  $n_{3d} = 6$  leading to the lower values. As already mentioned the magnetic moments measured in the present work were calculated for  $\text{Fe}^{2+}$  only. The theoretical values for  $\mu_{spin}$  and  $\mu_{orb}$  given for an  $\text{Fe}^{2+}$ ,  $\text{Fe}^{3+}$  and  $\text{Cr}^{3+}$  ion are assumed according to the Hund's rules, thus effects of the crystal structure like the crystal field or hybridisation are not taken into account.

It becomes obvious that the Fe spin magnetic moments published by Deb *et al.* (2003) are too small compared to the theoretical values, regardless of the assumed Fe valence state. This is also the case for the Cr spin magnetic moments, although here the differences are not as big as for the Fe ions. The measured Fe and Cr spin magnetic moments in the present work are even considerably smaller. Various reasons can be responsible for this discrepancy.

One reason could be the  $L_2 - L_3$  multiplet mixing leading to an underestimated spin magnetic moment resulting from the sum rules, which can be compensated by using the Teramura factor. For the Fe spin magnetic moment a factor was used that was calculated for a crystal field of  $10Dq = 1.5$  eV in an octahedral symmetry (Teramura *et al.*, 1996). Since the Fe ions in  $\text{Fe}_{0.5}\text{Cu}_{0.5}\text{Cr}_2\text{S}_4$  are situated in a tetrahedral crystal field of about  $10Dq = 0.5$  eV, the Teramura factor is not suited perfectly. For  $\text{Cr}^{3+}$  no factor was available and due to the strong multiplet mixing the  $\mu_{spin}$  value calculated here is most likely highly underestimated. In case of the values measured by Deb *et al.* (2003) it was not mentioned if a Teramura factor was used to calculate the Fe spin magnetic moment. The Cr  $\mu_{spin}$  was not calculated directly with the sum rules, but estimated by using the  $\mu_{orb}$  value and a SQUID measurement. This could explain the big difference between the measured Cr spin magnetic moment and the one published by Deb *et al.* (2003).

A second reason for the small  $\mu_{spin}$  values could be a strong covalent bonding or metallic hybridisation (Palmer and Greaves, 1999; Han *et al.*, 2006; Deb *et al.*, 2003; Lang *et al.*, 2000). Band structure calculations support this assumption and give reduced values for the Cr and Fe magnetic moments (Park *et al.*, 1999; Deb *et al.*, 2002, 2003; Lang *et al.*, 2000).

Also magnetic frustration effects were mentioned as a reason for the low spin magnetic moments (Lang *et al.*, 2000).

In addition antisite processes can be responsible for a reduced magnetic moment. If, for instance, Fe atoms situated at the A-site partially change positions with the Cr atoms of the B-site, both the Fe and Cr ions would become antiferromagnetically aligned to the Fe and Cr ions remaining at the former sites, respectively (see figure 4.16). This would lead to a reduction of the measured overall magnetic moments. However X-ray diffraction measurements confirmed the high quality of the samples having a single-phase crystal structure. Also magnetisation measurements revealed

homogenous ferrimagnetic behaviour without any irreversible magnetic effects characteristic of disordered systems (Deb *et al.*, 2003; Tsurkan *et al.*, 2005).

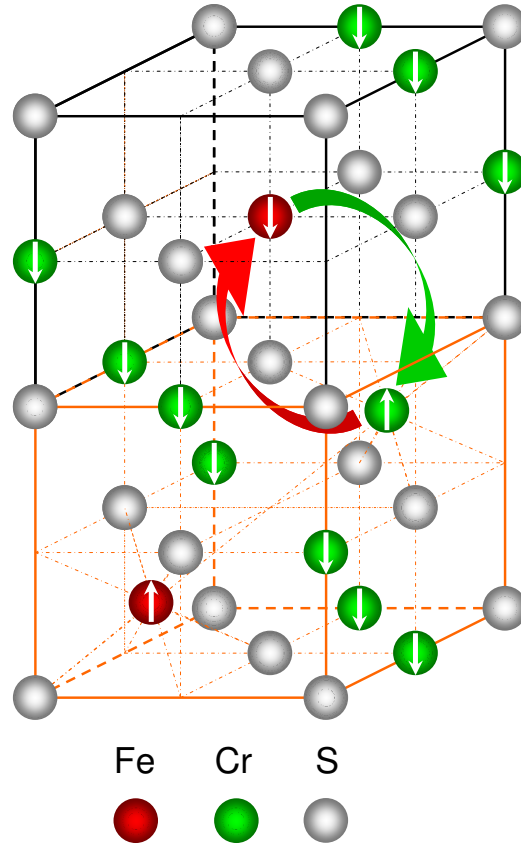


Figure 4.16: Illustration of an antisite process in which a Fe and Cr ion change positions. Here only the main part of the unit cell is shown. The spin direction is indicated by white arrows.

The appearance of low spin states could also cause a reduction of the magnetic moments. In figure 2.8 this is illustrated for a  $\text{Fe}^{2+}$  ion. Divalent Fe is a  $d^6$  electron system. In  $\text{Fe}_{1-x}\text{Cu}_x\text{Cr}_2\text{S}_4$  the Fe is surrounded by S tetrahedrally. The resulting crystal field splits the d orbitals energetically as shown in figure 2.8. In the high spin state all spin up states lie energetically below the spin down states. This leads to the occupation of five spin up and one spin down state resulting in a magnetic moment of  $\mu_s = 4\mu_B$  in accordance with the Hund's rules. A low spin state can occur if due to changes in the crystal field the spin down states decrease energetically below the spin up states. This can lead to additional occupations of spin down states resulting in a reduction of the magnetic moments from  $\mu_s = 4\mu_B$  to  $\mu_s = 2\mu_B$ .

Beside these explanations, which consider intrinsic properties of the material or the measurement technique to be the origin of the discrepancies, experimental results indicate an additional reason for the reduced magnetic moments. Measurements done by Tsurkan *et al.* (2005) give rise to the assumption that a considerable lowering of the magnetic moment is connected with the sample treatment. In figure 4.17 the field

dependence of the magnetisation for bulk and powdered  $\text{FeCr}_2\text{S}_4$  poly- and single crystals at a temperature of  $T = 4.2$  K are given attached from Tsurkan *et al.* (2005). As illustrated the single crystalline sample shows a saturation magnetisation of about  $1.8 \mu_B/f.u.$ , which is only a little reduced in comparison to the ionic value of  $2 \mu_B/f.u.$  and could be explained by covalent bonding or hybridisation effects. Surprisingly the polycrystalline sample shows a considerable reduction of the saturation magnetisation. In case of the powdered samples the lowering of the magnetisation is even increased down to values less than half of the single crystalline magnetisation. Here the effect is present regardless if the powdered sample was single- or polycrystalline. For the single crystal the reduction seems to be even higher. Note that the XMCD measurements presented in this work were performed with an external magnetic field of  $B = 0.5$  T, while the ones published by Deb *et al.* (2003) were done with  $B = 1.4$  T. These values are stressed out in figure 4.17.

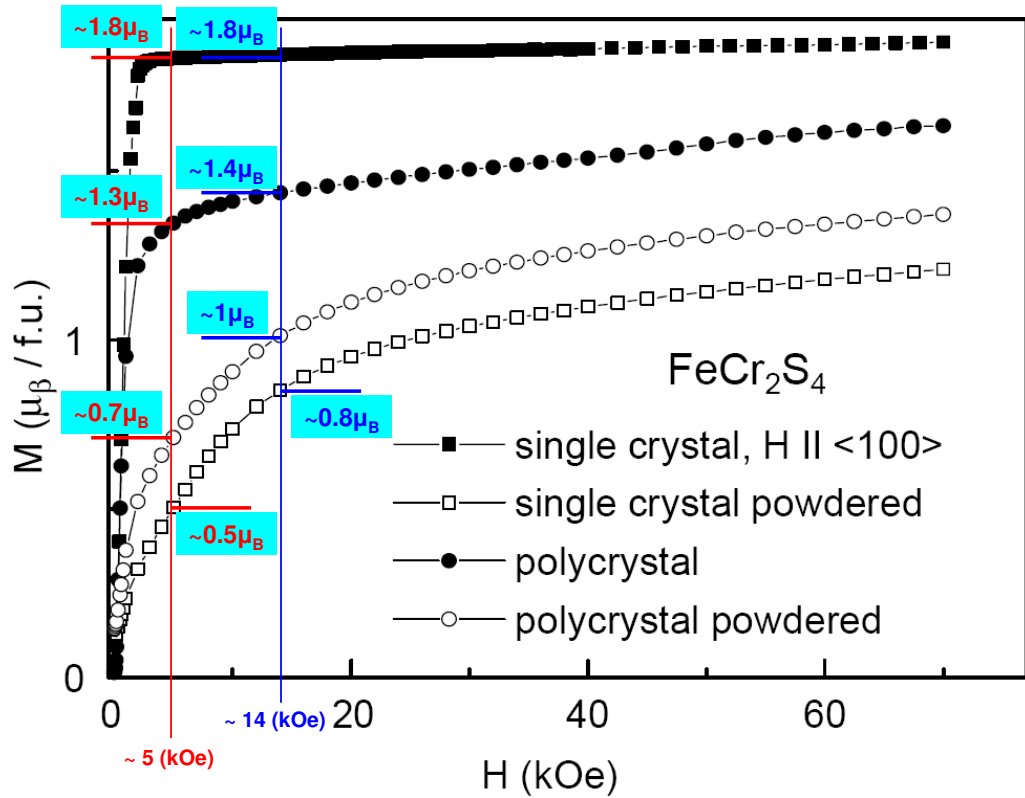


Figure 4.17: Field dependence of the magnetisation at  $T = 4.2$  K for bulk and powdered  $\text{FeCr}_2\text{S}_4$  poly- and single crystals attached from Tsurkan *et al.* (2005). The magnetisation of the samples at a magnetic field of  $B = 0.5$  T and  $B = 1.4$  T are stressed out.

One explanation for the decrease of the magnetisation in the polycrystalline and powdered samples could be a surface anisotropy (Tsurkan *et al.*, 2005), which can be caused by various reasons. For instance, while in case of nanoparticles anisotropy is believed to be present due to shape effects, it can also have a crystallographic nature. Here the anisotropy would be caused by symmetry reduction of the spin-orbit coupling (and/or crystal field) at the sample surface (Bakuzis and Morais (2001) and citations

within). Due to surface anisotropy magnetic ordered spin systems in a solid may show canting of the spins near the surface if the easy axis associated with the surface is non collinear with the bulk magnetisation (Mills, 1989; Conte, 2007) (figure 4.18). This could lead to a reduced magnetisation of the sample especially when powdered due to the bigger contribution of the surface layers. Considering the values presented in table 4.1 for  $\text{Fe}_{0.5}\text{Cu}_{0.5}\text{Cr}_2\text{S}_4$  it also has to be mentioned that the measurements were performed in the TEY-mode, which is very surface sensitive and therefore increases the effect of a surface anisotropy. In addition the values were obtained at much higher temperatures ( $T = 80 \text{ K}$ ;  $T = 50 \text{ K}$  (Deb)), which could decrease the measured spin magnetic moment as well. However it remains unclear why the reduction of the spin magnetic moments is so strong and why it is considerable stronger in the measured sample compared to the one published by Deb *et al.* (2003), since both measurements were performed on single crystals.

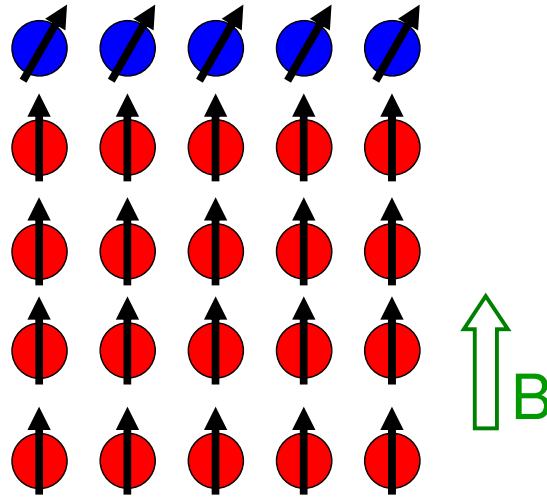


Figure 4.18: Illustration of a surface anisotropy resulting in an easy axis of the surface layers (blue), which is non collinear with the bulk magnetisation (red). This causes a canting of the spins (black arrows) at the surface.

In this work an additional process was found, which can explain the significant reduction of the measured spin magnetic moments in  $\text{Fe}_{0.5}\text{Cu}_{0.5}\text{Cr}_2\text{S}_4$ . This is the formation of  $\text{Fe}^{3+}$  ions at the sample surface. In section 4.3.3 it was shown that this  $\text{Fe}^{3+}$  formation can be increased by powdering of the sample and can reach deeper into the sample bulk. In addition it was found that the trivalent Fe ions do not show macroscopic magnetic behaviour and therefore would not contribute to the magnetisation in overall magnetic measurements like SQUID. Therefore this chemical process can cause a considerable reduction of the magnetisation especially in powdered or uncleaned samples. However note that in contrast to the surface anisotropy this process would not directly affect the  $\text{Fe}^{2+}$  spin magnetic moment measured by XMCD. But an explanation can be found if one considers that only a thin surface layer is affected by the chemical change. As mentioned before the surface sensitive TEY Fe 2p XMCD spectrum of an uncleaned  $\text{Fe}_{0.5}\text{Cu}_{0.5}\text{Cr}_2\text{S}_4$  sample shows no macroscopic



magnetic behaviour of the  $\text{Fe}^{3+}$  ions, while there is a clear magnetic behaviour of the  $\text{Fe}^{2+}$  ions (see figure 4.9). This can also be found for the  $\text{Fe}_3\text{O}_4$ , which has a spinel structure as well. Here the trivalent Fe ions are antiferromagnetic aligned, while the divalent Fe is ferromagnetic. It was shown that a small film of  $\text{Fe}_3\text{O}_4$  on NiO shows a considerable reduction of its magnetisation, thus the  $\text{Fe}^{2+}$  magnetic moment, due to surface anisotropy effects and frustration (Lind *et al.*, 1993). In addition strong surface anisotropy was found for surface oxide phases on metallic iron particles consisting of an  $\text{Fe}_2\text{O}_3$  or  $\text{Fe}_3\text{O}_4$  spinel phase (Bodker *et al.* (1994) and citations within). So if one assumes a similar behaviour of the  $\text{Fe}^{3+}$  containing surface layers in uncleaned  $\text{Fe}_{0.5}\text{Cu}_{0.5}\text{Cr}_2\text{S}_4$  the reduction of the  $\text{Fe}^{2+}$   $\mu_{\text{spin}}$  can be due to surface anisotropy and/or frustration as well. The difference between the measured  $\mu_{\text{spin}}$  and the one published by Deb *et al.* (2003) can then be explained by the different sample treatment, since the latter cleaned the sample in situ, which showed nearly no  $\text{Fe}^{3+}$  features in the XAS and XMCD spectral shape.

Looking at the measured orbital magnetic moments of the Cr and Fe ions in  $\text{Fe}_{0.5}\text{Cu}_{0.5}\text{Cr}_2\text{S}_4$  one can see that they are almost quenched. This can be explained by the crystal field, which lifts the degeneracy of the electron d states and can annul the Hund's rules.

In addition strong covalent bonding or metallic hybridisation could explain the small orbital magnetic moments. As mentioned before band structure calculations support this assumption and give reduced values for the Cr and Fe magnetic moments (Park *et al.*, 1999; Deb *et al.*, 2002, 2003; Lang *et al.*, 2000).

The values measured during this work are even smaller than the ones measured by Deb *et al.* (2003) and in case of Cr also inversed. This can indicate a change in the crystal field possibly caused by a change in the crystal structure of the surface layers. In summary one can say that there are various reasons for the measurement of too small spin magnetic moments in  $\text{Fe}_{0.5}\text{Cu}_{0.5}\text{Cr}_2\text{S}_4$ . But due to the experimental findings there is much evidence that the reduction of the magnetic moments is caused by the sample treatment. Possible reasons for this are surface anisotropy and/or a chemical change at the sample surface found in this work causing spin frustration. The differences in the measured orbital magnetic moments could indicate a change in the crystal field, thus the crystal structure in the surface layers.

## 4.4 Discussion

As previously described there is no evidence for a mixed valence state of Fe, Cu or Cr found in the bulk of  $\text{Fe}_{1-x}\text{Cu}_x\text{Cr}_2\text{S}_4$ . More precisely the results contradict both the Lotgering and the Goodenough model. Neither divalent Cu for high Cu concentrations nor a change of the Fe valence state from  $\text{Fe}^{2+}$  for  $x = 0$  to  $\text{Fe}^{3+}$  for  $x = 0.5$  was found. This could be explained by the fact that S exhibits a lot of extra holes in the 3p band (Kimura *et al.*, 2001), much more than predicted by Lotgering *et al.* (1969).

Since there is only divalent Fe found in  $\text{Fe}_{1-x}\text{Cu}_x\text{Cr}_2\text{S}_4$ , beside the fact that neither the presented measurements nor measurements in the literature reveal an intermediate  $\text{Cr}^{2+}$  state, the tripleexchange model fails to describe the conduction mechanism.

Therefore one has to think of other models describing the magnetism, M-I crossover

and the MR. In the following sections possible explanations for the magnetic and electric behaviour of  $\text{Fe}_{1-x}\text{Cu}_x\text{Cr}_2\text{S}_4$  will be discussed.

#### 4.4.1 Magnetism in $\text{Fe}_{1-x}\text{Cu}_x\text{Cr}_2\text{S}_4$

$\text{Fe}_{1-x}\text{Cu}_x\text{Cr}_2\text{S}_4$  is a ferrimagnet for the hole substitution range except  $x=1$ .  $\text{CuCr}_2\text{S}_4$  is ferromagnetic. Beside the double- or tripleexchange model, the so called direct exchange or the superexchange interaction between the spin magnetic moments of atoms can determine the magnetism in an atomic system. While in the direct exchange two spins interact directly over a short distance, in the superexchange interaction two spin magnetic moments interact with each other over a non-magnetic ligand (see also section 1.5).

Two superexchange interactions are predicted to be present in  $\text{Fe}_{1-x}\text{Cu}_x\text{Cr}_2\text{S}_4$ . One is an antiferromagnetic intersublattice superexchange interaction between  $\text{Fe(A)}-\text{Cr(B)}$ , the other an intrasublattice superexchange interaction between  $\text{Cr(B)}-\text{Cr(B)}$  that is ferromagnetic (Kim *et al.*, 1993; Son *et al.*, 2005; Kim *et al.*, 2002; Tsurkan *et al.*, 2005). This results in a ferrimagnetic ground state. In figure 4.19 the magnetic ground state and the two superexchange interactions are illustrated.

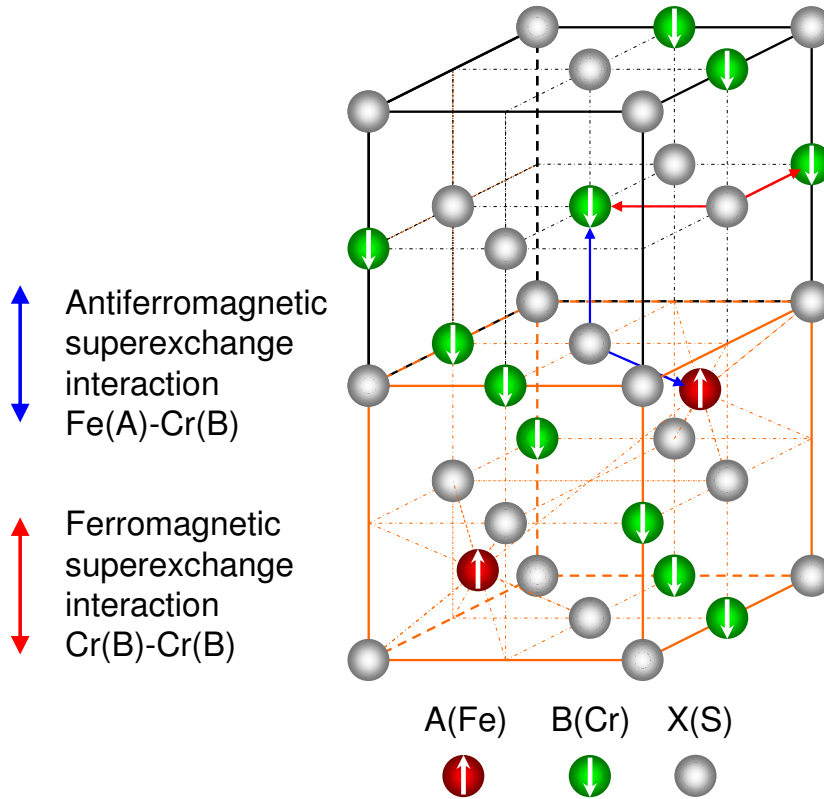


Figure 4.19: Illustration of two superexchange interactions in  $\text{Fe}_{1-x}\text{Cu}_x\text{Cr}_2\text{S}_4$ . One is an antiferromagnetic interaction between  $\text{Fe(A)}-\text{Cr(B)}$ , the other a ferromagnetic interaction between  $\text{Cr(B)}-\text{Cr(B)}$ . Here only the main part of the unit cell is shown. The spin direction is indicated by white arrows.

Often also a superexchange between the Fe ions is mentioned, but this can only be present in inverse spinels. Since  $\text{Fe}_{1-x}\text{Cu}_x\text{Cr}_2\text{S}_4$  has a normal spinel structure where Fe only occupies the A-site such an interaction is not possible. Figure 4.20 shows the interacting orbitals in more detail. In the  $90^\circ$   $\text{Cr}^{3+}$  - anion -  $\text{Cr}^{3+}$  interaction, a half-filled  $\pi$ -bonding t orbital shares a common anion p orbital with an empty  $\sigma$ -bonding e orbital on the neighbouring cation. According to Kanamori (1959) this results in a ferromagnetic spin interaction. In case of the  $123.2^\circ$   $\text{Fe}^{2+}$  - anion -  $\text{Cr}^{3+}$  interaction, not shown here, the prediction of the resulting spin interaction is difficult due to the changing symmetry and the not vanishing orbital moment of the  $\text{Fe}^{2+}$  ion. But experimental results proof that this interaction is antiferromagnetic.

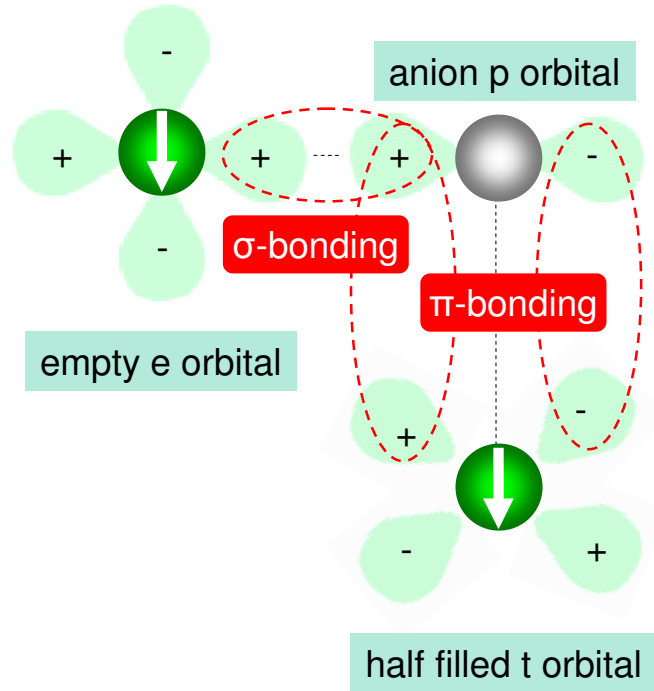


Figure 4.20: Interacting orbitals of the  $90^\circ$   $\text{Cr}^{3+}$  - anion -  $\text{Cr}^{3+}$  superexchange interaction.

The assumption of superexchange interactions to be responsible for the magnetism in  $\text{Fe}_{1-x}\text{Cu}_x\text{Cr}_2\text{S}_4$  is supported by Tsurkan *et al.* (2005). Here it is pointed out that the non-monotonic variation of the conductivity for  $0.2 < x < 0.5$ , the increase of  $T_C$  with decreasing lattice constant  $a_0$  and the insulating character of the samples for the whole substitution range, except  $x=1$ , indicate the superexchange to be the dominant magnetic exchange mechanism in  $\text{Fe}_{1-x}\text{Cu}_x\text{Cr}_2\text{S}_4$ . Here it has to be mentioned that there is evidence that beside the superexchange interaction additional exchange interactions are present in chalcogenide spinels (Yang *et al.*, 2004; Baltzer *et al.*, 1966). In case of Cr this could be easily seen by comparison of the magnetic ground state of  $\text{CdCr}_2\text{S}_4$  and  $\text{ZnCr}_2\text{S}_4$ .  $\text{CdCr}_2\text{S}_4$  is found to be ferromagnetic, while  $\text{ZnCr}_2\text{S}_4$  is an antiferromagnetic, even though they are isostructural. This could be explained by more distant neighbour antiferromagnetic Cr - Cr interactions competing with the nearest-neighbour ferromagnetic superexchange

interactions, both modulated by the distance between the Cr ions. Since  $\text{CdCr}_2\text{S}_4$  has a bigger lattice constant (lattice parameter 1.0243 nm) than  $\text{ZnCr}_2\text{S}_4$  (lattice parameter 0.9974 nm), it was deduced that in case of  $\text{CdCr}_2\text{S}_4$  the sum of the ferromagnetic superexchange interactions is stronger than that of the more distant neighbour anti-ferromagnetic Cr – Cr interactions.  $\text{ZnCr}_2\text{S}_4$  with a shorter Cr – Cr distance shows antiferromagnetism due to dominant more distant neighbour Cr – Cr interactions. Note that for  $\text{Fe}_{1-x}\text{Cu}_x\text{Cr}_2\text{S}_4$  the situation becomes more complex, since also magnetic ions are situated at the A-site making additional more distant neighbour interactions possible. This gives rise to canting or frustration effects in  $\text{Fe}_{1-x}\text{Cu}_x\text{Cr}_2\text{S}_4$ . As shown by Tsurkan *et al.* (2005) also the lattice parameter changes considerably with the Cu substitution  $x$ , which is significant for the spin interactions.

Since for  $\text{CuCr}_2\text{S}_4$  the lattice parameter (0.9925nm) is even smaller than for the antiferromagnetic  $\text{ZnCr}_2\text{S}_4$ , the origin of the ferromagnetic Cr ground state is unclear. One explanation for this could be an local atomic displacement due to exchangetriction (Martin *et al.*, 1969). In  $\text{CdCr}_2\text{S}_4/\text{Se}_4$  an anomalous absorption edge shift was found as the temperature decreases below the Curie temperature. This shift was attributed to a change in the lattice parameter. Although it could be shown that this change is too small to cause such a shift, Martin *et al.* (1969) admit that if the local atomic displacements attributed to exchangetriction are quite different from the local displacements associated with an equivalent unit cell change under hydrostatic pressure, exchangetriction could cause the absorption edge shift after all. If one assumes an exchangetriction to cause the Cr-Cr distance to increase in  $\text{CuCr}_2\text{S}_4$  without a unit cell parameter change, one could explain the different magnetic ground states of  $\text{CuCr}_2\text{S}_4$  and  $\text{ZnCr}_2\text{S}_4$ .

It also has to be mentioned that  $\text{CuCr}_2\text{S}_4$  is metallic in contrast to the semiconducting  $\text{CdCr}_2\text{S}_4$  and  $\text{ZnCr}_2\text{S}_4$ .  $\text{CuCr}_2\text{S}_4$ , which also shows mainly a  $d^{10}$  configuration at the A(Cu)-site (see section 4.3.2), can be seen as a heavily p-type doped  $\text{ZnCr}_2\text{S}_4$  causing the system to become metallic possibly due to reasons summerised in the next section. It will be shown that there is evidence for a strong interaction between charge carriers and local magnetic moments in these spinel systems. It is possible that this interaction supports a ferromagnetic Cr ground state making it stronger than the antiferromagnetic short range interaction.

In summary one can say that in  $\text{Fe}_{1-x}\text{Cu}_x\text{Cr}_2\text{S}_4$  the magnetism can be explained by exchange interactions. Thereby for the hole substitution range except  $x=1$  the dominant exchange interactions in  $\text{Fe}_{1-x}\text{Cu}_x\text{Cr}_2\text{S}_4$  seem to be superexchange interactions between Fe and Cr ions resulting in a ferrimagnetic ground state. However in chalcogenide spinel systems additional more distant neighbour interactions can be present and compete with the superexchange interactions. This could lead to spin canting or frustration effects. It was also mentioned that the ferromagnetic ground state of  $\text{CuCr}_2\text{S}_4$  ( $x=1$ ) could not be explained by the existing interaction models. As a possible explanation the interaction of charge carriers and local magnetic moments supporting ferromagnetism was mentioned.

#### 4.4.2 Conduction and magnetoresistance in $\text{Fe}_{1-x}\text{Cu}_x\text{Cr}_2\text{S}_4$

The temperature dependence of the resistivity and magnetoresistance of  $\text{Fe}_{1-x}\text{Cu}_x\text{Cr}_2\text{S}_4$  ( $x=0$ ,  $x=0.5$ ) are shown in figure 4.21 (panel (a) and (b)). As one can see, although there are differences in value and behaviour, the basic features of the so called metal to insulator (M-I) crossovers are the same. This is illustrated in panel (c). For  $T > T_C$  the resistivity increases with decreasing temperature exhibiting a maximum about  $T_C$  (area A). With further cooling the resistivity decreases (area B), but starts to increase again below a certain temperature far below  $T_C$  (area C). In addition both samples show a maximum of the MR-effect about  $T_C$ . As mentioned before with increasing substitution  $x$  the value of  $T_C$  increases monotonically, whereas the room temperature resistivity and the MR change non-monotonously exhibiting a minimum near  $x = 0.2$  and maximum at  $x = 0.5$  (Lotgering *et al.*, 1969; Haacke and Beegle, 1967; Ando *et al.*, 1979; Fritsch *et al.*, 2003).

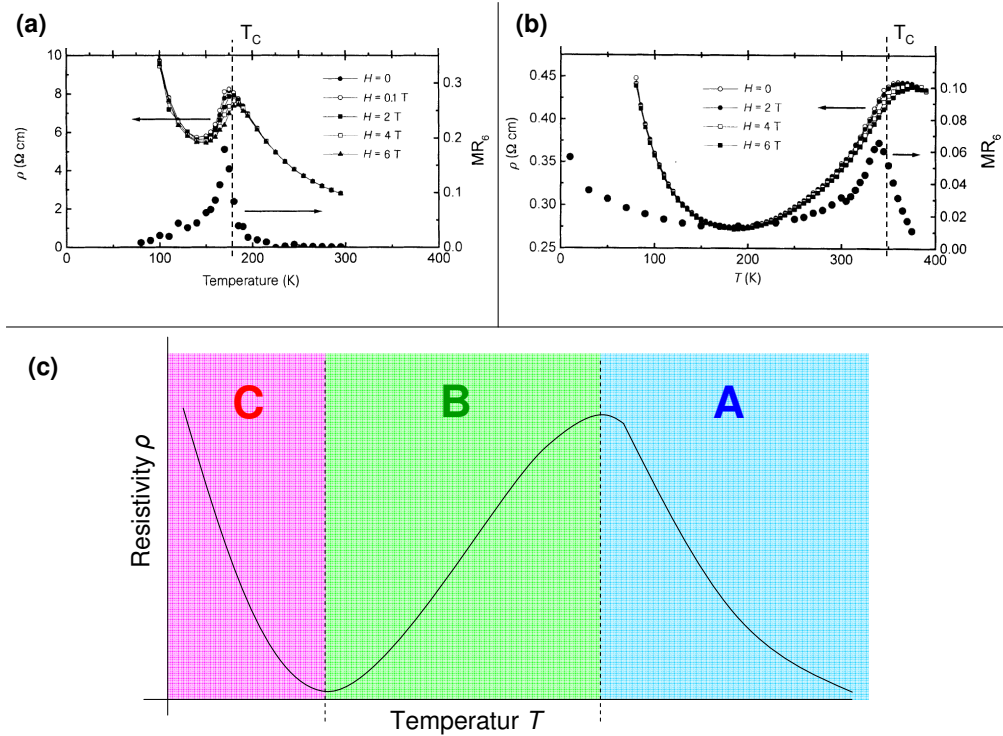


Figure 4.21: Resistivity and magnetoresistance versus temperature for  $\text{FeCr}_2\text{S}_4$  (panel (a)) and  $\text{Fe}_{0.5}\text{Cu}_{0.5}\text{Cr}_2\text{S}_4$  (panel (b)), attached from Ramirez *et al.* (1997). Panel (c) illustrates the characteristics of the resistivity spectra.

Since the tripleexchange process can not be responsible for the conduction mechanism in  $\text{Fe}_{1-x}\text{Cu}_x\text{Cr}_2\text{S}_4$  one has to think of other possible explanations for the resistivity- and MR-behaviour. Surprisingly in case of  $\text{Fe}_{1-x}\text{Cu}_x\text{Cr}_2\text{S}_4$  nearly no other models can be found that try to explain its electric properties. This is different for spinels like  $\text{CdCr}_2\text{S}_4$  or  $\text{CdCr}_2\text{Se}_4$ . Here one can find a variety of different conduction models. Since some of these systems are very similar to  $\text{Fe}_{1-x}\text{Cu}_x\text{Cr}_2\text{S}_4$  and show

nearly the same behaviour (Bongers *et al.*, 1969; Yang *et al.*, 2004), it is reasonable to introduce and discuss these theories.

### Band splitting model

The report of strange magnetic and electric properties of n-type doped  $\text{CdCr}_2\text{S}_4$  and  $\text{CdCr}_2\text{Se}_4$  (Lehmann and Robbins, 1966; Lehmann and Harbeke, 1967), including magnetoresistance, initialised a variety of different investigation and explanation efforts. One of the first models giving an explanation for the resistivity and MR behaviour was presented by Haas *et al.* (1967); Haas (1968); Bongers *et al.* (1969). Here it was assumed that there are two distinct types of electronic states in the crystal. One is derived mainly from outer s and p orbital states, which overlap strongly and are properly described by energy-band theory. The charge carriers are assumed to occupy states in this broad energy band. The other type of states is derived from 3d orbitals of the Cr-ions. Electrons in these d states are more localised and assumed to be responsible for the localised magnetic moments.

An interaction between charge carriers and the ionic spins now causes a splitting of the conduction band and can lead to two different effects. One is a possible intra-band or inter-band scattering of the charge carriers (spin disorder resistivity), changing their mobility (figure 4.22 panel (a)). The other is a change of the charge carrier concentration due to an additional splitting of the donor levels (figure 4.22 panel (b)). These effects are magnetic field and temperature dependent and affect the conductivity.

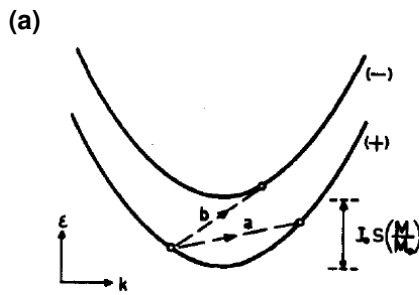


**FIG. 4**

**Splitting of the conduction band due to interaction between charge carrier spin and core spin. Process a: intra-band scattering; process b: inter-band (spin-flip) scattering.**

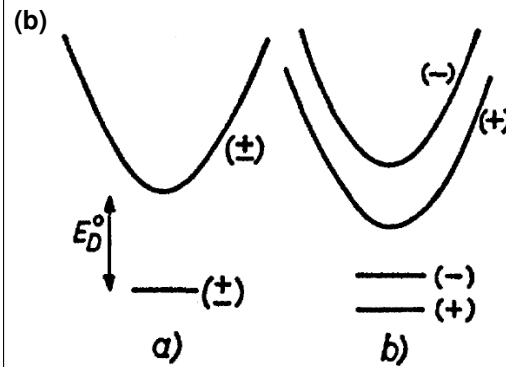


**FIG. 6. Donor levels in a ferromagnetic semiconductor: (a) paramagnetic region, with  $H=0$ ; (b) ferromagnetic region, or paramagnetic region, with  $H \neq 0$ .**

Figure 4.22: In panel (a) the conduction band splitting and the charge carrier scattering is illustrated (attached from Haas *et al.* (1967)). Panel (b) also illustrates the donor level splitting (attached from Haas (1968)).

The corresponding calculations give a good qualitative agreement with the resistivity and MR behaviour (see figure 4.23).

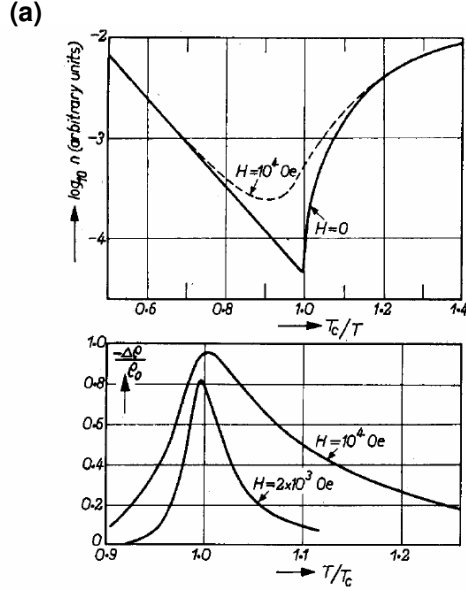


FIG. 2. Calculated curves [Eq. (3)], for an n-type ferromagnetic semiconductor, with  $S=\frac{1}{2}$ ,  $J=0.5$  eV,  $\gamma=\frac{1}{2}$  and  $E_D=0.2$  eV. (a) Carrier concentration as a function of reciprocal temperature. (b) Magnetoresistance for the case of a field-independent mobility, i.e., with  $\rho(H)/\rho(0) = n(0)/n(H)$ ;  $\Delta\rho = \rho(H) - \rho(0)$ .

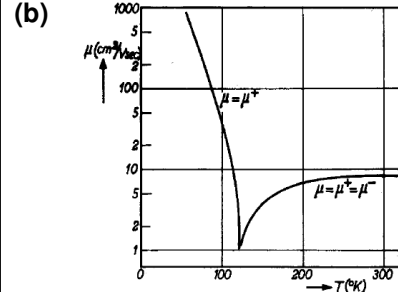


FIG. 3. Mobility  $\mu$  calculated for a ferromagnetic semiconductor as a function of temperature.

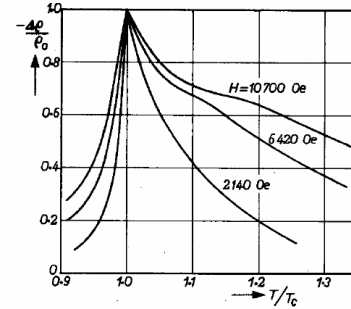


FIG. 4. Magnetoresistance, calculated for  $\text{CdCr}_2\text{Se}_4$  (i.e., with  $J=0.5$  eV), assuming that the carrier concentration is field independent.

Figure 4.23: Calculation results of the band splitting model. Panel (a) shows the carrier concentration versus reciprocal temperature and the magnetoresistance versus temperature, in case of a field-independent mobility. In panel (b) the mobility and the MR versus temperature in case of a field-independent carrier concentration is shown. Spectra are attached from Bongers *et al.* (1969)

However this model only is applicable for the temperature range around  $T_C$  (area A,B in figure 4.21 (c)). The behaviour at low temperatures (area C figure 4.21 (c)) can not be explained by this. In addition it was pointed out that the calculated mobilities are quite small showing strong scattering, for which this simple perturbation theory becomes less reliable. Also a possible appearance of magnons or magnetic polarons is mentioned, which is not considered in this model (Haas, 1968).

Bongers *et al.* (1969) further pointed out based on the valence model and energy level diagram of Lotgering *et al.* (1969) that in case of  $\text{Fe}_{1-x}\text{Cd}_x\text{Cr}_2\text{S}_4$  the magnetoresistance seems to be caused by a different mechanism. Lotgering *et al.* (1969) assumes a relative narrow  $\text{Fe}^{2+}$  band to be present in the energy gap. Since the described splitting model is based on charge carriers situated in a broad conduction band it is not applicable in this situation. Therefore the conduction in these materials is attributed to hopping  $\text{Fe}^{2+}$ ,  $\text{Fe}^{3+}$  conduction or to itinerant electrons (holes). But as shown above (section 4.3) the found experimental results contradict the Lotgering valence model and also Bongers *et al.* (1969) mentions that if the level diagram assumed by Lotgering would be correct n-type doped  $\text{FeCr}_2\text{S}_4$  should show a magnetoresistance effect, which is not the case.

### Magnon-hole interaction and Magnetic polaron conductivity

Haas (1968) pointed out that an increased but not too strong coupling between charge carriers and spins can lead to a so called magnon-drag effect (Wasscher and Haas, 1964). If the coupling becomes very strong, magnetic selftrapping of the charge carriers can occur, leading to magnetic polarons (von Molnar and Methfessel, 1967; Ramirez, 1997).

Haacke and Beegle (1966) found an anomalous increase of the thermoelectric power  $\alpha$  in p-type  $\text{FeCr}_2\text{S}_4$  near the Curie temperature and attributed it to a magnon-hole interaction. This assumption is based on the magnon-drag effect. This effect arises from a strong interaction between spin waves (magnons) and charge carriers through which additional carriers are dragged along a temperature gradient, thereby increasing the thermoelectric power  $\alpha$  above the normal diffusion term. In case of  $\text{FeCr}_2\text{S}_4$  it is assumed that the increase of  $\alpha$  is due to an increase of the kinetic energy of the charge carriers caused by an interaction between magnons and holes. An explanation for the resistivity and MR behaviour was not given.

A model involving magnetic polarons was published by Yang *et al.* (2000, 2004) to describe the conductivity in  $\text{Fe}_{1-x}\text{Cd}_x\text{Cr}_2\text{S}_4$ . Based on the experimental results of thermoelectric power measurements and Electron-Spin-Resonance (ESR) measurements it is concluded that magnetic polarons dominate the conduction above  $T_C$ . The decrease in the resistivity below  $T_C$  is explained by a gradual change of the conduction mechanism. Evidence was found that a paramagnetic state still exists at this temperature range making polaron formation possible. Due to this the resistivity in this region is described in terms of a two-fluid model concerning the coexistence of magnetic polarons and naked carriers. The naked carriers are assumed to originate from  $\text{Fe}^{2+}$  narrow bands. The increase of the resistivity and MR with increasing Cd substitution  $x$  is attributed to a decrease of the carrier density.

However the polaron conduction can only describe the resistivity behaviour above  $T_C$  and partly in a small temperature region below  $T_C$  where a paramagnetic state is still present (area A,B in figure 4.21 (c)).

### Mixed-Conduction Model

Amith and Gunsalus (1969) investigated the resistivity, the normal Hall coefficient and the thermoelectric power (Seebeck coefficient) of n-type doped  $\text{CdCr}_2\text{Se}_4$  (1-2% In). The result could not be explained by existing theories and did point to a multi-band model in which different mechanisms dominate at different temperatures. Later a mixed-conduction model was presented (Amith and Friedman, 1970) consisting of two bands, an n-type conduction band and a subsidiary hole band in the band gap. These bands are assumed to change their energy edges with temperature leading to the measured changes of resistivity, Hall coefficient and Seebeck coefficient.

Within this model the increase of the resistivity for  $T > T_C$  with decreasing temperature (area A in figure 4.21 (c)) is explained by an electron freeze out onto the donors in competition with an increase of the hole concentration. The decrease of the resistivity with further cooling (area B in figure 4.21 (c)) is attributed to a rapid increase of the electron concentration due to the reduction of the donor ionization energy while the hole concentration decreases and becomes insignificant. The increase of the resistivity



at low temperatures (area C in figure 4.21 (c)) is ascribed to impurity conduction. It was pointed out that the resistivity like the Hall coefficient behaviour strongly indicate a change in the carrier density rather than a mobility variation and that the presented dual band model is the simplest one which can account for the measured data in a consistent manner. Furthermore it is shown that the results cannot be explained in terms of a single band, even if the spin splitting of the band and the effect of spin-disorder scattering are included (see *band splitting model* above), nor in terms of two n-type conduction bands.

It has to be mentioned that this model differs from the previous mentioned theories in that extrinsic sources of charge carriers, like added indium impurities and intrinsic defects, are assumed to be essential for the electric behaviour. The postulated p-type band situated in the band gap cannot be the materials intrinsic valence band, since this lies much too far below the conduction band to account for any free holes. Therefore it is assumed that this hole band originates from combined effects of added indium impurities and intrinsic defects. In more detail two electrons are expected to arise from a missing selenium ion in a selenium-deficient sample. These electrons now can fill an impurity band formed by the indium donor in the n-type doped  $\text{CdCr}_2\text{Se}_4$  resulting in an more-than-half-filled band with p-like behaviour. The donor levels are ascribed not to the In ions, but to selenium deficiencies. This interpretation of the roles of the indium and selenium defects is strongly supported by experimental findings. It was shown that vacuum-annealing of a not doped p-type  $\text{CdCr}_2\text{Se}_4$  sample (increased selenium deficiencies) leads to a negative Seebeck coefficient indicating n-type conduction even without indium doping. On the other hand defect free samples showed p-type conduction regardless of whether or not they were doped with indium. In addition in defect free n-type doped samples the decrease of the resistivity about  $T_C$  was absent like in not-doped samples. This strongly suggest that selenium deficiencies are indeed responsible for the n-type conduction and that indium impurities are essential for the resistivity behaviour.

Note that the dual band model gives an explanation for a lot of experimental results but is not directly concerned with the magnetoresistance effect.

### Magnetic impurity state (MIS) model

Larsen and Voermans (1973) investigated n-type doped (2% Ga)  $\text{CdCr}_2\text{Se}_4$  and  $\text{CdCr}_2\text{S}_4$  samples that were differently treated. A model was introduced explaining the resistivity maximum and the negative magnetoresistance around  $T_C$  not with a change in the mobility and/or the number of charge carriers in the conduction band, but with a so called magnetic impurity state (MIS)-type conduction. In this model, originally proposed for EuSe and EuS (Kasuya and Yanase, 1968), a point defect structure, also called Schottky-Wagner defect structure, with vacancies of chalcogen and cadmium is considered to be present. The concentration of this defects is altered by annealing of the samples at different gas pressure.

It was found that in undoped samples a resistivity maximum near  $T_C$  as well as a considerably large MR was absent. Therefore it was concluded that if the present conduction mechanism can be ascribed to charge carriers in the conduction band, the long range magnetic ordering has practically no influence on the electron mobility and the numbers of electrons in the conduction band. This is in contradiction to the

spin splitting model. The resistivity behaviour for undoped samples is explained by an decrease of the electron density in the conduction band, that is partly cancelled by an increase of the mobility.

Samples that were doped with 2 per cent Ga showed a resistivity maximum near  $T_C$  and a large MR. It is believed that at high temperatures (area A in figure 4.21 (c)) the conductivity is the sum of a band conductivity and an impurity conductivity. The conduction is assumed to be determined by the electrons ionised into the conduction band, whereas the Ga dopant forms an impurity band separated from the conduction band, which can participate in the conduction if partly filled. According to the MIS model the s-d exchange interaction may be the main source of the activation energy. This energy is needed to align the spins between a  $\text{Ga}^{3+}$  and a  $\text{Cr}^{3+}$  ion in spite of an empty donor place, which enables electrons to move from an occupied to an unoccupied donor position. The activation energy decreases with increasing magnetic ordering. Therefore the impurity conduction increases with decreasing temperature. The resistivity maximum (area B in figure 4.21 (c)) will be observed at the temperature where the main conduction mechanism shifts from band conduction to impurity conduction. Since the activation energy is influenced by the magnetic ordering an external magnetic field can change the resistivity, which leads to the negative magnetoresistance. It is further proposed that the anomaly of the thermoelectric power is due to spin polarisations around the s-electrons in the impurity band.

The conduction via magnetic impurities can explain the MR and resistivity behaviour in differently treated  $\text{CdCr}_2\text{Se}_4$  and  $\text{CdCr}_2\text{S}_4$  in the  $T_C$  temperature region (area A and B in figure 4.21 (c)). But the increase of the resistivity for low temperatures (area C in figure 4.21 (c)) can not be explained by this model.

### In summary

Now it becomes clear that there are a lot of different explanations for the anomalous electric behaviour of chalcogenide spinel systems. Some models propose intrinsic mechanisms to be responsible for the conductivity, other models involve extrinsic charge carrier sources. Also the temperature region for which the models are appropriate differs.

In my opinion an adequate model describing the resistivity behaviour of chalcogenide spinel systems has to involve extrinsic conduction mechanisms. This is most likely also the case for the  $\text{Fe}_{1-x}\text{Cu}_x\text{Cr}_2\text{S}_4$  system. The simple fact that there are no mixed valence states found to be present in the bulk of  $\text{Fe}_{1-x}\text{Cu}_x\text{Cr}_2\text{S}_4$  makes the formation of S holes and/or defects necessary for charge compensation. As shown in Amith and Friedman (1970) and Larsen and Voermans (1973) the formation of chalcogenide defects is essential for the electric behaviour of these compounds. Without defects these materials do not show an anomalous resistivity behaviour. Interestingly also a small n-type doping (about 2% In or Ga) seems to be necessary for the resistivity maximum and MR in  $\text{CdCr}_2\text{Se}_4$  and  $\text{CdCr}_2\text{S}_4$ . Such a small doping due to  $\text{Fe}^{3+}$  ions could also be present in  $\text{Fe}_{1-x}\text{Cu}_x\text{Cr}_2\text{S}_4$ , since XAS measurement would not detect such a small  $\text{Fe}^{3+}$  amount. Therefore I would propose a model involving the dual band conduction and/or the magnetic impurity state (MIS) conduction. These models can not only explain the anomalous electric behaviour of these materials, but also the changes due to different doping and treatment. The fact that also Lotgering

*et al.* (1969) found a complete change of the Seebeck coefficient caused by different treatment of  $\text{Fe}_{0.5}\text{Cu}_{0.5}\text{Cr}_2\text{S}_4$  strongly supports this.

The changes of the MR and resistivity with the Cu substitution  $x$  in  $\text{Fe}_{1-x}\text{Cu}_x\text{Cr}_2\text{S}_4$  can thereby be explained by a change of the amount of magnetic impurities and/or chalcogenide defects. According to the MIS model also the exchange interactions of the spin magnetic moments is important for the impurity conduction. Tsurkan *et al.* (2005) showed that the lattice constant changes considerably with  $x$ , which would affect exchange interactions. In addition as shown in figure 4.24 the possible pathways of the superexchange interaction between Fe and Cr ions is significantly changed by  $x$ .

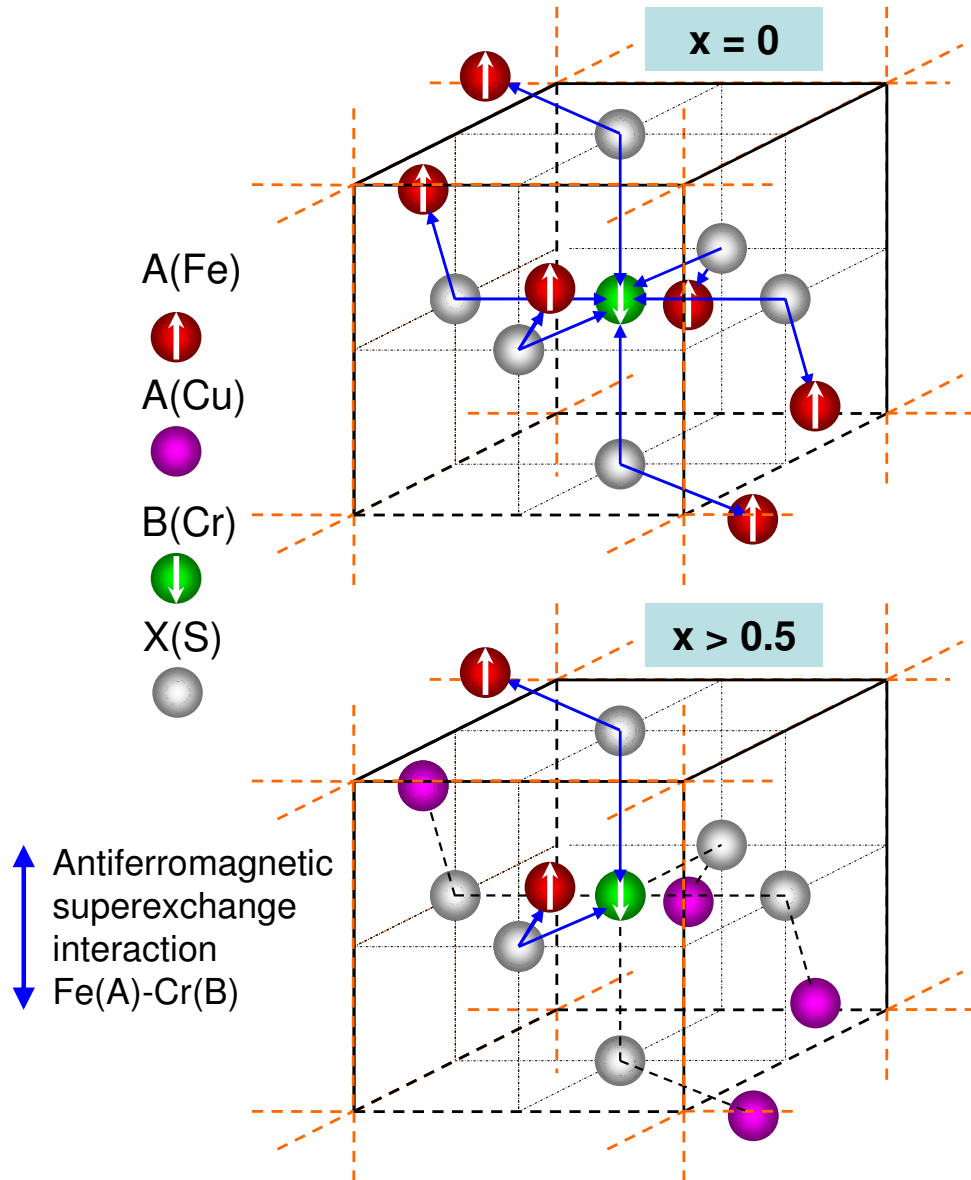


Figure 4.24: Possible channels of the Fe(A)–Cr(B) antiferromagnetic superexchange interaction in  $\text{Fe}_{1-x}\text{Cu}_x\text{Cr}_2\text{S}_4$  for different Cu concentrations.

The finding of a considerable  $\text{Fe}^{3+}$  and a small  $\text{Cu}^{2+}$  amount on the surface of air treated  $\text{Fe}_{0.5}\text{Cu}_{0.5}\text{Cr}_2\text{S}_4$  single crystals also introduces an additional source of extrinsic charge carriers, since many conduction experiments are performed in air and/or on powdered samples. It is likely that an impurity layer on the surface of  $\text{Fe}_{1-x}\text{Cu}_x\text{Cr}_2\text{S}_4$  plays a significant role in the conduction mechanisms.

Here it has to be mentioned that all these models are concerned with the resistivity and MR behaviour of the Curie temperature region in the first place (area A and B in figure 4.21 (c)). The reason of the resistivity increase at low temperatures (area C in figure 4.21 (c)) is still unclear. In case of  $\text{CdCr}_2\text{Se}_4$  it was assumed that this behaviour is due to an impurity conduction (Kondo effect) (Amith and Gunsalus, 1969).

## 4.5 Conclusion

The valence state of the Cu and Cr ions in  $\text{Fe}_{1-x}\text{Cu}_x\text{Cr}_2\text{S}_4$  ( $x = 0.2, 0.5, 0.6, 0.9$ ) single crystals was investigated using XPS spectroscopy. The results indicate that Cu and Cr remain mainly monovalent and trivalent, respectively, throughout the various Cu concentrations. Furthermore XAS, XPS and XMCD measurements of single crystalline  $\text{Fe}_{0.5}\text{Cu}_{0.5}\text{Cr}_2\text{S}_4$  were performed. The comparison with reference measurements and literature data revealed that a small amount of  $\text{Cu}^{2+}$  observed in  $\text{Fe}_{0.5}\text{Cu}_{0.5}\text{Cr}_2\text{S}_4$  is sample dependent and therefore most likely related to an impurity phase, possibly due to oxidation on the surface.

In addition the measurements do not show trivalent Fe ions to be present in in-situ cleaned  $\text{Fe}_{0.5}\text{Cu}_{0.5}\text{Cr}_2\text{S}_4$ . Reference measurements and multiplet calculations clearly identify divalent Fe ions in the measured spectra of the sample bulk. Also evidence was found that the only known reference that claimed to have measured XAS and XMCD spectra of  $\text{Fe}^{3+}$  in  $\text{Fe}_{0.5}\text{Cu}_{0.5}\text{Cr}_2\text{S}_4$  (Deb *et al.*, 2003) most likely measured divalent Fe ions as well.

However a considerable amount of  $\text{Fe}^{3+}$  was found to be present in the surface layers of  $\text{Fe}_{0.5}\text{Cu}_{0.5}\text{Cr}_2\text{S}_4$  samples, that were not cleaned in-situ prior to the measurements. It also could be shown that in samples treated in air, especially in powdered samples, a considerable amount of  $\text{Fe}^{3+}$  appears. In addition XAS measurements with different beam positions on the in-situ cleaved surface of a small  $\text{Fe}_{0.5}\text{Cu}_{0.5}\text{Cr}_2\text{S}_4$  sample gave evidence that the Fe valence change can reach surprisingly deep into the sample bulk. Since many complementary experiments use powdered samples and measure in air or low vacuum, the finding of this Fe valence instability might explain the differing results concerning the Fe valence in  $\text{Fe}_{0.5}\text{Cu}_{0.5}\text{Cr}_2\text{S}_4$ .

Calculation of the magnetic moments from the XMCD measurements revealed the Fe and Cr spin magnetic moments to be significantly reduced compared to the ionic ones. Possible explanations were discussed revealing the sample preparation and the found Fe valence change in the surface layers to be most likely involved causing magnetic frustration and/or surface anisotropy. Differences in the orbital moments in comparison to published values give rise to the assumption of a change of the crystal field, thus the crystal structure, at the sample surface.

In summary, these results provide evidence that the Cu- and Cr-ions in the bulk of  $\text{Fe}_{1-x}\text{Cu}_x\text{Cr}_2\text{S}_4$  do not change their valence state over the whole Cu concentration

range. Furthermore, these data suggest that most of the Fe ions stay divalent at least for  $x \leq 0.5$ . Since without a mixed Fe valence state the tripleexchange process fails to describe the electric and magnetic behaviour of  $\text{Fe}_{1-x}\text{Cu}_x\text{Cr}_2\text{S}_4$ , other models explaining the conduction mechanism and magnetism in chalcogenide spinel systems were introduced and discussed. The ferrimagnetic ground state could be explained by inter- and intrasublattice superexchange interactions between the Cr and Fe ions. Concerning the anomalous electric behaviour of  $\text{Fe}_{1-x}\text{Cu}_x\text{Cr}_2\text{S}_4$  it was found that an appropriate model has to involve extrinsic charge carrier sources like chalcogenide defects and/or magnetic impurities. Furthermore the experimental results also give rise to the assumption of an additional extrinsic charge carrier source. It is imaginable that an impurity layer on the surface of  $\text{Fe}_{1-x}\text{Cu}_x\text{Cr}_2\text{S}_4$  plays a significant role in the conduction mechanisms.



# Chapter 5

## Summary and Outlook

### 5.1 Summary

In this work the electronic and magnetic structure of various chalcogenide systems was investigated by means of X-ray spectroscopic techniques.

In chapter 1 the history of X-ray spectroscopy is introduced together with basics concerning the measurement techniques X-ray photoelectron spectroscopy (XPS), X-ray absorption spectroscopy (XAS) and X-ray magnetic circular dichroism (XMCD), their spectral features and instrumentation. In addition a short introduction in multiplet calculations and magnetism is given.

The goal of this work was the investigation of iron (Fe) in various chalcogenides in order to reveal reasons for the contradictory results found in the attempt to clarify the electronic and magnetic Fe state in these compounds. This is essential if one wants to understand the interesting electric and magnetic properties of these materials and highly necessary for the development of new materials, electric structures and devices for future applications.

The main finding of this work is the presents of a valence instability of the Fe ions in many chalcogenide advanced materials. Thereby the Fe valence-change process seems to differ between the crystalline and molecular materials. The crystals show a temporally change of the Fe valence state from  $\text{Fe}^{2+}$  to  $\text{Fe}^{3+}$  at the surface layers while stored ex situ (oxidation like process). In contrast to this for the molecules a Fe valence state change from  $\text{Fe}^{3+}$  to  $\text{Fe}^{2+}$  is found induced by a photon beam (reduction like process). In the following the results of this thesis are summarised in more detail.

#### 5.1.1 Fe in different chalcogenide compounds

In chapter 2 an overview of Fe 2p XAS and XMCD measurements on different chalcogenide systems was given. The investigated materials were the crystals  $\text{Sr}_2\text{FeMoO}_6$ ,  $\text{Fe}_{0.5}\text{Cu}_{0.5}\text{Cr}_2\text{S}_4$  and  $\text{LuFe}_2\text{O}_4$  as well as the molecules FeStar,  $\text{Mo}_{72}\text{Fe}_{30}$  and  $\text{W}_{72}\text{Fe}_{30}$ . The measurements revealed additional temporally effects changing the magnetic and electronic iron state in these compounds. Thereby the crystalline materials showed a different behaviour than the molecular ones. In case of the crystals a chemical change seems to occur ex situ with time, which leads to the appearance of paramagnetic or antiferromagnetic  $\text{Fe}^{3+}$  ions at the surface layers. In contrast to this

for the molecules a structure and/or valence instability seems to be present activated by the synchrotron beam, which leads to the appearance of  $\text{Fe}^{2+}$  ions showing an overall magnetic alignment. Evidence was found that this instability is caused by the ligand structure of the molecules.

- XAS and XMCD measurements of  $\text{Sr}_2\text{FeMoO}_6$  crystals gave first evidence for a change of the Fe valence state with time described and discussed in more detail in chapter 3. It could be shown that with ageing of the samples an increase of the  $\text{Fe}^{3+}$  contribution to the absorption spectrum occurred, which could not be seen in the XMCD signal indicating a para- or antiferromagnetic ground state of the ions.
- XAS and XMCD measurements of  $\text{Fe}_{0.5}\text{Cu}_{0.5}\text{Cr}_2\text{S}_4$  revealed a similar effect. Here the whole  $\text{Fe}^{3+}$  contribution to the absorption spectrum was found to be due to changes of the Fe valence state. Further investigations of differently treated samples indicated that the trivalent Fe ions are only present in the surface layers, while the bulk of the sample only contains divalent Fe ions. This led to new explanations for the interesting magnetic and electric properties of  $\text{Fe}_{0.5}\text{Cu}_{0.5}\text{Cr}_2\text{S}_4$  described and discussed in more detail in chapter 4.
- Also for the crystal  $\text{LuFe}_2\text{O}_4$  an increased  $\text{Fe}^{3+}$  amount was detected in the XAS spectrum measured in the surface sensitive total electron yield (TEY) mode. By assuming this additional  $\text{Fe}^{3+}$  ions also to be due to an ageing effect and not to contribute to the dichroic signal, the XAS and XMCD spectra could be well simulated by multiplet calculations. Thereby it could be shown that no frustration is present in the Fe magnetic ground state of  $\text{LuFe}_2\text{O}_4$ .
- Investigation of the FeStar molecule revealed at least 90% of the Fe ions to be divalent in contradiction to basic magnetochemical investigations and magnetic measurements showing all Fe ions to be trivalent. In the following evidence was found that the photon beam radiated onto the sample causes a change of the Fe valence state from  $\text{Fe}^{3+}$  to  $\text{Fe}^{2+}$  and a structure distortion of the ferric star molecule. Comparison with the very similar  $\text{Fe}_4$  molecule revealed the ligand structure in the FeStar to be most likely responsible for this instability.
- Finally the molecules  $\text{Mo}_{72}\text{Fe}_{30}$  and  $\text{W}_{72}\text{Fe}_{30}$  were investigated. In both compounds Fe is predicted to be trivalent surrounded by oxygen octahedrally. While this could be supported by XAS and XMCD measurements in case of  $\text{W}_{72}\text{Fe}_{30}$ , for  $\text{Mo}_{72}\text{Fe}_{30}$  about 45% of the Fe ions were detected to be divalent. In addition indication for a distortion of the Fe surrounding in  $\text{Mo}_{72}\text{Fe}_{30}$  was found. Since the ligand structure of  $\text{Mo}_{72}\text{Fe}_{30}$  differs considerably from the one of  $\text{W}_{72}\text{Fe}_{30}$  it could be concluded that, like found for the FeStar molecule, also in case of the  $\text{Fe}_{30}$  molecules the ligand structure could cause a structure and/or Fe valence instability.

### 5.1.2 Ageing effect in $\text{Sr}_2\text{FeMoO}_6$

In chapter 3 Fe 2p XAS and XMCD measurements of the double perovskite  $\text{Sr}_2\text{FeMoO}_6$  were compared to charge transfer multiplet calculations. While in the



absorption spectrum a surprisingly high amount of trivalent Fe was found, in the XMCD measurement the  $\text{Fe}^{3+}$  signal was not increased. This led to the assumption of para- or antiferromagnetic  $\text{Fe}^{3+}$  ions to occur in  $\text{Sr}_2\text{FeMoO}_6$ .

Based on these findings Fe 2p XAS and XMCD measurements of  $\text{Sr}_2\text{FeMoO}_6$  that recurred over several years were compared to CT multiplet calculations. This revealed an ageing effect causing a considerable increase of para- or antiferromagnetic  $\text{Fe}^{3+}$  ions in  $\text{Sr}_2\text{FeMoO}_6$  samples with time. As a possible explanation the appearance of  $\text{SrFeO}_{3-x}$  particles was assumed. Since in  $\text{Sr}_2\text{FeMoO}_6$  not a double-exchange process was found to cause the magnetoresistive behaviour, but an impurity induced tunnelling-type magnetoresistance (TMR) process, it was pointed out that the found ageing effect could have a major influence on the magnetoresistive properties of  $\text{Sr}_2\text{FeMoO}_6$  crucial for possible future applications.

### 5.1.3 Valence states in $\text{Fe}_{1-x}\text{Cu}_x\text{Cr}_2\text{S}_4$

In chapter 4 the valence states of Cu, Cr and Fe in  $\text{Fe}_{1-x}\text{Cu}_x\text{Cr}_2\text{S}_4$  ( $x = 0.2, 0.5, 0.6, 0.9$ ) single crystals were investigated using XAS, XMCD and XPS. The results indicated that the Cu and Cr ions remain mainly monovalent and trivalent, respectively, throughout the various Cu concentrations. Furthermore the Fe ions were found to stay divalent at least for  $x \leq 0.5$ .

In addition the investigation of  $\text{Fe}_{0.5}\text{Cu}_{0.5}\text{Cr}_2\text{S}_4$  revealed  $\text{Cu}^{2+}$  and  $\text{Fe}^{3+}$  to be present in the sample most likely due to an ageing effect. Samples treated in air especially when pulverised showed a considerable high amount of trivalent Fe. However when cleaned in situ the whole  $\text{Fe}^{3+}$  signal disappeared showing only divalent Fe to be present in the bulk of the sample. Comparison with literature results and reference measurements revealed the  $\text{Cu}^{2+}$  amount to be sample dependened, possibly also due to an ageing effect. Since many complementary experiments use powdered samples and measure in air or low vacuum, this finding might explain the differing results concerning the Fe and Cu valence in  $\text{Fe}_{0.5}\text{Cu}_{0.5}\text{Cr}_2\text{S}_4$ .

Since without a mixed Fe valence state the tripleexchange process fails to describe the electric and magnetic behaviour of  $\text{Fe}_{1-x}\text{Cu}_x\text{Cr}_2\text{S}_4$ , other models explaining the conduction mechanism and magnetism in chalcogenide spinel systems were introduced and discussed. Thereby the ferrimagnetic ground state could be explained by inter- and intrasublattice superexchange interactions between the Cr and Fe ions. Concerning the anomalous electric behaviour of  $\text{Fe}_{1-x}\text{Cu}_x\text{Cr}_2\text{S}_4$  it was found that an appropriate model has to involve extrinsic charge carrier sources like chalcogenide defects and/or magnetic impurities. Furthermore the experimental results also gave rise to the assumption of an additional extrinsic charge carrier source. It was assumed that an impurity layer on the surface of  $\text{Fe}_{1-x}\text{Cu}_x\text{Cr}_2\text{S}_4$  could play a significant role in the conduction mechanisms.

## 5.2 Outlook

In this work evidence was found that for many different compounds the electronic and magnetic state of iron changes due to sample ageing, the sample treatment or the measurement technique (photon radiation). In the next step it would be appropriate

to further elucidate the origin and course of these changes.

In case of the crystalline materials like  $\text{Fe}_{1-x}\text{Cu}_x\text{Cr}_2\text{S}_4$ ,  $\text{Sr}_2\text{FeMoO}_6$  and  $\text{LuFe}_2\text{O}_4$  it would be interesting to study the time dependence of the found ageing effect in more detail. The investigation of samples that were exposed to chosen atmospheres and pressures for different time periods could help to find out more about this effect. In addition to get more information about the characteristics of the found surface changes, aged samples could be investigated with Atomic Force Microscopy (AFM), Scanning Tunneling Microscope (STM) or X-ray Diffraction (XRD). It also would be important to find out how the found changes could affect or initiate the anomalous magnetic and electronic behaviour of these materials.

In case of the molecular materials like FeStar,  $\text{Mo}_{72}\text{Fe}_{30}$  and  $\text{W}_{72}\text{Fe}_{30}$  it would be interesting to study the influence of the ligand structure on the valence or structure instability in more detail. For instance the production of  $\text{Mo}_{72}\text{Fe}_{30}$  and  $\text{W}_{72}\text{Fe}_{30}$  with both types of ligand structures could help to identify the origin of this effect. Also the investigation of samples already radiated and changed with a photon beam could give a lot of information about the course and characteristics of this light induced effect. Note that this investigation could also be extended to molecules containing different magnetic elements. For instance, experimental results indicate that a similar valence instability could be present for manganese (Mn) and copper (Cu) containing molecules (Prinz, 2009; Taubitz).

# Acknowledgement

It is gratefully acknowledged that this work was facilitated by the Ph.D. program ”*Synthesis and Characterisation of Surfaces and Interfaces assembled from Clusters and Molecules*” of Lower Saxony, Germany. Furthermore I want to acknowledge the financial support by the Department of Physics of the University of Osnabrück.

At first I want to thank **apl. Prof. Prof. h.c. Dr. Dr. h.c. Manfred Neumann** for enabling me to do this work in his working group *Elektronenspektroskopie* at the University of Osnabrück. His scientific experience, intuition and guidance were an essential help and made this work possible. Furthermore his support of and interest in social activities developed a nice and friendly atmosphere in the working group.

Then I have to thank collaborating scientists for their scientific help and support. First of all **Dr. Karsten Küpper**, who always was a guide and supporter of my scientific approaches. No e-mail remained unanswered and no request unattended. His help was the cornerstone of this work.

I also want to thank **Prof. Dr. Frank de Groot** from the Department of Inorganic Chemistry and Catalysis of the University of Utrecht. He provided us with the TTMultiplet program, which made the simulations presented in this work possible. Furthermore discussions with him were very fruitful and helped understanding the experimental results.

**Prof. Dr. Vladimir Tsurkan** from the Academy of Science of Moldova is acknowledged for providing the spinel system  $\text{Fe}_{1-x}\text{Cu}_x\text{Cr}_2\text{S}_4$ . His work and help led to the findings presented here.

Then I want to thank **Prof. Dr. Vadim R. Galakhov** from the Ural State Mining University in Yekaterinburg for his measurement support at the BESSY synchrotron in Berlin. He also provided me with reference measurements that helped a lot to understand the experimental results.

Here also the **working group of Prof. Dr. Tjeng** from the II. Physical Institute of the University of Köln has to be mentioned. They kindly made some measurement period available at the NSRRC synchrotron in Taiwan and measurements on the  $\text{Fe}_{0.5}\text{Cu}_{0.5}\text{Cr}_2\text{S}_4$  spinel possible. These measurements confirmed my assumptions in every way.

Of course I also have to thank all the **beamline scientists** at the ALS in Berkeley (USA), the BESSY in Berlin, the DELTA in Dortmund and the SLS in Villigen (Switzerland), which supported me during my measurement periods. Regardless of what and when a problem occurred at the beamline they always were willing to help.

Now I want to mention my working group at the University of Osnabrück. This group enabled me to graduate as Bachelor- and Master of Science and guided me through my Ph.D. time. Thereby in the past six years this group became more than a working place, it was a friendly and wonderful part of my live.

At first I want to mention **Dr. Michael Räkera**. He became a good friend during my studies and also a hard working and competent colleague during my stay at the working group. His support and friendship helped me overcome several kickbacks.

Also **Dr. Manuel Prinz** became a good friend rather than a colleague. He introduced me to the world of metal containing molecules as well as to the world of heavy metal bands.

In the last years **Dipl. Phys. Christine Derks** and **Dipl. Phys. Anna Buling** joined the working group as diploma students and later as my Ph.D. colleagues. While becoming valuable and experienced co-workers they also became good friends, which I have to thank for the great time.

I also want to mention **Dipl. Phys. Stefan Bartkowski**. His long experience with photoelectron spectroscopy and his great skills in handling the ESCA was a wonderful gift during my Ph.D. time.

Then I also have to mention **Werner Dudas**, who helped me a lot during my measurement periods at the DELTA in Dortmund.

Of course I also want to thank my little brother **B. Sc. Daniel Taubitz**, who achieved his Bachelor degree in this working group and is now becoming a diploma student. His constant good mood and optimism often eased my mind and helped me go on.

There are also a lot of former members of the working group, which I want to thank here for their help and the great time. To mention just a few: **Dipl. Phys. Miriam Baensch**, **Dipl. Phys. Niklas Damnik**, **Dipl. Phys. Sabine Binder**, **Dipl. Phys. Sebastian Voget**, **Dr. Wasile** and **Lydia Rednic**.

I also want to thank the Department of Physics of the University of Osnabrück.

Without the help and support of the **electrical and mechanical workshops** a lot of measurements would not have been possible.

The **crystal growth facility** helped me a lot with the preparation of my samples.

Also the nice working atmosphere in the Department, which is due to the kind and helpful **secretaries** has to be acknowledged. Here I especially want to mention **Marion von Landsberg**, **Claudia Meyer** and **Kerstin Brockhues**.

Finally I hearty want to thank my **Family and Friends**, which supported me the whole time. They gave me a place to come home.

# Bibliography

- Abbate, M., G. Zampieri, J. Okamoto, A. Fujimori *et al.* (2002). X-ray absorption of the negative charge-transfer material  $\text{SrFe}_{1-x}\text{Co}_x\text{O}_3$ . *Phys. Rev. B* **65**, 165120.
- Accorsi, S., A. L. Barra, A. Caneschi, G. Chastanet *et al.* (2006). Tuning Anisotropy Barriers in a Family of Tetrairon(III) Single-Molecule Magnets with an  $S=5$  Ground State. *J. Am. Chem. Soc.* **128**, 4742.
- Amith, A. and L. Friedman (1970). Mixed-Conduction Model for Charge Transport in n-Type  $\text{CdCr}_2\text{Se}_4$ . *Phys. Rev. B* **2**, 434.
- Amith, A. and G. L. Gunsalus (1969). Unique behavior of Seebeck Coefficient in N-Type  $\text{CdCr}_2\text{Se}_4$ . *Journal of Applied Physics* **40**, 1020.
- Anderson, P. W. (1950). Antiferromagnetism. Theory of Superexchange Interaction. *Phys. Rev.* **79**, 350.
- Ando, K., Y. Nishihara, T. Okuda and T. Tsuchima (1979). Hall effect and magnetoresistance in  $\text{Fe}_{1-x}\text{Cu}_x\text{Cr}_2\text{S}_4$ . *J. Appl. Phys.* **50**, 1917.
- Angst, M., R. P. Hermann, A. D. Christianson, M. D. Lumsden *et al.* (2008). Charge Order in  $\text{LuFe}_2\text{O}_4$ : Antiferroelectric Ground State and Coupling to Magnetism. *Phys. Rev. Letters* **101**, 227601.
- Arenholz, E. and S. O. Prestemon (2005). Design and performance of an eight-pole resistive magnet for soft x-ray magnetic dichroism measurements. *Rev. Sci. Instrum.* **76**, 083908.
- Attwood, D. (1999). *Soft X-rays and Extreme Ultraviolet Radiation*. Cambridge University Press.
- Auger, P. (1925). Sur l'Effect Photoelectrique Compose. *Le Journal de Physique et le Radium* **6**, 205.
- Bagus, P. S., A. J. Freeman and F. Sasaki (1973). Prediction of New Multiplet Structure in Photoemission Experiments. *Phys.Rev.Letters* **30**, 850.
- Bakuzis, A. F. and P. C. Morais (2001). On the origin of the surface magnetic anisotropy in manganese-ferrite nanoparticles. *J. Magn. Magn. Matter* **226-230**, 1924.
- Balcells, L., J. Navarro, M. Bibes, A. Roig *et al.* (2001). Cationic ordering control of magnetization in  $\text{Sr}_2\text{FeMoO}_6$  double perovskite. *appl.phys.letters* **78**, 781.
- Baltzer, P. K., P. J. Wojtowicz, R. M. and E. Lopatin (1966). Exchange Interaction in Ferromagnetic Chromium Chalcogenide Spinel. *Phys. Rev.* **151**, 367.
- Barra, A. L., A. Caneschi, A. Cornia, F. Fabrizi de Biani *et al.* (1999). Single-Molecule Magnet Behavior of a Tetranuclear Iron(III) Complex. The Origin of Slow Magnetic Relaxation in Iron(III) Clusters. *J. Am. Chem. Soc.* **121**, 5302.

- Besse, M., V. Cros, A. Barthelemy, H. Jaffres *et al.* (2002). Experimental evidence of the ferromagnetic ground state of  $\text{Sr}_2\text{FeMoO}_6$  probed by X-ray magnetic circular dichroism. *Eur. Phys. Letters* **60**, 608.
- Bodker, F., S. Morup and S. Linderorth (1994). Surface Effects in Metallic Iron Nanoparticles. *Phys.Rev.Letters* **72**, 282.
- Bongers, P. F., C. Haas, A. M. J. G. van Run and G. Zanmarchi (1969). Magnetoresistance in Chalcogenide Spinels. *Journal of Applied Physics* **40**, 958.
- Butler, P. H. (1981). *Point Group Symmetry Applications: Methods and Tables*. Plenum Press: New York.
- Carra, P., B. T. Thole, M. Altarelli and X. Wang (1993). X-ray Circular Dichroism and local magnetic fields. *Phys. Rev. Letters* **70**, 694.
- Chastain, J. (1992). *Handbook of X-ray Photoelectron Spectroscopy*. Perkin-Elmer Corporation.
- Chen, C. T., Y. U. Idzerda, H. J. Lin, N. V. Smith *et al.* (1995). Experimental confirmation of the X-ray magnetic circular dichroism sum rules for iron and cobalt. *Phys. Rev. Letters* **75**, 152.
- Colominas, C. (1967). Neutron-diffraction investigation of  $\text{CuCr}_2\text{Se}_4$  and  $\text{CuCr}_2\text{Te}_4$ . *Physical Review* **153**, 558.
- Conte, A. M. (2007). Quantum mechanical modeling of nano magnetism. Ph.D. thesis, International school for advanced studies.
- Cowan, R. D. (1981). *The Theory of Atomic Structure and Spectra*. University of California.
- Cramer, S. P., F. M. F. deGroot, Y. Ma, C. T. Chen *et al.* (1991). Ligand Field Strengths and Oxidation States from Manganese L-Edges Spectroscopy. *J. Am. Chem. Soc.* **113**, 7937.
- de Groot, F. M. F. (1994). X-ray-absorption and dichroism of transition-metals and their compounds. *J. Electron Spectrosc. Relat. Phenom.* **67**, 529.
- de Groot, F. M. F. (2001). High-Resolution X-ray Emission and X-ray Absorption Spectroscopy. *Chem. Rev.* **101**, 1779.
- de Groot, F. M. F., J. Faber, J. J. M. Michiels, M. T. Czyzyk *et al.* (1993). Oxygen 1s X-ray absorption of tetravalent titanium oxides: A comparison with single-particle calculations. *Phys. Rev. B* **48**, 2074.
- de Groot, F. M. F., J. C. Fuggle, B. T. Thole and G. A. Sawatzky (1990a). 2p x-ray absorption of 3d transition-metal compounds: An atomic multiplet description including the crystal field. *Phys. Rev. B* **42**, 5459.
- de Groot, F. M. F., J. C. Fuggle, B. T. Thole and G. A. Sawatzky (1990b).  $L_{2,3}$  x-ray-absorption edges of  $d^0$  compounds:  $\text{K}^+$ ,  $\text{Ca}^{2+}$ ,  $\text{Sc}^{3+}$ , and  $\text{Ti}^{4+}$  in  $O_h$  (octahedral) symmetry. *Phys. Rev. B* **41**, 928.
- de Groot, F. M. F. and A. Kotani (2008). *Core level spectroscopy of solids*. CRC Press, London.
- Deb, A., N. Hiraoka, M. Itou, Y. Sakurai *et al.* (2002). Magnetic Compton scattering study of colossal magnetoresistance materials  $\text{Fe}_{1-x}\text{Cu}_x\text{Cr}_2\text{S}_4$ . *Physical Review B* **66**, 100407(R).
- Deb, A., N. Hiraoka, M. Ituo, Y. Sakurai *et al.* (2004). Evidence of negative spin polarization in ferromagnetic  $\text{Sr}_2\text{FeMoO}_6$  as observed in a magnetic Compton profile study. *Phys. Rev. B* **70**.

- Deb, A., M. Mizumaki, T. Muro, Y. Sakurai *et al.* (2003). Soft-x-ray magnetic-circular-dichroism study of the colossal-magnetoresistance spinel  $\text{Fe}_{0.5}\text{Cu}_{0.5}\text{Cr}_2\text{S}_4$ . *Physical Review B* **68**, 014427.
- di Trolio, A., R. Larciprete, A. M. Testa, D. Fiorani *et al.* (2006). Double perovskite  $\text{Sr}_2\text{FeMoO}_6$  films: Growth, structure, and magnetic behavior. *Journal of Applied Physics* **100**.
- Dzyaloshinsky, I. (1958). A thermodynamic theory of weak ferromagnetism of antiferromagnetics. *J. Phys. Chem. Solids* **4**, 241.
- Ebert, H. (1996). Magneto-optical effects in transition metal systems. *Rep. Prog. Phys.* **59**, 1665.
- Einstein, A. (1905). Über einen die Erzeugung und Verwandlung des Lichtes betreffenden heuristischen Gesichtspunkt. *Annalen der Physik* **17**, 132.
- Fadley, C. S. and D. A. Shirley (1970). Multiplet Splitting of Metal-Atom Electron Binding Energies. *Phys. Rev. A* **2**, 1109.
- Fang, T. T. (2005). Reassessment of the role of antiphase boundaries in the low-field magnetoresistance of  $\text{Sr}_2\text{FeMoO}_6$ . *Phys. Rev. B* **71**.
- Fix, T., A. Barla, C. Ulhaq-Bouillet, S. Colis *et al.* (2007). Absence of tunnel magnetoresistance in  $\text{Sr}_2\text{FeMoO}_6$ -based magnetic tunnel junctions. *Chem.phys.letters* **434**, 276.
- Fontaine, A. (1995). *Interaction of X-rays with Matter: Absorption Spectroscopy*. HERCULES: Grenoble.
- Fritsch, V., J. Deisenhofer, R. Fichtl, J. Hemberger *et al.* (2003). Anisotropic colossal magnetoresistance effects in  $\text{Fe}_{1-x}\text{Cu}_x\text{Cr}_2\text{S}_4$ . *Physical Review B* **67**, 144419.
- Galakhov, V. R., M. Demeter, S. Bartkowski, M. Neumann *et al.* (2002). Mn 3s exchange splitting in mixed-valence manganites. *Phys. Rev. B* **65**, 113102.
- Garcia-Landa, B., C. Ritter, M. R. Ibarra, J. Blasco *et al.* (1999). Magnetic and magnetotransport properties of the ordered perovskite  $\text{Sr}_2\text{FeMoO}_6$ . *Solid State Communications* **110**, 435.
- Goodenough, J. B. (1969). Description of outer d electrons in thiospinels. *J. Phys. Chem. Solids* **30**, 261.
- Gota, S., M. Gautier-Soyer and M. Sacchi (2000). Fe 2p absorption in magnetic oxides: Quantifying angular-dependent saturation effects. *Phys. Rev. B* **62**.
- Günther, A. (2003). Magnetische Anisotropie gebänderter Eisenerze und deren Beziehung zu kristallographischen Vorzugsorientierungen. Ph.D. thesis, TU Clausthal.
- Haacke, G. and L. C. Beegle (1966). Anomalous thermoelectric power of  $\text{FeCr}_2\text{S}_4$  near the curie temperature. *Physical Review Letters* **17**, 427.
- Haacke, G. and L. C. Beegle (1967). Magnetic properties of the spinel system  $\text{Fe}_{1-x}\text{Cu}_x\text{Cr}_2\text{S}_4$ . *J.Phys.Chem.Solids* **28**, 1699.
- Haas, C. (1968). Spin-Disorder Scattering and Magnetoresistance of Magnetic Semiconductors. *Physical Review* **168**, 531.
- Haas, C., A. M. J. G. van Run, P. F. Bongers and W. Albers (1967). The Magnetoresistance of n-type  $\text{CdCr}_2\text{S}_4$ . *Solid State Communications* **5**, 657.
- Hallwachs, W. (1888). Über den Einfluss des ultravioletten Lichtes auf die elektrische Entladung. *Wiedemannsche Annalen* **33**, 301.

- Han, S. W., J. S. Kang, S. S. Lee, G. Kim *et al.* (2006). Photoemission, soft x-ray absorption, and magnetic circular dichroism spectroscopy study of  $\text{Fe}_{1-x}\text{Cu}_x\text{Cr}_2\text{S}_4$  ( $0.1 \leq x \leq 0.5$ ) spinel sulfides. *J. Phys.: Condens. Matter* **18**, 7413.
- Hebrew University of Jerusalem (2004). Heinrich Rudolf Hertz. *Institute of Chemistry* URL: <http://chem.ch.huji.ac.il/history/hertz.htm> (updated and corrected on July 30, 2004).
- Hertz, H. (1887). Über den Einfluss des ultravioletten Lichtes auf die elektrische Entladung. *Wiedemannsche Annalen* **31**, 983.
- Hollas, J. M. (1998). *High resolution spectroscopy*. Wiley (2 edition).
- Hu, Z., G. Kaindl, S. A. Warda, D. Reinen *et al.* (1998a). On the electronic structure of Cu(III) and Ni(III) in  $\text{La}_2\text{Li}_{1/2}\text{Co}_{1/2}\text{O}_4$ ,  $\text{Nd}_2\text{Li}_{1/2}\text{Ni}_{1/2}\text{O}_4$ , and  $\text{Cs}_2\text{KCuF}_6$ . *Chem. Phys.* **232**, 63.
- Hu, Z., C. Mazumdar, G. Kaindl, F. M. F. de Groot *et al.* (1998b). Valence electron distribution in  $\text{La}_2\text{Li}_{1/2}\text{Cu}_{1/2}\text{O}_4$ ,  $\text{Nd}_2\text{Li}_{1/2}\text{Ni}_{1/2}\text{O}_4$ , and  $\text{La}_2\text{Li}_{1/2}\text{Co}_{1/2}\text{O}_4$ . *Chem. Phys. Lett.* **297**, 321.
- Ikeda, N., H. Ohsumi, K. Ohwada, K. Ishii *et al.* (2005a). Ferroelectricity from iron valence ordering in the charge-frustrated system  $\text{LuFe}_2\text{O}_4$ . *Nature (London)* **436**, 1136.
- Ikeda, N., M. Shigeo and K. Kohn (2005b). Charge Ordering and Dielectric Dispersion in Mixed Valence Oxides  $\text{RFe}_2\text{O}_4$ . *Ferroelectrics* **314**, 41.
- Isobe, M., N. Kimizuka, J. Iida and S. Takekawa (1990). Structures of  $\text{LuFeCoO}_4$  and  $\text{LuFe}_2\text{O}_4$ . *Acta Cryst.* **C46**, 1917.
- Kanamori, J. (1959). Superexchange interaction and symmetry properties of electron orbitals. *J. Phys. Chem. Solids* **10**, 87.
- Kanchana, V., G. Vaitheeswaran, M. Alouani and A. Delin (2007). Electronic structure and x-ray magnetic circular dichroism of  $\text{Sr}_2\text{FeMoO}_6$ : Ab initio calculations. *Phys. Rev. B* **75**.
- Kang, J. S., S. W. Han, S. S. Lee, G. Kim *et al.* (2007). Valence States of Transition-Metal Ions and Electronic Structures of Spinel  $\text{Fe}_{1-x}\text{Cu}_x\text{Cr}_2\text{S}_4$ . *IEEE Trans. Magn.* **43**, 3046.
- Kang, J. S., J. H. Kim, A. Sekiyama, S. Kasai *et al.* (2002). Bulk-sensitive photoemission spectroscopy of  $\text{A}_2\text{FeMoO}_6$  double perovskites ( $\text{A} = \text{Sr}, \text{Ba}$ ). *Phys. Rev. B* **66**.
- Kapusta, C., P. Fischer and G. Schütz (1999). Magnetic X-ray absorption spectroscopy. *Journal of Alloys and Compounds* **286**, 37.
- Kasuya, T. and A. Yanase (1968). Anomalous transport phenomena in eu-chalcogenide alloys. *Reviews of modern physics* **40**, 4.
- Kim, C. S., I. B. Shim, M. Y. Ha, C. S. Kim *et al.* (1993). Magnetic properties of the monoclinic  $\text{FeRh}_2\text{Se}_4$ . *J. Appl. Phys.* **73**, 5707.
- Kim, D.-Y., J. S. Kim, B. H. Park, J.-K. Lee *et al.* (2004).  $\text{SrFeO}_3$  nanoparticles-dispersed  $\text{SrMoO}_4$  insulating thin films deposited from  $\text{Sr}_2\text{FeMoO}_6$  target in oxygen atmosphere. *Applied Physics Letters* **84**, 5037.
- Kim, J., S. B. Kim, C. U. Jung and B. W. Lee (2009). Magnetic Anisotropy in  $\text{LuFe}_2\text{O}_4$  Single Crystal. *IEEE Trans. Magn.* **45**, 2608.
- Kim, S. J., W. C. Kim and C. S. Kim (2002). Neutron diffraction and Mossbauer studies on  $\text{Fe}_{1-x}\text{Cr}_2\text{S}_4$  ( $x = 0.0, 0.04, 0.08$ ). *J. Appl. Phys.* **91**, 7935.



- Kimura, A., J. Matsuno, J. Okabayashi, A. Fujimori *et al.* (2001). Soft x-ray magnetic circular dichroism study of the ferromagnetic spinel-type Cr chalcogenides. *Physical Review B* **63**, 224420.
- Klencsar, Z., E. Kuzmann, Z. Homonnay, Z. Nemeth *et al.* (2005). Mossbauer study of Cr-based chalcogenide spinels  $\text{Fe}_{1-x}\text{Cu}_x\text{Cr}_2\text{S}_4$ . *Physica B* **358**, 212401.
- Klencsar, Z., E. Kuzmann, Z. Homonnay, A. Vertes *et al.* (2002). Magnetic Relaxation and Its Relation to Magnetoresistance in  $\text{FeCr}_2\text{S}_4$  Spinel. *Hyperfine Interact.* **144**, 261.
- Kobayashi, K. L., T. Kimura, H. Sawada, K. Terakura *et al.* (1998). Room-temperature magnetoresistance in an oxide material with an ordered double-perovskite structure. *Nature* **395**, 677.
- Kovtun, N. M., V. T. Kalinnikov, A. A. Shemyakov, V. K. Prokopenko *et al.* (1977). Concerning one mechanism of Phase-transition from ferromagnetic into ferrimagnetic state. *JETP LETTERS* **25**, 148.
- Kovtun, N. M., E. P. Naiden, V. K. Prokopenko and A. A. Shemyakov (1979). Neutron-diffraction investigation of the magnetic-structure of the copper-chromium chalcogenide spinel  $\text{CuCr}_2\text{S}_4$ . *Sov. Phys. JETP* **50**, 207.
- Kovtun, N. M., V. K. Prokopenko and A. A. Shemyakov (1978). Electroconductivity and electron exchange in spinel structures. *Solid State Communications* **26**, 877.
- Kramers, H. A. (1934). L'interaction Entre les Atomes Magnetogenes dans un Cristal Paramagnetique. *Physica* **1**, 182.
- Kuepper, K. (2005). Electronic and magnetic properties of transition metal compounds: An x-ray spectroscopic study. Ph.D. thesis, Universität Osnabrück.
- Kuepper, K., I. Balasz, H. Hesse, A. Winiarski *et al.* (2004). Electronic and magnetic properties of highly ordered  $\text{Sr}_2\text{FeMoO}_6$ . *phys.stat.sol. (a)* **15**, 3252.
- Kuepper, K., M. Kadiroglu, A. V. Postnikov, K. C. Prince *et al.* (2005). Electronic structure of highly ordered  $\text{Sr}_2\text{FeMoO}_6$  XPS and XES studies. *J.Phys.: Condens. Matter* **17**, 4309.
- Kuepper, K., M. Raekers, C. Taubitz, H. Hesse *et al.* (2008). Fe valence state of  $\text{Sr}_2\text{FeMoO}_6$  probed by x-ray absorption spectroscopy: The sample age matters. *J. Appl. Phys.* **104**, 036103.
- Kuepper, K., M. Raekers, C. Taubitz, M. Prinz *et al.* (2009). Charge order, enhanced orbital moment, and absence of magnetic frustration in layered multiferroic  $\text{LuFe}_2\text{O}_4$ . *Phys. Rev. B* **80**, 220409.
- Kurmaev, E. Z., A. V. Postnikov, H. M. Palmer, C. Greaves *et al.* (2000). Electronic structure of  $\text{FeCr}_2\text{S}_4$  and  $\text{Fe}_{0.5}\text{Cu}_{0.5}\text{Cr}_2\text{S}_4$ . *J.Phys.: Condens. Matter* **12**, 5411.
- Kuzmany, H. (1998). *Solid state spectroscopy- an introduction*. Springer-Verlag, Berlin Heidelberg.
- Lang, O., C. Felser, R. Seshadri, F. Renz *et al.* (2000). Magnetic and Electronic Structure of the CMR Chalcospinel  $\text{Fe}_{0.5}\text{Cu}_{0.5}\text{Cr}_2\text{S}_4$ . *Adv. Matter.* **12**, 65.
- Larsen, P. K. and A. B. Voermans (1973). Origin of the conductivity minimum and the negative magnetoresistance in n-type sulpho-spinels. *J.Phys.Chem.Solids* **34**, 645.
- Lehmann, H. W. and G. Harbeke (1967). Semiconducting and Optical Properties of Ferromagnetic  $\text{CdCr}_2\text{S}_4$  and  $\text{CdCr}_2\text{Se}_4$ . *Journal of Applied Physics* **38**, 946.
- Lehmann, H. W. and M. Robbins (1966). Electrical Transport Properties of the Insulating Ferromagnetic Spinel  $\text{CdCr}_2\text{S}_4$  and  $\text{CdCr}_2\text{Se}_4$ . *Journal of Applied Physics* **37**, 1389.

- Li, C. H., F. Wang, Y. Liu, X. Q. Zhang *et al.* (2009). Electrical control of magnetization in charge-ordered multiferroic  $\text{LuFe}_2\text{O}_4$ . *Phys. Rev. B* **79**, 172412.
- Li, C. H., X. Q. Zhang, Z. H. Cheng and Y. Sun (2008). Electric field induced phase transition in charge-ordered  $\text{LuFe}_2\text{O}_4$ . *Applied Physics Letters* **93**, 152103.
- Lind, D. M., S. P. Tay, S. D. Berry, J. A. Borchers *et al.* (1993). Structural and magnetic ordering in iron oxide/nickel oxide multilayers by X-ray and neutron diffraction. *J. Appl. Phys.* **73**, 6886.
- Linden, J., T. Yamamoto, M. Karppinen, H. Yamauchi *et al.* (2000). Evidence for valence fluctuations of Fe in  $\text{Sr}_2\text{FeMoO}_{6-w}$  double perovskite. *appl.phys.letters* **76**, 2925.
- Lotgering, F. K. and R. P. van Staple (1967). Magnetic and electrical properties of copper containing sulphides and selenides with spinel structure. *Solid State Communications* **5**, 143.
- Lotgering, F. K., R. P. van Staple, G. H. A. M. van der Steen and J. S. van Wieringen (1969). Magnetic properties, conductivity and ionic ordering in  $\text{Fe}_{1-x}\text{Cu}_x\text{Cr}_2\text{S}_4$ . *J. Phys. Chem. Solids* **30**, 799.
- Lytle, F. W. and R. B. Gregor (1988). Discussion of X-ray absorption near-edge structure-application to Cu in the High- $T_C$  superconductors  $\text{La}_{1.8}\text{Sr}_{0.2}\text{CuO}_4$  and  $\text{YBa}_2\text{Cu}_3\text{O}_7$ . *Phys. Rev. B* **37**, 1550.
- Mannini, M., F. Pineider, P. Saintavit, C. Danieli *et al.* (2009a). Magnetic memory of a single-molecule quantum magnet wired to a gold surface. *Nature Materials* **8**, 194.
- Mannini, M., F. Pineider, P. Saintavit, L. Joly *et al.* (2009b). X-Ray Magnetic Circular Dichroism Picks out Single-Molecule Magnets Suitable for Nanodevices. *Adv. Matter.* **21**, 167.
- Martin, G. W., A. T. Kellogg, R. White, R. M. White *et al.* (1969). Exchangestriction in  $\text{CdCr}_2\text{S}_4$  and  $\text{CdCr}_2\text{Se}_4$ . *Journal of Applied Physics* **40**, 1015.
- Martinez, B., J. Navarro, L. I. Balcells and J. Fontcuberta (2000). Electronic transfer in  $\text{Sr}_2\text{FeMoO}_6$  perovskites. *J.Phys.: Condens. Matter* **12**, 10515.
- Mills, D. L. (1989). Surface anisotropy and surface spin canting in the semi-infinite ferromagnet. *Phys. Rev. B* **39**, 12307.
- Moffit, W. and C. J. Ballhausen (1956). Quantum Theory. *Annu. Rev. Phys. Chem.* **7**, 107.
- Moreno, M. S., J. E. Gayone, M. Abbate, A. Caneiro *et al.* (2001). Fe and Mo Valences in  $\text{Sr}_2\text{FeMoO}_6$ . *Solid State Communications* **120**, 161.
- Moulder, J. F., W. F. Stickle, P. E. Sobol and K. D. Bomben (1992). *Handbook of X-ray Photoelectron Spectroscopy*. Perkin-Elmer Corporation, Minnesota.
- Müller, A., L. Marshall, C. Schröder, R. Modler *et al.* (2001). Classical and Quantum Magnetism in Giant Keplerate Magnetic Molecules. *Chem. Phys. Chem.* **2**, 517.
- Müller, A., S. Sarkar, S. Q. N. Shah, H. Bögge *et al.* (1999). Archimedean Synthesis and Magic Numbers: "Sizing" Giant Molybdenum-Oxide-Based Molecular Spheres of the Keplerate Type. *Angew. Chem. Int. Ed.* **38**, 3238.
- Muller, J. E., O. Jepsen, O. K. Andersen and J. W. Wilkins (1978). Systematic structure in the K-edge photoabsorption spectra of the 4d Transition Metals: Theory **40**, 720.
- Nagano, A., M. Naka, J. Nasu and S. Ishihara (2007). Electric Polarization, Magnetoelectric Effect, and Orbital State of a Layered Iron Oxide with Frustrated Geometry. *Phys. Rev. Letters* **99**, 217202.

- Naka, M., A. Nagano and S. Ishihara (2008). Magnetodielectric phenomena in a charge- and spin-frustrated system of layered iron oxide. *Phys. Rev. B* **77**, 224441.
- Nakajima, R., J. Stöhr and Y. U. Idzerda (1999). Electron-yield saturation effects in L-edge x-ray magnetic circular dichroism spectra of Fe, Co, and Ni. *Phys. Rev. B* **59**, 6421.
- Nakatani, I., H. Nose and K. Masumoto (1978). Magnetic properties of  $\text{CuCr}_2\text{Se}_4$  single crystals. *J. Phys. Chem. Solids* **39**, 743.
- Nath, A., Z. Klencsar, E. Kuzmann, Z. Homonnay *et al.* (2002). Nanoscale magnetism in the chalcogenide spinel  $\text{FeCr}_2\text{S}_4$  : Common origin of colossal magnetoresistivity. *Phys. Rev. B* **66**, 212401.
- Natoli, C. R., M. Benfatto and S. Doniach (1986). Use of general potentials in multiple-scattering theory. *Phys. Rev. A* **34**, 4682.
- Navarro, J., C. Frontera, D. Rubi, N. Mestres *et al.* (2003). Aging of  $\text{Sr}_2\text{FeMoO}_6$  and related oxides. *Mater. Res. Bull.* **38**, 1477.
- Okada, K. and A. Kotani (1992a). Complementary roles of Co 2p X-ray absorption and photoemission spectra in CoO. *J. Phys. Soc. Jpn.* **61**(2), 449.
- Okada, K. and A. Kotani (1992b). Interatomic and intraatomic configuration interactions in core-level X-ray photoemission spectra of late transition-metal compounds. *J. Phys. Soc. Jpn.* **61**(12), 4619.
- Okada, K. and A. Kotani (1993). Theory of core-level X-ray photoemission and photoabsorption in Ti compounds. *J. Electron Spectrosc. Relat. Phenom.* **62**(1-2), 131.
- Okada, K., A. Kotani and B. T. Thole (1992). Charge-transfer satellites and multiplet splitting in X-ray photoemission spectra of late transition-metal halides. *J. Electron Spectrosc. Relat. Phenom.* **58**, 325.
- Palmer, H. M. and C. Greaves (1999). Structural, magnetic and electronic properties of  $\text{Fe}_{0.5}\text{Cu}_{0.5}\text{Cr}_2\text{S}_4$ . *J. Mater. Chem.* **9**, 637.
- Park, J. H., E. Vescovo, H. J. Kim, C. Kwon *et al.* (1998). Direct evidence for a half-metallic ferromagnet. *Nature* **392**, 794.
- Park, M. S., S. K. Kwon, S. J. Youn and B. I. Min (1999). Half-metallic electronic structures of giant magnetoresistive spinels:  $\text{Fe}_{1-x}\text{Cu}_x\text{Cr}_2\text{S}_4$  ( $x=0.0, 0.5, 1.0$ ). *Physical Review B* **59**, 15.
- Peatman, W. B. (1997). *Gratings, Mirrors and Slits: Beamline Design for Soft X-ray Synchrotron Radiation Sources*. Amsterdam: Gordon and Reach Science Publishers.
- Prinz, M. (2009). X-ray spectroscopic and magnetic investigations of selected manganese-containing molecular high-spin complexes. Ph.D. thesis, University of Osnabrueck.
- Raekers, M. (2009). An x-ray spectroscopic study of novel materials for electronic applications. Ph.D. thesis, University of Osnabrueck.
- Raekers, M., K. Kuepper, H. Hesse, I. Balasz *et al.* (2006). Investigation of chemical and grain boundary effects in highly ordered  $\text{Sr}_2\text{FeMoO}_6$ : XPS and Mossbauer studies. *Journal of Optoelectronics and Advanced Materials* **8**, 455.
- Ramirez, A. P. (1997). Colossal magnetoresistance. *J. Phys.: Condens. Matter* **9**, 8171.
- Ramirez, A. P., R. J. Cava and J. Krajewski (1997). Colossal magnetoresistance in Cr-based chalcogenide spinels. *Nature* **386**, 156 .

- Ray, S., K. Ashwani, D. D. Sarma, R. Cimino *et al.* (2001). Electronic and Magnetic Structures of  $\text{Sr}_2\text{FeMoO}_6$ . *Physical Review Letters* **87**.
- Regan, T. J., H. Ohldag, C. Stamm, F. Nolting *et al.* (2001). Chemical effects at metal/oxide interfaces studied by x-ray-absorption spectroscopy. *Physical Review B* **64**, 214422.
- Rehr, J. J., A. Ankudinov and S. Zabinsky (1998). New developments in NEXAFS/EXAFS theory. *Catalysis Today* **39**, 263.
- Riedel, E. and E. Horvath (1973). Cation-anion intervals in copper and chromium thiospinels. *Mater. Res. Bull.* **8**, 973.
- Robbins, M., H. W. Lehmann and J. G. White (1967). Neutron diffraction and electrical transport properties of  $\text{CuCr}_2\text{Se}_4$ . *J. Phys. Chem. Solids* **153**, 558.
- Saalfank, R. W., I. Bernt, M. M. Chowdhry, F. Hampel *et al.* (2001). Ligand-to-metal ratio controlled assembly of tetra- and hexanuclear clusters towards single-molecule magnets. *Chemistry-A European Journal* **7**, 2765.
- Saalfank, R. W., A. Scheurer, I. Bernt, F. W. Heinemann *et al.* (2006). The  $\text{Fe}^{III}[\text{Fe}^{III}(\text{L}^1_2)]_3$  star-type single-molecule magnet. *Dalton transactions* **23**, 2865.
- Saitoh, T., M. Nakatake, A. Kakizaki, H. Nakajima *et al.* (2002). Half-metallic density of states in  $\text{Sr}_2\text{FeMoO}_6$  due to Hund's rule coupling. *Phys. Rev. B* **66**.
- Sanchez, D., J. A. Alonso, M. Garcia-Hernandez, M. J. Martinez-Lope *et al.* (2002). Origin of neutron magnetic scattering in antisite-disordered  $\text{Sr}_2\text{FeMoO}_6$  double perovskites. *Phys. Rev. B* **65**.
- Sangaletti, L., L. E. Depero, P. S. Bagus and F. Parmigiani (1995). A proper Anderson Hamiltonian treatment of the 3s photoelectron spectra of MnO, FeO, CoO, NiO. *Chemical Physics Letters* **245**, 463.
- Schnack, J. and M. Luban (2000). Rotational modes in molecular magnets with antiferromagnetic Heisenberg exchange. *Phys. Rev. B* **63**, 014418.
- Schnalle, R., A. M. Lauchli and J. Schnack (2009). Approximate eigenvalue determination of geometrically frustrated magnetic molecules. *Condensed matter physics* **12**, 331.
- Schütz, G., W. Wagner, W. Wilhelm, P. Kienle *et al.* (1987). Absorption of circularly polarised X-rays in iron. *Phys. Rev. Lett.* **58**, 737.
- Shirane, G., D. E. Cox and S. J. Pickart (1964). Magnetic Structures in  $\text{FeCr}_2\text{S}_4$  and  $\text{FeCr}_2\text{O}_4$ . *J. Appl. Phys.* **35**, 954.
- Shirley, D. A. (1972). High-resolution x-ray photoemission spectrum of the valence band of gold. *Phys. Rev. B* **5**, 4709.
- Siegbahn, K., D. Hammond, H. Fellner-Feldegg and E. F. Barnett (1972). Electron spectroscopy with monochromatized X-rays. *Nature* **176**, 245.
- Siegbahn, K., C. Nordling, A. Fahlman, R. Nordberg *et al.* (1967). *ESCA-Atomic, Molecular and Solid State Structure Studied by Means of Electron Spectroscopy*. Almquist and Wicksell, Uppsala.
- Siegbahn, K., C. Nordling, G. Johansson, J. Hedman *et al.* (1969). *ESCA Applied to Free Molecules*. North Holland, Amsterdam.
- Siratori, K., S. Funahashi, J. Iida and M. Tanaka (1992). Ferrites, proc. 6th int. conf. on ferrites tokyo and kyoto, p.703. In *The Japan Society of Powder and Powder Metallurgy*.

- Son, B. S., S. J. Kim, B. W. Lee and C. S. Kim (2005). Anomalous electron structure and magnetic properties in copper doped sulphur spinel. *J. Magn. Magn. Mater.* **290**, 381.
- Spender, M. R. and A. H. Morrish (1972). Mossbauer study of Ferrimagnetic spinel  $\text{FeCr}_2\text{S}_4$ . *Can. J. Phys.* **50**, 1125.
- Stöhr, J. (1992). *NEXAFS Spectroscopy*. Springer-Verlag, Berlin.
- Stöhr, J. and H. C. Siegmann (2006). *Magnetism- From Fundamentals to Nanoscale Dynamics*. Springer-Verlag, Berlin, Heidelberg, New York.
- Subramanian, M. A., T. He, J. Chen, N. S. Rogado *et al.* (2006). Giant Room-Temperature Magnetodielectric Response in the Electronic Ferroelectric  $\text{LuFe}_2\text{O}_4$ . *Adv. Matter.* **18**, 1737.
- Sugano, S., Y. Tanabe and H. Kamimura (1970). *Multiplets of Transition Metal Ions*. Academic Press: New York.
- Takacs, A. F. (2005). Electronic structure studies of metal-organic and intermetallic compounds. Ph.D. thesis, University of Osnabrueck.
- Takacs, A. F., M. Neumann, A. V. Postnikov, K. Kuepper *et al.* (2006). Electronic structure study by means of x-ray spectroscopy and theoretical calculations of the "ferric star" single molecule magnet. *J. Chem. Phys.* **124**, 044503.
- Tarling, D. H. and F. Hrouda (1993). *The magnetic anisotropy of rocks*. Chapman and Hall.
- Taubitz, C., K. Kuepper, M. Raekers, V. R. Galakhov *et al.* (2009). Reinvestigation of the Fe, Cu and Cr valences in  $(\text{FeCu})\text{Cr}_2\text{S}_4$  spinels. *phys.stat.sol. (b)* **246**, 1470.
- Taubitz, D. (). Time dependend X-ray spectroscopic investigations of  $\text{Cu}^{2+}$  to  $\text{Cu}^{1+}$  valency change in copper-substituted heteropolyanions. Bachelor Thesis, AG Neumann, Osnabrück (2008).
- Teramura, Y., A. Tanaka and J. Takeo (1996). Effect of Coulomb interaction on the X-ray magnetic circular dichroism spin sum rule in 3d transition elements. *J. Phys. Soc. Jpn.* **65**, 1053.
- Thole, B. T., P. Carra, F. Sette and G. van der Laan (1992). X-ray Circular Dichroism as a probe of orbital magnetization. *Phys. Rev. Letters* **68**, 1943.
- Thole, B. T., G. Van der Laan and P. H. Butler (1988). Spin-mixed ground state of Fe phthalocyanine and the temperature-dependent branching ratio in X-ray absorption spectroscopy. *Chem. Phys. Letters* **149**, 295.
- Thomson, J. J. (1897). Cathode rays. *Philosophical Magazine* **44**, 293.
- Todea, A. M., A. Merca, H. Bögge, T. Glaser *et al.* (2010). Porous Capsules  $\{(M)M_5\}_{12} \text{Fe}_{30}^{\text{III}}$  ( $M = \text{Mo}^{\text{VI}}, \text{W}^{\text{VI}}$ ): Sphere Surface Supramolecular Chemistry with 20 Ammonium Ions, Related Solution Properties, and Tuning of Magnetic Exchange Interactions. *Angew. Chem. Int. Ed.* **49**, 514.
- Tomioka, Y., T. Okuda, Y. Okimoto, R. Kumai *et al.* (2000). Magnetic and electronic properties of a single crystal of ordered double perovskite  $\text{Sr}_2\text{FeMoO}_6$ . *Phys. Rev. B* **61**, 422.
- Tougaard, S. (1990). Inelastic background correction and quantitative surface analysis. *J. Electron. Spectr. Rel. Phen.* **52**, 243.
- Tsurkan, V., J. Groza, G. Bocelli, D. Samusi *et al.* (2005). Influence of cation substitution on the magnetic properties of the  $\text{FeCr}_2\text{S}_4$  ferrimagnet. *J. Phys. Chem. Solids* **66**, 2040.

- Tsurkan, V., S. Plogmann, M. Demeter, D. Hartmann *et al.* (2000). Splitting of the Cr 2p ions states in some ternary sulphides and selenides. *Eur. Phys. J. B* **15**, 401.
- Uhlenbrock, S. (1994). Untersuchungen zur elektronischen Struktur einfacher ÜbergangsmetallOxide unter besonderer Berücksichtigung des NickelOxids. Ph.D. thesis, Universität Osnabrück.
- van der Laan, G., R. A. D. Patrick, J. M. Charnock and B. A. Grguric (2002). Cu L<sub>2,3</sub> x-ray absorption and the electronic structure of nonstoichiometric Cu<sub>5</sub>FeS<sub>4</sub>. *Physical Review B* **66**, 045104.
- van der Laan, G., M. Surman, M. A. Hoyland, C. F. J. Flipse *et al.* (1992). Resonant photoemission at the Ni 2p core level as a probe of electron correlation effects in nickel. *Phys. Rev. B* **46**.
- van der Laan, G., J. Zaanen and G. A. Sawatzky (1986). Comparison of X-ray absorption with X-ray photoemission of nickel dihalides and NiO. *Phys. Rev. B* **33**, 4253.
- van Diepen, A. M. and R. P. van Staple (1973). Ordered local distortion in cubic FeCr<sub>2</sub>S<sub>4</sub>. *Solid State Communications* **13**, 1651.
- van Vleck, J. H. (1934). The Dirac Vector Model in Complex Spectra. *Physical Review* **45**, 405.
- Veal, B. W. and A. P. Paulikas (1983). X-Ray-Photoelectron Final-State Screening in Transition-Metal Compounds. *Phys.Rev.Letters* **51**, 1995.
- von Molnar, S. and S. Methfessel (1967). Giant Negative Magnetoresistance in Ferromagnetic Eu<sub>1-x</sub>Gd<sub>x</sub>Se. *Journal of Applied Physics* **38**, 959.
- Vvdensky, D. D. (1992). *In Unoccupied electronic states*. Springer-Verlag, Berlin.
- Wasscher, C. D. and C. Haas (1964). Contribution of magnon-drag to the thermoelectric power of antiferromagnetic MnTe. *Physics Letters* **8**, 302.
- Watanabe, T. and I. Nakada (1978). Preparation of some chalcogenide spinel single-crystals and their electronic properties. *Jpn. J. Appl. Phys.* **17**, 1745.
- Weissbluth, M. (1978). *Atoms and Molecules*. Plenum Press: New York.
- Wen, J., G. Xu, G. Gu and S. M. Shapiro (2009). Magnetic-field control of charge structures in the magnetically disordered phase of multiferroic LuFe<sub>2</sub>O<sub>4</sub>. *Phys. Rev. B* **80**, 020403.
- Wu, W., V. Kiryukhin, H. J. Noh, K. T. Ko *et al.* (2008). Formation of Pancakelike Ising Domains and Giant Magnetic Coercivity in Ferrimagnetic LuFe<sub>2</sub>O<sub>4</sub>. *Phys. Rev. Letters* **101**, 137203.
- Xiang, H. J., E. J. Kan, S. H. Wei, M. H. Whangbo *et al.* (2009). Origin of the Ising ferrimagnetism and spin-charge coupling in LuFe<sub>2</sub>O<sub>4</sub>. *Phys. Rev. B* **80**, 132408.
- Xiang, H. J. and M. H. Whangbo (2007). Charge Order and the Origin of Giant Magnetocapacitance in LuFe<sub>2</sub>O<sub>4</sub>. *Phys. Rev. Letters* **98**, 246403.
- Xu, X. S., M. Angst, T. V. Brinzari, R. P. Hermann *et al.* (2008). Charge Order, Dynamics, and Magnetostructural Transition in Multiferroic LuFe<sub>2</sub>O<sub>4</sub>. *Phys. Rev. Letters* **101**, 227602.
- Yamada, Y., K. Kitsuda, S. Nohdo and N. Ikeda (2000). Charge and spin ordering process in the mixed-valence system LuFe<sub>2</sub>O<sub>4</sub>: Charge ordering. *Phys. Rev. B* **62**, 12167.
- Yamashita, O., Y. Yamaguchi, I. Nakatani, H. Watanabe *et al.* (1979). Polarized neutron-diffraction study of a CuCrSe<sub>4</sub> single-crystal. *J. Phys. Soc. Jpn.* **46**, 1145.

- Yang, Z., X. Bao, S. Tan and Y. Zhang (2004). Magnetic polaron conduction in the colossal magnetoresistance material  $\text{Fe}_{1-x}\text{Cd}_x\text{Cr}_2\text{S}_4$ . *Phys. Rev. B* **69**, 144407.
- Yang, Z., S. Tan, Z. Chen and Y. Zhang (2000). Magnetic polaron conductivity in  $\text{FeCr}_2\text{S}_4$  with the colossal magnetoresistance effect. *Phys. Rev. B* **62**, 13872.
- Yokoyama, H., R. Watanabe and S. Chiba (1967). Nuclear magnetic resonance studies of  $\text{CuCr}_2\text{Se}_4$  and  $\text{CuCr}_2\text{Te}_4$ . *J. Phys. Soc. Jpn.* **23**, 450.
- Yuan, C. L., Y. Zhu and P. P. Ong (2003). Enhancement of room-temperature magnetoresistance in  $\text{Sr}_2\text{FeMoO}_6$  by reducing its grain size and adjusting its tunnel-barrier thickness. *Applied Physics Letters* **82**, 934.
- Zaanen, J., G. A. Sawatzky and J. W. Allen (1985). Band Gaps and Electronic Structure of Transition-Metal Compounds. *Phys. Rev. Letters* **55**, 418.
- Zangwill, A. (1988). *Physics at Surfaces*. Cambridge University Press.
- Zeller, R. (1992). *In Unoccupied electronic states*. Springer-Verlag, Berlin.
- Zener, C. (1951). Interaction between the d-Shells in the Transition Metals. II. Ferromagnetic Compounds of Manganese with Perovskite Structure. *Phys. Rev.* **82**, 403.
- Zeng, L. J., H. X. Yang, Y. Zhang, H. F. Tian *et al.* (2008). Nonlinear current-voltage behavior and electrically driven phase transition in charge-frustrated  $\text{LuFe}_2\text{O}_4$ . *EPL* **84**, 57011.





# List of Publications

- M. Raekers, K. Kuepper, C. Taubitz, M. Prinz, C. Derks, A. Postnikov, S.J. Blundell, D. Prabakharan, S. George and M. Neumann. *Investigation of the electronic structure of  $\text{LuFe}_2\text{O}_4$  by means of XPS, XAS, XES, XMCD and calculations*, in preparation
- T.V. Kuznetsova, V.I. Grebennikov, C. Taubitz, M. Neumann, M.V. Kuznetsov, R.W. Martin and M.V. Yakushev. *A photoelectron spectroscopy study of the evolution of the electronic structure in  $\text{CuInSe}_2$ -based compounds with copper content increase*, in preparation
- M. Prinz, K. Kuepper, C. Taubitz, M. Raekers, B. Biswas, T. Weyhermüller, M. Uhlarz, J. Wosnitza, J. Schnack, A.V. Postnikov, C. Schröder, S.J. George, M. Neumann, P. Chaudhuri. *A star-shaped heteronuclear  $\text{Cr}^{\text{III}}\text{Mn}_3^{\text{II}}$  species and its electronic and reconsidered magnetic structure: Spin frustration studied by X-ray spectroscopic, magnetic and theoretical methods*, Inorg. Chem. **49**, 2093-2102 (2010)
- K. Kuepper, M. Raekers, C. Taubitz, M. Prinz, C. Derks, M. Neumann, A.V. Postnikov, F.M.F. de Groot, C. Piamonteze, D. Prabakharan, S.J. Blundell. *Charge order, enhanced orbital moment, and absence of magnetic frustration in layered multiferroic  $\text{LuFe}_2\text{O}_4$* , Phys. Rev. B **80**, 220409(R) (2009)
- C. Taubitz, K. Kuepper, M. Raekers, V.R. Galakhov, V. Felea, V. Tsurkan, M. Neumann. *Reinvestigation of the Fe, Cu and Cr valences in  $(\text{FeCu})\text{Cr}_2\text{S}_4$  spinels*, phys. stat. sol. B **246**, 1470-1475 DOI 10.1002/pssb.200945057 (2009)
- K. Kuepper, M. Raekers, C. Taubitz, H. Hesse, M. Neumann, A.T. Young, C. Piamonteze, F. Bondino, K.C. Prince. *Fe valence state of  $\text{Sr}_2\text{FeMoO}_6$  probed by x-ray absorption spectroscopy: The sample age matters*, J. Appl. Phys. **104**, 036103 (2008)



# Erklärung über die Eigenständigkeit der erbrachten wissenschaftlichen Leistung

Ich erkläre hiermit, dass ich die vorliegende Arbeit ohne unzulässige Hilfe Dritter und ohne Benutzung anderer als der angegebenen Hilfsmittel angefertigt habe. Die aus anderen Quellen direkt oder indirekt übernommenen Daten und Konzepte sind unter Angabe der Quelle gekennzeichnet.

Ich habe keine entgeltliche Hilfe von Vermittlungs- bzw. Beratungsdiensten (Promotionsberater oder andere Personen) in Anspruch genommen. Niemand hat von mir unmittelbar oder mittelbar geldwerte Leistungen für Arbeiten erhalten, die im Zusammenhang mit dem Inhalt der vorgelegten Dissertation stehen.

Die Arbeit wurde bisher weder im In- noch im Ausland in gleicher oder ähnlicher Form einer anderen Prüfungsbehörde vorgelegt.

.....  
(Ort. Datum)

.....  
(Unterschrift)